Complex Electrochemical Processes in Materials Science: Case Studies of Aluminum Alloy Corrosion and Sonoelectrochemistry

Habilitation Thesis

submitted to the

Faculty of Natural and Materials Sciences
Clausthal University of Technology

by

Dr. rer. nat. Oliver Schneider
Diplom-Chemiker
Institute of Metallurgy
Clausthal University of Technology
Clausthal-Zellerfeld, Germany

June 2010

Fachgebiet: Angewandte Physikalische Chemie

Wissenschaftlicher Vortrag und Kolloquium:

Datum: 16.11.2010

Titel des Vortrags: Metallorganische Gerüstverbindungen (MOFs) als neuartige Wasserstoffspeicher

Probevorlesung:

Datum: 17.12.2010

Thema der Vorlesung: Die Abscheidung von Kohlendioxid aus Rauchgasen und seine permanente Speicherung

Acknowledgments

The experimental work for this thesis has been performed at two places: Part of the corrosion studies was performed in the Center for Electrochemical Science and Engineering at University of Virgina, Charlottesville, USA. The other part of the corrosion studies and the sonoelectrochemical and conducting polymer work was performed in the Institute of Metallurgy at Clausthal University of Technology.

I would like to thank Prof. Borchardt and Prof. Holger Fritze for the opportunity to come to Clausthal after my postdoctoral stay in the United States. I would also like to thank the entire group of Prof. Borchardt and the other present and past colleagues in the Institute of Metallury. Prof. Dr. R. G. Kelly I would like to thank for the great time in his group at UVa.

A special acknowledgment is given to all my co-authors in the work summarized in this thesis. This concerns especially Ms. Sladjana Martens, Ms. Jovana Zecevic, and Prof. Christos Argirusis for the sonoelectrochemical work, and Dr. Gabriel Ilevbare, Ms. Jackie Williams, Prof. R. G. Kelly, and Prof. J. R. Scully for the work at UVa. A special thanks also to Prof. Andreas Bund (Dresden) for many fruitful discussions and joint work.

The work presented here would not have been possible without the help of all the technicians both at UVa and in Clausthal. In Clausthal this includes the members of the mechanical and electrical workshop, the metallographic, and the chemical lab, especially Mr. Werman. A special thank to Mr. Ebeling and to Ms. Hofmann. Outside of the IMET I would like to thank Mr. Herrmann for the EPMA measurements.

The financial funding of the work by German Research Foundation (DFG), European Union, and AFOSR is acknowledged.

Finally I would like to thank my family and my friends, and to all those I just forgot to mention.

Standard Abbreviations

AFM	Atomic Force Microscopy
BV	Butler-Volmer
CCC	Chromate Conversion Coating
CLSM	Confocal Laser Scanning Microscopy
CV	Cyclic Voltammetry
CTAHS	Cetyl Trimethyl Ammonium Hydrogen Sulfate
DMSO	Dimethylsulfoxide
E_{corr}	Corrosion Potential
E_{pit}	Pitting Potential
ECM	Electrochemical Machining
EDX	Energy Dispersive Spectroscopy
EIS	Electrochemical Impedance Spectroscopy
EQCM	Electrochemical Quartz Crystal Microbalance
EPMA	Electron Probe Microanalysis
EPR	Electron Paramagnetic Resonance
ETR	Electron Transfer Reaction
EXAFS	Extended X-Ray Absorption Fine Structure
FTIR	Fourier Transform Infrared Spectroscopy
HER	Hydrogen Evolution Reaction
HOPG	Highly Oriented Pyrolytic Graphite
IL	Ionic Liquid
IMC	Intermetallic Compound Phase
LEIM	Local Electrochemical Impedance Mapping
LEIS	Local Electrochemical Impedance Spectroscopy
LSV	Linear Sweep Voltammetry
MEIS	Microelectrode Impedance Spectroscopy
MIES	Metastable Impact Electron Spectroscopy
OCP	Open Circuit Potential
ORR	Oxygen Evolution Reaction
PPP	Polyparaphenylene
PREN	Pitting Resistance Equivalency Number
QCM	Quartz Crystal Microbalance
R_{corr}	Corrosion Resistance
RDE	Rotating Disc Electrode
RE	Reference Electrode
RRDE	Rotating Ring Disc Electrode
SDS	Sodium Dodecyl Sulfonate
SECM	Scanning Electrochemical Microscopy
SEM	Scanning Electron Microscopy
SIMS	Secondary Ion Mass Spectroscopy
SKP	Scanning Kelvin Probe
SKPFM	Scanning Kelvin Probe Force Microscopy
SRET	Scanning Reference Electrode Technique

STM	Scanning Tunneling Microscopy
SVET	Scanning Vibrating Electrode Technique
TEM	Transmission Electron Microscopy
UME	Ultramicroelectrode
UPD	Underpotential Deposition
WE	Working Electrode
wt%	weight percent
XANES	X-ray Absorption Near Edge Structure
XPS	X-Ray Photoelectron Spectroscopy

List of Symbols

a	chemical activity
c	concentration
C	capacitance
C_{coat}	coating capacitance
C_{dl}	double layer capacitance
C_m	capacitance in motional arm of BvD equivalent circuit
CPE_{dl}	double layer constant phase element
c_{red}	concentration of reduced species in front of electrode
c^0_{red}	bulk concentration of reduced species
c_{ox}	concentration of oxidized species in front of electrode
c^0_{ox}	bulk concentration of oxidized species
c_0	bulk concentration of oxidized species
$c(x=0)$	surface concentration
d	film thickness (coatings)
d	electrode-horn separation (sonoelectrochemistry)
d	diffusion length (impedance)
D	diffusion coefficient
D_{app}, D_{eff}	effective diffusion coefficient
E	Electrode potential
E^0	standard electrode potential
E_{corr}	corrosion potential
E_{pit}	pitting potential
f	electrical frequency
f	frequency of resonator
f_0	resonance frequency of bare quartz
f_R	general resonance frequency of quartz
Δf	resonance frequency change
F	Faraday constant, 96487 C/mol
i, j	current density
i_{cath}	current density of cathodic partial currents
i_{corr}	corrosion current density
i_{pit}	pit current density
I_a	ultrasonic acoustic intensity
$Im(Z)$	imaginary part of electrical impedance
i_{max}	peak current density
j	$\sqrt{-1}$
j_a	anodic partial current density
j_c	cathodic partial current density
j_{corr}	corrosion current density
j_{lim}	mass transport limiting current density
$j_{lim,\ cath}$	cathodic mass transport limiting current density

$j_{lim, an}$	anodic mass transport limiting current density
j_M, j_m	current calculated from mass changes
j_0	exchange current density
L	inductivity
L_m	inductance in motional arm of BvD equivalent circuit
m	mass
Δm	mass change
P	constant phase angle element (and Warburg) exponent
P_W	ultrasonic power
Q	charge density
ΔQ	change in charge density
r	electrode radius
r_{pit}	radius of pit
R_{corr}	corrosion current density
Re(Z)	real part of electrical impedance
R_m	resistance in motional arm of BvD equivalent circuit
R_{pol}	polarization resistance (=R_{ct})
R_{pore}	pore resistance
R_{ct}	charge transfer resistance
R_L	special resistance for impedance of coated alloys
R_T	finite Warburg element resistance
t	time
t_b	breakthrough time
v	scan rate
w	damping of quartz
x	degree of doping
y_{IL}	fomula units of ionic liquid per polymer unit
Y	electrical admittance
Y_T	finite Warburg impedance coefficient
z	number of electrons
$z_a(E)$	relative contribution of anion exchange to total current
$z_c(E)$	relative contribution of cation exchange to total current
Z	electrical impedance
Z_Q	mechanical impedance of quartz
Z_T	finite Warburg element impedance
α	charge transfer coefficient
α_{Me}	charge transfer coefficient for anodic metal dissolution reaction
α_{red}	charge transfer coefficient for cathodic electrode reaction
δ, δ_N	diffusion boundary layer thickness
ε	current efficiency
ε_{app}	apparent current efficiency
η	viscosity
η_D	overpotential
μ_q	shear modulus of quartz
ν	stoichiometric coefficient (Equation 1 only)

ν	kinematic viscosity
ρ	density
ρ_q	density of quartz
υ	stoichiometric coefficient (Equation 1 only)
ϕ	crystallographic angles
Ø	diameter
χ	standard deviation
ω	rotation rate for RDE experiments
ω	ac frequency for impedance measurements

Table of Contents

1. Introduction

1.1. Electrochemistry in materials science

Electrochemistry is a branch of physical chemistry that deals with chemical properties and reactions in the presence of electric fields and currents. This includes properties of charged species and systems containing charged species (*Ionics*, *e.g.* activity coefficients and ionic conductivity of electrolyte solutions), and reactions at interfaces involving charge transfer through a potential gradient (*Electrodics*, e.g. reduction of metal ions to solid metal or of Fe^{3+} to Fe^{2+}). Electrochemistry is of utmost importance in industrial production and processing of all kinds of products like aluminum foil, household cleaners, electronics, bikes, cars, etc., in production and storage of energy (fuel cells, batteries), but also in many degradation processes. Additionally, it is the basis for many physiological processes occurring in biological organisms including the human one. There are three different areas where electrochemistry and materials science meet:

- Materials for a variety of applications can be synthesized or modified by electrochemical methods. Metals and alloys and coatings thereof are prepared by electroplating [1]. The experimental conditions allow adjusting the microstructure of the deposits in a wide range, from smooth deposits with large grains to powdery deposits and nanomaterials. Metal/ceramic composites are made by electrodeposition in the presence of ceramic particles dispersed in the electrolyte. Conducting polymers can be electrodeposited, and their conductivity and state of charge are adjusted electrochemically. Oxide films and especially porous oxide films are grown by electrochemical oxidation. Porous films can be filled with other materials as done for a long time on Al panels in order to seal them or to dye them. In addition ordered pore arrays can be used as templates to electrochemically grow nanowire arrays, for instance Ni arrays [2-4]. Electrodissolution is employed as well for modification of materials and work pieces: Surfaces can be electropolished, and three-dimensional structures can be created from work pieces by electrochemical machining.
- Materials in service can degrade by electrochemical mechanisms. The major electrochemical degradation pathway is corrosion of metals and alloys.
- Materials can be synthesized and optimized for use in electrochemical devices. This includes electrolytes and electrodes for fuel cells and batteries, for industrial electrochemical applications, and for electrochemical sensors.

Electrochemical processes can be quite complex even in the case of well-defined, single crystalline metal electrodes without oxide layer in an aqueous electrolyte [5-8]. The rate of electrochemical reactions (for a single electrode reaction proportional to the electric current) is controlled by charge transfer reactions through the electrochemical double layer, by the mass transport of reactants to and products away from the electrode and thus concentration gradients at the electrode surface, by adsorption processes at the electrode surface, by nucleation processes in the case of electrochemical phase formation and by coupled chemical reactions. Mass transport can take place by diffusion, convection and migration. The latter contribution often is suppressed in electrochemical experiments by addition of supporting electrolyte that increases the electrolyte conductivity and therefore decreases potential gradients in solution. A second effect of supporting electrolyte is an increase in ionic strength and therefore a compression of the width of the diffuse part of the electrochemical double layer. Absence of a diffuse double layer facilitates mathematical treatment of charge transfer processes. The overall control variable in many electrochemical experiments is the electrode potential, measured with respect to a reference electrode. For a given redox couple (like $[Fe(CN)_6]^{3-}/[Fe(CN)_6]^{4-}$, $Cu^{2+}/[CuCl_2]^-$ or Cu/Cu^{2+}) the Nernst equation describes the concentration (activity) dependence of the electrode potential at electrochemical equilibrium:

$$\nu_1 A_1 + \nu_2 A_2 + ... + \nu_n A_n + ze^- \quad \Leftrightarrow \quad \upsilon_1 B_1 + \upsilon_2 B_2 + ... + \upsilon_m B_m$$

$$E = E^0 + \frac{RT}{zF} \ln \frac{\prod_{i=1}^{n} a(A_i)^{\nu_i}}{\prod_{i=1}^{m} a(B_i)^{\upsilon_i}} \tag{1}$$

E^0 is the standard electrode potential. Electrochemical equilibrium is a dynamic equilibrium, i.e. both cathodic (reduction) and anodic (oxidation) partial reactions are taking place, but at the same rate. Therefore they cancel each other out, and the total current in electrochemical equilibrium is 0. At potentials different from the equilibrium potential, anodic and cathodic reaction rates are different, and a net current flows. If only transfer of the electric charge across the electrochemical double layer determines the reaction rates (activation controlled current), the current-potential relationship is given by the Butler-Volmer equation:

$$j = j_a + j_c = j_0 \left(\frac{c_{red}}{c^0_{red}} \exp\left[\frac{\alpha z F \eta_D}{RT} \right] - \frac{c_{ox}}{c^0_{ox}} \exp\left[-\frac{(1-\alpha) z F \eta_D}{RT} \right] \right) \tag{2}$$

In this equation j_0 is the exchange current density that is a measure of the reaction rates of anodic and cathodic partial reactions at equilibrium, and α is the so-called transfer coefficient or barrier symmetry factor. c_{red} and c_{ox} are the concentrations of reduced and oxidized species at the electrode surface, whereas c^0_{red} and c^0_{ox} are the corresponding bulk concentrations. η_D is the activation overpotential ($\eta_D = E(i)-E(i=0)$).

A typical starting point in order to explore an electrochemical system is cyclic voltammetry (CV) or linear sweep voltammetry (LSV). In LSV the potential is ramped linearly at a constant rate of potential change (sweep rate or scan rate v) from a starting value, where no electrochemical reactions take place (e.g. from potentials above the Nernst potential for metal electrodeposition), to a final value in the electrochemically active region (e.g. at potentials sufficiently negative of the equilibrium potential), and the current is measured as a function of potential. Even in the simple case of a non-stirred, ideally quiescent solution with fast heterogeneous electron transfer kinetics, and pure diffusion control of the electrochemical reaction rate, a closed analytical equation for the current-potential relationship cannot be given. However, the problem has been solved numerically: The current increases with change in potential, and therefore an increasing amount of the electroactive species is consumed close to the electrode. This finally leads to a depletion of reactant close to the electrode and lower concentration gradients at the surface, and currents consequently decrease. A plot of current version potential therefore shows a pronounced maximum. The region over which the reactant concentration changes from the surface concentration (thermodynamically controlled at low overpotentials, zero at large overpotentials) to the bulk value is called the Nernst diffusion layer. In unstirred solutions the thickness of this diffusion layer increases with time. The maximum current (positive for oxidation and negative for reduction processes) increases with $v^{0.5}$, and the diffusion coefficient of the electroactive species in solution can be determined from a plot of i_{max} versus $v^{0.5}$. In the case of multi-step reactions, adsorption processes, phase formation on the electrode, the occurrence of several electrode reactions and coupled chemical reactions the situation becomes more complicated. In real experiments after some tens of seconds density changes close to the electrode induce natural convection, enhancing

mass transport and imposing an upper limit to the diffusion boundary layer thickness (typically ~100 µm). Whenever mass transport is influencing the rate of an electrochemical reaction, hydrodynamics in the electrolyte plays a crucial role. An elegant way to control the hydrodynamics in an electrochemical experiment is the rotating disc electrode. The rotation rate induces a laminar electrolyte flow towards the electrode. Close to the electrode the electrolyte flows turns radially outward. Therefore a thin electrolyte layer in front of the electrode can be considered as unstirred and mass transport through this layer occurs solely by diffusion. The thickness of the Nernstian diffusion layer is now a function of rotation rate instead of time. Therefore current increases with increasing overpotential to a maximum value and becomes constant. This potential-independent current - the so-called diffusion limited current - scales with the square root of the rotation rate. The mathematical treatment of these simple cases and also of some of the more complex situations including charge transfer reactions, adsorption processes and coupled chemical reactions have been treated in detail in the literature and in electrochemical textbooks. Especially in the excellent textbook by Bard and Faulkner the mathematics of LSV and CV, but also of many other electrochemical techniques is treated in detail [5]. An extensive treatment of the physical chemistry of both electrolyte solutions and electrode reactions can be found in the books by Bockris, Reddy, and Gamboa-Aldeco [6-8].

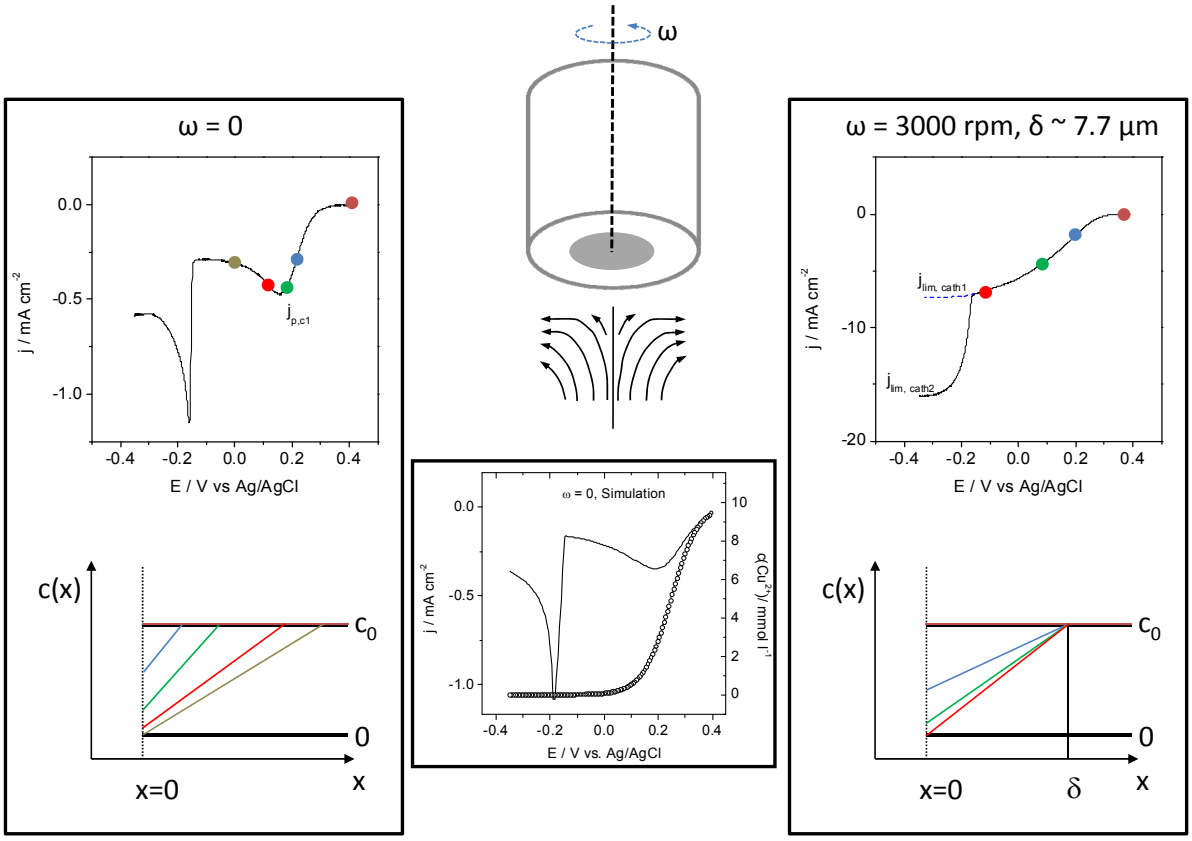

Figure 1. Typical shapes of linear sweep voltammograms under silent conditions (left) and using a rotating disc electrode (RDE) at 3000 rpm (right). The example shown is the reduction of Cu^{2+} in a 0.01 M $CuCl_2$ + 0.5 M NaCl solution with pH adjusted to 1. A simplified (linearized) representation of the corresponding concentration gradients for Cu^{2+} is given below the voltammograms. A schematic of the RDE including resulting streamlines is shown in the center. The lower figure in the center shows the result of a numerical simulation of the LSV under silent conditions together with *c(Cu^{2+})* computed at the electrode surface.

In the normal laboratory practice and especially in industrial applications polycrystalline electrodes are used. These are composed of grains with different surface orientations, and grain boundaries. However studies with single crystals have shown that exchange current densities and adsorption processes depend on surface orientation and electron density at the surface as well as on surface defects [9]. The same is true for the properties and electrochemical growth of oxide layers. Electrochemical measurements at polycrystalline surfaces even of very pure materials therefore provide information averaged across the surface. Less pure metals have surfaces where the chemical composition is not the same everywhere. Less noble metals often show (ill-defined) oxide layers at the surface, and have to be pre-treated before use as an electrode in electrochemical experiments. A typical example is surface finishing of less noble work pieces by electroplating for corrosion protection, enhancement of mechanical properties, and modification of friction or improvement of optical appearance [10]. Such work pieces have to be pretreated by degreasing and e.g. acid pickling before the actual electrochemical processes can be applied. Electrochemical phase formation and growth on real three-dimensional specimens is influenced also by the current distribution (primary / secondary distribution) that can lead to pronounced edge effects and differences in the thickness of electroplated coatings. A measure for the expected coating thickness distribution for irregularly shaped substrates is the throwing power. The electroplating processes depend also on the roughness of the surface: Sometimes the amount of material deposited is less in recessed (lower) regions, and special additives need to be added into the electrolyte bath to achieve even deposition without alteration of surface roughness and geometry. Other additives will influence the grain size (grain refiners), will flatten the grains and brighten the deposit or will level the deposit (decreasing surface roughness). Whenever a surface is altered during an electrochemical process, electrochemical reaction rates will be altered as well, or the driving force required for keeping the reaction rate and thus the current constant will be altered.

Another field where spatial heterogeneities of the substrate surface are of great importance is corrosion. Corrosion of metals and alloys used in machines, buildings, and transportation often starts at local sites, and causes local material changes. In addition also the timescale is of great importance, as will be shown in the next section.

These few examples already demonstrate that a complete mechanistic understanding of electrochemical processes in general and especially in the field of materials science requires methods with temporal and/or spatial resolution to be applied, and requires information additional to purely electrical data (current / potential / time). In this work the application of some of these methods will be reviewed. The review is broadly divided into two subjects: On the one hand the focus in on the complex spatial and temporal interactions between different intermetallic phases in heterogeneous aluminum alloys and the resulting corrosion behaviour both of the bare alloy and of alloys protected by polymer coatings. On the other hand electrochemical reactions, especially electrodeposition experiments, in the presence of ultrasound will be discussed. This unique combination known as sonoelectrochemistry uses ultrasound as an additional way to introduce energy into the system, and takes advantage of the extraordinary effects on mass transfer and surface processes introduced by acoustic cavitation. In the remainder of Section 1 some general remarks about corrosion and corrosion of heterogeneous Al alloys will be made, including findings on blister formation of epoxy-coated Al alloys, and some fundamentals of sonoelectrochemistry will be reviewed. In Section 2 the focus will be on different electrochemical approaches including the use of well-defined synthetic model alloys in order to mimic the behaviour of the real commercial Al alloys, the application of microelectrodes and of microcapillaries in corrosion science, and the application of the electrochemical quartz crystal microbalance to corrosion studies,

sonoelectrochemical reactions and conducting polymers. Section 3 reviews some microscopy and mapping techniques in electrochemistry with a clear focus on the Confocal Laser Scanning Microscopy technique (CLSM). The specific examples given are mainly taken from the author's own work, however, important findings from other authors are also summarized. This review does not cover solid state electrochemistry and electrochemistry involving semiconductors, nor the important materials aspects in batteries and fuel cells.

1.2. General remarks on corrosion

Corrosion is defined as reaction of a material with the environment that causes a detectable change of the material and can lead to deterioration of the function of a component or the entire system [11, 12]. This is a comprehensive definition for all types of materials classes, and does not necessarily require electrochemical mechanisms. Corrosion of metals and alloys however is usually electrochemical in nature. The specific aspect of corrosion is that different anodic and cathodic reactions are taking place at the same time at the same metal or alloy (= electrode) surface (both of which are composed by anodic and cathodic partial reactions). The anodic reaction typically is metal dissolution and the cathodic reaction oxygen reduction reaction (ORR) or hydrogen evolution reaction (HER). Under free corrosion conditions (no potential control by an external circuit, no net current flowing to an auxiliary electrode) electrons consumed by the cathodic reactions are provided by the metal dissolution, and the electrode assumes a mixed potential which is above the equilibrium potential for the metal dissolution and below the one for ORR (HER), and controlled by the heterogeneous kinetics of both processes: The potential will assume exactly that value were the current for metal dissolution equals the (absolute) one for ORR (HER). This so-called corrosion potential E_{corr} therefore is no equilibrium potential, and the specimen is not at equilibrium either. If E_{corr} is constant and the corrosion rate also does not change, the system at least is steady-state. Current-potential curves are similar to the behavior seen for simple equilibrium systems, and for the case of pure charge transfer control for both reactions an equation similar to the Butler-Volmer equation can be written:

$$j = j_{corr} \cdot \left[\exp\left(\frac{\alpha_{Me} z_{Me} F\left(E - E_{corr}\right)}{RT} \right) - \exp\left(- \frac{\left(1 - \alpha_{red}\right) z_{red} F\left(E - E_{corr}\right)}{RT} \right) \right]$$

$$j = j_{corr} \cdot \frac{F}{RT} \left(\alpha_{Me} z_{Me} + \left(1 - \alpha_{red}\right) z_{red}\right) \left[E - E_{corr}\right] \tag{3}$$

$$\frac{\partial j}{\partial E} = j_{corr} \cdot \frac{F}{RT} \left(\alpha_{Me} z_{Me} + \left(1 - \alpha_{red}\right) z_{red}\right) = \frac{1}{R_{corr}}$$

This equation is known as the Stern-Geary equation. The major difference is that whereas j_0 in the Butler-Volmer equation at equilibrium causes no detectable chemical changes in the system, j_{corr} is directly proportional to the rate of metal loss at E_{corr}. In addition α_{Me} and α_{red} are different. In the vicinity of E_{corr} the equation can be linearized, and from the slope of the potential-current curve the corrosion resistance R_{corr} can be determined. Calculation of corrosion current and thus corrosion rate however requires knowledge of α_{Me} and α_{red} that can be obtained from log *j*-*E* plots at potentials significantly above (for α_{Me}) and below (for α_{red}) E_{corr}. The validity of the Stern-Geary equation can be limited if the system is non-stationary (e.g. if pH or oxygen concentration change, or the surface composition of the alloy is altered during corrosion), or if passivation or precipitation reactions occur. It is also not generally valid for some local corrosion processes.

Corrosion can be taking place more or less homogeneously across the surfaces with anodic and cathodic reactions taking place at random sites and fluctuating in a statistical manner (Wagner-Traud model) [8]. This is especially the case for very pure metals and under conditions where oxide layers are unstable. Because metal loss takes places homogeneously across the surface one also speaks of general corrosion. In the presence of oxide layers or protective organic coatings, laterally heterogeneous surface composition and local gradients in electrolyte composition and oxygen content corrosion can become localized. Typical forms of localized corrosion are pitting corrosion, crevice corrosion, galvanic corrosion, and filiform corrosion and blister formation in the case of underfilm corrosion. Pitting corrosion often is studied by linear polarization of the specimen at slow scan rates towards potentials >> E_{corr}, until breakdown of the passive layer occurs and one or several stable pits are formed. The so-called pitting potential E_{pit} is a pit stabilization potential. Some important aspects of pitting corrosion have been reviewed by Frankel [13]. Stable pits show low pH, high metal and chloride concentrations. The anodic dissolution of the metal takes place at the bottom of the pit, whereas the cathodic reaction takes place on the outer metal (alloy) surface. If the pit is very small full contact to the electrolyte (collapse of an oxide cover) can increase pH and lower chloride content, so that repassivation is possible. Such pits are called metastable. If a pit is deep enough diffusion is no longer fast enough to lower concentrations sufficiently, and the pit continues to grow. The processes leading to the onset of metastable and stable pitting are often studied by potentiostatic transients. Pit nucleation events and metastable pitting take place at potentials significantly lower than E_{pit}. The currents of single events often are very small, so that they are difficult to detect. This will be discussed later in the section on microelectrochemistry. Pitting corrosion often is induced by impurities like inclusions, and therefore depends on the number density and size distribution of such impurities. Crevice corrosion is caused by differential aeration. In regions of a specimen with restricted access of fresh electrolyte and oxygen like in lap joints of aircrafts, underneath rivets, in contact zones of artificial joints (hip implants), in any kind of fissure or simply underneath a sealing O-ring oxygen can be rapidly used up, and the surface oxide film be reduced, leading to depassivation. A local galvanic cell is set-up with oxygen being reduced on the outer metal surface and corrosion taking place within the crevice. Also the ohmic potential drop within the crevice has been shown to play a role. Crevice corrosion often is a problem when O-rings seals are used when attaching a specimen to an electrochemical cell for corrosion studies. Galvanic corrosion and underfilm corrosion are discussed in Section 1.3. Recently also microbiologically influenced corrosion has moved into the focus of research. Here the corrosion processes are influenced by the metabolism of bacteria, algae and other organisms.

1.3. Corrosion behavior of heterogeneous aluminum alloys

Despite the increasing significance of composite materials in aircraft industry aluminum alloys still remain a major material for aircraft construction. Even the new Airbus A380 still contains approximately 60 wt% Al [14-16]. For a long time a standard material for aircraft fuselage was AA2024-T3. The designation of this alloy is based on the ANSI standard H35.1 [17]. Nowadays also other alloys like AA6013 (AlMgSiCu), AlMgLi (1424), AlMgSc, and the Al-alloy-based composite Glare are of importance [14, 15, 18-21]. In the designation AAabcd, “a” defines the major alloying element aside Al (cmp. Table 1), “cd” identifies a specific alloy or defines impurity levels, and “b” indicates a modification of the alloy with respect to “cd” of the original alloy. The composition of AA2024 alloy is given in Table 2.

The alloy designation is completed by the temper descriptor that defines how the material was post-treated. Post-treatment is necessary in order to adjust the microstructure and therefore mechanical and thermal properties. In case of aluminum alloys it leads to the precipitation of intermetallic compound phases (IMC) serving as strengthening particles. In AA2024-T3 “T3”

refers to solution heat treatment followed by cold work and natural ageing. Typically the material is cold-rolled, leading to flat elongated grains (Figure 3a).

The strengthening particles embedded in the Al-Cu solid solution matrix of AA2024 constitute ~4% of the alloy surface [22]. Up to 300000 constituent particles / cm^2 alloy area with a diameter larger than 1 µm have been reported [23]. The IMC particles are comprised of many large second phase particles (up to several tens of µm), needle-shaped hardening precipitates (Al_2CuMg) in grain and grain boundaries, and Al-Cu-Mn dispersoids [24]. The particles show also compositional variation. A typical size distribution of IMC particles on AA2024 obtained from CLSM image analysis is shown in Figure 2.

Table 1. Major alloying elements in aluminum alloys and corresponding number a in designation abcd of wrought aluminum alloys.

a	Element	a	Element
1	>99% Al	5	Mg
2	Cu	6	Mg+Si
3	Mn	7	Zn
4	Si	8	Sonst.

Table 2. Composition of two aluminum alloys [17]. Numbers are in wt% and define upper limits, except for Al, where it is a minimum amount and when a range is given.

Alloy	Si	Fe	Cu	Mn	Mg	Cr	Zn	Ti	Other each	Other total	Al
1100	0.95 sum		0.05-0.20	0.05	-	-	0.10	-	0.05	0.15	99.00
2024	0.50	0.50	3.8-4.9	0.30-0.9	1.2-1.8	0.1	0.25	0.15	0.05	0.15	Diff.

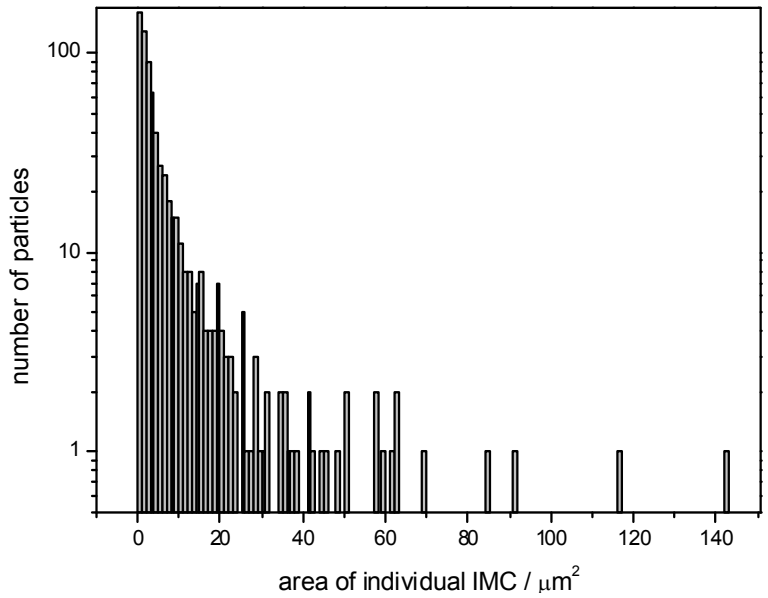

Figure 2. Typical size distribution of intermetallic particles with a diameter of > 1 µm on AA2024-T3.

The corrosion behavior of a heterogeneous precipitation hardened Al alloy like AA2024-T3 is controlled by the presence of these intermetallic compound phases (IMC) differing in their electrochemical behavior from the surrounding Al-matrix, thus causing galvanic coupling and inducing localized corrosion processes [23, 25-28]. These can be connected to local pH changes influencing the further corrosion propagation [26, 27, 29, 30]. Corrosion processes seen on such alloys comprise etching of the matrix, pitting of particles and the matrix, selective dissolution and dealloying of some IMC, whereas others show no sign of corrosion at all, and the formation of trenches or grooves at the interface between particles and matrix [22-24, 26-29, 31-35]. The cathodes in these local galvanic cells are often Cu- and Fe-containing intermetallics or replated Cu, with the anodes being either Al-Cu-Mg particles or the alloy matrix [22, 23, 25-28, 36-38]. In AA2024-T3, pit initiation sites include Al-Cu-Mg particles [22-24, 26, 38], the periphery of Cu-enriched Al-Cu-Mg particles that have been dealloyed of Al and Mg [22], and the matrix adjacent to Al-Cu and Al-Cu-Fe-Mn particles [22, 23, 27, 28, 38]. Of these intermetallics, the Al-Cu-Mg type is the most active. It is anodic to the Al alloy-matrix and generally de-alloys leaving a fine Cu-sponge as a result of the selective removal of both Al and Mg. Thus, with time it becomes cathodic to the matrix [22-24, 29, 39]. In some cases a more noble character of the Al-Cu-Mg phase was reported, according to measurements with the Kelvinprobe (cmp. Section 3.4.3), that was due to the presence of a surface film [28, 40]. Scratching with an AFM tip then revealed the true, anodic nature of these particles. Under certain conditions, some authors have observed rings of redeposited Cu around these Al-Cu-Mg precipitates [41]. Replated Cu has been shown to contribute significantly to the overall oxygen reduction reaction on AA2024-T3 [29]. As much as 60% of the intermetallics on the surface of an AA 2024-T3 sample are of the Al-Cu-Mg type [22, 42]. The Al-Cu and Al-Cu-Mn-Fe types of intermetallic compounds are noble relative to the Al-matrix and therefore serve as cathodic sites [43]. As a result, any Cu^{2+} ions dissolved in solution can be reduced readily on these particles [23]. The generation of OH^- ions at these particles due to the reduction of oxygen is believed to contribute to alkaline attack of the Al adjacent to these particles, resulting in an attack morphology known as trenching which often forms a perimeter around the particle [23, 27-29, 34, 35, 38, 44-48]. This process is discussed in detail in Section 3.2.2. In addition, pitting can occur in the matrix in halide-containing solutions [43].

The formation of trenches at the interface between the matrix of AA2024-T3 and intermetallic particles has been extensively discussed in the literature [23, 27-29, 34, 35, 38, 39, 44-48]. However, the actual mechanism behind this form of corrosion is not clear. It resembles the corrosion morphology observed on Al-Cu alloys containing Cu-rich particles under cathodic polarization [45]. This observation led to the development of the cathodic model. This model relates a local increase in pH to the products associated with the oxygen reduction reaction at the cathodic Al-Cu and Al-Cu-Mn-Fe particles. Subsequent destabilization of the oxide film at the interface between the particles and the alloy matrix occurs due to OH^- accumulation and higher oxide solubility at elevated pH. Thus, increased dissolution at the interface occurs and appears as trenching due to the strong pH gradient near the particle.

Nisancioglu et al. originally introduced the idea of cathodic trenching [29, 47]. Park et al. showed both theoretically and experimentally that the pH on isolated cathodic intermetallics (Al_3Fe) can be high enough to promote matrix dissolution in Al6061 [34]. Moreover, they showed that the addition of buffering capacity to a solution prevented formation of grooves around these particles, and tried to explain how the alkaline-induced corrosion could later lead to an acidic pit [34]. Vukmirovic measured pH values of close to 10 next to Al-Cu-Mg particles on AA2024 exposed to 0.1 M NaCl (bulk pH 5.3) [29]. This observation is in conflict with others that indicate the inability of Al-Cu-Mg particles to support cathodic

reactions at high rates [48] especially prior to dealloying and the formation of a Cu-rich surface. Alodan and Smyrl simulated the pH close to a single IMC particle for different bulk pH solutions by computational means [37]. They assumed an oxygen reduction current of 0.1 mA cm^{-2} and accounted for the aluminum hydrolysis reaction due to localized corrosion in the matrix adjacent to the IMC/matrix boundary. Their results show that no local alkalinization occurs with a bulk pH of 4, whereas in neutral bulk solution local alkalinization occurs. Based on these results, Büchler et al. concluded that the total cathodic current is larger than the anodic current at sites where trenching occurs (i.e., trenches occur at IMC particles that are net cathodes) [44]. Therefore, it could be proposed that under alkaline and near-neutral conditions, the pH above IMC could become sufficiently alkaline via galvanic coupling between matrix and IMC, which are net cathodes, to initiate alkaline-induced trenching corrosion. This speculation was supported by pH measurements showing a local pH increase at IMC sites [29, 34].

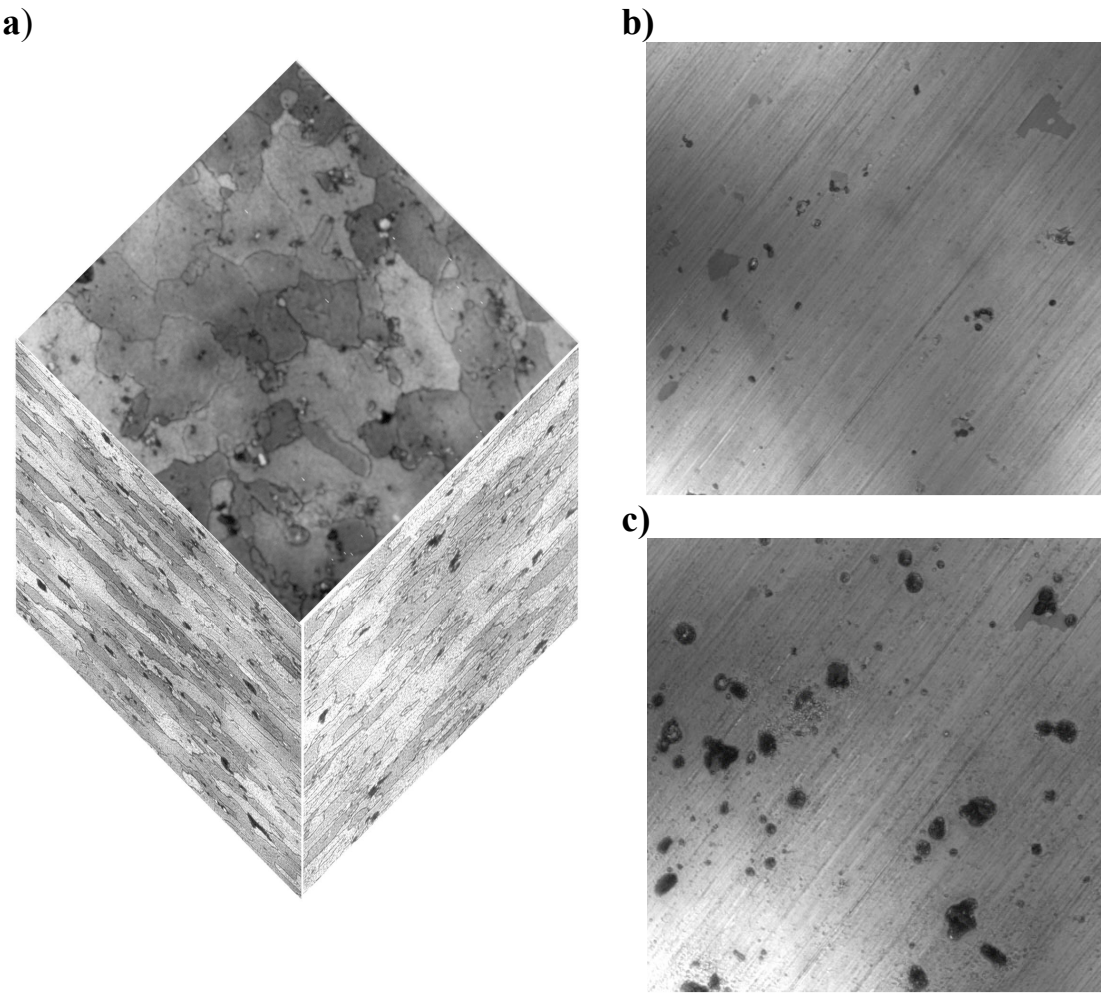

Figure 3. Aluminum Alloy 2024-T3: a) Grain structure of the alloy after mechanical polishing and etching with Kellers reagent in planes parallel to the surface and normal to the surface in rolling direction and normal to the rolling direction. b) Confocal laser scanning microscopy image of a polished alloy section (130 x 130 µm frame): grey particles are intermetallic phases. c) Confocal laser scanning microscopy image after 100 min of exposure to 0.5 M NaCl.

Trench formation was also observed in artificial model alloys [29, 49] where certain other microstructural complexities cannot exist (e.g., dealloyed Al-Cu-Mg-phase that supports enhanced local ORR or Cu-depletion in adjacent matrix that might support increased rates of

anodic processes). Recently, Missert et al. used model Al-Cu alloys to study pit initiation and local alkalinization next to Cu-islands on pure Al in an effort to mimic the role of the IMC under controlled geometric conditions [49]. They showed that the actual pit initiation and breakdown at selected Cu islands occurred before the pH increased [49]. In fact, although a pH increase was observed at some Cu islands, a pH decrease was seen at the Cu island acting as a dominant net cathode [50]. This result suggests that trench formation at the site of the IMC is caused by acid pitting, for which the probability might be higher close to a cathode due to a shorter ionic current path. It also has been observed that trenches form around Al-Cu-Mg particles, once they are converted to cathodic particles by the removal of Mg through de-alloying [22, 24, 29].

Mechanistic understanding and modeling of these corrosion processes is hampered by the complex nature of the materials, especially with respect to the intermetallic phases present [30, 31, 49, 51]. Those show a large variation in size, covering a range from 10 nm up to 20 μm or more, different compositions, the formation of clusters in some areas whereas other areas are virtually particle-free, are connected to local depletion of alloying elements in the Al matrix and are statistically distributed across the surface [22-24, 26-28, 52]. Al-Cu-Mg intermetallic particles are often spherical whereas Al-Cu and especially Al-Cu-Mn-Fe intermetallics have blocky angular features [32]. Some large Al-Cu-Mg particles show deviations from the spherical geometry. Al-Cu-Mg particles were observed that had three almost linear sides forming angles of ca. 120 degrees [32]. Clustering of distinct Al-Cu and Al-Cu-Mn-Fe particles is often observed [32].

Metals in service are often protected by organic coatings. Upon exposure to electrolytes or humid atmospheres, organic coatings often fail locally. Such failure leads to the loss of protection of the substrate, the formation of blisters and underfilm corrosion. There are different types of underfilm corrosion, including filiform corrosion and blister formation, and different mechanisms are proposed to explain how these defects form and grow. A number of reviews on the subject is available [53-58]. Cathodic delamination, anodic undermining, osmotic blistering, corrosion product wedging and other mechanisms were identified in the early literature [56, 57]. A more detailed understanding of the mechanisms involved developed recently, when methods became available that allow characterization of the processes at the interface metal/coating on a local scale. These methods include electrochemical techniques [59-72], quantitative topographic techniques [73-76], and chemical techniques for analysis of solutions [67, 77, 78] and surfaces [57, 62, 79, 80].

Blister formation and filiform corrosion are important modes of coating failure on aluminum alloys like AA2024-T3 [67, 68, 72, 79, 81-85]. Filiform corrosion occurs in humid air in the presence of chloride, whereas blister formation dominates in full immersion [86]. The formation and growth of blisters in the coating can be due to several mechanisms [53, 56, 57, 70, 87-89].

Typical paint film formulations are based on epoxies and polyurethanes. These coatings are quite permeable to oxygen and water [53, 84, 90-92]. Generally it is assumed that a good barrier coating is characterized by a low permeability for corrosive ions and thus a large resistance to ionic currents [54, 90, 91, 93]. However, other effects can contribute to the corrosion protection as well. Most organic coatings acquire a negative surface charge upon immersion, which may introduce a preferential permeability for anions or cations (depending on whether the transport is taking place along some defects in the coating or through the bulk of the coating) [54]. Some authors point to the mechanical properties of the coating and rather connect those with good barrier properties of a polymer film [94], and also to adhesion [90].

Finally it has been found that the chemical reactivity at the polymer/substrate interface is extremely low. At this interface, an extended diffuse double layer forms which imposes a strong kinetic limitation on all electrochemical reactions [58, 61].

Different microscopic areas on the same coating can show a very different ionic resistance [53, 54, 93, 95]. The resistance of areas with high crosslinking density decreases with increasing resistance of the immersion solution (indirect-type conduction, I areas). Other areas have a low crosslinking density, low molecular weight, are formed by partially polymerised molecules and therefore more polar. They have diameters between 75 and 250 μm, and can absorb large amounts of water (45-75%) [53, 54]. The lower the resistance of the solution is, the lower the resistance of these areas (direct-type conduction, D-areas). Ions can mainly penetrate through D type areas [53, 95], and through defects in the coating like pores, cracks and crevices [53].

The first step leading to underfilm corrosion and coating failure is water uptake. Water uptake can be measured by gravimetric methods [93, 96]. The most common method however is based on the impedance response, from which one can determine the coating capacitance [84, 97, 98]. Since the dielectric constant of water is much larger than the one of the coating ($\varepsilon_r \sim 5$ [95, 99]), one can calculate the water content from the increase of the capacitance with time [84, 96, 97]. In addition to water uptake rate one also can obtain information on water diffusion coefficient and solubility in the polymer [84, 100]. Water uptake is not taking place homogeneously across the polymer [84]. Water diffusion first proceeds along boundaries of polymer structure units before penetration of the actual structure occurs [53]. Water molecules are first incorporated into pores and interstitial sites [84, 101]. When these sites are full, the mechanism must change [84, 101]. Swelling of the polymer can occur, allowing uptake of water into spaces which were too small initially [84, 93, 95]. Water can be present in molecularly dispersed form or in the form of clusters [95]. The incorporation of water in a later stage can damage the polymer network structure [53, 95, 102]. The mechanical properties of a coating strongly change during water uptake [94, 102]: After curing they are under tensile stress, which often changes to a compressive stress after water uptake.

Corrosion on coated metals is assumed to start even for monolayer coatings at coating defects [53, 103-105], like scratches, I-areas, pores, or cracks, or defects formed with time during immersion [53, 54, 57, 92, 95, 101, 104, 105], like ion conducting channels [53, 57, 102, 103]. Once corrosive ions reach the metal surface, corrosion can start, if the substrate is depassivated and cathodic reactions can take place. The further processes depend on many factors.

If there is a macroscopic defect like a scratch, and the substrate surface allows electron transfer reactions (ETR), cathodic delamination will take place [53, 54, 57, 58, 60-62, 70, 71, 95, 102, 104, 106]. The defect and the passive surface underneath the coating galvanically couple [60, 62, 70, 107, 108], causing oxygen to be reduced underneath the coating. For sake of charge neutrality, cations migrate along the metal/coating interface from the defect to the cathodic reduction site, driven by the potential gradient [53, 54, 57, 60-62, 102]. Anions other than hydroxide cannot be found far away from the defect [60, 62]. The exact delamination mechanism still is under debate. Most studies see the high pH developing at the delamination front as the culprit, attacking the bonds between polymer and substrate, leading to cohesive failure within the polymer, or attacking the passive oxide surface [53, 54, 93, 102]. Newer studies emphasize the role of highly reactive radical intermediates during oxgen reduction reaction damaging the coating [60, 73]. Other approaches included aqueous displacement and the role of interfacial water [109]. Another type of cathodic delamination is the formation of

cathodic blisters (high pH, no corrosion) [53, 94, 98, 102, 104, 110], that are believed to form at a defect site of the coating, where cations can enter through the coating [54, 94].

For a microscopic defect similar considerations apply [53]. However, now a solution filled blister with an anodic center forms. Blister formation on steel involves the formation of conductive channels through the coating [53]. These channels serve as a coating defect, through which chloride ions can reach the metal surface and initiate corrosion. The formation of the conductive channels (due to small inhomogeneities in composition or the presence of intrinsic defects) and the depassivation of the surface at the coating defect site due to the chloride (which will depend on the surface chemistry of the substrate) are statistical in nature. Therefore corrosion initiation is localized. The cathodic reaction can take place at the metal surface underneath the coating surrounding the blister, causing cathodic delamination [56, 57, 60, 70]. In comparison to the situation for the macroscopic defect other effects can contribute. Delamination can be driven by osmotic water-uptake [53, 54, 86, 87, 102]. In addition the compressive stress of the coating itself can drive the coating delamination once the bonds between polymer and substrate become weak enough [94, 102]. A model connecting the mechanical properties of the polymer and the delamination rate has been given in literature [102]. During blister growth anodic and cathodic regions can change [87, 111, 112]. The formation of corrosion product on iron or steel can lead to pore clogging, the original anodic site can turn into a cathode, and new anodes form close to it [105, 111, 113].

The blister formation in Al and Al alloys like AA2024-T3 is more complicated than in steel due to the more complex microstructure and the blockage of ETR reactions by the aluminum passive film. Of particular importance is the slowing of the oxygen reduction reaction (ORR) [25, 35, 56-58, 114-116]. Most of the cathodic reactions on AA2024-T3 take place on the cathodic IMC, which do support electron transfer reactions [25, 35, 114, 115, 117, 118]. Cathodic reactions taking place on the cathodic IMC still would be insufficient to drive cathodic delamination if the spacing between the IMC was larger than the width of the delamination zone [58]. Therefore an anode/cathode separation like on iron and steel does not occur as easily, and cathodic delamination is not considered as a viable mechanism [56-58, 89]. A different mechanism compared to steel therefore should control blister growth, like (osmotic) pressure driven blister growth, anodic undermining or corrosion product wedging [56, 58, 86, 89]. For intact coatings though it was claimed that cathodic delamination always was the operating mechanism [89].

The phenomenology of blister formation and growth on coated AA2024-T3 exposed to aqueous NaCl solutions has been subject of several publications [67, 68, 72, 76, 85, 119]. Three types of blisters were observed. Red blisters showed active corrosion, had an acidic pH within them and low open circuit potentials (OCP). In near-neutral immersion solutions, usually only one or two red blisters formed, the formation of which correlated to a strong drop in the OCP. Black blisters (much more seldom) appeared to be repassivated red blisters. Clear blisters showed no corrosion damage, high pH and passive OCP values, suggesting they might be sites of the cathodic reaction.

The low pH inside red blisters led to the question in how far the low pH within the blister affects the further coating degradation, delamination and corrosion reactions. Therefore Schneider and Kelly studied the blister formation in NaCl solutions of different pH in more detail, and determined also the influence of the pH on water uptake and ion permeability of the coating [85]. In near-neutral solutions, the potential of the coated substrate before blister formation was above the pitting potential for AA2024-T3. Therefore after formation of a coating defect easily corrosion could take place inducing blister formation. The potential drop

associated with formation of a single blister was due to the local activation of the surface [57, 61, 67, 70, 72] and decreased the susceptibility for further blister formation, because now OCP < E_{pit}. If the blister stifled, and solid corrosion products formed, the potential increased again, and formation of another blister became possible. These observations pointed to an important role of pitting for blister formation on AA2024-T3. Significant changes were seen at pH < 3.5. Red blisters formed earlier, in larger numbers, grew faster and therefore became larger the lower the pH was. Substantial scatter in the blistering behavior was observed between nominally identical samples. This concerned the number of blisters on different specimens, the size of different blisters on the same specimen, and the total corroded area. A summary of the observations is given in Figure 4. The potential drop was less sudden in acidic solutions. Rather a continuous decay was observed, and very active values were reached soon after immersion. In addition to the red blisters numerous tiny clear blisters surrounding the red blisters were seen as well.

Large blisters (~ 1 cm) always contained gas and showed red plating at the delamination front. The gas stemmed from hydrogen evolution, and the gas pressure in fact might have increased the delamination rate . Smaller blisters were sometimes red throughout, whereas others showed formation of red rings and red spots. Occasionally the red material was rather loose and did not form an adherent film. Determination of corrosion damage after removal of coating and corrosion products revealed that underneath the red areas corrosion was most severe. Probably the replated Cu served as additional cathode accelerating corrosion. For a sample exposed to near-neutral NaCl a corrosion depth of 30 µm was found after 21 days of immersion.

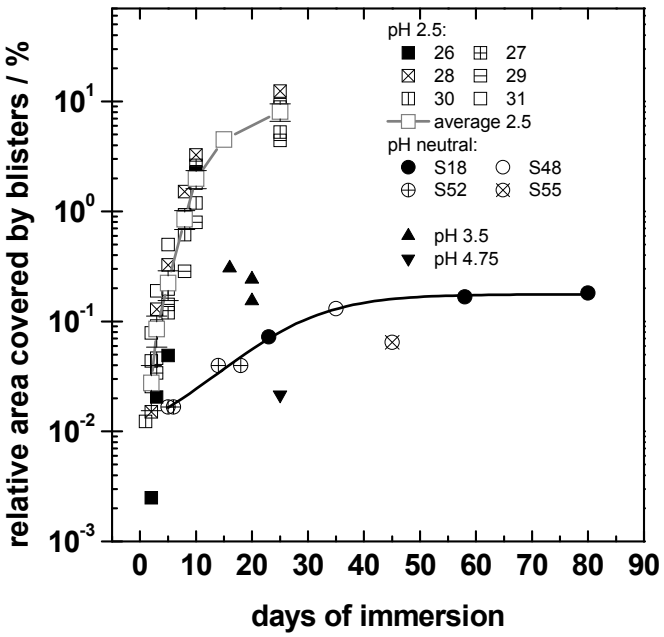

Figure 4. pH-dependence of the sample area affected by corrosion as a function of immersion time. In spite of a large scatter, the huge difference between samples exposed to pH 2.5 (six samples) and neutral NaCl (three samples) is obvious. Lines: Sigmoidal fits of data at pH = 2.5 and pH = 6.5 (from [85]).

The occluded solutions inside the blisters were characterized by high ionic strength (~ 1 M). The chloride concentration surpassed the one of the bulk solution. At bulk pH ≥ 3 the major counter ion was Na^+, whereas at bulk pH = 2.5 it was Al^{3+}, with concentrations of up to 0.6

mol/l. The occluded pH under these conditions also was < 3. Such high ionic strength will cause osmotically driven water ingress into the blister contributing to its growth.

The uptake of water into the coatings was studied by measurements of the coatings capacitance using impedance spectroscopy (details see Section 2.2.3). Already a pH of 3.5 enhanced water uptake rate in 13 µm thick coatings: after 1.2 h in near-neutral NaCl the water content was 8.3 %, whereas it was 16.5% at pH 3.5. At pH= 2.5 water uptake was even faster. An increased water uptake should cause a stronger volume expansion of the coating [84], and facilitate ingress of ions from the electrolyte [53, 57]. At least at moderately acidic pH the increased water uptake was probably due to a stronger hydration of individual, preexisting pathways in the coating. Transport studies on free-standing coating membranes showed, that also the permeability of the coating for ions was enhanced at lower pH (Table 3). There was a certain induction time at low pH, before any ion transport could be detected. This induction time was larger than the breakthrough time calculated from the diffusion coefficients. Therefore it was concluded that the enhanced transport was caused by partial decomposition of the polymer chains in the coating by the acid, and thus by the creation of new pathways for ion transport through the coating. This was confirmed by a test with neutral NaCl using a membrane pretreated with acid. In addition the transport rate for protons was found to be larger than for any other ions, and the water transport rate through the coating was increased as well. In acidic solutions, the enhanced water uptake will increase mechanical stresses in the coating facilitating delamination, and the enhanced ion permeability will make corrosive ions like chloride and protons available at the alloy surface. This lowers the occluded pH to less than 3. Thus the passive layer will not be stable under these conditions, and general corrosion can drive blister formation and growth even at potentials below the pitting potential found for neutral exposure. In turn it was concluded that in near-neutral solutions the coating on the internal side of a blister is additionally harmed by the low pH solutions inside, facilitating the delamination and influencing the blister growth rate [85].

Table 3. Apparent diffusion coefficients through epoxy-polyamide coatings [85]. Errors are calculated from errors in concentration measurements, in the film thickness (d ~ 13 ± 2 µm), and the film cross section (S ~ 4.2 ± 0.7 cm^2). t_b: Breakthrough time in s calculated using the formula $t_b = d^2/6D$ [120].

pH	D_{Na+} / cm^2s^{-1}	$t_{b, Na+}$	D_{Cl-} / cm^2s^{-1}	$t_{b, Cl-}$	D_{Cl-}/D_{Na+}	D_{H+} / cm^2s^{-1}
2	$5.6 \times 10^{-11} \pm 2.3 \times 10^{-11}$	5030 ± 3600	$1.7 \times 10^{-10} \pm 6 \times 10^{-11}$	1660 ± 1100	3	$5.7 \times 10^{-9} \pm 2.3 \times 10^{-9}$
3	$7 \times 10^{-12} \pm 2.5 \times 10^{-12}$	40240 ± 27000	$1.9 \times 10^{-11} \pm 7 \times 10^{-12}$	14800 ± 10000	2.7	-
6	$< 1.1 \times 10^{-12}$	> 256000	$< 3.8 \times 10^{-12}$	> 74000	-	-

Blister stifling in part led to blisters filled completely with solid corrosion products. It was related to an increase in occluded pH. This led to a lower solubility of Al^{3+} causing precipitation of solid corrosion products. As a result, the dissolution rate of the metal slowed down, and the potential increased. For near-neutral solutions, blister stifling was related to the location of anodic and cathodic reactions. Cathodic reactions can take place at IMC within the blister and underneath the surrounding coating close to the blister, as well as on any replated Cu. Evidence for part of the cathodic reaction taking place at IMC outside the actual blister (which becomes a net anode) was presented [85], including the formation of low-pH occluded solutions throughout the blister volume, observation of the Cu redeposition underneath not-yet delaminated parts of the coating, and the occurrence of clear blisters, reminiscent of

cathodic blistering. The major part of cathodic reaction still must be expected to take place within the blister. Upon blister growth, local alkaline regions at IMC-sites underneath the coating will become part of the blister, therefore increasing the pH. If one takes the width of the zone outside the blister, where ORR at IMC can contribute to the total cathodic reaction, to be constant, then the anode/cathode separation should decrease during blister growth. Another important aspect is the increasing depth of the corroded region causing the accumulation of more and more corrosion products, which will slow down further dissolution. Pore clogging in the coating above the blister could contribute as well, similar to the case of blisters on coated iron, where conversion of the anodic site to a cathode has been observed [111]. A change of internal pH and accumulation of corrosion product also happens in acidic solutions, where it is probably connected to a change of individual blisters from anodic to purely cathodic sites. Because there are always some blisters actively growing at bulk pH $\leq$ 3, the change in OCP is small.

The behavior of epoxy-coated AA2024-T3 samples exposed to 0.1 M Na_2SO_4 or 0.1 M Na_2SO_4 + 0.005 M NaCl was very pH-dependent [85, 121]. A sample exposed to near-neutral solution showed no blister formation during its lifetime (> 3.5 months). However, the formation of some white spots on the substrate underneath the coating was observed. At pH of ~ 4.1 some samples showed no formation of blisters during several months, whereas others showed a limited number of blisters after about 2 weeks of immersion time. At a pH of 3.6 or less, rapid coating deterioration and the formation of many blisters scattered across the surface was observed. Those blisters were visible to the bare eye the latest after 2-3 days of immersion, and they were clear in the beginning. Later the blisters turned green, brown, or reddish due to the deposition of corrosion products. The occluded solutions had an acidic pH (although sometimes less acidic than the bulk immersion solution), and were enriched in sulfate (see also Section 2.2.1). There was no significant enrichment in chloride. In blisters showing more positive potentials less dissolved aluminum and higher pH values were found. Similar to chloride-based electrolytes, water uptake of the coating was enhanced at low pH. Diffusion coefficients of sulfate ions through free-standing polymer films were lower than those for chloride ions.

1.4. Basics of Sonoelectrochemistry

In the past decades ultrasound has been increasingly applied in electrochemistry, and several reviews on the emerging field of sonoelectrochemistry have been published [122-124]. Ultrasound has been shown beneficial in the fields of electroplating, where denser and harder deposits were obtained, electroorganic synthesis, electropolymerisation, electroanalytical chemistry and for the electrochemical production of nanoparticles [20, 122-128].

One of the major effects of ultrasound propagation in a liquid medium is acoustic cavitation. There are a number of good reviews covering this phenomenon, but the processes are still not completely understood [129-137]. During the negative pressure phase small bubbles can be formed either because the cohesive forces of the solvent are overcome by the negative acoustic pressure or due to the presence of dissolved gas clusters in solution. One distinguishes between stable cavitation and transient cavitation [124, 133, 138]. High speed photography studies on single bubbles in an acoustic trap have shown that those bubbles "slowly" grow during the rarefaction cycle, and rapidly collapse in the compression cycle. During the collapse the temperature within the bubble raises to values of up to 15000 K. Often a series of small oscillations is observed after the collapse, before the bubble starts to grow again in the next period. Single bubbles trapped in an acoustic field can oscillate in a reproducible manner over many cycles. The bubble dynamics (i.e. the radius of the bubble as a function of time) depends on many variables, like the acoustic pressure and the frequency of

ultrasound, the rest radius of the bubble, the vapour pressure, gas content, viscosity, and density of the medium, and the proximity of a surface [133, 136, 137]. In part phenomena like period doubling and chaotic behaviour are observed. There are a number of mathematical models describing the oscillation processes like the Rayleigh model and the Gilmore model, typically based on ordinary non-linear differential equations [133, 139]. Single bubbles can show sonoluminescence with emission of light pulses in the ns regime [130]. In transient cavitation, the rest radius of the bubble grows from one period of ultrasound to the next one by rectified diffusion [133, 137, 140]. During the growth phase of the bubble more solvent vapour enters the cavity than is condensed during the compression cycle. The bubbles grow to sizes much larger than the equilibrium size. Typical sizes are 5-20 μm [141, 142]. The acoustic field is fluctuating due to the presence of other bubbles, which themselves emit acoustic waves during oscillation thereby disturbing the externally applied sound field [136]. In addition any gas/liquid interface is instable under compression [136]. At some point, the bubble experiences a violent collapse connected with a local increase of temperature to values of a few thousand K, very high pressures, high heating and cooling rates and, in the immediate surroundings of the bubble, strong shock waves (hot spot theory) [133, 136, 143]. Due to the instability of the collapsing bubble surface liquid jets directed to the bubble interior form [136]. Those extreme conditions are generally considered as the base of sonochemistry. The plasma-like conditions can also excite the gas within the bubble and induce visible light emission, the so-called sonoluminescence. The light emission also permits to determine time-averaged temperatures of the bubble interior [144]. If volatile precursors are used, they can react immediately within the cavity. Reactive intermediates like hydroxyl radicals and hydrogen atoms can be formed by solvent decomposition, and then participate in chemical reactions [133, 145-147]. The temperature of the hot spots and their surroundings were determined by different indirect methods: Mišík et al. used the kinetic isotope effect for the homolytic splitting of the O-H and O-D-bonds, respectively, in order to estimate the cavitation temperatures in aqueous media [148]. They sonicated H_2O, D_2O, and an H_2O/D_2O-mixture in the presence of spin-traps, organic molecules, that form a (meta)stable adduct with the H and D radicals, and determined the ratio of the adducts formed by sonication using Electron Paramagnetic Resonance (EPR) spectroscopy. They obtained temperatures between 2000 and 4000 K in their most reliable measurements. Suslick et al. determined the first order rate constants for the decomposition of metal carbonyls as a function of metal carbonyl vapour pressure [149]. By using activation parameters from gas phase laser pyrolysis they obtained temperatures of ~ 5200 K for the cavity and 1900 K for the adjacent liquid phase. Another popular method for temperature determination is based on the recombination of methyl radicals created for instance by decomposition of alcohols or methane [129, 142, 150, 151]. These radicals can form ethane and ethylene, where the rate constant for ethylene formation is strongly temperature-dependent and the one for ethane is not [142]. Shockwaves can cause particle collision leading to agglomeration in the case of metals and to fragmentation in the case of brittle materials like oxides [143]. Additional effects occur if the bubble collapses in the immediate vicinity of a surface that disturbs the local sound field and the hydrodynamics [136]. In that situation the bubbles become toroidal during collapse, and a strong microjet directed to the surface forms [133, 136, 152]. Jet velocities of ~100 m/s are reported [143]. Experiments with laser-induced single bubbles have shown that typical life times of these jets are 1 μs or less, and that sometimes secondary cavitation is taking place during collapse. This liquid jet as well as the shock waves can erode the surface [124, 136, 143, 145, 153]. This only occurs when the ratio γ of the distance of the bubble from the surface and its maximum radius is ≤ 2. The jet contributes only if $\gamma \leq 0.7$. There are also other reports based on electrochemical experiments with microelectrodes stating that jet formation does not occur at ultrasound frequencies [154]. In this case directional microstreaming can be explained by replacement of the volume taken up by the bubble by solution after the collapse

[154]. The interactions between bubbles and the formation of bubble structures is also subject of intensive research. Bubble clouds can scatter the acoustic waves, leading sometimes to a maximum useful intensity for sonochemical reactions [133]. Often frequencies of 20 kHz are used in sonoelectrochemistry. At higher frequencies cavitation bubbles are smaller, their collapse is less violent, and the cavitation threshold (minimum pressure amplitude required to induce bubble formation) increases [136, 155]. On the other hand, the number of cavitation events increases due to the shorter period length of the acoustic wave, and possibly a larger number of radicals is formed [136, 156]. Cavitational activity is also large when the ultrasonic frequency is close to the resonance frequency of the oscillating bubbles. Within a sonochemical reactor or a sonoelectrochemical cell the cavitational activity is not homogeneous throughout [157], and the exact reactor design can influence the sound field [136]. Cavitational collapse becomes less violent with increasing vapour pressure of the solvent and therefore with increasing temperature, because the larger amount of gas contained within the bubble dampens the implosion [133, 143].

Another important effect caused by ultrasound is acoustic streaming [138, 158-164]. It is the analogue of the so-called quartz wind, and caused by momentum transfer of the propagating ultrasonic wave to the medium, converting acoustic energy of the sound wave into kinetic energy of the medium. Therefore a strong, nonlaminar convection of the liquid medium in the direction of the propagating wave is taking place in the area, where ultrasound enters the medium.

Sonoelectrochemical experiments can be conducted in many ways differing by how ultrasound is introduced in the system, the geometry of the setup including the arrangement of electrode and ultrasonic transducer, and intensity and frequency of the ultrasound. Experiments have been conducted in ultrasonic baths [122, 165, 166], in ultrasonic cup-horns and variants thereof [135, 167, 168], and using ultrasonic horn probes immersed in solution [122, 124, 135]. In the latter case the working electrode can be placed at a fixed distance in line with the ultrasonic horn probe such that the electrode surface and the surface of the probe tip are parallel, and that the ultrasonic wave is moving towards the electrode. This is the so-called face-on geometry [127]. The acoustic streaming is then directed towards the electrode. Alternatively, the ultrasonic horn tip can directly serve as the electrode [20, 125], and then is called a sonotrode. The latter technique enables a facile way for the production of nanoparticles by a combination of current and ultrasound pulsing [20, 125, 169-171]: A short current pulse under silent conditions leads to the deposition of small nanocrystals of a metal on the horn tip surface. These are then removed by an ultrasound pulse from the sonotrode and therefore can no longer grow. Addition of surfactants might then stabilize the nanoparticles in suspension. Repetition of the procedure allows production of larger numbers of nanoparticles. An overview of nanoparticles prepared so far by sonoelectrochemistry has been given in a recent review [172]. In order to be able to compare the results obtained by different generators and different setups, and in order to correlate measured electrochemical quantities with the ultrasonic energy, it is necessary to calibrate the power output of the ultrasound system. The method for this has been developed by Margulis et al. [173, 174]: One typically applies ultrasound for a certain time (without external cooling), and measures the temperature before, during and after ultrasound application. Afterwards, in the same setup, electric heating is applied for the same time, and, in repeated experiments, the electric power modified until the temperature-time curves for the ultrasound irradiation and the electrical heating match. The obtained electric power then can be considered equal to the ultrasonic power. Normalizing to the solution volume gives the power density, and normalization to the tip area gives the ultrasonic intensity, I_a.

There is a strong need to improve the understanding how ultrasound affects electrode reactions, and to come to a quantitative understanding of the processes involved. At large electrode / horn separation mainly acoustic streaming effects are of importance. It causes at high ultrasonic intensities a decrease of the diffusion layer thickness to ~ 0.5 – 7 μm [141], leading therefore to enlarged mass transport limiting currents. At smaller separation between horn and electrode there is a strong contribution of cavitation [141]. Cavitation events and associated microstreaming can disrupt the diffusion layer, and cause a further increase in currents [141]. Typical currents associated with a single cavitation event were measured by using microelectrodes and are in the range of a few hundred nA at most [141]. At macroelectrodes multiple events take place at the same time and cause a noisy current response, which is less well defined than the transients observed at microelectrodes. Birkin et al. studied in how far the presence of the electrode modifies the sound field [175]. In the past years there were several reports regarding the correlation between the limiting current densities j_{lim} and ultrasonically induced mass transport. Banks developed an experimental correlation between limiting current densities and ultrasonic power P measured for simple solution-based redox systems [176]. They found a proportionality of j_{lim} to $P^{0.5}$, and gave the ultrasound analogue to the Levich equation for rotating disc electrodes [5]. The dependence on diffusion coefficient D of the electroactive species and the kinematic viscosity v of the electrolyte proved to be identical to the one of the Levich equation. Henley et al. supported the results by computer simulations [177]. Later, Pollet and co-authors verified the approach of Banks [178], and quantified the influence of electrode-horn separation d. They also converted the limiting currents to equivalent electrolyte flow velocities, and found at small numbers of d values larger than the true solution velocity obtained from acoustic streaming alone (up to 16 m/s for I_a = 118 W cm^{-2}). They explained those with asymmetric cavitation close to the electrode surface [178]. Recently, Pollet et al. showed that the proportionality between $P^{0.5}$ and j_{lim} also holds for the electrodeposition of Cu on a Pt wire electrode from a $CuCl_2$ electrolyte at neutral pH [166]. They employed d = 2 mm in these experiments. Bubble collapse and microjets are also known to erode the surface of the electrode [126]. The alteration in concentration profiles, the turbulent streaming and local temperature changes might also impact nucleation processes [179-181]. In addition generated radicals might influence electrode processes [172]. Under conditions where reactions, especially metal deposition processes, were under charge-transfer control, a smaller influence of ultrasound was found [126].

2. Basic electrochemical approaches

2.1. Bulk analogues, thin films and model alloys

2.1.1. Concepts

One way to achieve a better understanding of the corrosion behaviour of complex materials like heterogeneous aluminum alloys lies in the preparation of well-defined model compounds and alloys representative of the metallurgical phases actually present in the real, commercial alloys [29, 30, 35, 49, 51, 182]. Similarly, the mechanism of dealloying, i.e. selective dissolution of the less noble component of a homogeneous alloy phase, has been studied for a long time using single phase Ag-Au alloys [183-189]. The study of bulk analogues of the intermetallic compound phases has been applied for many years in order to determine pitting potentials, oxygen reduction rates, and the action of inhibitors of the individual components of the alloys, and to predict the galvanic coupling behavior with the alloy matrix [25, 114, 190, 191]. Often these bulk analogues are multiphase materials, and partial masking is required to study only the phases with the desired composition. More recently thin film analogues of intermetallic compounds have been prepared by sputtering, flash evaporation or pulsed laser

deposition techniques, which permits also the application of the electrochemical quartz crystal microbalance (EQCM) technique [35, 117, 182, 192-194]. Finally galvanic coupling experiments were conducted in order to study the interaction between local anodes and cathodes [195, 196]. Galvanic coupling was achieved by connecting anode and cathode via an external cable, by inserting one material within the other, and by creation of islands of one material, e.g. Cu, on the alloy matrix material, applying photolithography.

Liao and Wei coupled bulk analogues of Al_3Fe and a multiphase Al-Fe-Cu-Mn alloys with pure Al in neutral and acidic NaCl solutions [196]. They varied the cathode / anode area. In acidic solutions they found much larger cathodic limiting currents. From the measurements they determined at which cathode / anode area ratio there was a crossover from cathodic to anodic control. They concluded that pitting in aluminum alloys is always controlled by the limiting current density on the cathodic IMC, and takes place much faster in acidic solutions.

Clark et al. used galvanic coupling experiments in single compartment and split cells in order to study the corrosion inhibition mechanism provided by chromate species [197]. They coupled pure Al or AA2024-T3 with pure Cu or coupled two AA2024-T3 samples and measured the current between the two electrodes. In the latter case one compartment was deaerated and therefore made an anode. In all experiments with a Cu cathode only addition of the inhibitor to the cathode compartment or pretreatment of the cathode with a chromate conversion coating bath were effectively lowering the current between the electrodes. Therefore chromate was proven to be a cathodic inhibitor – for copper. This finding is in agreement with results by Ilevbare et al. which showed a reduction of cathodic currents on Cu in the presence of chromate [43]. In the case of two AA2024-T3 electrodes there was an effect also when adding chromate to the anode side, which could be explained from polarization curves by a reduced passive current density in the presence of chromate. Later Iannuzzi et al. investigated corrosion inhibition by vanadates using a similar procedure [198]. They found strong cathodic inhibition by clear metavanadates containing monovanadates (and some inhibition of S-phase corrosion), but a much smaller to negligible effect by orange decavanadate. In contrast to chromate, where the inhibition was thought to be caused by reduction and monolayer film formation (supported by observation of a cathodic peak during injection) [197], metavanadate is supposed to act by a chemisorption instead of a reduction mechanism [198].

Jorcin et al. studied the corrosion behavior of a galvanic couple made from a pure Cu wire tightly inserted in an Al wire [195]. They used an aerated 1 mM Na_2SO_4 solution as electrolyte, and performed finite element simulations in order to calculate the local potential and current distribution along the galvanic couple. Calculations predicted large cathodic current densities at the Al/Cu interface. Experiments showed the formation of a crevice at the Al/Cu interface caused by local alkalinization, the corrosion of Al close to the interface, the corrosion of Cu within the crevice and the replating of Cu in a ring on the Al surface. This suggested that replated Cu observed during corrosion of Al alloys might also be caused by crevice corrosion.

The understanding of the microscopic processes and the thermodynamics involved in the phenomenon of dealloying has improved much over the past decade [183, 185-188]. The dealloying process is also known as depletion gilding and has already been applied by the Incans and in medieval Europe in order to create a surface of pure gold on an artifact made from a Cu/Au or Ag/Au alloy [183, 189, 199]. Mechanistic understanding came from experimental and computational studies of the selective Ag dissolution from Ag-Au alloys. Those alloys are single phase across the entire range of compositions [188] and are therefore

good model compounds to study the mechanism of dealloying. If the Ag concentration (or in general the concentration of the less noble element) is above a certain threshold (~60 at% Ag), the so-called parting limit [186-188, 200], the dissolution of the alloy by immersion in nitric acid or application of a sufficiently positive anodic overpotential in an electrolyte causes the selective dissolution of the Ag component. Whereas in the original alloy the distribution of Ag and Au was completely homogeneous, the dealloying process leaves a bicontinuous porous Au behind, where both the Au phase and the pore phase are continuous. During prolonged exposure to electrolyte or during annealing the porous metal structure coarsens with time [187, 199, 201]. A minimum (over)potential is required for the porous structure to form, the so-called critical potential. Below the critical potential the surface passivates. Typically the critical potential is determined by potential sweep methods applying a current threshold criterion. The critical potential thus obtained depends on scanrate. Dursun et al. showed that the true critical potential can be determined by long-term potentiostatic experiments, and is much lower than the results from potential sweeps [185]. Monte-Carlo simulations by Erlebacher confirmed this finding [187]. Already Forty suggested based on TEM studies of dealloying that Au surface diffusion leads to island formation exposing free patches of alloy surface to the electrolyte [189]. Surface diffusion of gold in an electrolyte solution is several orders of magnitude faster than in vacuum [187, 199], with $D \sim 10^{-14}$ cm^2s^{-1} in H_2SO_4 as compared to $2.7 \cdot 10^{-19}$ cm^2s^{-1} [187]. In the presence of halides surface diffusion further increases [202]. In several papers Erlebacher et al. derived the critical issues in dealloying and developed a continuum kinetic model for dealloying considering silver dissolution and diffusion of silver and gold which reproduced all the experimental features described in literature [183, 186-188]: Gold adatoms left over after silver dissolution coalesce in Au islands by surface diffusion exposing fresh alloy to the electrolyte. Therefore Au mounds form, which eventually are undercut by further alloy dissolution. In order to explain the high tendency of the Au to coalesce to islands Erlebacher et al. considered the interface of Au adatoms and electrolyte to behave as a regular solution, and found a low equilibrium concentration for isolated Au atoms. Dealloying therefore leads to a large supersaturation of the electrolyte layer with Au atoms. Under these conditions spinodal decomposition occurs causing Au diffusion against the concentration gradient. Phase separation occurs most rapidly at intermediate length scales. For quantitative modeling they used the Cahn-Hilliard equation. When the porous structure grows into the depth the free Au atoms formed diffuse to the next Au island, until the diffusion length is too large. Then formation of a new Au island is favored. The surface energy depends on the curvature, and its reduction causes therefore the coarsening of the porous structure during dealloying. Below the critical potential, dissolution starts out the same as above, by dissolution of Ag atoms, and roughening of the surface occurs. However, in this case capillary action of the Au atoms finally wins and the surface smoothens and passivates. The time dependence of the current decay measured under these conditions had been described in literature either as a t^{-1} or as a $t^{-0.5}$ behavior. Erlebacher's simulations showed that both of these laws describe at certain times the current transients, but only approximately. Slightly above the critical potential, most of the surface is passive at later times, and further dissolution occurs by distinct pitting events, where large amounts of material are dissolved at once.

The porous gold material itself is of great interest for applications in the area of catalysis, sensing, and filtration [199], because it has an adjustable pore size, a very large surface area and shows excellent conductivity. More sophisticated structures were derived from the material. Ding and Erlebacher created a multimodal pore size material by dealloying and annealing of a 50 wt% Au leaf in nitric acid, then by plating Ag electroless in the coarsened Au alloy created, annealing to cause alloy formation at the Ag/Au interface, and dealloying again [199]. Porous Au with main pore size of 150 nm – 1 μm was created that way, the walls

of which were decorated with 8-15 nm large pores. Later Ding et al. plated obtained nanotubular mesoporous Pt by plating nanoporous Au with Pt, and then dissolving the Au [201]. The interconnected nanotubes had wall thicknesses of ~ 1 nm, and the membranes were mechanically stable at room temperature.

2.1.2. Polarisation measurements and open circuit behavior of bulk and thin film analogues

The metallurgical preparation of pure intermetallic phases often is impossible. It is only possible to prepare (large) grains of the desired phases embedded in a matrix or together with grains of a different material. For electrochemical measurements it must be made sure that only the phase of interest is in contact with the electrolyte.

Buchheit et al. prepared Al_2CuMg material by a standard melting process with a long hold at 510 °C to create mm-sized crystals in the ingot [203]. They masked parts of the surface not being Al_2CuMg with a corrosion resistant lacquer, and used the material as a disc in a rotating ring disc electrode setup. Their results unequivocally showed that corrosion of Al_2CuMg at its open circuit potential or under anodic (and also slightly cathodic) polarization leads to the creation of Cu ions in solution. This effect was less in nitrogen-sparged solutions. They concluded that Cu clusters break off from the nanoporous structure formed during dealloying and dissolve by corrosion at the free corrosion potential. A direct electrochemical oxidation of Cu from the alloy due to complex formation with chloride was ruled out, but a contribution from direct oxidation of Cu from the Cu remnant due to the small radius and therefore large surface energy of the particles was not.

Dimitrov et al. dealloyed S-phase in alkaline solution because Mg should not dissolve under these conditions [39]. They claimed to see a critical potential (but the currents were already quite large below that potential) and correlated it with a model by Wagner et al. predicting a patch size of less noble metal, and calculated a ligament width of 2 nm. During constant potential dissolution they saw oscillatory behaviour, which they explained with the repeated deposition and (mass transport controlled) dissolution of a salt film at the bottom of each pit, and a coupling of the concentration fields of the individual pits. After dealloying at constant potential the authors found a bi-continuous void structure with length scale of 20-50 nm underneath a surface layer, which had a different morphology due to the mass-induced collapse of Cu-rich ligaments.

Ilevbare and co-authors studied the corrosion behaviour of Al_2Cu, Al_2CuMg and $Al_{20}Cu_2(FeMn)_3$ bulk analogues in order to elucidate galvanic coupling processes and corrosion inhibition by chromate and chromate conversion coatings [43, 114, 115]. They reported OCP values of -0.86 V for Al_2CuMg, -0.41 V for Al_2Cu and -0.34 V vs. SCE for $Al_{20}Cu_2(FeMn)_3$ after 2 h of immersion in 0.1 M Na_2SO_4 + 0.005 M NaCl, and found with exception of $Al_{20}Cu_2(FeMn)_3$ no change in OCP by chromate conversion coating (CCC) treatment [43]. Al_2Cu was passive in 0.1 M Na_2SO_4 + 0.005 M NaCl but E_{pit} was close to OCP [114]. During two hours of immersion corrosion and associated roughening and dealloying in the absence of chromate were already taking place on $Al_{20}Cu_2(FeMn)_3$ and Al_2CuMg, respectively, as proven by EIS measurements [114]. This increased the apparent cathodic reduction rates measured on the IMC. A comparison of oxygen reduction rates in chloride-free sulfate electrolyte and electrolytes containing both chloride and chromate showed no significant difference. Ilevbare and Scully therefore believed that cathodic inhibition of real intermetallic compounds (not elemental Cu) were mainly apparent, and that the main effect was passivation of S-phase and prevention of pitting and Cu replating by chromate [114]. This was supported by a clear increase in pitting potential induced by

chromate and CCC. However, for chromate conversion coatings they considered also alternative effects like CCC functioning as a barrier for electron transfer reactions or oxygen diffusion to the cathodic IMC or chromate blocking adsorption sites of O_2.

Some of the most comprehensive surveys on electrochemical properties of IMC phases were carried out by Birbilis and Buchheit [31, 204]. They prepared (or sourced from earlier studies) bulk analogues of 14 different IMC phases relevant for corrosion of 7000 series and other alloys and characterized them by EDX and electron backscattering Kikuchi patterns. They measured the electrochemical properties with a microcapillary cell, as described in some detail in Section 2.2. This is more elegant than masking parts of the surface with nail polish or other lacquers, and permits also multiple reruns on the same substrate by choosing another sample position. Birbilis and Buchheit determined corrosion potentials in NaCl solutions of different concentrations, and measured the polarization curves [204]. The latter is very important because the relative ranking of the corrosion potential of the phases in terms of nobility alone does not tell, whether these phases really are of importance for the corrosion in commercial alloys, and it allows measurement of anodic or cathodic reactions rates important for failure prediction. The polarization curves for Al_2CuMg showed a rather high breakdown potential (0 V vs. SCE), however, already at lower potential the currents were rather large due to dealloying. The OCP values reported for Al_2Cu and Al_2CuMg in 0.01 M NaCl are -0.592 and -0.956 V vs. SCE, respectively [204]. These values are more negative than those found by Ilevbare and Scully in 0.1 M Na_2SO_4 + 0.005 M NaCl on macroscopic samples [115]. The differences might be due to different chloride concentration, different immersion times and sample history prior to measurements. In pH dependent studies Birbilis and Buchheit found that Al_2Cu was passive in NaCl over the entire range of pH and had a wide passive region [31]. This was different from studies of macroscopic samples, where the passive region was less wide [114]. The pitting potential increased at alkaline pH values [31]. The activity of S-phase decreased with an increase in pH, and the corrosion potential was more positive in the alkaline region as well, which was explained by the stability of Mg in alkaline solutions (see above). The cathodic reaction rate on Al_2Cu was found to be independent of pH. The electrochemical behaviour strongly depended on the intermetallic composition and the solution pH.

Ramgopal et al. studied 200-250 nm thin films of $Mg(Zn, Cu)_2$ and $Mg(Zn, Al)_2$ representative of the η-phase in 7xxx series alloys in 0.5 M NaCl at near-neutral pH and at pH ~ 11 in function of the Cu and Al content, respectively [182]. In 0.5 M NaCl they associated the breakdown potential with Zn dissolution (dealloying) and found Zn replating when sweeping the potential in the cathodic direction. Above Cu concentrations of 8 at% both OCP and breakdown potential shifted in the positive direction, and indication of Cu surface enrichment as a consequence of Zn dealloying was found. OCP backplay experiments from OCP recorded on AA7150 were performed in order to test what happens to IMC of the same composition in the commercial alloy. The tests showed a rapid and complete dissolution of the films at the alloy OCP. In alkaline NaCl the $Mg(OH)_2$ surface film was stabilized, and pitting of the thin films was observed. Because the breakdown potentials for these phases were far below those for the 7xxx series alloys it was concluded that the alloy breakdown potentials are unrelated to the presence of the η-phase.

Blanc and colleagues prepared both Al-Cu-Mg alloys and binary Al-Cu alloys by magnetron sputtering from the elements [193, 205, 206]. They found rather large OCP values and cathodic current densities for Al-Cu-Mg in pure sulfate solutions, and concluded that the cathodic behaviour of AA2024 was controlled by S-phase [193]. In the presence of chloride at low concentrations they reported pitting of S-phase, and concluded that also pitting of

AA2024 in presence of chloride was controlled by S-phase. Galvanic coupling experiments with Al-Cu alloys showed a change from anodic to cathodic behaviour. Idrac and co-authors determined the phase composition of a wide range of binary Al-Cu alloys by electron diffraction, and found systems representing the matrix (α-phase supersaturated with Cu), the matrix with hardening precipitates, θ-phase and η_2-phase [205]. The dependence of the OCP-time curves of the alloys in sulfate solution (decreasing at low Cu, increasing at high Cu content) was explained by the growth of a more stable passive layer, the influence of the Cu content on the conductivity of this layer and thus the relative importance of decreasing cathodic rates and decreasing passive current density. The dependence of OCP after stabilization on Cu content could be calculated from the increase in the cathodic current density (taken from polarization scans) with the amount of θ-phase (or η_2-phase) present in the specimens. Samples with higher Cu content showed a higher propensity to pitting. Idrac et al. also coupled alloy phases of different Cu content galvanically and measured the currents as a function of time [206]. The phase with the higher Cu content behaved as the cathode. The maximum current measured increased with the amount of Cu in the anode. The currents were due to the growth of a passive layer on the α-phase in both the anode and cathode. Pits were observed on the cathode after the experiments, with an increased susceptibility for larger Cu contents. The authors concluded from their findings that Cu replating can also be caused by pitting of θ-phase in AA2024.

Liu et al. also used element targets in order to prepare an Al-20at%Mg-20at% Cu film [192]. They performed polarization and anodization studies in 0.1 M ammonium pentaborate and 0.1 M sodium hydroxide electrolyte, and characterized the films and the passive layers formed during the experiments extensively using TEM, XPS, and MIES. They observed no classical dealloying under their experimental conditions. The oxide films were depleted in copper, but underneath the oxides a Cu-rich layer in the alloy was observed. Both Mg and Cu ions were transported faster than Al^{3+} through the film. Anodization in sodium tetraborate caused depletion of Mg in the film due to solubility in the electrolyte, whereas in NaOH enrichment and formation of an outer surface layer of $Mg(OH)_2$ was observed. In addition, due to solubility of Al in NaOH, Cu enrichment underneath the oxide was strong enough for Cu to be incorporated into the oxide film already during simple immersion. The formation of a protective MgO layer is necessary for passivity of the alloy. Based on the OCP, the authors concluded that in strongly alkaline solution S-phase should be a local cathode in an aluminum alloy. In addition copper oxidation might be possible in highly alkaline regions. The same authors demonstrated the formation of Cu nanoparticles without dealloying from a binary Al-30at%Cu alloy prepared by sputter deposition immersed in 0.1 M NaOH [207]. Under these harsh conditions rapid etching is taking place, and the OCP is much less than the one observed in their Al-Cu-Mg work. First Cu is enriched in the alloy close to the surface, then nanoparticles form which are undermined and included in the etching product film, where Cu can oxidize to form Cu(I). Studies of Al-Cu alloys with a lower Cu content showed that the corrosion rate and the enrichment of Cu underneath the surface oxide increases with increase in Cu content [208]. From a certain Cu concentration on Cu nanoparticles are incorporated in the oxide, and little is lost to solution. Enrichment in the alloy (2 nm layer) is up to 40-60 at%. The presence of Cu in the corrosion product accelerates corrosion.

2.1.3. Corrosion behavior of synthetic model alloys.

Electrode arrays made from Cu islands deposited in a regular pattern on an Al or Al-1%Cu matrix were used to study the initial stages of trench formation and the influence of the interaction between IMC phases and pH fields developing in solution [29, 30, 49, 50]. Metastable pitting was seen during open circuit exposure of these alloys to NaCl solution, and was correlated with spacing and size of the Cu islands [51].

Wall and co-authors were the first to prepare synthetic or "nano-engineered" Al alloys with a well-defined oxygen layer to improve the understanding of corrosion processes on aluminum alloys [51], especially with respect to the localized nature of the corrosion initiation. They deposited the Al (and later Cu) by electron-beam evaporation in a UHV chamber, and grew an oxide on the Al by an electron cyclotron resonance oxygen plasma, which led for pure Al films to lower passive current densities than by just oxygen backfilling of the preparation chamber. The Cu islands were 2-5 µm in diameter with distances of 10-100 µm between the islands. Exposure of the artificial alloys to 0.5 M NaCl caused metastable pitting events which stopped after some time because the Cu islands became undercut and isolated from the surrounding Al matrix. The individual pitting events apparently did not depend on particle size and spacing, the event-frequency however increased with increasing particle size.

Missert et al. studied the influence of cathodic particles on pit initiation using microelectrode arrays, because the complex microstructure makes it difficult to separate all the possible influence factors using real alloys [49]. They stated that there are basically two possibilities: the formation of local alkalinity over cathodic particles inducing breakdown of the oxide over the aluminum, if the passive current densities on the matrix are high, the cathode/anode ratio low and the pitting potential high, or the occurrence of pitting due to local polarization of the matrix by the cathodic particles above the pitting potential. Missert et al. measured the pH above cathodic intermetallic phases in-situ during the electrochemical experiments using confocal laser scanning microscopy in the fluorescence mode [30, 49, 50, 209]. Corrosion studies of a 10 by 10 array of 5 µm Cu islands in Al with 10 µm spacing in a solution of 0.05 M NaCl containing fluorescein showed, that the pH increase above the Cu particles took place after the OCP drop indicating pit initiation, and primary corrosion was therefore not induced by local alkalinity. A multielectrode study with five pure 150 µm Al squares containing each one 50 µm Cu island showed that pit formation and growth can be balanced not only by cathodic reactions on the nearest Cu island, but also on more remote Cu islands [49, 50]. In addition after repassivation and re-initiation of pits the anode/cathode distribution can be totally different [49]. This demonstrated that pit formation and growth are complicated processes even in simple geometries. In one experiment on four out of five electrodes the anodic reaction took place exclusively underneath the Cu island, and the corresponding cathodic current came solely from that Cu island. The fifth electrode showed excess anodic current and circumferential pitting in addition to corrosion underneath the Cu island compensated by cathodic currents on the other electrodes, where after a while the neighbouring electrode contributed more than the more remote electrodes [50]. The authors also pointed to the fact that on nominally identical Cu islands the limiting currents for oxygen reaction can differ by as much as a factor of five due to differences in the surface [50]. Further studies [30] revealed that the size of and spacing between individual Cu islands in a single electrode array had an impact on the development of pH: if spacing was small the individual pH fields overlapped. After exposure corrosion product rings were seen around the Cu islands, consisting of chloride-containing aluminum hydroxides. If the spacing was below 10 µm the corrosion products precipitated outside the entire Cu array [209]. In-situ fluorescence microscopy did not show acidic regions due to the pits, which was because the pits formed at the interface between Al and Cu and undercut the Cu in a crevice like geometry [30, 209]. Cu redistribution during corrosion was not observed for these samples [209].

Vukmirovic et al. [29] studied the behaviour of commercial AA2024 and of synthetic alloys made from 100 nm thick Cu islands of diameter 1.8, 80, and 1000 µm in a matrix of Al-1%Cu in order to clarify the relative importance of the S-phase and Cu dissolved in the matrix as a source for Cu accumulation at the surface of the alloy. The applied the RDE and RRDE technique, and determined the total Cu area on the surface by a Pb UPD technique. They also

carried out investigations of the diffusion limited ORR reaction, and found that for Cu values between 20 and 30 μA cm^{-2} were found, independent of pH. The authors found, that for commercial AA2024 the corrosion damage was maximum at intermediate rotation rates ω, but became more localized and less severe with increasing ω. This was explained by the ratio of the width of the diffusion boundary layer δ to the spacing of the intermetallic compounds. At low rotation rates δ was larger than the distance between the particles, which therefore acted like one big planar electrode. Under these circumstances the pH at the entire surface became alkaline due to the cathodic oxygen reduction, and the whole surface was activated. At larger ω δ decreased, and the IMC acted as individual microelectrodes, the field of pH increase was cut off by the diffusion boundary layer, and the enhanced diffusion overall caused the pH to become less alkaline, thereby reducing corrosion. The total amount of Cu on the surface increased with time until the entire surface was Cu decorated, even for highest rotation rates. With synthetic Al alloy, the corrosion damage was as well maximum at intermediate ω. At large rotation rate corrosion became more localized and clear trenches formed around the Cu islands. However, the amount of Cu on the surface never reached full coverage, and decreased even significantly at high rotation rates. RRDE experiments helped to determine the amount of Cu released into the solution during corrosion. Those studies ruled out the Al_2Cu phase as a source of replated Cu, and suggested that the Cu accumulated at the surface of real AA2024 stems about equally from two sources: The Al_2CuMg particles de-alloy and thereby form a porous, mechanically instable Cu sponge, causing Cu particles to break away from the remnant and dissolve in the electrolyte, and Cu finally replating somewhere else on the alloy surface. This mechanism is in agreement with other studies [22, 191, 203]. The Al matrix corrodes and leaves the Cu alloy component behind, which then enriches at the surface. The latter mechanism was valid both in the real and synthetic alloy samples of Vukmirovic et al, whereas the former could only occur in the real alloy [29].

Schneider manufactured synthetic Al alloys consisting of an Al matrix and Cu or Al-Cu-Mg islands on quartz resonators for the electrochemical quartz crystal microbalance measurements. These results will be discussed in Section 2.3.4.

2.2. Microelectrochemistry

A different approach for improving understanding of spatially heterogeneous electrochemical reactions and for probing the electrochemical behaviour of individual regions and phases on a technical alloy surface consists in local electrochemical measurements on real materials. The sample to be investigated is either fully exposed to the electrolyte, the excitation signal (e.g. voltage) applied globally with respect to a regular reference electrode and a large scale counter electrode, and the response (i.e. current) is monitored locally, or both excitation and response measurement are performed on a local scale in the μm-range. The first approach is realized in methods like local electrochemical impedance spectroscopy (LEIS) and the scanning reference electrode technique / scanning vibration electrode technique (SRET/SVET) that will be briefly discussed in Section 3.4. The second approach can be realized by masking techniques using photolithography or special inks / paints. More versatile however is the use of microelectrodes as presented in the following: First a general introduction to microelectrodes will be given, which goes beyond the characterization of localized corrosion processes (Section 2.2.1). Some yet unpublished results from Schneider and Kelly on local pH and potential measurements within individual coating blisters will be shown. In Section 2.2.2 results from literature on the application of microelectrode measurements on bare metals and alloys are reviewed. Section 2.2.3 describes the general characteristics of impedance spectra on coated alloys, with an emphasis on the work of Schneider and Kelly on AA2024-T3 exposed to chloride solutions of different pH [85].

Finally, the first impedance measurements with a simple but efficient microelectrode within individual coating blisters on AA2024-T3 will be highlighted (Section 2.2.4) [72].

As in many areas of materials science, also in electrochemistry there is an increasing interest towards micro- and nanstructuring, and towards decreasing the scale of electrochemical cells. A review paper on electrochemical micro- and nanosystem technologies was given by Schultze and Bressel [210]. Recommended readings are also the special issues from the journal "Electrochimica Acta" on this subject. Downsizing techniques are also of importance for electroanalytical techniques like lab on the chip approaches including the attoliter cells presented by Li et al. [211].

2.2.1. Introduction to microelectrodes

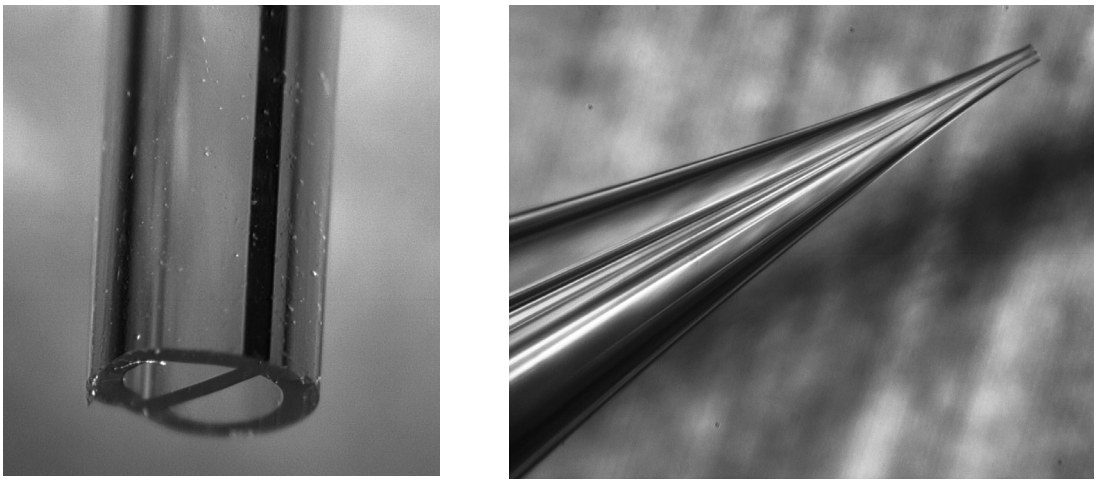

a) **b)**

Figure 5. a) Typical θ-style double-barreled glass capillary (ϕ = 1.5 mm) used for fabrication of microelectrodes b) tip of microelectrode after pulling (~ 50 µm).

The expression microelectrode originally referred to electrode / electrolyte systems with a small electrode area / electrolyte volume ratio [5]. Nowadays it is often used also for µ-sized metal electrodes with a radius smaller than 25 µm, more correctly named ultramicroelectrodes (UMEs) [5]. Another important kind of microelectrode system is based on microcapillaries.

UME discs are typically created by embedding a thin wire of metal like Pt in glass or epoxy, and carefully polishing a cross-sectional area to expose a circle of pure metal [5]. Smaller electrodes and nanoelectrodes can be made by thinning wires embedded in quartz using a so-called micropipet puller [212-215]. These devices are normally used for local heating and pulling of glass capillaries so that they develop a fine open tip at the end (Figure 5). UMEs as small as 1-35 nm in diameter have been reported applying this technique [212, 213, 215]. Other approaches for the manufacture of nanoelectrodes and nanoelectrode arrays for different purposes are based on carbon nanotubes [216], on the use of (electron beam) lithography, templates (e.g. porous alumina, HOPG [217], deposition of Au on metal nanowires embedded in a passive matrix grown by directional solidification of NiAl–Re or NiAl-W eutectics [218, 219]), focused ion beam milling [220], chemical etching of wires (in part combined with sputtering [221]) and isolation of all but the very tip (as in the preparation of STM tips) [214]. The latter approach allowed the manufacture of nanoelectrodes with diameters down to ~ 2 nm [214].

The application of ultramicroelectrodes in electrochemistry is complementary to experiments with mm-sized electrodes. In order to change the potential of an electrode to a new value, the double layer must be charged according to its capacity, and the capacitive current has to pass through the electrolyte. This process is characterized by the cell time constant, which is given by the product of uncompensated resistance between WE and RE and the double layer capacity of the electrode. In the case of mm-sized electrodes the time constant is of the order of ms, whereas with microelectrodes it is in the range of µs. Therefore fast processes taking place on shorter time scales can be studied, such as fast chemical reactions coupled to electrochemical reactions. Diffusion processes can be studied while the diffusion layer is still rather thin. In voltammetry the useful range of scan rates can be increased up to 10^6 V/s, because the lower time constant and the smaller effect of uncompensated resistance lead to a reduced distortion of the voltammogram. Diffusion experiments are expected to show linear diffusion behaviour at short time scales (while diffusion layer thickness is smaller than the electrode radius), but stationary diffusion behaviour at longer time scales (due to a radial diffusion component). Because of the onset of natural convection this transition cannot be observed for a macroscopic electrode. In the case of microelectrodes steady state measurements are no problem, because transition occurs at smaller diffusion layer thicknesses and therefore at shorter timescales. This facilitates determination of kinetic parameters. In linear sweep and cyclic voltammetry steady state voltammograms (radial diffusion) can be recorded up to $v \sim 100$ mV/s. The linear diffusion regime can be probed at high scanrates. Further advantages of UMEs are the measurements in highly resistive media (reduced IR-drop), their local probe capabilities, the applicability for measurements in small volumes including living cells [222], reduced need of materials and the possibility to create arrays. Hemispherical electrodes with a diameter of 50 nm and less deviate in their behaviour from classical diffuse double layer theory, because curvature effects become significant [223].

Steel ultramicroelectrodes have been applied for corrosion studies as well. Newman and Ajjawi investigated the influence of nitrate on inhibition of pit propagation after growing a stable pit into a 50 µm 304 stainless steel at controlled potential [224]. Riley at al performed pit initiation studies on 10 µm 18Cr-8Ni stainless steel electrodes because of the ability to monitor faster events and because of the reduced background current [225]. They indeed observed current transients in the pA range, and associated them with the presence of sulphide inclusions. Pistorius and Burstein studied the effect of chloride concentration and pH on metastable pitting [226], whereas Burstein and Ilevbare found an increase in pitting potential with decreasing specimen area [227]. Such observations were later confirmed by microcapillary techniques (see below).

Besides applications in fundamental studies on electrode kinetics and in electroanalytical chemistry, metal microelectrodes can be used as auxiliary electrodes in local mapping techniques like the scanning electrochemical microscopy technique (SECM), scanning vibrating electrode technique (use of a vibrating microelectrode as a sensor for potential gradient in solution), and the scanning Kelvin probe. The SECM technique can also be applied for microstructuring. Also the tip of an STM or an AFM can – in part after metallization – be employed as a microelectrode. Such approaches open a path for nanostructuring of a surface. A well known example is the deposition of small Cu islands on a gold surface, as originally performed by Ullmann, Will and Kolb [228, 229]. In these studies the potentials of both the STM tip and the gold substrate were controlled. The potential of the gold surface was held at a potential where a Cu UPD monolayer was present on the surface. The potential of the STM tip allowed slow Cu deposition on the tip. By approaching the STM tip close to the surface and applying a small potential step of a few tens of mV to the substrate (in the negative direction), the sign of the tunnel voltage changed, “jump to contact” occurred

and a small Cu island could be deposited precisely at a predetermined position. The height of the island could be varied by changing the size of the potential step (smaller potential steps causing an increase from 0.3 to 1.5 nm) [228], the magnitude of the tunnel current [228], or the integral feedback gain of the instrument [229]. The authors concluded that the Cu was transferred from the tip to the substrate during the contact, without damaging substrate or tip. It was also shown that the method could be applied to other systems, like Pb on Au(111), Ag on Au(111) [229], Pd on Au(111) [230] and Pb on Ag(111) [9], all UPD systems. A certain minimum approach between tip and substrate was necessary for the jump to contact to occur and material to be transferred, which defined a lower cluster size limit, whereas an upper limit was given by a direct contact between surface and tip (crash) [231]. Clusters could be grown to larger sizes by subsequent normal electrodeposition [9]. In the case of the non-UPD system Cu on Ag(111), where despite a strong interaction between Cu and Ag no UPD is taking place, formation of two-dimensional Cu islands instead of Cu clusters was observed [229], and in part several islands of different size were formed during a single approach [9]. Later automated systems were developed which allowed to "write" arrays of metal clusters on a foreign metal substrate in a short time. The creation of such arrays is of interest for fundamental studies on electrocatalysis, where however a minimum number of clusters needs to be presented in order to enable electrochemical measurements [231]. Examples for such arrays were a 20 x 20 array of Pd clusters on bare and UPD-Pd covered Au(111) (depending on substrate potential) [230], the deposition of a 100 x 100 array of Cu clusters on Au(111) on an area of 1.1 x 1.1 μm^2 [231], and the deposition of 25000 Pd clusters on Au(111) [9] The deposition on surfaces modified with a self assembled monolayer was also feasible under certain conditions [9]. The direction of mass transfer during the jump to contact was shown to depend on the cohesive energy: The deposition of Ni clusters was not possible, because the Au atoms instead were transferred from the substrate to the Ni coated tip [9]. The recent progress in the field of ionic liquids finally allowed also the deposition of clusters on Zn and Fe in regular arrays on gold surfaces [232, 233].

A different approach utilises the concentration dependence of the equilibrium potential for the deposition of nanoclusters [60]. A certain amount of metal is slowly electrochemically deposited on the STM tip. The substrate potential is close to the equilibrium potential at the bulk concentration. A potential change of the STM tip to large positive overpotentials causes a rapid dissolution of the metal, and therefore a strong concentration increase and consequently a positive shift of the deposition potential at the substrate surface close to the tip. This was demonstrated for deposition of Co clusters on a gold substrate: the cluster size was determined by the size of the tip apex, and larger than clusters made with the "jump to contact" technique [60]. Cluster heights of 7.5 nm and diameters of < 15 nm have been obtained [234]. The method was also applied for the deposition of Pb clusters on hydrogen terminated n-Si(111) [235].

Schuster et al. applied microelectrodes as a tool for the micromachining of electrochemically active work pieces [236]. They applied ultrashort voltage pulses (tens of ns) between work piece and tool. Because of the finite time required to charge the double layer the work piece achieved the potential required for dissolution to occur only close to the surface of the tool. At positions remote from the tool, the larger distance led to a higher ohmic resistance of the electrolyte and therefore to charging times longer than the pulse length. By moving the tool with an x,y,z-stage then very fine structures were inscribed into the workpiece. The presence of passivating layers had to be avoided. The resistance of a passive layer will influence the time constant, but does not depend on the distance between work piece and tool [237]. For some materials the use of an ionic liquid instead of an aqueous electrolyte can prevent passivation of the surface [238]. In addition the relatively large resistance of the ionic liquid is

beneficial [238]. Other non-aqueous solvents like DMSO were used as well [239]. Apart from (not-embedded) cyclindrical microelectrodes also differently shaped tools were employed, like a loop from Pt wire [240], STM tips [241] and W-tools (starting from wire with $\varnothing$ = 100 µm) with complex geometries patterned by focused ion beam milling, intended for faster microstructuring of large areas [242]. An upper limit for the tool size is given by the large currents required to charge the double layer within ns [237]. Decreasing the pulse length down to 500 ps allowed to increase the spatial resolution to below 100 nm [241]. A modification of the technique using an AFM tip as tool allowed an even finer nanostructuring of thin metal films, and was termed electrochemical nanolithography [243]. In a different approach, the local depletion of the electrolyte in the small gap between an STM tip and the substrate surface was exploited for nanostructuring [244]. During application of nanosecond pulses, the double layer charging consumed most ions, which lead to a suppression of electrochemical reactions everywhere but in a small region at the apex of the tip. In this region, distance between tip and substrate was only a few monolayers of solvent, and the double layers consequently interacted. This allowed highly localized dissolution of the substrate or deposition of small metal (Cu) monolayers (~ 5 nm diameter).

An early driving force for the development of microcapillary-based electrodes was the need of physiologists and neuroscientists to measure voltages across cell membranes, pH in single cells or tissue, and concentrations of neurotransmitters [245-247]. Later on these methods were then adapted for spatially resolved investigation of (localized) corrosion and the monitoring of local pH variation [248, 249]. These capillaries typically have a diameter in the mm range over most of their length, but their very tip can be pulled to an extremely fine size in the µm range. This tip then is the point of contact of the electrode with the object under study. The capillaries can have a single channel, consist of several fused capillaries, or be Θ-style, which means that the capillary is divided by a thin glass wall into two channels (Figure 5). Microcapillary based electrodes can provide local pH probes, local reference and local counter electrodes. For the latter two the corresponding electrodes can be inserted directly into the back part of the capillary after backfilling with electrolyte solution, or the capillary can be connected to a larger solution reservoir that holds the reference and the counter electrode. If necessary a hot Agar / KCl solution can be filled into the very tip of the reference before filling with electrolyte. This enhances the stability of the microelectrode with respect to electrolyte loss, but increases its impedance. The creation of a pH sensitive channel starts by hydrophobizing one side of a Θ-style capillary with a solution of trimethylchlorosilane in xylene followed by heating under an IR lamp [245, 247]. Thereafter the tip is filled with a pH sensitive membrane, like a solution of 8 mg hydrogen ionophore II cocktail A (Fluka) and 3 mg polyvinylchloride (PVC) powder in 90 µl Tetrahydrofuran. PVC serves for stabilization purposes only. After evaporation of the THF a proton conducting solid membrane is obtained. The channel is completed by backfilling with electrolyte of defined pH, like with a buffer solution of 0.1 M KCl and 0.01 M imidazole, and insertion of an Ag/AgCl wire. It is also possible to fill the tip with the pure ionophore cocktail, which serves then as a liquid membrane [248].

Schneider and Kelly constructed pH based microelectrodes with integrated reference electrodes based on the capillaries shown in Figure 5 for the measurement of local pH and local potential in individual coating blisters on AA2024-T3 [85, 121]. Such microelectrodes based on proton conducting organic membranes show in a wide pH range a linear relationship between pH and voltage measured between pH and reference channel (Figure 6). A tip with a rather short taper and large diameter was used in order to be able to pierce the coatings above the blister without destroying the tip. That way it was possible to analyze the occluded solutions in individual blisters. These measurements were complemented by an extraction

technique for small solution volumes as small as a few hundred nm [77, 78]. Extracted solutions were analyzed for ionic composition using capillary electrophoresis. An example for an AA2024-T3 specimen coated with an epoxy-polyamide primer exposed to 0.1 M Na_2SO_4 with pH adjusted to 3.5 is shown in Figure 7 [121].

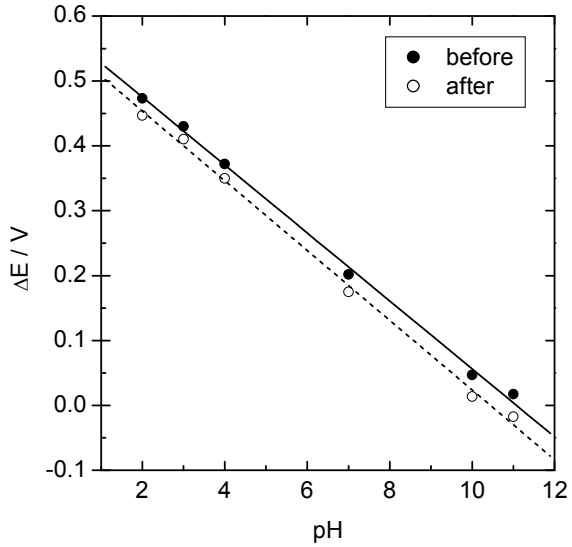

Figure 6. Calibration curve of pH-microelectrode before (filled circle) and after measurements of the local pH and potential in coating blisters. The calibration points were obtained by dipping the electrode into different pH buffer solutions and measuring the voltage between the two channels. Lines: Linear fits.

The specimen shows extensive corrosion after 13 day of immersion. Even though it must be expected that the coating has become quite transparent for ions, there is still a variation in pH between 4 and 5. The more acidic blisters show large amounts of Al in the electrolyte whereas there is little electrolyte in the higher pH blister, where the entire corroded Al has precipitated as solid corrosion products. The corrosion potential tentatively becomes more negative at pH<3.5.

Capillary-based electrochemical microcells enable localized electrochemical measurements on heterogeneous substrates like any polycrystalline metal exposing differently oriented grains, heterogeneous aluminum alloys and alloys containing impurities like MnS inclusions. An early version of such a setup was presented already 1972 by H. Lajain [250]. A small droplet was only placed at the position of interest using a capillary, and the resolution was between 100 µm and 3 mm. For higher resolution combination with a kind of masking technique was needed. Suter, Böhni and co-authors attached an improved capillary-based microcell to the nosepiece of an optical microscope [251-253], whereas Hassel and Lohrengel designed a scanning droplet cell attached to an x,y,z stage [254]. Only a small part of the working electrode with a diameter in the order of the tip diameter (1-1000 µm) is exposed to electrolyte in these studies. The capillary is backfilled with electrolyte using a microsyringe or a micropump, and a small droplet at the tip establishes contact with the specimen surface. Droplet size and shape are controlled by its weight, the surface forces and the capillary force [255, 256]. In most setups however a silicon rubber seal at the end of the capillary prevents leakage of the electrolyte [253, 256, 257]. The (unpulled) backside of the capillary can be attached to an electrolyte-filled holder that provides contact to reference and counter electrode [253, 257]. Alternatively a microreference electrode together with a thin wire as counter electrode can be placed inside the capillary [255]. Combined with a microscope these setups allow accurate positioning of the cell at points of interest of the substrate. The reduced area

leads to smaller background currents, which in turn can facilitate measurements of small current signals, for instance those corresponding to individual pit nucleation processes or to small metastable pitting events [253]. The smaller size requires current measurements in the pA – fA range, increasing the sensitivity to electromagnetic disturbance. Therefore shielding and low noise power sources may be required to perform such studies. A lower useful limit for the tip diameter of about 1 µm has been identified when passive surfaces with a high polarization resistance are studied [257, 258]. In addition, Vogel and Schultze developed a microcell not based on a capillary, but on microstructured glass panes, also with a silicon rubber seal [259]. This cell also allows incoupling of light for photoelectrochemical studies or surface modification. The different setups can be connected to syringes and/or micropumps in order to fill the capillary with electrolyte or to exchange the solution. Some important aspects regarding the application of capillary cells were highlighted by Birbilis et al. [260]:

- The large ohmic resistance of the capillary scales with the exposed sample area, and can distort obtained responses during electrochemical measurements.
- Errors are introduced when using too large scan rates in order to avoid problems with e.g. leakage and blockage of the capillary tip by corrosion products, because of the finite time for double layer charging and for obtaining a steady state response
- Mass transport issues and non-stationarity may be a problem in the case of impedance spectroscopy. Therefore the authors suggested to measure impedance by Fourier transformation of time domain data.
- Problems with mass transport can occur especially with respect to limiting currents due to the small solution volume, and the limiting currents have been shown to decrease with tip radius.

Oltra et al. explained the latter point and pointed out an important issue regarding corrosion measurements where oxygen reduction is the major cathodic reaction [261]: the silicon rubber seal allows rapid transport of oxygen from the air around the microcapillary to the metal surface under investigation, thus preventing the occurrence of limiting currents and altering the cathodic behavior. Application of an Ar atmosphere around the capillary dramatically decreased cathodic currents measured on a Pt surface.

Jorcin et al. compared impedance measurements with microcapillaries to global impedance data and LEIS data (cmp. Section 3.4.2) measured with a scanning bi-electrode [262]. They took a 316L stainless steel in NaCl solutions of different concentration as a model system. With microcapillaries they observed a time constant in the high frequency range unrelated to the specimen properties that was due to the potential distribution within the microelectrode. At lower frequencies the agreement with the global measurements was reasonable, except that there was indication of a second time constant, possibly related to the silicon rubber seal.

Microcapillary approaches were later modified in order to enable more sophisticated measurements. Eng et al. modified a setup mounting the sample on a stainless steel membrane with a piezoelectric sensor, allowing them to establish a non-contact feedback mode for capillary approach to the sample in order to enable scanning capillary microscopy [263]. Staemmler et al. used a modified approach with a laser-based feedback system [264]. In the work of Assi et al. a small Al_2O_3 tube was incorporated in the microcapillary, which was brought into contact with the sample at controlled load and rotated in order to perform experiments on tribocorrosion [265]. The method was then applied to different materials used for human implants [266]. In other studies a pH microelectrode or a pH-sensitive metal wire was inserted into the capillary for local pH measurement during the microelectrochemical experiments [258, 267, 268]. Local probes for sulfide and thiosulfate were inserted as well [268]. Insertion of a second capillary permitted electrolyte flow during the experiment [258],

which also helps avoiding mass transport problems. A more sophisticated approach permitting strong electrolyte flow to enable applications requiring high current densities like electrochemical machining was developed by Lohrengel et al. [269]: These authors removed part of the wall of a Θ-style capillary (cf. Figure 5) close to the tip, and used one of the channels as electrolyte inlet and the other one as electrolyte outlet. In one of the channels a wire was inserted as counter electrode. Electrolyte was pumped through the capillary with the aid of a gear pump, and electrolyte flow rates up to 75 m/s were achieved.

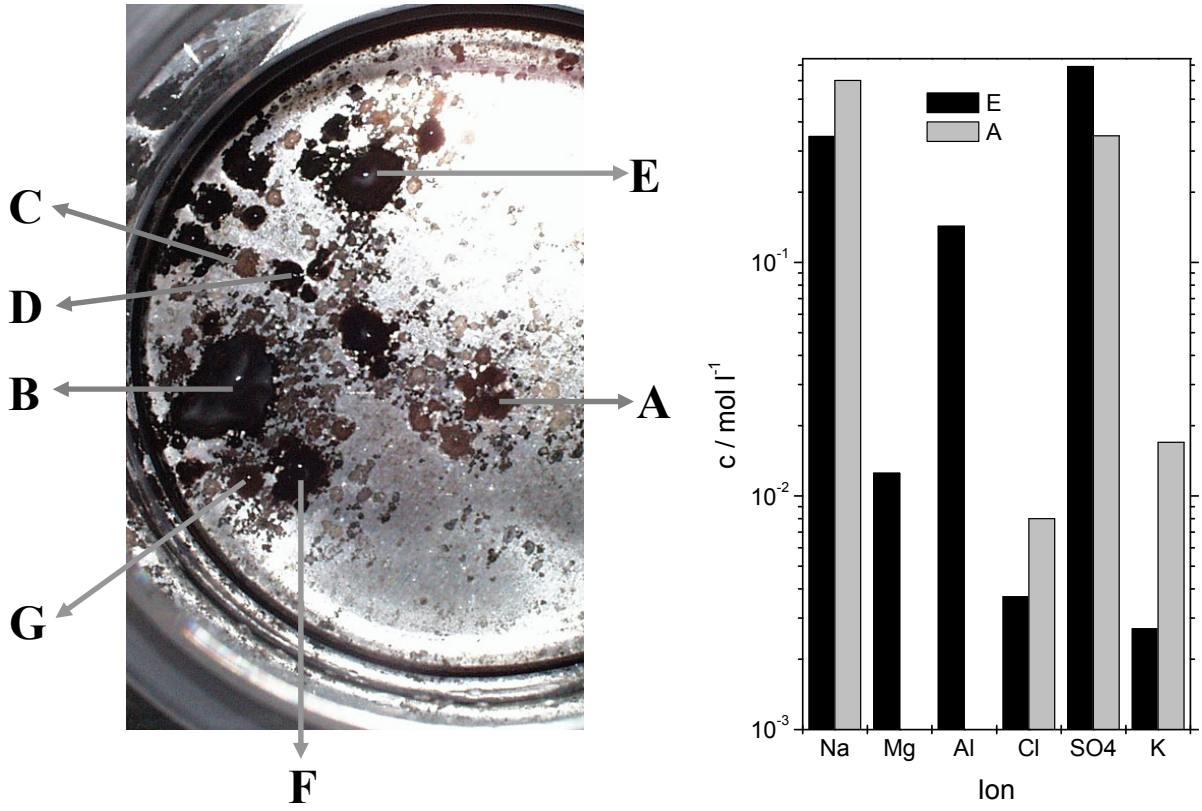

Blister	pH_1	pH_2	OCP	color
A	5.0 ± 0.2	4.6 ± 0.3	-0.530	red
B	3.9 ± 0.2	3.4 ± 0.2	-0.666	grey-green
C	4.3 ± 0.2	3.8 ± 0.2	-0.514	red
D	3.9 ± 0.2	3.5 ± 0.2	-	grey-green
E	3.9 ± 0.2	3.5 ± 0.2	-0.679	grey-green
F	-	-	-0.577	grey-green
G	-	-	-0.575	red

Figure 7. Local chemical and electrochemical properties inside coating blisters on AA2024-T3 after 13 days of exposure to 0.1 M Na_2SO_4 solution with pH adjusted to 3.5. Numerous blisters are visible on the substrate, some of them red in color, some of them grey-green. Local pH (index 1 and 2 refer to the calibration curves in Figure 6) and OCP of selected blisters are given in the table, and the ionic composition of two of the blisters is shown in the bar diagram.

Pilaski et al. built a special current-to-voltage converter in order to enable impedance measurements with a capillary-based microcell, considering the application of such a technique for the localized electrochemical characterization of technical microstructures as, e.g., present in printed circuit boards [270]. Mardare and Hassel developed a fully automated

scanning droplet cell setup permitting accurate positioning of the capillary for the purpose of high throughput screening of materials and obtained – with the aid of a silicon seal – very reproducible exposure areas [271]. They tested the setup by writing an array of oxide spots of different thickness onto a sputter-deposited Hf film.

In humid atmosphere, between an AFM or STM tip and a substrate condensation of water occurs, forming a water meniscus between tip and substrate of (a few hundred) nm dimension (controlled by size of tip apex) [272, 273]. Therefore a two electrode nanocell is formed. This configuration is less versatile than the electrochemical microcell, but it permits to write oxide structures with nm resolution by application of a voltage between substrate and tip. The water is different from bulk water, and presumably no classic Helmholtz layer exists [273]. Examples for applications are the local growth of SiO_2 on Si or of TiO_2 on Ti [272].

2.2.2. Microelectrochemical studies of bare metals and alloys

Böhni, Suter and co-authors studied pit initiation in stainless steels of varying sulphur content in electrolytes of different chloride content with the microelectrochemical cell [251-253]. They correlated metastable pitting events with the dissolution of MnS inclusions, taking place even in (nominally) chloride-free environments. Not all inclusions were found to be active. At higher chloride concentration more and larger pitting events due to the dissolution of smaller inclusions were observed, and pit growth was stabilized. An increase in the diameter of the capillary and thus the exposed area of metal led to a decrease in the pitting potential, supporting the notion that only large inclusions will develop conditions for stable pit propagation. The corrosion suppressing effect of molybdenum as an alloy component was found not to decrease the pit nucleation frequency, but rather to improve repassivation [274]. Therefore stainless steels with 6% Mo (DIN 1.4529) did not show breakdown even at elevated sulphur content (0.022%), except at very high (10 M) chloride concentration, even though the MnS inclusions dissolved [275]. A linear dependence between current noise in the passive region of stainless steels and the exposed area was found. Computer simulations indicated that this can only explained by a dependence of the size distribution of inclusions on the exposed area. The authors derived a correlation between pitting potentials of stainless steels and the size of (MnS) inclusions [274]. The local pH was found to decrease during dissolution of the inclusion and especially after onset of stable pitting, where the hydrolysis of dissolved metal ions contributed to the acidification [267]. The pitting potential was lowest at the interface between MnS inclusion and the bulk steel, where formation of a crevice/pit within the alloy was observed [258]. No pitting was observed when the microcell was placed on a part without (detectable) inclusion [258]. The application of mechanical stress facilitated stable pitting at single inclusions [258]. At higher temperatures faster dissolution of MnS inclusions and a higher propensity for stable pitting of AISI 304 stainless steel were found and explained with a higher dissolution rate of the metal and impeded repassivation [276]. High temperatures (90 °C) and large chloride concentration caused pitting initiation also at surface positions other that the interface to MnS inclusions [276]. Webb and Alkire carried out further studies on the role of sulfide inclusions on 304 stainless steel [268]. In case of shallow MnS inclusions they found an increase in dissolution rate of the inclusion with increasing chloride concentration, and metastable pitting events. Evidence for an eventual passivation of the inclusion was found. In the absence of chloride the inclusion still dissolved, and no metastable transients were seen. The addition of a certain amount of thiosulfate to chloride containing solutions initiated stable pitting onset during MnS dissolution, whereas large amounts of $S_2O_3^{2-}$ suppressed stable pitting. At the interface between steel matrix and deep MnS inclusions stable pits initiated in chloride containing solutions. The authors also found local pH decrease during MnS dissolution, metastable pitting, and stable pitting, no release of sulfide ions during MnS dissolution in neutral electrolytes, and evidence for the production of $S_2O_3^{2-}$ ions

during the electrochemical dissolution of MnS [268]. They finally formulated a model where the presence of a critical concentration of $S_2O_3^{2-}$ ions in the crevice between inclusion and steel prevents repassivation of the steel, leading to stable pitting. Numerical simulation then permitted to calculate pitting potentials [277]. Muto et al. studied the relationship between pitting and MnS dissolution in sulfate and chloride solutions, and combined microelectrochemical polarisation studies with SEM of corrosion morphology [278]. They suggested that in chloride solution MnS dissolution alters the local solution composition, causing the growth of polygonal metastable pits at the interface steel/inclusion, and then a stable polygonal pit turning later into a hemispherical pit. Later on they modified the inclusions by heat treatment and could increase the pitting potentials [279].

Perren et al. performed bulk and microelectrochemical corrosion studies on super duplex stainless steels differing in composition [280]. Whereas the bulk samples did not reveal their two-phase nature during the macroscopic experiments, the individual contributions of the austenite and ferrite phases were clearly revealed in microelectrochemical measurements in the phase boundary region in acidic chloride solutions. Either a simple superposition of the potentiodynamic scans was observed or the formation of a galvanic couple. The relative corrosion susceptibility of the individual phases depended on the exact composition and therefore heat treatment during preparation, especially with regard to nitrogen content, and correlated quite well with the so-called pitting resistance equivalency number (PREN) [280]. In an subsequent study the authors studied the behavior of precipitates like chromium nitrides, σ-phase, and secondary austenite [281]. Park et al. measured local polarization curves on the ferrite and austenite constituent phases in chloride-free solutions 1 [282]. They obtained for both phases anodic dissolution peaks, but at different potentials. The ferrite was electrochemically more active. The authors also studied the behavior of phase mixtures formed by decomposition of ferrite at 800 °C and by spinodal decomposition of ferrite at 450 °C. In both cases these phase mixtures were more active than the parental ferrite compound.

Lill et al. studied the grain-dependent dissolution of FeCrAl alloys by cyclic voltammetry at 50 mV/s in 0.5 M H_2SO_4, finding that (001) oriented grains showed higher dissolution currents / critical passivation current densities than (111) oriented grains [283]. For pure Fe it was found that (101) and (111) oriented grains corrode faster in an acetate buffer than (100) grains, which however develop the thickest oxide layer [284]. This behavior was qualitatively explained by combined effects of the atom density in the surface, the distance to the second layer (bonding strength for atoms in topmost layer), and the accessibility of the second layer. In a typical electrolyte for electrochemical machining (250 g/l $NaNO_3$) the currents in the passive region were largest for (100) grains, and also the oxygen evolution reaction at elevated potentials showed a distinct dependency on crystallographic angle [285]. Under ECM conditions (42 A/cm^2) dissolution of (111) oriented grains was fastest [285]. Hodges et al. studied passive layer breakdown events with pA-peak currents on alloy C-22 in chloride solutions below the critical pitting potential, where no pit stabilization can occur [286]. The method was also applied to the corrosion of dual phase iron aluminides [287]. Apart from corrosion work also other electrochemical studies have been performed, like cyclic voltammetry and scanning impedance spectroscopy on coarse-grain gold [255], cyclic voltammetry of single cementite or $Ni(OH)_2$ particles immobilized on Au [270], and deposition of submicron Cu dots [288]

Another field of study where microelectrochemical measurements have been applied is the electrochemistry and passivation of valve metals (Al, Ta, Nb, Ti, Zr, Hf) [254, 256, 270, 289]. These metals typically are characterized by good passive layers that often can be grown further by anodization to larger thickness, and therefore display superior corrosion resistance.

The electrochemical properties and the passive film growth of these metals depend on the crystallographic orientation of the individual grains. Grain orientation is typically determined by electron back scattering diffraction (EBSD). Capacitance measurements at fixed frequency permitted to map the local oxide thickness for electropolished Hf [270]. Schultze and co-authors published a detailed cyclovoltammetric study on local oxide growth on Zr, Nb and Ta, and determined local formation potentials, oxide thicknesses and capacities [289]. For Nb and Ta (bcc structure) they found that the half height potential and thus the initial oxide thickness depended on the orientation of the grain: Grains with more densely packed atoms showed a reduced oxide thickness. This observation was also seen in a small difference of the formation potential that was determined from extrapolation of the linear part of a plot of the reciprocal capacity versus the applied potential. In Zr (hcp structure) the behaviour was more complex, and the shape of the voltammogram depended clearly on both crystallographic angles (ϕ and ϕ_2 taken with respect to (0001)). Capacity curves showed indications for phase transformations. The oxide formation factor (in nm/V) increased for $\phi > 30°$ while the oxide formation potentials decreased by more than 1 V. Therefore it was concluded that the free energy of oxide formation was strongly orientation dependent for Zr [289]. There is also a great interest in alloys of valve metals, especially in order to achieve a good compromise between materials performance and cost. However, the variation of the metallurgical properties of such alloys as a function of composition can be complex, and the preparation of corresponding bulk alloy specimens for testing is challenging [290]. Therefore Mardare et al. sputter-deposited such alloys onto Si wafers using two sputter targets simultaneously in a way, that the ratio of the constituting elements varied continuously from one end of the specimen to the other. Basically in one step they managed to sputter an entire Ti-Ta library with a Ti content of 2-76 % Ti, and a compositional gradient of 0.25 at%/mm [290]. The oxide formation on this alloy and the corresponding oxide properties (dielectric constant, resistivity, flat band potential) then were studied with the scanning droplet cell [290].

Microelectrochemical cells have also been applied to study the behaviour of pure Al [38, 254, 291] and especially of heterogeneous Al alloys [31, 38, 204, 292-296]. Suter and Alkire used capillaries of 20-100 μm diameter in order to study the interaction between several inclusions on AA2024 [38]. Small areas showed increased pitting potentials, corrosion potentials and higher cathodic current densities. The pitting potentials spread also over an extremely large potential range for the microcapillary measurements, but this range decreased at higher chloride concentrations. Pitting potentials for areas with Al-Cu-Mg particles were 200-300 mV more negative than areas with only Al-Cu-Fe-Mn particles, and particle-free areas showed even higher pitting potentials. Pitting was found to initiate at the interface between matrix and Al-Cu-Mg particles or underneath and around a Cu-rich remnant, depending on actual pitting potential. Pitting at Al-Cu-Fe-Mn particles also started at the interface and involved preferential dissolution of Mn and Fe [38]. The work of Andreatta et al. focused on the role of Al_7Cu_2Fe and $(Al,Cu)_6(Fe,Cu)$ intermetallics in AA7075 [295]. Wloka and Virtanen correlated small current transient seen in microelectrochemical studies on AA7010-T76 with the dissolution of 100 nm sized η-$MgZn_2$ phases [296]. Eckermann et al. studied the effect of Mn content and surface roughness for two model alloys based on AA6016, finding an increase in E_{pit} for smoother surfaces and a decrease for higher Mn content [294]. Further work included exfoliation like attack on AA6016 and the influence of Fe containing intermetallics and Mg_2Si on corrosion initiation and propagation [292, 293]. Also the studies of Birbilis and Buchheit on intermetallic phases must be mentioned in this context [31, 204] that have already been discussed in Section 2.1.2.

2.2.3. Electrochemical impedance spectroscopy of coated metals and alloys

Impedance spectroscopy is abundantly applied in electrochemistry and corrosion science, and a number of reviews and books have been published about this method. The present discussion shall focus on underpaint corrosion.

Impedance spectroscopy is widely applied for the study of coated metals and alloys [89, 98, 111, 116, 297-303]. A large body of work is dedicated to quality screening and testing of coated systems [303-305]. The emphasis of some works lies on developing a fast testing method to predict long-term performance of the coatings [116, 305]. Traditional tests of coated metals and alloys are performed in the so-called salt spray chamber, which are not always representative for the coating behavior in the field [99], or by field exposure tests in industrial and marine environments, which are very time consuming (many months or even years) [305].

Impedance tests can also be applied to follow coating degradation and underfilm corrosion with time. As long as the coating film is defect-free, the response is capacitive and the impedance controlled by the coating, even after formation of a blister [89, 99, 113, 306-309]. Ideally, this behavior leads to a straight line in the $\log|Z|$ vs. $\log f$ - plot with a slope of -1. The spectra can be fitted then with the simple Randles-type circuit in Figure 8a. Schneider and Kelly measured the impedance spectra of coated AA2024-T3 panels in chloride and sulfate electrolytes [85, 121]. In these studies Randles behaviour was seen within the first hours after immersion [72, 76], while the coating was still absorbing water [84]. The impedance at low f was very large, on the order of 10^{10} Ω cm^2 at $f < 0.05$ Hz. The impedance at low f is often used to characterize the quality of coatings and is stable over years for excellent coating systems [309]. For coatings with defects, an equivalent circuit for a coated metal based on a single pore model has been given in literature, and was confirmed many times (Figure 8b) [297, 298, 300, 303, 310]. It contains the coating capacitance C_{coat}, the resistance of ionically conducting channels in the polymer (R_{pore}), the double layer capacitance of metal in contact with electrolyte at the bottom of pores (C_{dl} or CPE_{dl}), and the charge transfer resistance R_{ct}. In the complex plane representation of impedance results ($Im(Z)$ as function of $Re(Z)$), this circuit describes two (more or less) overlapping semicircles. The sum of R_{ct} and R_{pore} will be referred to as R_{corr}, and can be considered as a measure of the total corrosion resistance [311]. Often constant phase elements instead of capacities have to be used in order to compensate for non-idealities [90, 312, 313]. The major cause for the deviations from ideal capacitive behaviour is likely a distribution of time constants ($R_{pore} \bullet C_{coat}$) over the sample area and film thickness [313, 314]. The problem has been discussed extensively in literature, although controversy remains regarding its physical origins [90, 312-316]. Van Westing et al. correlated the constant phase element (CPE) of epoxy coatings with the curing of the coating, water uptake and mobility of polar groups in the coating [90]. For epoxy-coated AA2024-T3 at longer immersion times, the modulus deviated from a straight line and the impedance data became more complicated (cf. Figure 9) [72, 76, 85]. The entire surface of the coated aluminum alloy contributes to the global impedance spectra as long as no blister has formed. Therefore the data could be fitted by the equivalent circuit from Figure 8b. Because the model is a single pore model, the fit results constitute an average over the entire surface (and therefore all pores) and a perfect agreement between fit and spectrum should not be expected. Good coatings are characterised by large values for R_{pore} even after extended immersion, in the range of ~10^8 – 10^{10} Ω cm^2 [57, 305]. Models to determine the progress of delamination with time were suggested [98, 297]. However, other studies claimed that changes due to delamination were too small to inpact the impedance spectra sufficiently to derive accurate informations [89]. In addition, once blisters have formed, the impedance response usually

becomes more complicated, because the corroding metal surface has electrochemical properties different from the original ones at the bottom of the pores.

The coating used in the experiments shown in Figure 9 was only a thin layer of clear epoxy without pigments, inhibitors, or topcoat [72, 76, 85]. It was supposed to be a model coating to study the processes associated with coating failure in a reasonable time frame, and was designed to not retain excellent protective properties. Therefore the impedance characteristics of these coatings changed very rapidly. $|Z|$ at low frequencies decayed initially rapidly due to the uptake of water within the first hour of immersion [84, 98] which caused an increase in C_{coat} and at the same time a decrease in OCP. Once water reached the interface between alloy and metal, the OCP rose to a high value, likely determined by the extremely low passive metal dissolution at the interface, and a very low oxygen reduction rate, and $|Z|$ became constant until the passive layer under the coating broke down. Blister formation then was connected to a drop in OCP (cf. Section 1.3) and in $|Z|$ [72, 76, 85].

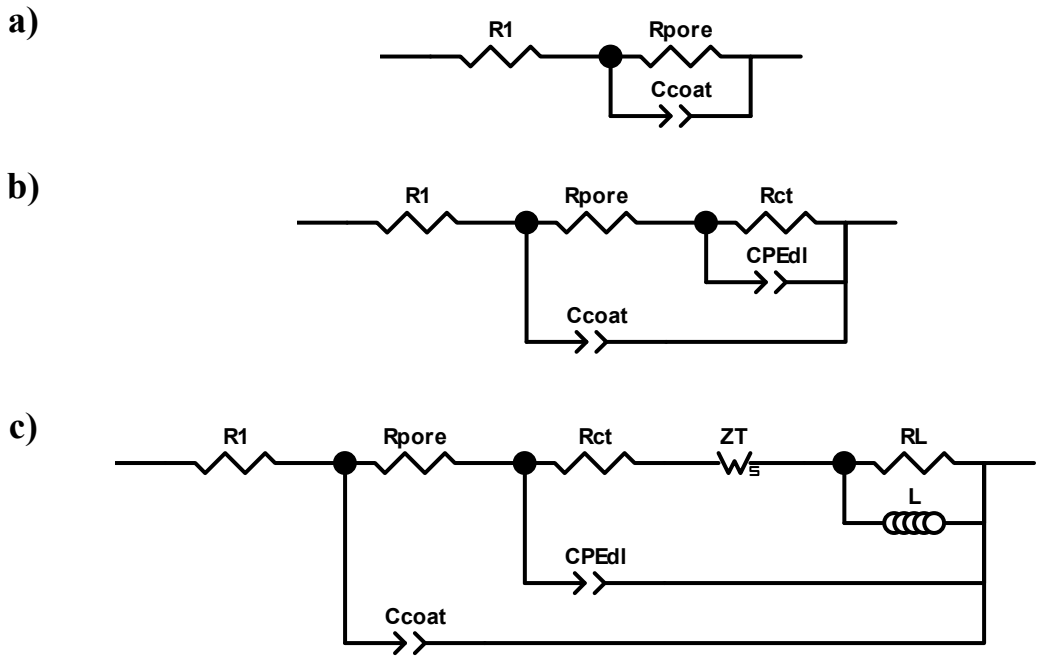

Figure 8. Equivalent circuit used for analysis of impedance data measured on epoxy-coated Al alloys at early immersion times or at high frequencies (a), before blister formation (b), and after blister formation (c). Constant phase elements (CPE) were used instead of simple capacities, except for water uptake measurement. R_{pore}: pore resistance, C_{coat}: coating capacitance, R_{pol}: polarization resistance, C_{dl}: capacitance at bottom of the pores, R_L: a resistor, L: inductance; Z_T: finite length Warburg impedance. Z_T is described by R_T (diameter of low frequency semicircle, decreases with increase in diffusion coefficient and decrease in diffusion layer thickness), Y_T, and an exponent P, which is 0.5 for ideal planar diffusion.

After blister formation on AA2024-T3 the impedance spectra usually showed three semicircular capacitive arcs and one inductive loop in the complex plane [72, 85]. The circuit shown in Figure 8c (based on [116]) was used for data analysis in these cases. It was sufficient to describe the global impedance data over the full range of frequencies for most spectra after blister formation. The inductive loop was located between the two semicircles at lower f. It was sometimes very pronounced, whereas often it only caused a mild distortion of the spectra in that frequency range. The formation of a red blister caused a strong local decrease in both R_{pore} (see below) and R_{pol}, because of the rapid corrosion occurring there.

The physical meaning of R_{pore} in the presence of a blister is discussed in Section 2.2.4. The circuit elements R_L and L are discussed in [317, 318] and were used in [72, 85] to achieve reasonable fits. R_L was usually smaller than R_{ct}, sometimes by an order of magnitude. The occurence of pseudo-inductive behavior on corroding metals has been described in literature [116, 317, 318], and been related to pitting corrosion (in Al stable pit propagation), relaxation processes within corrosion product films, and adsorbed intermediates [116, 317, 319]. Grandle and Taylor [116] discussed it for coated Al alloy 3104-H19 containers and Bessone et al. [317] for uncoated pure aluminum in sodium chloride. The processes in AA2024-T3 are much more complicated than for pure Al because of the different intermetallic compounds present and the occurrence of Cu-replating. The low corrosion resistance, the aggressive solution composition inside the blisters, and the investigations on the corrosion morphology inside blisters clearly showed that stable and severe pitting occurred in some of them [85].

Built-up of corrosion product in the blister or clogging of pores in the coating leads to the appearance of a Warburg impedance [72, 98, 113, 116, 299, 304], and often dominates the impedance response [113]. It is described by a finite diffusion Warburg impedance element Z_T that accounts for diffusion processes [116, 317, 320]:

$$Z_T = R_T \cdot \frac{\tanh\left(\frac{d^2}{D} j\omega\right)^P}{\left(\frac{d^2}{D} j\omega\right)^P} \tag{4}$$

$$R_T = \frac{RT \cdot d}{z^2 F^2 c(x=0) \cdot D} \tag{5}$$

where d diffusion length, D diffusion coefficient, z number of transferred electrons, F the Faraday constant, $c(x=0)$ surface concentration. Three parameters, R_T, Y_T, and P therefore describe it. R_T is the diameter of the low frequency semicircle, and $Y_T = (d^2/D)^P$. P is 0.5 for ideal diffusion processes. The model by Grandle and Taylor considers charge transport through the aluminum oxide passive layer as a diffusion-limited step. Corrosion took place within the coating blisters, and the presented local OCPs lay in the active range of AA2024 for acidic chloride solutions. The observed diffusion process was therefore probably due to diffusion through solid corrosion products/scales, similar to the situation discussed in [317].

Sometimes impedance spectra become quite complicated, and can no longer be described by a simple equivalent circuit.

From the time dependence of C_{coat} one can determine the amount of incorporated water, because the dielectric constant of water is much larger than the one of the polymer film. This was done by Schneider and Kelly [85] by analyzing the impedance response of epoxy-coated AA2024-T3 panels during immersion in 0.5 M NaCl of different pH using only a frequency window between 20 and 200 Hz in order to avoid contributions from the metal/coating interface. The capacitances of the dry coatings (C_0) before immersion were determined by extrapolating the early capacitance data to zero time (performing a linear regression). This led to ε_P between 4 and 4.5, which was in good agreement with literature data [99, 116]. Water uptake was then calculated in volume percent from the time-dependent capacitance data. The following formula given by Brasher and Kingsbury [97] was used:

$$water\ content = 125 \cdot \frac{\log \frac{C_{coat}(t)}{C_{coat}(t=0)}}{\log(80)} \tag{6}$$

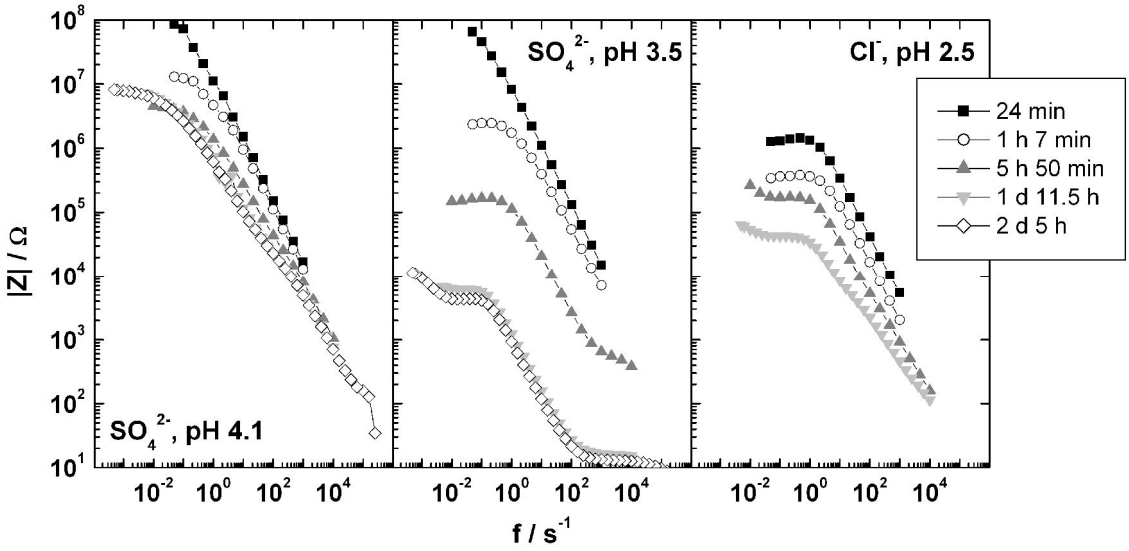

Figure 9. Change of the impedance modulus of epoxy-coated AA2024-T3 panels (area exposed: 31 cm^2) with immersion time in different electrolytes [76].

The corrosion resistance (R_{corr}) decayed more rapidly at low pH as well for thick as for thin films [85]. For a film exposed to NaCl at pH 2.5, the total decrease in R_{corr} amounted to almost 4 orders of magnitude within one day. The general reduction in coating performance was smaller in neutral or weakly acidic solutions, and the formation of a blister was connected with a sharp drop in R_{corr}. Thicker coatings always showed higher R_{corr} under similar immersion conditions than thinner coatings. Blister stifling was accompanied by an increase of the impedance normalized to the blister area. The area corrected R_{corr} increased with time, as well as the diameter of the low frequency semicircle and therefore the Warburg parameter R_T. This supports the contention that diffusion through corrosion product scales controls R_T [72, 111, 113]. R_T scales, as does the total impedance, reciprocally with the actually blistered area. A decrease in R_T by three orders of magnitude was seen for a sample exposed to pH 3.5 NaCl caused by blister growth and by the formation of a second blister, which led to an at least 300-fold increase in blister area.

The special behaviour of epoxy-polyamide coated AA2024-T3 is also revealed in Figure 9 [76]. In sulfate at pH 4.1 the impedance modulus decays during the period of water uptake. Thereafter it remains constant for a long time. At a somewhat lower pH of 3.5 however it continues to decrease very rapidly, even faster than in 0.5 M NaCl at pH of 2.5. Fitting of the data showed that R_{ct} and R_{pore} (the former being larger) and thus R_{corr} decreased as well for pH $\leq$ 3.5 (Figure 10). In parallel to the impedance decay, the above mentioned rapid and widespread coating delaminations took place. For pH = 4.1 R_{corr} passed through a minimum and increased thereafter again. R_{corr} for this specimen remained always above 4 MΩ until blister formation finally took place, leading to a decrease in R_{corr}.

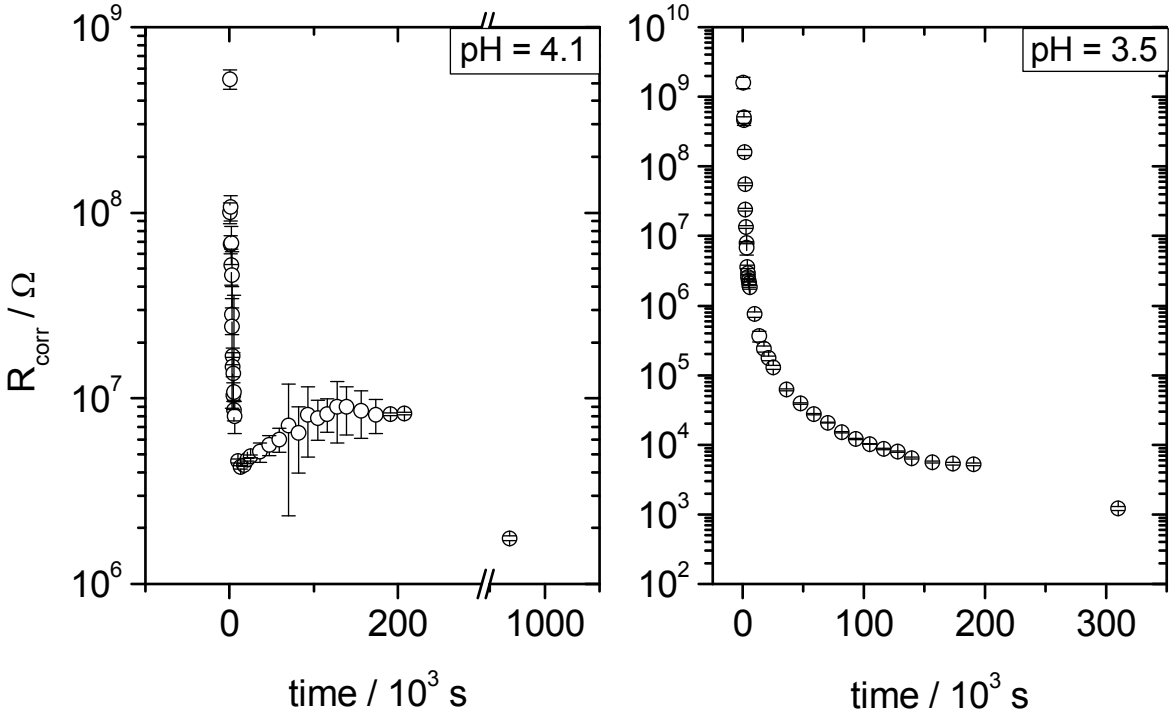

Figure 10. Change in corrosion resistance with immersion time of different epoxy-coated AA2024-T3 specimens exposed to 0.1 M Na_2SO_4 of pH 4.1 (left) and 3.5 (right). Please note the different scales.

2.2.4. Electrochemical impedance spectroscopy with microelectrodes [72]

Coating failure and underfilm corrosion are local processes. Therefore the impedance of the system will differ from site to site, and impedance spectroscopy only can give some averaged signals [69, 72, 306, 321]. In order to obtain local information, it is necessary to measure the impedance on a local scale as well. Such local measurements can be done by several techniques, either by localized electrochemical impedance spectroscopy (LEIS), which is based on a local current and in part also a local potential probe scanned in close proximity across the surface [68, 69, 306, 322-325], or by microelectrodes based on micro capillaries (see also Section 2.2.1, MEIS) [38, 72, 251, 254, 257], or by use of a scanning electrochemical microscope in the AC mode (AC-SECM) [321]. LEIS and AC-SECM also allow mapping of the surface at a given frequency, which can provide diagnostic information about the early stages of the corrosion process [68, 69, 306, 324]. Thereafter it is possible to record the local impedance spectrum at positions of interest. More details about LEIS will be given in Section 3.4.2. MEIS allows to perform measurements inside a blister (without contribution of the coating to the impedance) as well, and thus to separate the influence of coating and corroding substrate [72]. However, this type of experiment damages the coating. In literature, studies on artificial blisters with auxiliary electrodes underneath the coating have been reported, which also allowed separating the influence of coating and substrate [326, 327].

Schneider and Kelly performed electrochemical impedance spectroscopy with rather simple microcapillary electrodes on coating defects in epoxy-coated AA2024-T3 [72] in order to study the contribution of different coating defects on the surface to the overall impedance. The coating thickness ranged from 10 to 50 µm. The samples were exposed in an electrochemical cell to 0.5 M NaCl at different pH. Microelectrodes for current measurements consisted of pulled double-barrel glass capillaries (θ-style, Warner Instruments) with an outer glass diameter of 1.5 mm and tip diameters of 50 µm (cf. Figure 5). One barrel was filled with

3 M KCl / 1 wt%-Agar gel at the tip and then with 3 M KCl, and served as reference electrode channel (RE). The other barrel was filled with 0.5 M NaCl and served as counter electrode (CE). An Ag/AgCl electrode was inserted into each channel. For microelectrode measurements, the samples were disconnected from the cell, rinsed with Milli-Q water and the surface carefully dried under an air stream. The microelectrodes were approached to the sample (WE) under microscope control. Some microelectrode measurements were performed by placing a small droplet (~ 10 - 100 µl) on the interesting sample location. In other cases, a blister was pierced and the microelectrode measurements were taken with the microelectrode tip inside the occluded solution of the blister. This allowed separating the contribution of the coating to the impedance response.

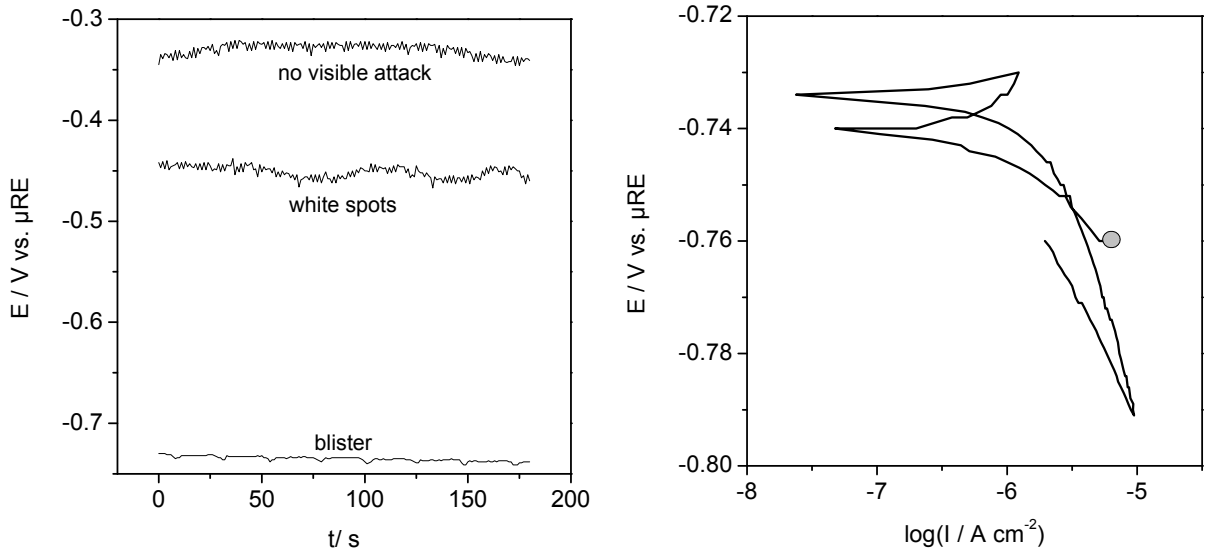

a) **b)**

Figure 11. a) Local potentials measured on different parts of a coated AA2024-T3 substrate after 21 days of immersion in 0.5 M NaCl. b) Polarization scan on red blister of the same specimen measured with a microcapillary-based electrode.

The correct operation of the microelectrodes made only from double-barrel capillaries, without attaching external electrodes via salt bridges, was verified by comparison of a normal impedance spectrum of a fully immersed specimen with two blisters with a normal configuration (global spectrum) with one where the microelectrode channels replaced Nb/Pt counter and SCE reference electrode, respectively. Reasonable agreement was found. At lower frequencies the shape of the spectra in the complex plane plot was very similar, showing two overlapping semicircles, except that the microelectrode impedance data were shifted to larger values of Re(Z) by 2.3 kΩ. During fitting, this had an impact on the solution resistance value, but all the other parameters could be determined accurately. At high frequencies the data recorded with the microelectrode showed a large inductive loop, which was explained by the influence of the current distribution and the high impedance of both channels of the microelectrode. The current distribution using a microelectrode to measure the impedance of a fully immersed panel is highly asymmetric, because all the current needs to pass through the microelectrode (channel area at tip: ~ 10^{-5} cm^2). The strong impact of current distribution effects on impedance data has been discussed in detail by Fleig and others using finite element simulations [328]. The latter assumption was supported by the observation that a higher impedance of the local substrate seemed to reduce the artefacts. Better agreement also was found for a specimen with a single blister between the global impedance spectrum and the local one measured in a small droplet placed on the blister (cf. Figure 12).

For immersion in near-neutral NaCl it was shown that the potentials of red blisters ranged between -0.73 and -0.8 V whereas they were somewhat lower in acidic NaCl (Figure 11), typical values for corroded AA2024-T3 in chloride solutions. The unattacked area still showed passive potentials of ~ -0.37 V (Figure 11). Polarisation curves recorded with the microelectrodes gave polarisation resistances of 6.7 kΩ cm^2 after immersion in neutral and 1.6 kΩ cm^2 in acidic NaCl. Interestingly, despite extended immersion times in 0.5 M NaCl the polarisation resistance found on uncorroded areas was still about 80 MΩ cm^2. This is one order of magnitude less than after two days of immersion, before blister formation.

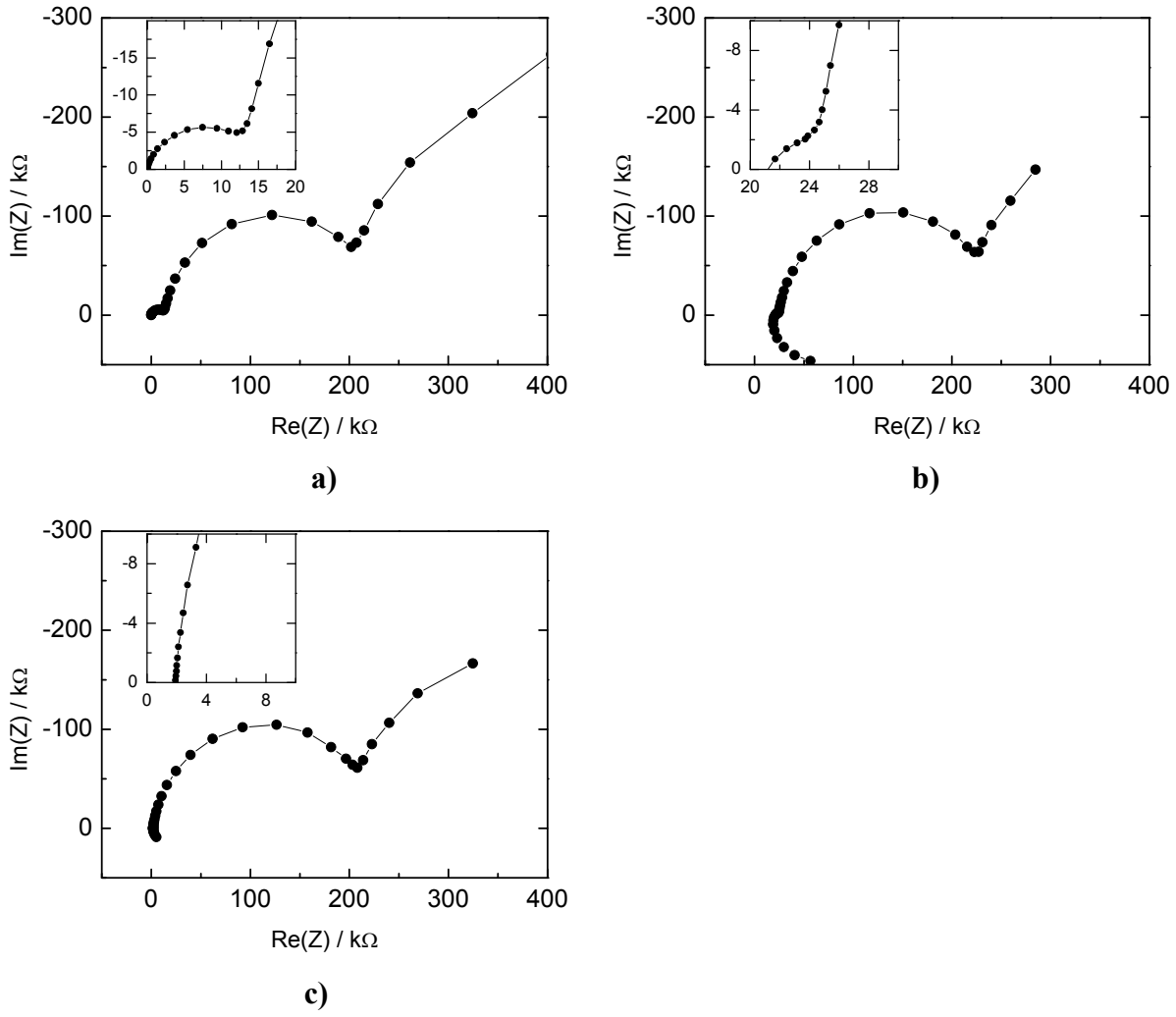

Figure 12. Impedance spectra measured on an epoxy-coated AA2024 specimen after 21 days of immersion in 0.5 M NaCl: a) last global impedance measurement b) spectrum measured with microelectrode on top of coating blister c) spectrum measured with microelectrode within coating blister after piercing the blister. High frequency part is shown enlarged in the inserts.

Comparison between global impedance spectra on a specimen with a single blister and the local impedance spectra measured on top and within the blister showed that for this type of samples the blister controls the global impedance spectrum entirely (Figure 12) [72]. It was characterized by three semicircles. The one at higher frequencies could be assigned to the properties of the blister coating (see Figure 12, inserts), because it disappeared upon piercing of the blister, and the remaining semicircles shifted to lower *Re(Z)*. It was characterized by a coating resistance many orders of magnitude less than on the intact substrate, showing, that the coating properties deteriorated due to the action of the occluded electrolyte within the blister and the mechanical strain exerted on the coating. The semicircle at intermediate

frequencies was assigned to the corrosion reactions taking place within the blister (R_{pol}, C_{dl}), and the one at lowest frequencies to transport of Al^{3+} species through corrosion product built up within the blister (Z_T). Blister formation was connected to a strong local lowering of both R_{coat} and R_{pol}. Therefore procedures described in literature to estimate the amount of delamination from the impedance data could not be applied [98, 297]. The model parameters found by fitting were identical for measurements on the blister and within, showing that all the relevant electrochemical reactions are confined to the interior and the immediate surroundings of the blister. Galvanic coupling via the bulk electrolyte away from the blister is therefore insignificant, as long as the coating is intact away from the blister.

On a sample with several blisters, information about local electrochemical properties can no longer be gained from global EIS [67, 72]. In a global impedance experiment all the different sample features are connected in parallel, and the area with the lowest impedance will dominate the overall impedance response, and also the globally measured OCP. This fact was demonstrated for a specimen with one large and one small blister. The global EIS spectrum was very close to the one of the large blister. The impedance of the small blister was much larger and therefore had a negligible influence on the global spectrum, and the calculated response of the two blisters in parallel was still very close to the spectrum of the large blister alone. Also the properties of the uncorroded areas, which might have changed after prolonged exposure, cannot be calculated from a global experiment. The influence of the uncorroded area on the total impedance response of the sample was calculated as well (correcting the data for total specimen area). Unfortunately, quantitative agreement between the theoretical spectrum and the real global spectrum could not be obtained because of the high-frequency artifacts. However, the general shape of the impedance response in the Bode Plot compared reasonably with the global EIS [72].

2.3. Applications of the (electrochemical) quartz crystal microbalance technique

2.3.1. Overview of the method

The electrochemical quartz crystal microbalance technique (EQCM) is an extension of the quartz crystal microbalance technique applied especially in vacuum deposition methods like sputtering as thickness monitor. Several reviews on the technique are available [329, 330]. A quartz resonator is an acoustic wave based sensor device, and takes advantage of the piezoelectric properties of quartz. Piezoelectricity is the effect that a mechanical stress applied to a crystal causes a potential difference, and it occurs in certain crystals with non-centrosymmetrical space-group. Specifically EQCM is based on the converse piezoelectric effect: The application of a voltage across the crystal causes a mechanical deformation, and the application of an alternating voltage causes an oscillation of the quartz. Typically thin AT-cut single-crystalline quartz discs coated with keyhole-shaped gold electrodes on each side are used for EQCM [331]. The application of a high frequency voltage induces transverse acoustic waves (thickness shear mode resonator), that are reflected at the crystal surfaces. For a given thickness (quartz + electrodes), there is a specific frequency where a standing wave can form by the interference of the original and the reflected wave, and this frequency is the resonance frequency of the quartz. The condition for the formation of a standing wave is that the thickness of the quartz including the electrodes equals half of the wavelength. The resonance frequency then depends on the shear modulus μ and the density ρ of the resonator. If a layer is deposited on one of the electrodes the layer interacts mechanically with the quartz and oscillates as well. Therefore the resonance condition changes and includes now a contribution from the inertial force of the deposited layer [330]. Thus the wavelength increases, and the resonance frequency decreases. From the change in resonance frequency

one can determine changes in the mass on the electrode with a very high sensitivity using the Sauerbrey equation [332]:

$$\Delta f_R = -\frac{2f_0^2}{Z_Q}\Delta m \quad = -\frac{2f_0^2}{\sqrt{\mu_q \rho_q}}\Delta m \tag{7}$$

In this equation Δf_R is the measured change in resonance frequency, f_0 is the resonance frequency of the uncoated quartz, Δm the change in areal mass density, and Z_Q is the mechanical impedance of the quartz ($8.849 \cdot 10^5$ g cm^{-2} s^{-1}), which is determined by the density ρ_q and the shear modulus μ_q of the quartz. The Sauerbrey equation only can be applied if certain conditions are fulfilled: The deposited films must be acoustically thin and rigid, therefore it cannot directly be applied to viscoelastic layers. It assumes no slip conditions, i.e. that particle displacement and shear stress are continuous across the interface to the deposited layer. Also surface roughness causes problems during the application in electrolyte solutions. In general the observed frequency shift contains contributions from the medium in which the quartz is operated, from the pressure, temperature changes, from surface roughness and slippage, all in addition to the pure mass effect [330].

Other piezoelectric materials include lithium niobate [333, 334], langasite [335-339], and gallium orthophosphate [337, 340]. Especially the latter two materials can be used at much higher temperatures than quartz and are therefore suitable as high temperature nanobalances for sensor applications [335-339]. Besides the thickness shear mode other modes of operation are possible, and other types of sensor devices can be made from these materials.

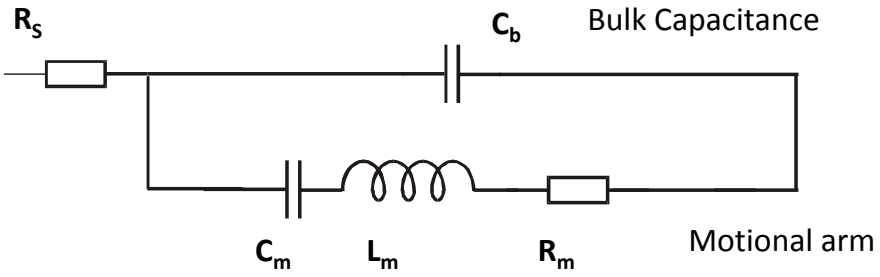

Figure 13. Butterworth-van Dyke equivalent circuit. The information about the resonance frequency is contained in C_m and L_m that represent the oscillating characteristics of the resonator, whereas energy losses are characterized by the resistance R_m. The mechanical impedance of a thin layer on the electrode or any contacting medium can be added in series in the motional arm.

Often, mechanical oscillations of the quartz are electrically excited with an oscillator circuit, and the resonance frequency of the quartz is measured with a frequency counter. However, if one studies the electrochemical behaviour or deposition of viscoelastic or very rough layers on the gold it is better to measure the electrical impedance or the electrical admittance between the two Au electrodes in a frequency range around the resonance frequency, e.g. with a network analyzer [341-343]. The impedance of the quartz can be described by an electrical equivalent circuit, the Butterworth-van Dyke circuit (Figure 13) [344, 345]. It consists of two parallel branches, one representing the static capacitance of the resonator, the other one – the motional arm- the oscillation behaviour. The circuit has been extended to consider the influence of the medium and the layers deposited on the quartz [344, 346-348]. In the simplest case the mechanical impedance of the layer can be added in serial connection to the motional arm. A more complete formula for the motional impedance of a coated or, more generally,

loaded resonator based on physical parameters instead of electrical circuit elements was given in [330, 346].

Figure 14 shows the change in the real part of the admittance of such a resonator in an electrolyte solution during electrochemical deposition. The resonance curve can be described by a Lorentzian function, and is characterized by the peak center frequency, the resonance frequency f_0, and the full width of the curve at half maximum, the damping w [330, 343, 349].

In a liquid the oscillating resonator induces laminar flow parallel to the surface of the resonator corresponding to a damped shear wave propagating into the solution. The velocity decay length of a 10 MHz resonator in water is about 177 nm, beyond that distance the quartz motion is not influenced by the liquid. The mass of the liquid coupled to the quartz induces a frequency decrease, and its viscosity increases the damping [330]. Nomura and Iijima applied the QCM technique for the first time in electrolyte solutions for analytical purposes (determination of cyanide, silver, and copper ion concentrations) [350]. Later Nomura and Okuhara conducted a very detailed study in organic solvents of different density ρ and viscosity η [351]. They correctly stated that the operation in a solvent induces a frequency decrease which is proportional to both $\rho^{0.5}$ and $\eta^{0.5}$, but assumed these effects where additive. Later Kanazwa and Gordon derived from a physical approach the following equation [352]:

$$\Delta f = \frac{\Delta w}{2} = \frac{f_0^{3/2}}{Z_Q}\sqrt{\frac{\eta\rho}{\pi}} \tag{8}$$

The same equation was also obtained by Bruckenstein and Shay who developed circuitry for the in-situ application of QCM during electrochemical measurements and called the method for the first time EQCM [331]. They also verified experimentally the applicability of Sauerbrey equation during electrochemical deposition. Bruckenstein and Swathrrajan applied the method also to underpotential deposition of silver and lead in acetonitrile solutions [353]. In the electrochemical quartz crystal microbalance (EQCM) technique one of the Au electrodes is in contact with the electrolyte and serves as the working electrode [331].

If a smooth rigid layer is deposited on the surface, the shape of this curve remains the same, but shifts to lower frequencies by an amount Δf_R. Under these conditions, one can directly calculate the areal mass density Δm of the layer from Δf_R applying the Sauerbrey equation [332]. If a rough or non-rigid layer of the same mass is deposited, the curves shift to even lower frequencies, the peak width increases and the maximum admittance becomes smaller, i.e. a damping increase $\Delta w > 0$ is observed [343, 349]. Then the application of equation (2.3.1) is only justified as long as Δf_R is as least ten times larger than Δw [342, 354]. Otherwise a complex frequency shift including the damping changes can be defined, which is proportional to the mechanical impedance of the load (i.e. the layer deposited on the resonator) [343, 355].

Deviations from Sauerbrey equation can arise also from inhomogeneous mass distribution [330]. If the lateral correlation length of the mass distribution is larger than the wavelength of the shear wave, this can cause the appearance of two resonance frequencies. If these are close together one single broad peak can appear in the admittance plot. Rough interfaces alter the coupling of the resonator motion to the surrounding liquid. One distinguishes between slight roughness, where the lateral length scale of surface corrugations is much larger than the vertical one, and strong roughness, where they are comparable [330]. In the case of slight roughness that can be treated by perturbation theory non uniform pressure distributions and

viscous contributions to Δf and Δw must be considered. In the case of strong roughness trapped liquid in the rough surface can cause an additional mass contribution, and hydrodynamics in the liquid layer is characterized by non-laminar flow and normal contributions to liquid movement.

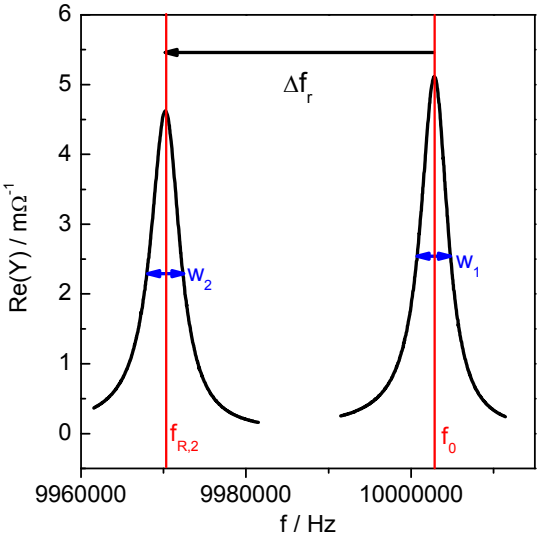

Figure 14. Admittance of a quartz resonator in the vicinity of the resonance frequency f_0 before (right curve) and $f_{R,2} = f_0 - \Delta f_R$ after a metal deposition process (left curve). The width of the peak w at half peak height is the damping of the quartz resonator.

For ideal Sauerbrey-type response, from comparison of the electrical charge flux measured and the mass it is possible to draw conclusions e.g. about the nature of the species deposited, current efficiencies, ion exchange processes, and mechanisms of electrochemical measurements.

For the electrodeposition of a pure metal at 100% current efficiency the expected ratio of mass density Δm and charge density ΔQ is given by:

$$\frac{\Delta m}{\Delta Q} = -\frac{M}{zF} \quad or \quad \frac{dm}{dQ} = -\frac{1}{j}\frac{dm}{dt} = -\frac{M}{zF} \tag{9}$$

where M is the molar mass of the metal, z the number of electrons transferred, and F the Faraday constant. Therefore dm/dt can be considered as the mass-analogue to the electrical current, and has been used in literature [356, 357]. This equation also permits to calculate the expected electric current j_M from dm/dt.

Therefore one can determine from the measurement of Δm and ΔQ measured during electrodeposition the ratio of molar mass and number of electrons transferred. This allows on the one hand determining how many electrons are transferred for each metal atom deposited. On the other hand, for electrode processes where M and z are known, one can calculate the current efficiency ε for the electrode reaction by comparing the measured values to the expected ones (Equation (10)). The use of the differential form dm/dQ enables the determination of ε as a function of electrode potential (e.g. in cyclic voltammetry) or deposition time. This analysis sometimes suffers from two complications: When the current density j is close to 0 (i.e. a change from oxidation to reduction occurs), a mathematic discontinuity appears (cf. Equation (9)), and the numbers tend to infinity. This situation is

worsened by small time delays between current and mass measurement. In addition the derivation of the mass with respect to time often is very noisy.

$$\varepsilon = \frac{(dm/dQ)_{\exp}}{(dm/dQ)_{th}} = -\frac{zF \cdot (dm/dQ)_{\exp}}{M} \tag{10}$$

If several electrode reactions or coupled processes like ion or solvent incorporation can take place, the contributions of the individual reactions to mass and charge can be written down separately in order to determine theoretical values for *dm/dQ* [358]. In these cases a complete analysis sometimes is no more possible without additional assumptions or independent experimental methods.

2.3.2. Application of EQCM for the study of sonoelectrochemical processes

Operation under conditions of acoustic streaming
All the additional informations gained by the application of the quartz crystal microbalance technique in electrochemical experiments are also very attractive in sonoelectrochemistry. However, a quartz crystal is an acoustic wave based device and very sensitive to mechanical disturbances, and power ultrasound causes significant perturbations in the electrochemical cell. This concerns on the one hand the acoustic streaming, and on the other hand the occurrence of cavitation bubbles at the electrode surface. Therefore, until recently, the quartz crystal microbalance technique had only been used to study the effect of (weak) ultrasonic radiation on DNA polymerase reactions [359]. With respect to acoustic streaming it was encouraging that the EQCM technique had been employed before in streaming media, for instance in impinging jet cells [343, 360] and in the rotating quartz crystal microbalance (RQCM) [361-364]. Therefore Schneider et al. performed basic studies on the applicability of the (E)QCM technique in the presence of ultrasound using the electrodeposition of copper from sulfate and chloride-based electrolytes as a model system [365-367]. Some simple experiments were also conducted in water. In addition, the technique was applied in sonoelectrochemical studies of the deposition of metal-ceramic and metal-metal composites [368, 369]. Those experiments were performed in the “face on” geometry, where the tip of the ultrasonic horn probe faces the working electrode at a fixed distance *d*, and the streaming caused by ultrasound is directed towards the quartz (cmp. Section 1.4). The setup used is shown schematically in Figure 15.

It could be shown than only in very few cases in the beginning of the EQCM experiment ultrasound caused the resonance spectra to be extremely noisy [366]. In most cases at $d = 22$ mm, there was no strong impact of ultrasonic fields on the shape and quality of the resonance spectra. Only some additional noise was seen. This noise had no impact on the fitting of the admittance curve with a Lorentz function. The conditions (electrode-horn separation, ultrasound intensity) in those experiments were such that no strong cavitation was taking place at the quartz surface. In order to quantify theses observations a series of QCM measurements was performed in water (no deaeration) at different horn-quartz distances and at different ultrasonic intensities [370]. The noise was determined from the standard deviation of a fit of the admittance spectra to a Lorentz function. The noise of the QCM signal increased with increasing I_a and decreasing *d* (cf. Figure 16).

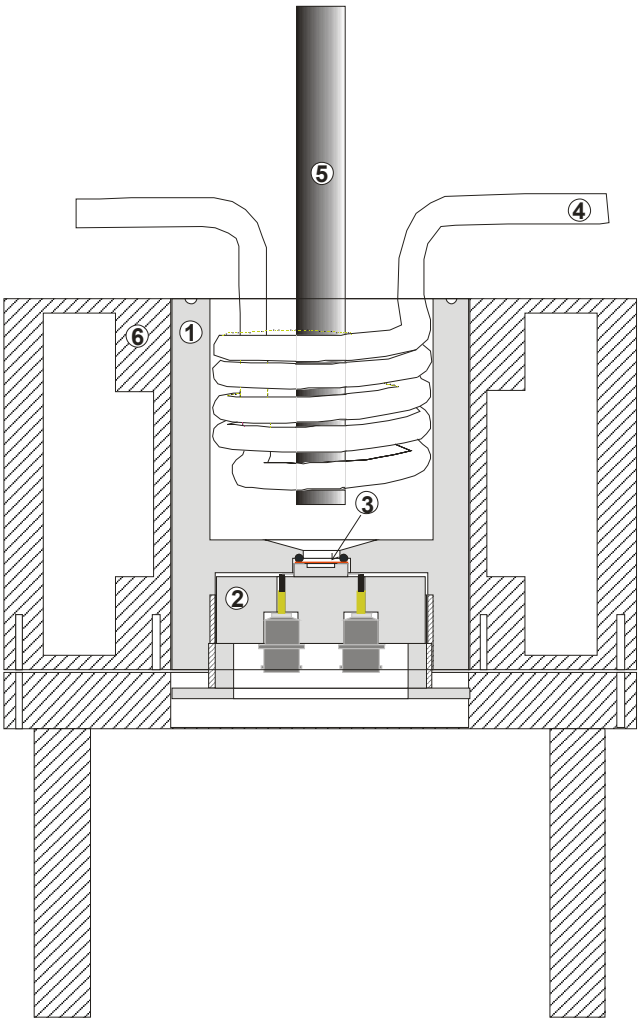

Figure 15. Electrochemical quartz crystal microbalance setup for sonoelectrochemical experiments (schematically) [366]: (1) Cell body machined from Teflon, (2) contact unit, made from teflon body, and two BNC connectors with soldered Pt foil to provide contact to electrodes on quartz, (3) 10 MHz EQCM quartz and sealing O-Ring. Working electrode contact from backside through use of conductive silver paint, (4) glass cooling coil, (5) lower end of ultrasonic horn with tip facing quartz at a distance of 22 mm, (6) stainless steel cooling jacket serving at the same time as holder for the EQCM cell. Reference electrode (Ag/AgCl, not shown) and counter electrode (Cu or Ti/Pt, not shown) are introduced from the top, taking care that the reference electrode is low enough so that the horn does not shield it from the quartz, and that the electrodes do not touch the horn.

It has been demonstrated that the presence of ultrasound and the directional movement of the electrolyte alters also the resonance frequency itself [366, 369]. The resonance frequency of a deposit-free quartz was monitored for a period of 10 minutes in a Cu electrolyte, while ultrasound (I_a ~ 29 W cm^{-2}) was pulsed with $t_{on} = t_{off} = 30$ seconds. Each time ultrasound was turned on the resonance frequency shifted to lower frequencies, and gradually increased again after turning it off. On average the frequency in the ultrasound field was 64 ± 20 Hz lower than under silent conditions. This effect was more systematically studied in distilled water [369, 370], where it was found that at a fixed distance the shift in resonance frequency increased with I_a, and at fixed intensity it increased with increasing distance. The maximum frequency changes found in these experiments compared to silent conditions were up to -450 Hz at d = 8 mm and I_a = 76 W cm^{-2}. In addition it took some time until a stable Δf_R was obtained, and there were considerable fluctuations in the data obtained for f_R and w.

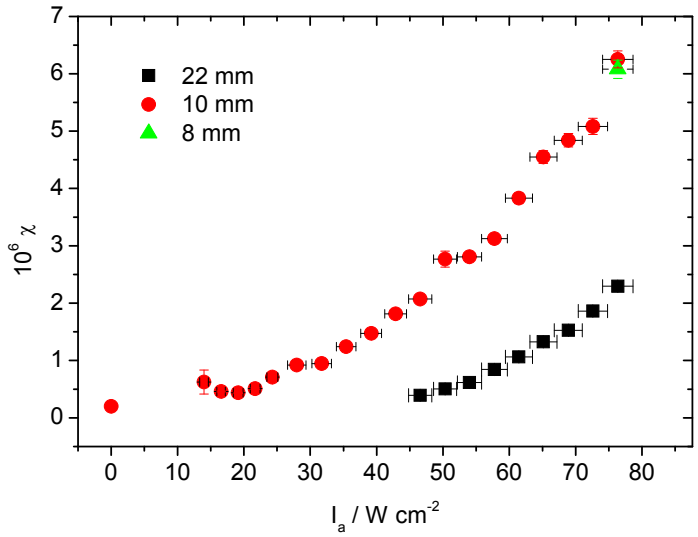

Figure 16. Standard deviation obtained during fitting of quartz admittance spectra to a Lorentz function (cf. Figure 14). The spectra were recorded at different distances between horn and quartz and different ultrasonic intensities.

These studies showed that the QCM can be operated under the influence of an ultrasonic field in solution [366, 367]. The frequency decrease observed during application of ultrasound was far less than the frequency changes usually dealt with in EQCM, and does therefore not constitute an obstacle to the data analysis with the Sauerbrey equation. It is however recommendable to turn on the ultrasound before the start of the electrochemical experiment. Problems could occur in experiments where very small mass changes have to be resolved, as in the case of underpotential deposition experiments. The frequency decrease in the presence of ultrasound was explained by the influence of the mechanical pressure of the streaming liquid directed towards the quartz [366, 367], which increases with increasing intensity and decreasing distance. It has been shown in literature that a pressure difference between the two sides of the quartz crystal induces a frequency shift, and that this shift is negative for AT-cut quartz crystals [364]. After turning the ultrasound off it took a while for convection to slow down which is why the frequency needed some seconds to stabilize at higher frequencies. Fluctuations in the streaming rate were responsible for the noise in f_R. Acoustic streaming is usually turbulent. In addition the liquid which impinges on the quartz will be reflected and stream back into the electrolyte on the outer edge, which may cause some turbulences in the given experimental setup. Surface cavitation was not significant under these conditions.

Figure 17 shows typical cyclic voltammograms obtained in an acidic $CuSO_4$ electrolyte without ultrasound (left) and at d = 10 mm, I_a = 76 W cm^{-2} (right) similar to the data published in [366]. The shape of the voltammograms and frequency curves under silent conditions was in agreement with EQCM literature data. The cathodic peak was caused by mass transfer limitation and is commonly observed at lower Cu concentrations [358, 371]. At elevated copper concentrations no cathodic peak appears [341, 343]. For the sulfate system the voltammogram is well understood. Deposition is taking place by successive transfer of two electrons, i.e. by reduction of Cu^{2+} [358]. Opposite to the literature [358], where incomplete dissolution during stripping was observed and explained by passivation of a part of the deposit, the copper was stripped completely in the experiments reported in [366]. Reasons for this discrepancy can be found in the less negative potentials applied in the experiments shown in Figure 17 leading to less hydrogen evolution and therefore less precipitation of copper hydroxides.

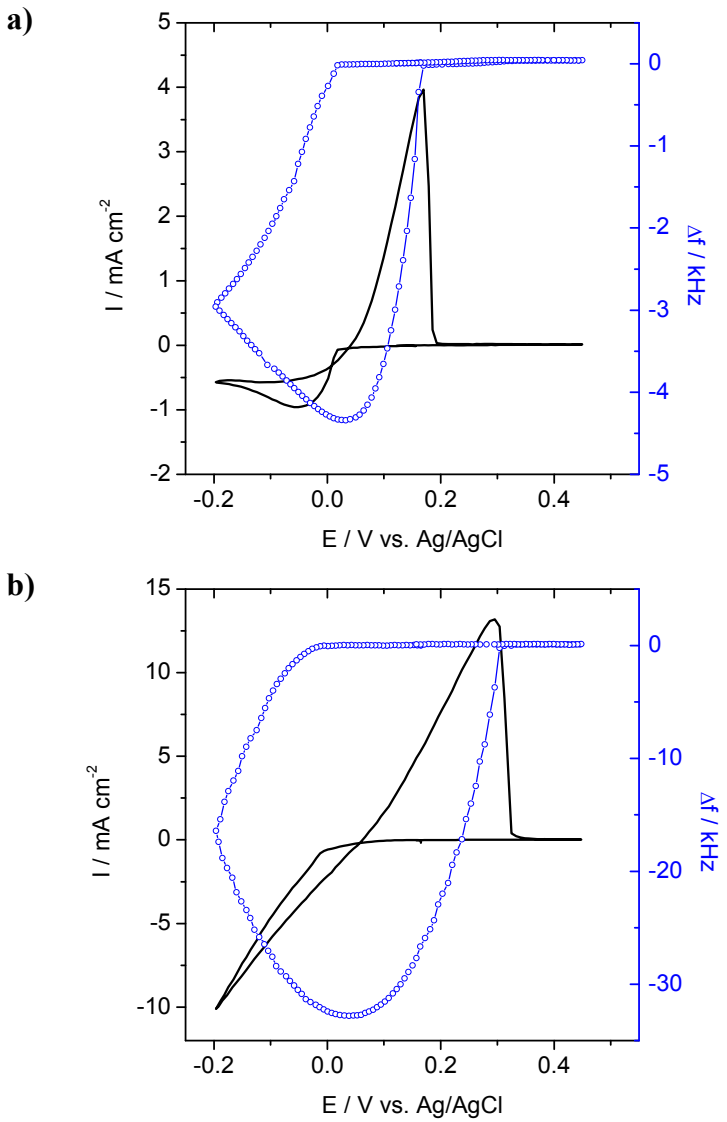

Figure 17. Current densities (lines) and associated frequency changes of quartz resonator (circles) during cyclic voltammetry in 0.01 M $CuSO_4$ + 0.1 M Na_2SO_4 of pH ~ 1 at a scanrate of 0.005 V/s a) under silent conditions and b) under ultrasonic irradiation at an intensity of 76 W cm^{-2}. All experiments were conducted under Ar.

In an ultrasonic field the cathodic current peak disappeared, and currents continued to increase when lowering the potential [366]. In part a loop was observed in the voltammogram during Cu deposition, i.e. currents on the backsweep were larger than on the forward sweep. The maximum cathodic currents and charges, the maximum frequency and thus mass changes, the widths and peak currents of the anodic peak became much larger, and the anodic peak potential was shifted to positive values. All parameters depended in a similar way on the ultrasonic intensity, first strongly increasing, and leveling off or less strongly increasing at higher intensities. The disappearance of the cathodic peak of copper deposition together with the strong increase in the cathodic currents was explained by a gradual transition to charge transfer control due to a strong enhancement in mass transfer, as observed in the literature for many metal systems [126]. The limiting currents due to mass transfer have been shown to be proportional to the square root of the ultrasonic power [176-178] and a reduction in diffusion layer thickness to values of a few µm and less [138, 176]. The resulting increase in deposition rate was reflected in the 7-8 times stronger frequency decrease during the Cu deposition from sulfate solution. The shift in anodic peak potential was simply due to the presence of more Cu

on the electrode, and not an effect of ultrasound on the surface or electrochemical potentials, as clearly proven by an analogous change seen during experiments with a rotating disc electrode at higher rotation rates [366]. Damping changes were negligible, except that in the very end of Cu stripping often a strong short-time increase in w was observed, in agreement with findings from literature [343]. Ultrasound did not alter the potentials significantly, where deposition and dissolution begin in sulfate-based electrolytes, indicating that there was no significant effect of ultrasound on charge transfer kinetics or nucleation overpotentials in these studies [366]. Cyclic voltammograms recorded on rotating disc electrodes showed similar (though not identical) behavior like stationary electrodes in the presence of ultrasound. Especially the gradual change from mass transfer control to charge transfer control proven by the finite intercept in the Koutecký-Levich plot, the increase in currents and consequently the increased amounts of Cu deposited were evident [366]. This proved that the enhanced mass transport was the dominant influence factor of ultrasound on Cu electrodeposition under the conditions applied in that study. Cyclic voltammograms recorded in Cu-free 0.1 M Na_2SO_4 of pH = 1 showed background currents almost three orders of magnitude less than the values in the presence of 0.01 M $CuSO_4$.

In sulfate solutions, the general potential dependence of ε calculated from Equation (10) assuming $z = 2$ was found to be similar with and without ultrasound [366]. This is shown in Figure 18. Especially at low potentials current efficiencies were close to 100% ($\varepsilon = 1$), whereas during early stages of the deposition (more pronounced under silent conditions) values larger than 100% were found. Those were only in part due to an enlarged error by the zero crossing of current. A contribution by the reduction of Cu(I) accumulated close to the electrode, but not sensed by the quartz before beginning of deposition is discussed in the literature as a possible origin of the large numbers for dm/dQ and therefore ε found [358]. This interpretation was supported in [366] by the presence of small cathodic current below ~0.1 V which was not connected with any significant mass change. However ε remained larger than 1 in the beginning of deposition even after correction for the charge caused by this current. Therefore other contributions like the co-adsorption of sulfate ions from the electrolyte stripped off later during deposition or an impact of nucleation processes leading to an inhomogeneous mass distribution in the beginning of deposition were suggested. The strong decrease of ε close to the end of deposition, during the anodic sweep, was explained by the much smaller amount of copper deposition and therefore a relatively larger contribution of side reactions as the reduction of Cu(II) to Cu(I) and the reduction of some residual dissolved oxygen to the total current. During dissolution the current efficiencies were above 100% due to the dissolution path via Cu^+. The oxidation of metallic Cu to Cu^+ proceeds at low currents faster in acidic sulfate solutions than the further oxidation from Cu^+ to Cu^{2+} [372, 373]. Therefore especially at low overpotentials high values are expected for ε, whereas at higher overpotentials a larger fraction of the Cu^+ formed will be further oxidized to Cu^{2+}. This caused the observed decrease of ε with increasing potential.

In the presence of ultrasound of intermediate intensities mass-charge plots were more linear and closer to the theoretical expectations than under silent conditions [366]. The enhanced rate of copper deposition may reduce the importance of side reactions (whether they contribute to mass or not). For the dissolution process in an intermediate potential range also ε-values closer to 1 and thus less dissolution via Cu(I) were reported (Figure 18). This is insofar surprising as also the transport of Cu(I) away from the dissolving electrode should be supported by the enhanced mass transport, and because also loss of Cu without external current in the presence of ultrasound was seen [366]. However, dissolution via Cu(I) involves an adsorbed intermediate which might not be so strongly affected by mass transport, and is only favorable at low current densities [373]. In cyclic voltammetry, dissolution in an

ultrasonic field mainly takes place at higher potentials and larger current densities as discussed above (because a thicker Cu layer is present after deposition), which favors dissolution via Cu(II). In general ultrasound does accelerate cyclic Cu deposition and dissolution, but has only a minor impact on current efficiencies.

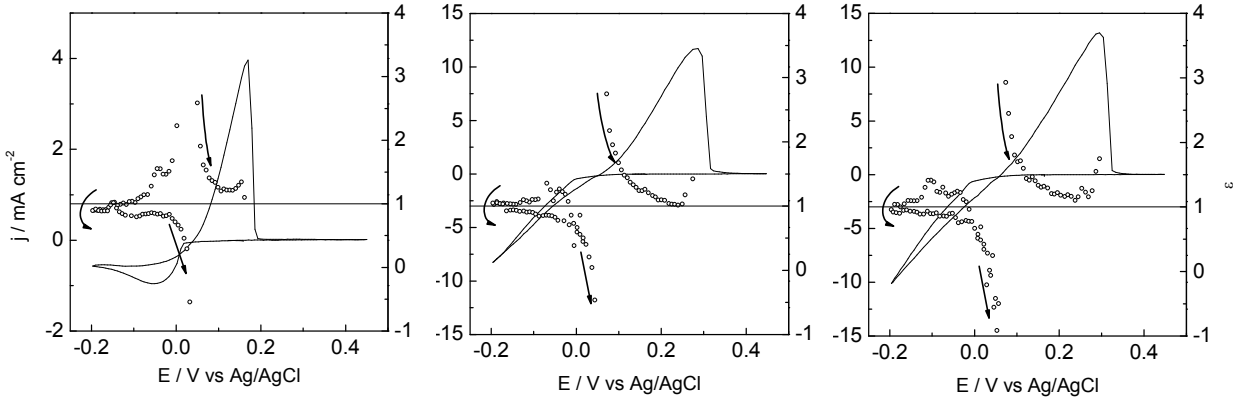

Figure 18. Current densities (lines) and associated (apparent) current efficiencies (circles) during cyclic voltammetry in 0.01 M $CuSO_4$ + 0.1 M Na_2SO_4 of pH ~ 1 at a scanrate of 0.005 V/s under silent conditions (left) and under ultrasonic irradiation at intensities of 24 W cm^{-2} (center) and 76 W cm^{-2} (right) at d = 10 mm. All experiments were conducted under Ar.

In the case of potentiostatic depositions at –0.15 V vs. Ag/AgCl somewhat different results were seen [366]. Under silent conditions, the current decreased rapidly in the beginning of electrodeposition and then continued to decrease slowly with time. The current efficiency was 84%. Under these conditions, the diffusion layer thickness rapidly increased with time, and the zone of Cu(II) depletion expanded into the solution. With ultrasound, no depletion effect took place, the current of Cu-reduction increased with time due to changes in surface condition and roughening, and the current efficiency was 96% at 28 W cm^{-2}. Also the morphology of the deposits was altered by ultrasound. Without ultrasound, in 1 h of electrodeposition a bright, glossy Cu film of 580 nm thickness was obtained. At I_a =28 W cm^{-2}, after only 14 min of electrodeposition a more dull Cu film was obtained (1.5 µm). Whereas films deposited under silent conditions and at I_a ~ 11 W cm^{-2} showed a similar morphology, grain size and appearance were markedly different at I_a ~ 26 W cm^{-2} and I_a ~ 30 W cm^{-2}. The grains appeared larger and flatter. It is known that the morphology of deposits is affected by the extent of mass transport control, and that often the quality of films deposited under charge transfer control is better than under mass transport control [374]. For some metals a grain refinement upon application of ultrasound was observed, and the formation of brighter deposits was observed for a number of metals [165, 179]. Already in the early literature it has been suggested that ultrasound may favor two-dimensional growth over three-dimensional growth normal to the surface, and that therefore less powdery deposits are formed [165].

The two-step nature of Cu electrodeposition is especially obvious during electrodeposition from chloride solutions, where due to the stabilization of Cu(I) by complex formation two well separated reduction (and oxidation) waves appear in cyclic and linear sweep voltammetry [166, 358, 371, 375-379]. Kekesi and Isshiki have reviewed the complex formation constants and other data for the Cu-chloride system [375]. They and others point to the large values of exchange current densities for Cu deposition from chloride that makes deposition of Cu from chloride electrolytes unfavorable [374, 375]. Here the application of ultrasound might prove beneficial to enhance the quality of deposits. Giménez-Romero et al.

studied the electrodeposition and –dissolution of Cu from electrolytes with low concentrations of chloride present using EQCM [358]. They analyzed their data based on the ratio of *dm/dQ* (cf. below), discussed the importance of Cu(I) accumulation at the beginning of the cathodic scan and showed adsorption of Cu(I) on the surface. Zhou et al. showed that at elevated chloride concentrations the anodic and cathodic waves at higher potentials are not associated with any mass change, and that the anodic peak at lower potentials corresponds to the dissolution of Cu(0) to Cu(I) [371]. Similar findings have been reported by Ovchinnikiva et al. [376]. Pollet et al. presented rotating disc electrode studies besides the sonoelectrochemical results [166].

The sonoelectrochemical studies of Cu deposition and dissolution from chloride-based electrolyte was the focus of recent research work of Schneider et al. [367]. Similar to the experiments discussed above, all electrochemical QCM experiments were performed under Ar atmosphere in the face on arrangement. The electrolyte had an initial composition of 0.01 M $CuCl_2$, 0.5 M NaCl, at pH~1.

Cyclovoltammetric experiments were performed at electrode-horn separations of 8, 15, and 22 mm. Typical cyclic voltammograms and the frequency response of the quartz resonator under silent conditions and at ultrasonic intensities of 14 and 76 W cm^{-2} (15 mm distance) are shown in Figure 19. Under silent conditions (Figure 19a), both peak couples known from literature have been reproduced. Frequency changes due to Cu deposition and dissolution were only observed for the peak pair at lower potentials. In agreement with literature data [166, 358, 371, 375] the peak pair at higher potentials was assigned to the Cu^{2+}/Cu^{+}- redox couple, and the one at lower potentials to Cu deposition and dissolution. The total charge per cycle was negative because only part of Cu(II) reduced to Cu(I) is reoxidized thereafter. Based on a potential – log *c(Cl-)* diagram for the copper system and the equilibrium constants for the various possible copper species from the paper by Kekesi and Isshiki [375] it was estimated that in the electrolyte used in [367] originally 53% of the Cu(II) should be present as free Cu^{2+} ions, 41% as $[CuCl]^{+}$, and 6% as $CuCl_2$ (taking the chloride concentration as 0.6 mol/l and neglecting activity coefficients). The major Cu(I) species formed during repeated cycling should be $[CuCl_2]^{-}$ (61%), followed by $[CuCl_3]^{2-}$ (25%) and $[CuCl_4]^{3-}$ (6%). No CuCl precipitation can occur at the high levels of chloride present. Therefore the mass changes in [367] were similar to the observations of Zhou et al. in 0.3 M KCl [371], and very different from the observations of Giménez-Romero et al. at 0.05 M KCl [358], where CuCl precipitation played an important role. The standard potential for the $Cu^{2+}/[CuCl_2]^{-}$ system was calculated from the standard potential for Cu^{2+}/Cu^{+} (0.159V [5]) and the complex stability constant from [375] as 0.525 V vs. NHE and thus 0.328 V vs. Ag/AgCl. For the deposition of Cu from $[CuCl_2]^{-}$ one calculates a standard potential of –0.048 V vs. Ag/AgCl. Already under a rather low ultrasonic intensity I_a the shape of the voltammogram severely changed (Figure 19b), and both cathodic peaks and the anodic peak of Cu(I)/Cu(II) oxidation disappeared. In the potential range above 0.1 V anodic and cathodic current traces now were found to be nearly identical (at 22 mm), or even reversed. The currents became slightly positive at elevated potentials, but there was no more anodic peak in that region. At potentials below 0.3 V the current became negative and its magnitude increased almost linearly with decreasing potential, the slope *di/dE* increasing with I_a. At 8 W cm^{-2} and d = 22 mm it finally leveled off. There was little if any influence of I_a on the potential where the corresponding reduction process set in. At I_a > 9 W cm^{-2} the cathodic currents continued to increase linearly until Cu deposition started (Figure 19b, c). With increasing intensity the entire voltammogram was found to shift into the negative current region (Figure 19c).

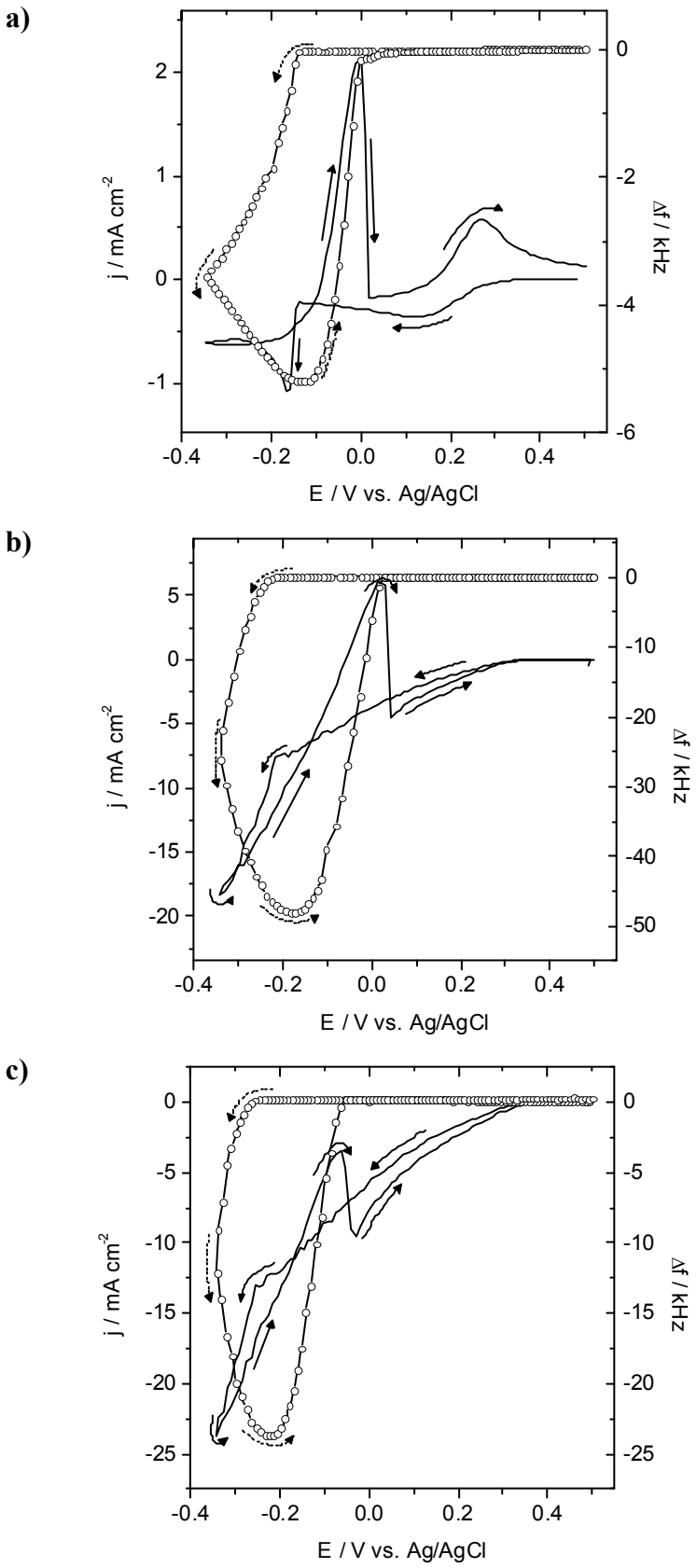

Figure 19. Electrodeposition and –dissolution of Cu from an electrolyte of 0.01 M $CuCl_2$ + 0.5 M NaCl, pH ~ 1 a) under silent conditions and at d = 15 mm under an ultrasonic intensity of b) 14 W cm^{-2} and c) 76 W cm^{-2}. Line: Current density at Au WE. Circles: Frequency changes of quartz resonator. Arrows indicate direction of potential sweeps, sweep rate 5 mV/s.

The potential where Cu deposition began was determined from Δf_R and was reported to be clearly to shift in the presence of ultrasound and with increasing I_a to more negative values. Ultrasound of low intensity increased maximum cathodic currents and the amount of Cu deposited on the quartz by a factor of ten or more (Figure 20a). A further increase in ultrasonic intensity still caused an increase in the maximum cathodic current densities, but the anodic peak currents decreased in magnitude, finally becoming negative, and less Cu was deposited. After correction for the background currents the anodic peak currents were positive, but still decreased with I_a, because a smaller amount of Cu deposited will lead to lower maximum dissolution currents. From the total mass deposited and the total cathodic charge flux (Figure 20a) an averaged (apparent) current efficiency ε for the deposition (assuming $z = 2$), and from the anodic peak charge (after background correction, assuming $z = 1$) for the dissolution was calculated (Figure 20b). For the deposition process ε was reported to be far below 1, and to decrease further with increasing I_a. For the dissolution the ε-values were > 1.

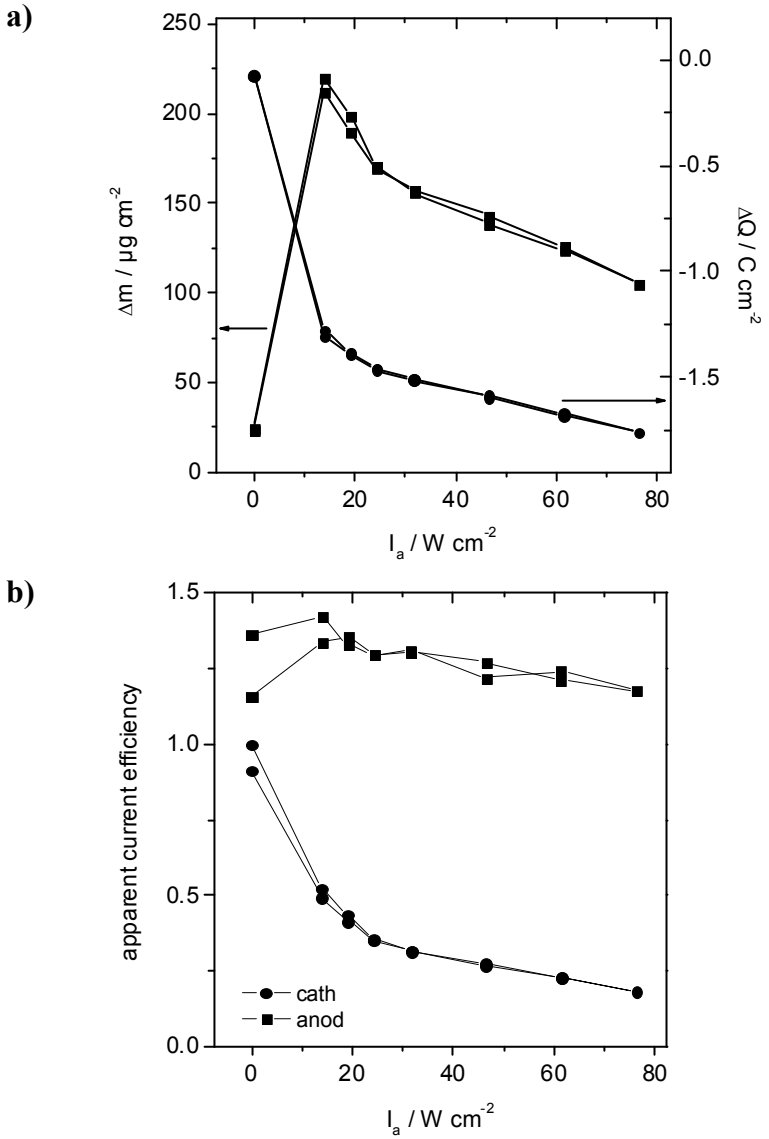

Figure 20. Electrodeposition and –dissolution of Cu from an electrolyte of 0.01 M $CuCl_2$ + 0.5 M NaCl, pH ~ 1 at d = 15 mm. a) maximum mass deposited and dissolved and total cathodic charge density in a single voltammetric cycle (E: 0.5 V – (-0.35 V), 5 mV/s) b) corresponding averaged cathodic and anodic apparent current efficiencies.

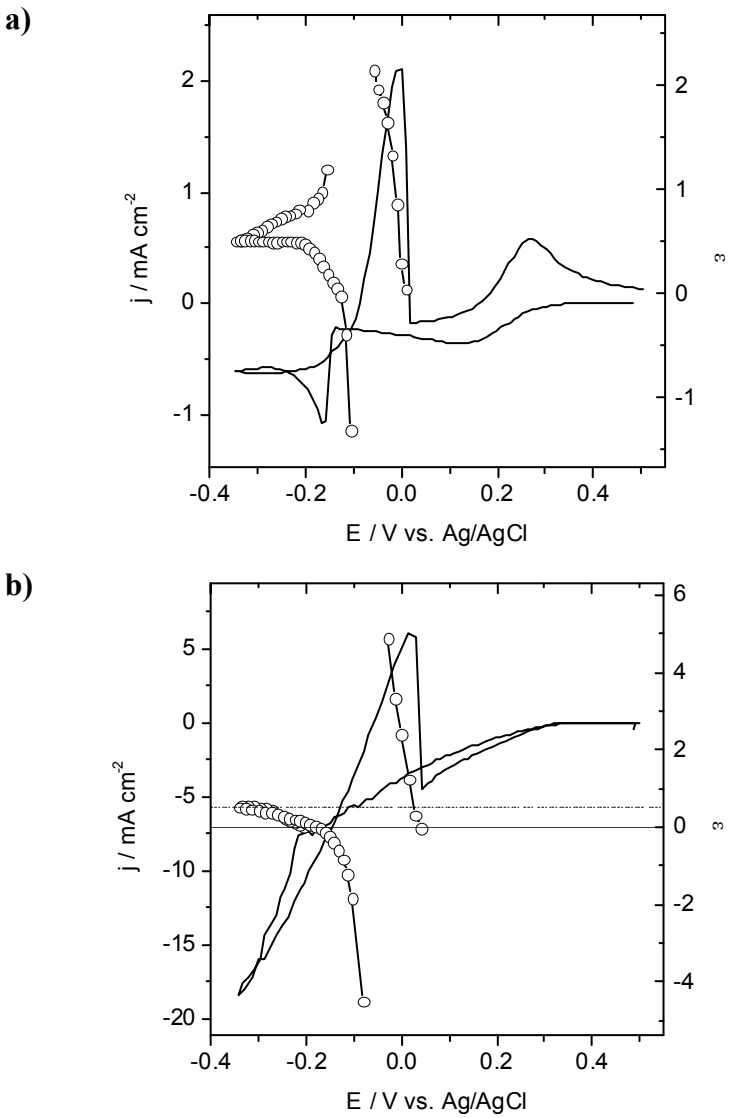

Figure 21. Electrodeposition and –dissolution of Cu from an electrolyte of 0.01 M $CuCl_2$ + 0.5 M NaCl, pH ~ 1 at d = 15 mm and 5 mV/s: currents and instantaneous apparent current efficiencies a) under silent conditions b) at I_a = 14 W cm^{-2}.

Potential-resolved current efficiencies were calculated assuming z = 1 (Figure 21). The shapes of the curves for Cu dissolution were similar with and without ultrasound, starting out at very large numbers and then decreasing with continuing dissolution. The ε-curves for Cu deposition under silent conditions were similar to those reported in sulfate-based electrolytes (Figure 18): ε started at high values, and decreased while lowering the potential. After potential reversal ε finally became negative. With ultrasound, though, ε started at zero, and then increased with decreasing potentials. The behavior after potential reversal was similar like under silent conditions. At low potentials ε was nearly constant around 0.5, but decreased at higher I_a. At higher I_a, ε for the anodic process was negative, because the current remained negative even during Cu dissolution.

All these results were easily explained by the enhancement of mass transport due to the ultrasound. Immediately before the start of Cu deposition under silent conditions, the electrolyte close to the electrode is enriched with Cu(I) that was formed at higher potentials by reduction of Cu(II). This reduction process is already under mass transport control indicating far-reaching depletion of Cu(II) and enrichment of Cu(I) close to the electrode

surface. First Cu deposition therefore proceeds by a one electron transfer reaction from Cu(I), while some Cu(II) is still reduced to Cu(I), which explains ε-values close to 1. At lower potentials Cu(I) is depleted as well, and reduction now occurs by mass transport limited reduction of Cu(II), and therefore ε approaches 0.5. At these low potentials all incoming Cu(II) ions are reduced to Cu(0). On the reverse sweep, with increasing potentials, only part of the Cu(II) ions reaching the electrode are reduced to Cu(0), and part to Cu(I). Therefore ε decreases to values below 0.5. Finally Cu dissolution starts while the overall currents are still negative, and ε becomes negative. During dissolution of Cu ε-values significantly larger than 1 are found in the beginning once the currents are positive. This was explained by the current-less Cu dissolution through Cu(II) species in solution under the formation of further Cu(I). Based on the charge vs. potential curve five different regions in the cycle were distinguished, based on the combination of Cu(II)/Cu(I) and Cu(I)/Cu(0) redox reactions taking place. These interpretations were confirmed by numerical simulation of the voltammogram under silent conditions (Figure 22). The data demonstrated the enrichment and depletion of Cu(I) at the surface as function of potential due to the interplay between Cu(II) reduction, Cu deposition / dissolution, Cu(I) oxidation and chemical diffusion due to concentration gradients. They also allowed to calculate the deposited mass of copper and therefore to reproduce the measured current efficiencies qualitatively.

In the presence of ultrasound the disappearance of all cathodic peaks together with the strong increase in the cathodic currents was explained by a gradual transition to charge transfer control due to a strong enhancement in mass transfer. In chloride solutions more Cu(II) is reduced to Cu(I) at potentials positive of the Cu deposition, which leads to a strong negative background current. The removal of Cu(I) formed during Cu(II) reduction and during Cu dissolution from the electrode is enhanced as well. Opposite to silent conditions, ε for the deposition started at 0 because of the large currents associated with reduction of Cu(II) to Cu(I). Due to the enhanced mass transport, the accumulation of Cu(I) and depletion of Cu(II) close to the electrode were less. At lower potentials an increasing number of Cu(I) was further reduced to Cu(0), until basically every arriving Cu(II) ion was reduced to Cu. Upon reversal of the sweep direction ε first was similar to the forward sweep. But then electrochemical Cu dissolution to Cu(I) was taking place, while the currents remained negative due to Cu(II) reduction. Therefore ε became negative, and then jumped to positive values as soon as the current became positive (not at very large I_a). The cause for the very large ε values is the continued Cu(II) reduction, which diminishes dQ, while dm is quite large.

Enhanced mass transport keeps the concentration of Cu(II) close to the electrode large, which favours formation of Cu(I), but also Cu corrosion and therefore is detrimental for Cu deposition. In addition the intermediate Cu(I) needed for Cu deposition is removed efficiently from the electrode. This could explain why Cu deposition was maximum at low I_a and the total efficiency of the deposition process decreased with I_a. The altered speciation at the surface is also responsible for the more negative start potentials for Cu deposition.

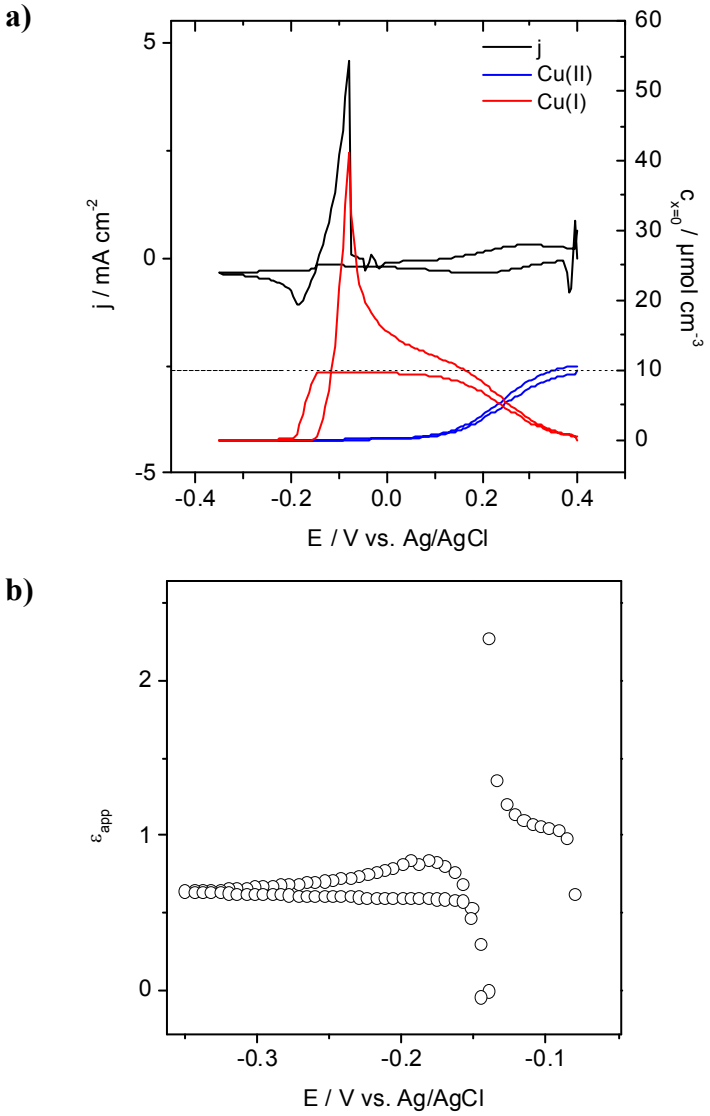

Figure 22. a) Simulated cyclic voltammogram for the redox processes in a chloride based copper electrolyte (black line) and surface concentrations of Cu(II) (blue) and Cu(I) (red). Simulations were carried out using a finite difference method to compute diffusional concentration changes, and employed modified Butler-Volmer equations to describe the electrode kinetics. Experimental diffusion coefficients were used for Cu(II) and Cu(I). b) Current efficiencies obtained from simulation in the potential range of Cu deposition / dissolution.

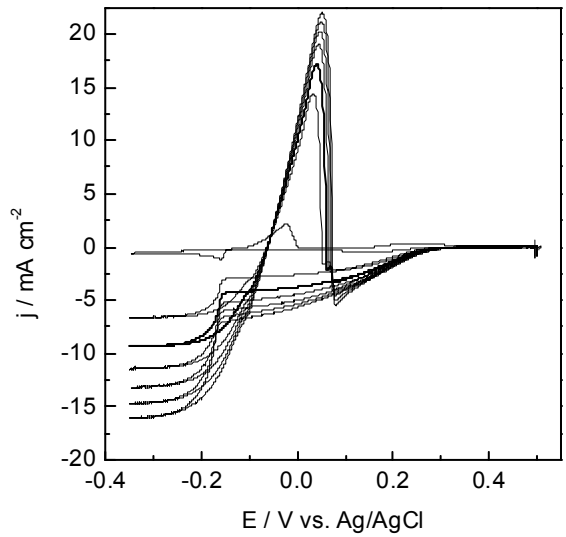

Figure 23. Electrodeposition and –dissolution of Cu from an electrolyte of 0.01 M $CuCl_2$ + 0.5 M NaCl, pH ~ 1 on a rotating Pt disc electrode at rotation rates of 0, 500, 1000, 1500, 2000, 2500, and 3000 rpm. Sweep rate: 0.005 V/s. Experiments were performed under Ar.

For a more quantitative description comparison to voltammograms recorded with a rotating disc electrode was made (Figure 23). Mass transport rates are also enhanced in experiments with the RDE. Similar to sonoelectrochemical measurements during rotation a part of the anodic dissolution peak was characterized by negative total currents. However, the total anodic currents even without background correction increased with increasing rotation rate and therefore with decreasing diffusion layer thickness. Thus also the amount of Cu deposited increased. The theory of RDE is well-established [5], and one can easily extract diffusion coefficients and diffusion layer thicknesses. The limiting current is given by:

$$j_{\lim} = 0.62zFD^{2/3}\nu^{-1/6}\omega^{1/2}c_0 \tag{11}$$

and the diffusion layer thickness by

$$\delta_N = 1.61\omega^{-1/2}\nu^{1/6}D^{1/3} \tag{12}$$

where D is the diffusion coefficient, ν the kinematic viscosity, ω the angular rotation rate (314 s-1 for 3000 rpm) and c_0 the bulk concentration of the electroactive species. Figure 23 shows limiting current behavior for both Cu(I) and Cu(0) formation. Taking ν as 0.0103 $cm^2\ s^{-1}$ (value for 0.5 M NaCl obtained by interpolation from a series of literature values (42)) and z = 1 for Cu(I) formation and z = 2 for Cu(0) formation diffusion coefficients of $5.6 \cdot 10^{-6}$ and $6.7 \cdot 10^{-6}$ $cm^2\ s^{-1}$ were obtained. These values were in good agreement with literature data of $5\text{-}8 \cdot 10^{-6}$ $cm^2 s^{-1}$ [166, 375]. Diffusion layer thicknesses of 11 µm at 1500 rpm and 7.7 µm at 3000 rpm were calculated. The cathodic sweep at potentials positive of Cu deposition could be reasonably well fitted using a variant of the Butler-Volmer equation for mixed control, taking the cathodic limiting current from the Levich plot, while the much lower anodic limiting current (due to the low bulk concentration of Cu(I)) was taken from the maximum anodic currents at the beginning of the cathodic sweep (Eq. (13)). This approach is very simplified and basically a steady state approximation. This procedure lead to exchange current densities between $4 \cdot 10^{-4}$ and $2.9 \cdot 10^{-4}$ A cm^{-2}, α-values of 0.69-0.72, and E^0 close to 0.4 V vs. Ag/AgCl. A similar analysis for the system Cu(I)/Cu(0) gave unsatisfactory results. For currents taken from CV data at intermediate potentials, where Cu deposition was already

taking place, but not yet under diffusion control, a Koutecký-Levich plot also was not linear. The non-linearity is caused by the presence of two coupled electrochemical reactions, one being under diffusion control, the other one under mixed control, and also by the presence of nucleation processes. The potential of zero current during Cu dissolution depended only very weakly on the rotation rate. It is a mixed potential where the currents for Cu dissolution to Cu(I) match the currents for Cu(II) reduction. An exchange current density of 50 mA cm^{-2} for Cu dissolution was estimated from that dependency.

$$j = \frac{j_0 \left\{ exp\left[\frac{\alpha z F}{RT}(E - E^0)\right] - exp\left[-\frac{(1-\alpha) z F}{RT}(E - E^0)\right]\right\}}{1 + \frac{j_0}{j_{lim,an}} exp\left[\frac{\alpha z F}{RT}(E - E^0)\right] - \frac{j_0}{j_{lim,cath}} exp\left[-\frac{(1-\alpha) z F}{RT}(E - E^0)\right]} \quad (13)$$

Similar to Eq. (11) a correlation between ultrasonic power P_W and j_{lim} has been suggested, verified and expanded in literature [176-178]:

$$j_{\lim} = K d^{-1/2} D^{2/3} c_0 P_w^{1/2} \quad (14)$$

where K is a constant depending on v. Also the equivalent flow velocity of the electrolyte towards the electrode was given as [178]:

$$U = \frac{1}{(0.45 z F c_0)^2} \cdot D^{-\frac{4}{3}} v^{\frac{1}{3}} r i_{lim}^2 \quad (15)$$

where r is the radius of the electrode, and the other symbols have the same meaning as before.

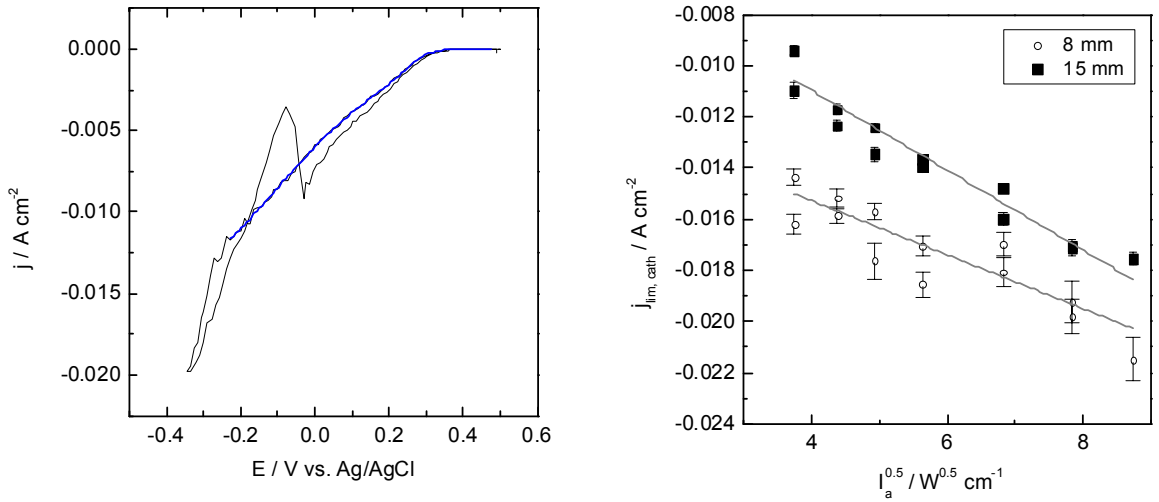

a) **b)**

Figure 24. a) Cyclic voltammogram recorded in an electrolyte of 0.01 M $CuCl_2$ + 0.5 M NaCl, pH ~ 1 at v = 5 mV/s, I_a = 47 W cm^{-2}, and d = 8 mm. Bold curve: Fit of Cu(II)/Cu(I) reduction applying Equation (13). b) Fit results for limiting currents from data at different I_a and horn-electrode separations of 8 and 15 mm.

Equation (13) was also fitted to the sonovoltammograms (Figure 24a). In contrast to the RDE experiments the cathodic limiting current cannot be directly taken from the voltammograms, except at very low ultrasonic intensities. Therefore $j_{lim,\ cath}$ was determined from the fits. The only exception was for the measurement at d = 22 mm and I_a = 10 W cm^{-2}, where a limiting current similar to the RDE experiment at 2000 rpm was obtained. However, for that

experiment the subsequent Cu deposition started at lower potentials and was more sluggish than with the RDE, and the dissolution peak current was smaller. The limiting current data obtained as function of I_a were noisy (Figure 24b). They increased with increasing intensity and decreasing distance between horn and electrode. A Levich type plot was roughly linear, but the linear fit did not pass through the origin. However, it was clear that the limiting currents were significantly larger than in RDE studies, which is why Cu(II) reduction was under mixed control for the entire potential range above Cu deposition. Calculation of RDE rotation rates needed to achieve limiting currents as large as in the sonoelectrochemical experiments led to numbers up to 27000 rpm (at d = 8 mm, I_a = 76 W cm^{-2}), and equivalent flow velocities of up to 13 m/s were obtained.

The maximum cathodic current observed during sonovoltammetric Cu deposition experiments was -24 mA cm^{-2} at -0.35 V, and the current trace did not reach limiting current behavior. Extending the potential range to -0.7 V also caused no saturation of the currents. Even though at these low potentials hydrogen evolution should be of increasing importance, no decrease in the apparent efficiencies was seen, but rather an increase above the value of 0.5 – possibly caused by deposition of Cu hydroxide.

In a potentiostatic experiment at -0.2 V and I_a = 29 W cm^{-2} no Cu deposition took place. At lower potentials Cu deposition took place. A series of potential step experiments between -0.25 V and -0.3 V was performed in order to study the influence of ultrasonic intensity on the current efficiency of Cu deposition from $CuCl_2$ electrolytes more closely. Typical current traces at -0.31 V together with the corresponding mass plots are shown in Figure 25a. In the presence of ultrasound the currents became constant after an initial phase, but were rather noisy. At later times, a slight decrease in currents was observed. The mass of the deposited layers grew almost linearly with time. The electrical current densities with ultrasound always were much larger than without. With increasing I_a a further increase in the current densities was observed. This effect increased with more negative potentials, i.e. larger overpotentials. A similar observation was made for the currents calculated from the mass of the Cu deposit assuming z = 2. Here however the relative increase in j_m by further increasing I_a was much less, and even negligible for $I_a \geq$ 19 W cm^{-2}. In part even a slight decrease in j_m with increasing I_a was seen.

The current efficiencies ε typically increased upon application of ultrasound at I_a = 9 W cm^{-2}, and decreased thereafter when increasing I_a. At low overpotentials ε at I_a = 30 W cm^{-2} was as low as under silent conditions even though the deposition rate was much higher. Larger overpotentials favored higher current efficiencies and the decrease with I_a was less pronounced. A series of potentiostatic depositions at E = -0.33 V and I_a = 30 W cm^{-2} gave an average ε_{app} = 0.90 ± 0.009 towards the end of the experiment, and in the beginning of the experiment ε_{app} = 1.006 ± 0.006.

An analogue of a Koutecký-Levich plot for one set of ultrasonic data (d = 22 mm), by plotting $1/j$ versus $1/I_a^{0.5}$, was linear only at a potential of -0.25 V, a potential where most of the electric current was due to Cu(II) reduction, and only little Cu deposition occurred (Figure 25b). From the intercept an activation-controlled current density of 56 mA cm^{-2} was calculated and from the slope a value of $K = 1.37 \cdot 10^6$ $\Omega^{-0.5}$ cm$^{1/6}$ mol^{-1} s$^{2/3}$, which is close to values obtained by Pollet and co-authors for a different redox system [178]. This directly lead to $j_{lim} = 3.17 \cdot 10^{-3}$ $I_a^{0.5}$, and therefore to currents of j_{lim} = 9.5 mA cm^{-2} at 9 W cm^{-2} and j_{lim} = 17 mA cm^{-2} at 30 W cm^{-2}. These values are larger than the currents measured at -0.25 V in cyclic voltammetry, which once more explains why especially at higher I_a no limiting behavior is seen in the sonovoltammograms for the Cu(II)/Cu(I) reduction step.

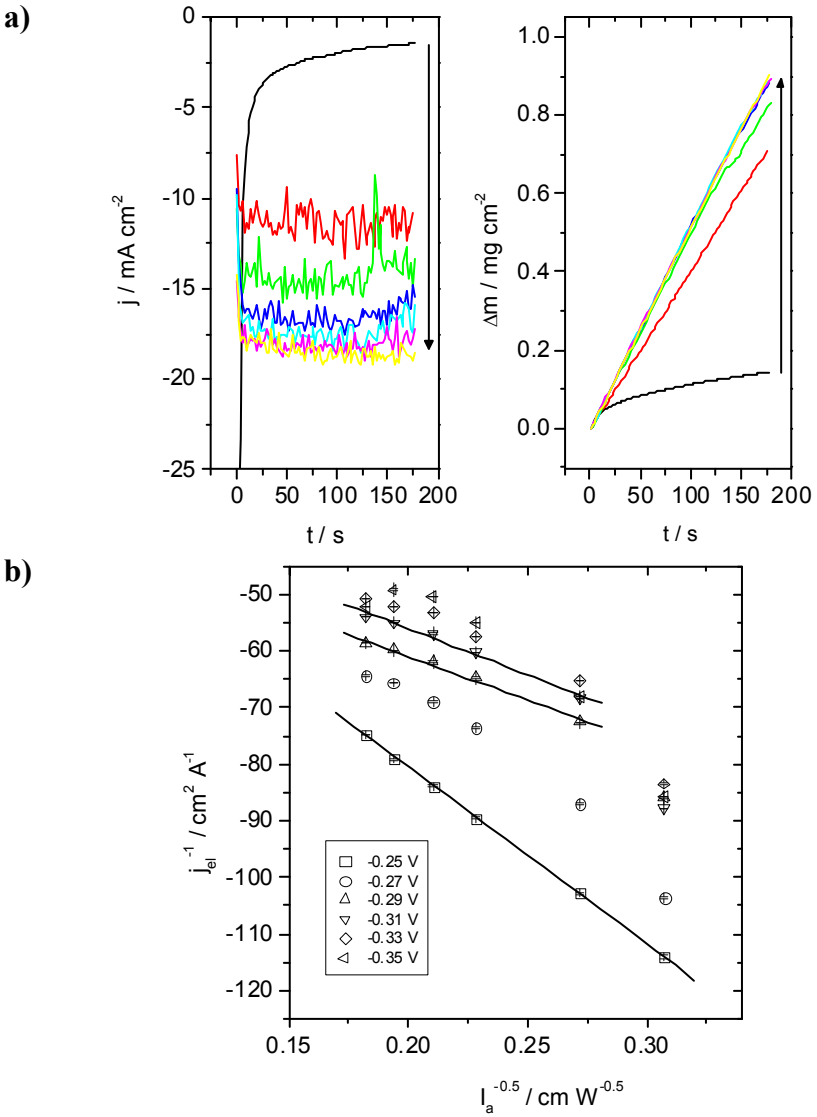

Figure 25. a) Current transients at E = -0.31 V vs. Ag/AgCl and corresponding mass changes recorded in an electrolyte of 0.01 M $CuCl_2$ + 0.5 M NaCl, pH ~ 1 at ultrasonic intensities of 0 (silent conditions, black curve), 11, 14, 20, 22, 25, and 29 W cm^{-2}. b) Koutecký-Levich analogue plot of electric current as a function of potential and ultrasonic intensity. Lines: Linear fits.

The influence of ultrasound on the corrosion of Cu by $CuCl_2$ and possibly of Cu erosion was also studied. Cu was repeatedly deposited at E = -0.33 V and I_a = 30 W cm^{-2} for 3 minutes. The electric current and therefore the actual surface area of the electrode did not increase significantly during the deposition of the Cu-layer. After each deposition, OCP was recorded for several minutes, one minute under silent conditions, and the remaining time with ultrasound of varying intensity applied. The mass loss rate was ~ -0.24 µg cm^{-2} s^{-1} under silent conditions, and increased in the presence of ultrasound to 7.2 µg cm^{-2} s^{-1} at I_a = 30 W cm^{-2}. This corresponds to corrosion currents between 0.36 mA cm^{-2} and almost 11 mA cm^{-2}. While there was still Cu on the electrode the open circuit potential slightly increased with time by about 0.024 mV s^{-1} under silent conditions and 0.2 mV s^{-1} at I_a = 30 W cm^{-2}. Once all Cu was dissolved the potential jumped by several hundred mV to a potential of about 0.35 V vs. Ag/AgCl. For all intensities the limiting currents calculated for the reduction of Cu(II) were larger than these corrosion currents j_{corr}. Therefore the mass changes during these experiments could be completely understood by corrosion processes (Cu + Cu^{2+} + 4 Cl^- -> 2 $[CuCl_2]^-$.

However, cathodic currents j_{cath} actually measured in the absence of a Cu layer at the same potential recorded during corrosion (~-0.055 V vs. Ag/AgCl) are much smaller than j_{lim}, and also $|j_{cath}| < |j_{corr}|$ except at very low I_a (Fig. 16). Therefore, at larger I_a, mass loss probably was not caused by corrosion alone, but also by erosion caused by cavitation. Further aspects of the role of cavitation are discussed below.

Influence of Cavitation

The noisy current observed in the cyclic voltammograms during deposition of Cu from chloride-based electrolytes gave already a clear indication of surface cavitation taking place under these conditions. For a series of cylic voltammograms at slow scan rates the acoustic intensity was first increased from experiment to experiment, and thereafter stepwise decreased. It was found that the resonance frequency of the bare quartz after stripping of all the copper increased in the course of the experiments, pointing to erosion of the gold. Furthermore evidence for surface cavitation came from a shift in the onset potentials for Cu deposition when increasing the ultrasonic intensity (however not caused by erosion, because current increase due to Cu deposition and mass change still were taking place concurrently), and the fact that even for lowest I_a the potentials applied were insufficient to reach diffusion limitation, even though the cathodic currents were less than in the RDE experiments with highest rotation rates. In some of the Cu deposits obtained after potentiostatic deposition from sulfate solution circular features were seen that may have been caused by cavitation bubbles at the surface.

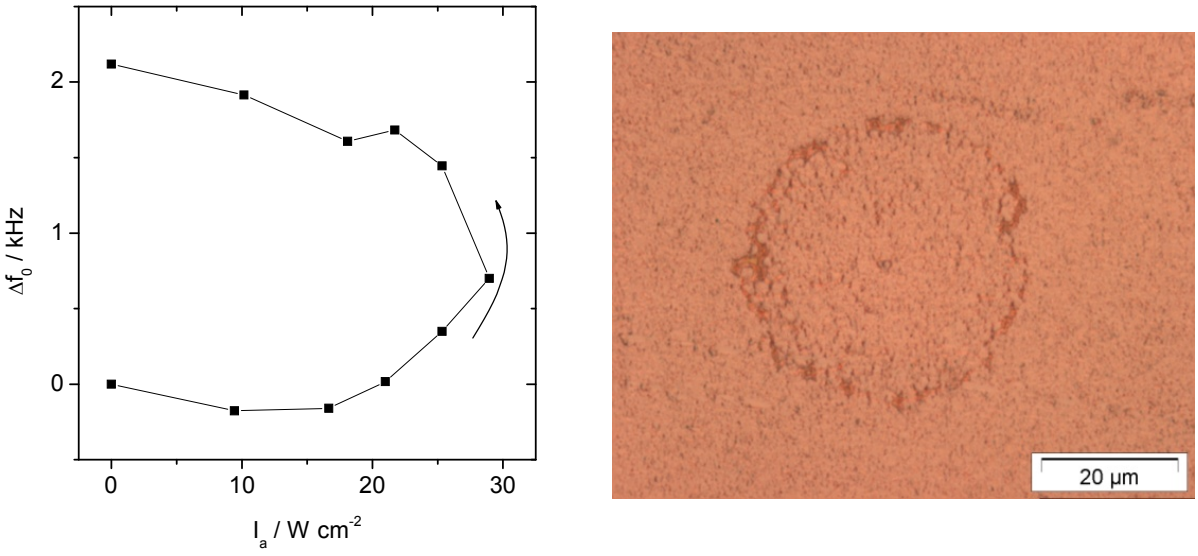

Figure 26. a) Resonance frequency measured before start of Cu deposition during a series of cyclovoltammetric experiments in Cu chloride based electrolyte. Arrow indicates order of experiments. b) Optical micrograph of a Cu layer deposited from sulfate-based electrolyte. Deposition conditions: E = -0.15 V cm^{-2}, d = 10 mm, I_a = 76 W cm^{-2}. Experiment was terminated after deposition of 1.4 mg cm^{-2} Cu.

During a Cu deposition experiment from chloride-based electrolyte at E = -0.33 V vs. Ag/AgCl, I_a = 76 W cm^{-2} and d = 8 mm (minimum possible distance between horn and quartz surface with the setup used) more severe cavitation was taking place (cf. Figure 27). Under these conditions the resonance spectrum was extremely noisy and no Cu deposition was taking place. After lowering of I_a to 47 W cm^{-2} the noise decreased by two orders of magnitude and deposition started (as expressed by an increase in current efficiency from 0.6

% to 49%). After performing an extended number of Cu deposition and dissolution experiments, the part of the Au surface exposed to ultrasound was much rougher than the original surface, and parts of the surface at the edge of the resonator that had not been in contact with the electrolyte.

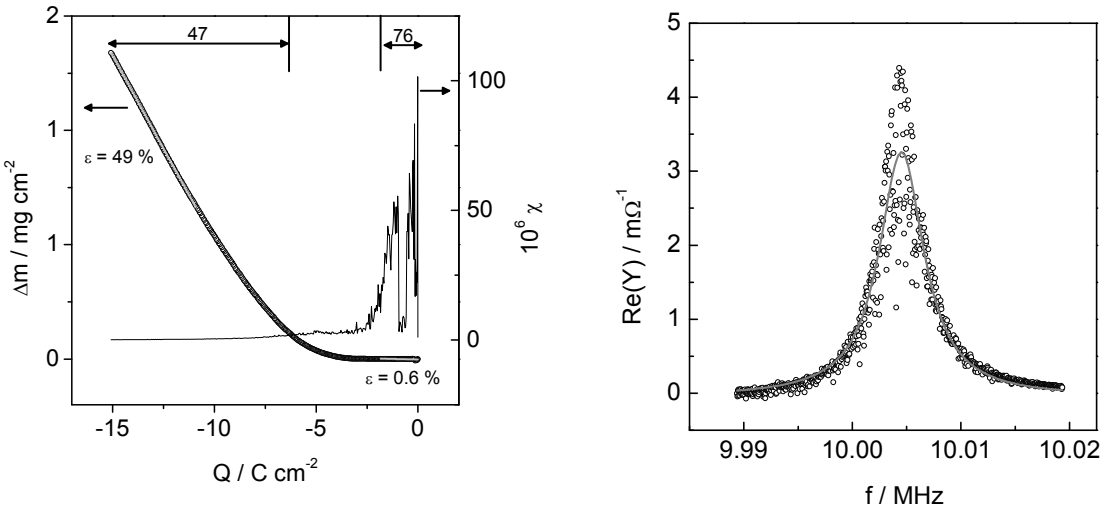

Figure 27. a) Potentiostatic deposition of Cu from 0.01 M $CuCl_2$ + 0.5 M NaCl, pH ~ 1, at E = -0.33 V vs. Ag/AgCl, at a range of ultrasonic intensities (76 W cm^{-2} – 47 W cm^{-2}, see text): Total mass change Δm as function of total charge Q (ε determined from slope, I_a given on top of figure) and the corresponding standard deviation χ of Lorentzian peak fit of the quartz admittance spectra. b) characteristic resonance spectrum in the presence of cavitation at quartz surface at I_a = 76 W cm^{-2} (from [369]).

Electrodeposition of Composites

Ultrasound is also beneficial for the electrochemical deposition of composites [368, 380, 381]. In the simplest case metal-ceramic composites can be prepared by the incorporation of oxides dispersed in the electrolyte during electroplating of metals (electrocodeposition). Here ultrasound has been applied in literature for the desagglomeration of particles both by pretreatment of the deposition suspensions before and during the electrodeposition process [380, 382, 383]. In addition the directional movement of the oxides due to acoustic streaming might enhance transport of the oxides to the electrode. However, one may also make use of the face-on configuration for the in-situ production of nanomaterial to be embedded in a growing metal film on the working electrode [381]. This could be achieved by sonochemical decomposition of precursors directly in the electrolyte solution, or by using the horn itself as a supporting electrode. So one (nano)material could be prepared and stripped by pulsed sonoelectrochemistry at the horn probe tip, while at the same time a metal is deposited on the working electrode, under incorporation of the particles created at the ultrasonic horn.

The electrodeposition of metals reinforced with micron-sized and in part also nano-sized ceramic particles of Al_2O_3, SiO_2, SiC, TiO_2, CeO_2, ZrO_2, borides and others has been state of the art for many decades [384]. Such metal/ceramic composites often show superior corrosion resistance [385]. Other major fields of application have been the improvement and tailoring of the mechanical properties, like hardness (dispersion hardening), yield strength, resistance to plastic deformation and wear resistance, and lubrication of metals by codepositing graphite or PTFE, or liquid lubricant filled microcapsules [385].

The mechanism of the electrocodeposition so far has not been completely understood. However, over the past decades a number of models in order to explain the kinetics and the amount of particle incorporation into a growing deposit have been presented. Some of them have been reviewed in [386]. Early mechanisms involved simple mechanical inclusion, adsorption and electrophoresis [387, 388]. Guglielmi suggested a two step adsorption mechanism with a first physical (weak) adsorption step of particles still covered with solvent and adsorbed ions, followed by a field assisted chemical adsorption step [388]. The strongly bound particles were then supposed to be embedded in the growing metal layer. A quantitative model for the concentration and current dependence of the embedded volume fraction was given and verified by experiments. Celis and Roos applied this model to the codeposition of α-Al_2O_3 in Cu from acidic sulfate electrolytes in the presence and absence of Tl^+ ions [387]. They concluded that the second adsorption step was rate determining, correlated one constant (v_0) in Guglielmis equations with the reduction of Cu^{2+} ions adsorbed on the particles, considered that Tl^+ was catalyzing this reaction step and found in the charge transfer controlled regime an increase in the amount of oxide incorporated with increasing current. Celis et al. later introduced an extended model operative under hydrodynamic conditions, in which they assume five stages of relevance: the adsorption of ions on top of the particle, the convectional transport to the hydrodynamic boundary layer, the diffusion of the particle through the diffusion layer, its adsorption on the surface and finally the reduction of a minimum number of adsorbed ions in order to embed the particle in the growing layer [389]. They calculated the probability for one ion to be reduced from the electrical current density and the total average ion concentration in the diffusion layer, and from that the probability for one particle to be embedded as the probability that k out of a total of K ions adsorbed on the particles have to be reduced. Turbulent flows are considered to reduce the probability of particle incorporation to zero. The authors end up with an expression that describes the weight percentage of embedded particles as a function of the applied current (or overpotential), the transition current to mass transport control, the particle and ion concentrations in solution and the hydrodynamic conditions. They applied this model to the Cu/Al_2O_3 and the Au/Al_2O_3 system and found excellent agreement between experiment and theory. Valdes performed computer simulations for particle codeposition from $CuSO_4$ electrolyte applying a model considering diffusion, electromigration, diffusomigration, and convection using a Butler-Volmer-type surface boundary condition [390]. His data suggested that particle incorporation increases first with current density, but decreases again at higher currents, and that there is a strong influence by the ratio of particle and electrolyte diffusivity. Fransaer et al. developed an elaborate hydrodynamic model (trajectory analysis) for the codeposition based on a detailed consideration of forces acting in the electrolyte bulk and close to the surface of a rotating disc electrode on a spherical particle large enough to neglect Brownian motion [391]. They distinguished between the forces exerted by the moving liquid and external forces, the latter including gravity, buoyancy and electrophoretic force in the bulk of the solution and also dispersion forces and double layer forces between particles and the electrode surface at small separations. In order to calculate the electrophoretic force and the double layer force they calculated local ion concentrations and potential distribution using the orthogonal collocation technique. This allowed them to calculate how many particles arrived at the electrode surface in a certain time. However, their model could not describe the entrapment / detachment of particles, which is why they introduced a reaction term into the model, and correlated the probability for a particle to stick to the surface with a critical shear force. They tested the model using polydisperse spherical polystyrene particles in copper electrolyte and compared the experimental and theoretical degree of particle incorporation as function of bath concentration. They showed that the experimental degree of incorporation depended both on the radial position and on the electrical current. The latter effect was not predicted by trajectory analysis, leading to the conclusion that the particle adhesion strength depended on

current. Fransaer et al. then presented evidence that the crossing of the point of zero charge of the copper electrode was responsible for that behavior, with a lack of structural ordering of the solvent molecules due to the absence of an electric field at the pzc being responsible for a maximum rate of codeposition. Such so-called structural forces like hydration forces are repulsive, and introduce a secondary minimum in the force-distance curve as described by DLVO theory. Hydration forces differ also between hydrophilic and hydrophobic particles (the latter ones being more readily incorporated) and can be influenced by additives (monovalent cations, surfactants). The authors also pointed to the importance of the interaction between incoming particles and deposited particles at more concentrated solutions, not included in the theory. Takahashi et al. studied experimentally the codeposition of SiO_2 particles in Zn-Fe and Zn-Cr alloys [392]. They found a mutual acceleration of the deposition of SiO_2 and iron, and the presence of SiO_2 was also required to codeposit Cr with Zn. These results are supporting the role of ions adsorbed on the particles for the codeposition process. A more detailed review of the models developed before 1995 as well as a survey of experimental findings those models have to explain are given in the review by Hovestad and Janssen [385]. Wang et al. presented a phenomenological model to explain the dependence of extent of co-deposition as function of suspension concentration and current density [393]. They did not consider the hydrodynamic conditions which they kept constant in the experiments, but assumed that the amount of adsorbed particles equals the sum of incoming particles and detached particles, which are in dynamic equilibrium, that the adsorption energy follows a normal distribution, and that a particle is incorporated once its adsorption energy exceeds a critical value. From these two assumptions the authors derived a formula, which allowed them to determine the average adsorption energies (with respect to the critical adsorption energy), and to describe their experimental data. They found the particle coverage at the surface to decrease with increasing current density, but the average adsorption strength to increase at the same time. This explained also the occurrence of a maximum in the embedded number of particles as a function of current density. Nowak et al. performed impedance measurements during electrodeposition of Ni in the presence of SiC and SiO_2 particles [394]. The double layer capacitance was found to decrease in the presence of SiC, but less than expected due to an increase in surface roughness, whereas it increased in the presence of SiO_2. SiC was embedded in the Ni film, whereas incorporation of SiO_2 was negligible. Based on the findings from literature, that SiC particles immersed in aqueous environment are covered by a few monolayers of SiO_2 and have a similar point of zero charge, but that SiC is hydrophobic, the authors suggested that incorporation into a growing deposit requires the removal of the water film on top of the particles, which is easier for hydrophobic particles. This hypothesis was further supported by Terzieva et, who studied the codeposition of hydrophilic and hydrophobic silica particles during Cu electrodeposition in the presence of different surfactants (cetyl trimethyl ammonium hydrogen sulfate (CTAHS) and sodium dodecyl sulfonate (SDS)) [395]. They observed no incorporation of hydrophilic silica, but obtained incorporation of hydrophobic silica in the presence of 10^{-4} M CTAHS, but not in the presence of SDS. Whereas the hydration force could explain these results (Cu ions are expected to adsorb neither on hydrophilic nor on hydrophobic silica), the exact role of the surfactant on the deposition process had not been understood. Vereecken et al. developed a model for the codeposition of nanosized particles on a rotating disc electrode [396]. Opposite to the treatment of Fransaer [391] for large particles Vereecken et al. assumed that transport of particles is solely taking place by diffusive transport across the diffusion layer, the thickness of which is adjusted by the rotation rate [396]. The model holds as long as the particle diameter is smaller than the diffusion layer thickness. The incorporation probability for a particle is considered to increase with current density, which translates to a lowered surface particle concentration in the model, and to be 1 above a certain current threshold. The result is an equation giving the volume fraction of particles in the film as a function of

rotation rate, current density and bulk particle concentration. The authors fitted that formula to experimental data of Ni / 300 nm Al_2O_3, and found excellent agreement. Dedeloudis et al. applied the colloidal probe technique for the direct measurement of the surface forces between a metal electrode (copper) in a plating electrolyte and hydrophilic and hydrophobic particles (glass / polystyrene beads) [397]. The forces measured between Cu and polystyrene were attractive, permitting a direct surface contact between particles and Cu. This was explained by prevailance of the hydrophobic interaction and van der Waals forces. During deposition the Cu grows around the polystyrene sphere, and the interaction between substrate and particle increases. On the other hand, repulsive interactions were found for the hydrophilic glass particles, and explained with the hydration force, that causes an electrolyte film to be present between Cu and particle, and prevents direct contact. Therefore Cu plating can take place underneath the particle as well, and the particle is not incorporated in the deposit. Lee and Talbot focused on the modification of the metallic film growth by the presence of a non-conducting particle close to or even at the interface [398]. They performed finite element simulations for the limiting cases of primary and secondary current distribution, neglecting fluid motion underneath the particle. The current distribution was found to be altered strongly by the presence of the particle. In the case of a primary current distribution, the growth of the film was found to be much slower within the area covered by the particle, and the current initially becomes largest at a distance of twice the particles center. With growth the position of the maximum current shifts towards the edge of the particle and drops to zero below the entire particle radius. This leads to formation of a void below the particle. In the case of a secondary current distribution, the current density is more uniformly distributed, and void formation underneath the particle is avoided. However, a small void is formed on top of the particle. The same authors later published a model to calculate the amount of incorporated nanosized particles during electrocodeposition on a rotating cylinder electrode, which is based in part on the model of Celis et al. and mainly focused on transport properties [399].

The deposition of ceria containing metals has been studied to a lesser extent than the incorporation of Al_2O_3 and others. Ni/ceria and Co/ceria composites are interesting in the context of high temperature fuel cells [400]. Carac et al. incorporated µ-sized ceria particles from Watts-type electrolytes in Ni and Co without using ultrasound and registered an increase in microhardness [401]. Lee et al. applied ultrasound during the preparation of Cu/Al_2O_3 and Cu/CeO_2 composites, but not in the face on geometry [380]. They found that ultrasound was less efficient in breaking up agglomerates in the case of ceria. Lampke et al. performed the electrodeposition of Ni/TiO_2 and Ni/Al_2O_3 deposits in an ultrasonic bath [179]. Qu et al. treated the electrolyte with ultrasound before electrodeposition of Ni/ceria composites [402].

The deposition of Ni/CeO_2 and Co/CeO_2 films was studied by EQCM in the presence of ultrasound in [368, 381]. The aim of these studies was to enhance the incorporation of ceria in Ni and Co films using ultrasound even at low solids loading, to monitor the deposition in-situ by EQCM and to compare different Ni and Co electrolytes. The major anticipated effects of ultrasound were to act as a very efficient means of stirring in order to distribute the ceria homogeneously in the electrolyte, to drive the particles towards the electrode, and to – possibly – help in breaking up soft agglomerates [179, 380, 402]. In the case of nickel experiments were performed in typical concentrated nickel electrolytes at 50 °C, namely a Watts type electrolyte (30 g/l $NiCl_2$ + 234 g/l $NiSO_4$ x 6 H_2O + 30 g/l H_3BO_3 + 3 mg/l sodium dodecylsulfate (SDS), based on [179]) and in a sulphamate bath (100 ml of a 50wt% solution of $Ni(NH_2SO_3)_2$/ l electrolyte, 10 g/l $NiCl_2$ x 6 H_2O, and 40 g/l H_3BO_3, based on [403]). Co deposition was performed from a concentrated electrolyte (1 mol/l $CoSO_4$ x 7 H_2O, 0.2 mol/l $CoCl_2$ x 6 H_2O, 0.28 mol/l H_3BO_3, 0.4 g/l SDS, pH ~ 4.5) and a less concentrated one (0.1 M $CoSO_4$ + 0.1 M Na_2SO_4 with pH adjusted to 4, based on [404]), both at 25 °C. For

codeposition of ceria 0.5-5 g/l gadolinia doped ceria (FuelCellMaterials, 5-10 nm crystallite size, softly agglomerated, particle size < 149 μm) were added to the solution and dispersed for 20 minutes using ultrasound in order to break up the agglomerates. Ultrasound was also applied during electrodeposition. The ultrasonic intensity (I_a) was determined using the calorimetric calibration procedure [173, 174]. Prior to depositions cyclic voltammetry at a scanrate of 5 mV/s and different ultrasonic amplitudes was performed in order to characterize the electrochemical behavior of the systems. In parallel to all electrochemical experiments changes in f_R and w of the quartz were recorded. The deposit thickness was determined by profilometry (Tencor Alpha-Step 500 Surface Profiler). The ceria content in the deposits was determined by electron probe microanalysis (EPMA) and EDX, and the morphology characterized by scanning electron microscopy (SEM).

Deposition of Ni/CeO_2

Watts electrolyte. Ni deposition was performed under variation of the ultrasonic intensity with and without addition of 5 g/l ceria. The application of ultrasound altered neither the shape of the voltammograms nor the start potential of the Ni deposition (~ -0.65 V vs. Ag/AgCl). A double dissolution peak feature during the anodic sweep was less pronounced in the presence of ultrasound. Without ceria, the maximum mass deposited in a voltammetric cycle increased from 63 to 78 μg cm^{-2} when raising I_a from 0 to 26 W cm^{-2}. The current efficiency ε was slightly larger under silent conditions. A variation of I_a between 15 and 30 W cm^{-2} did not alter ε significantly. Also the addition of 5 g/l ceria seemed to have no strong influence on voltammograms and current efficiencies. This also means that in this case a calculation of the embedded amount of ceria from EQCM data was not possible.

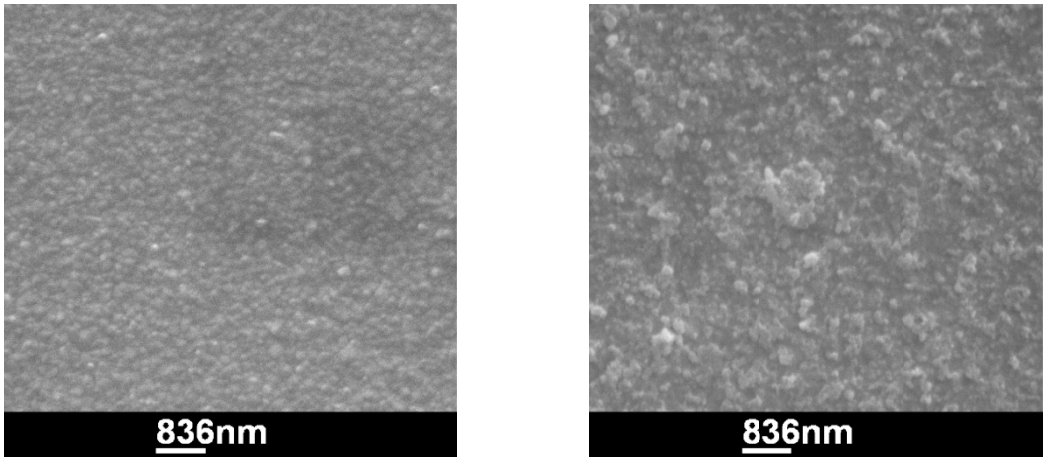

a) **b)**

Figure 28. SEM images of Ni films deposited from Watts electrolyte at a potential of –0.8 V for 10 minutes without (a) and with (b) addition of 5 g/l ceria (from [381]).

Potentiostatic depositions were performed at E= –0.8 V and I_a ~ 28 W cm^{-2} in order to study the influence of ceria addition on the morphology of deposits and to determine the amount of ceria embedded. The current efficiency was 78% for pure Ni deposition and 79% for deposition of Ni/ceria, and therefore basically identical. The average current density was –7.6 mA cm^{-2}. The amount of ceria embedded was found by EDX to be 1.8 wt% (applying a correction factor of 1.15 based on EPMA measurements). An EDX measurement at a specific location (point analysis) gave a much larger ceria content of 12%. At this position presumably a larger CeO_2 particle had been embedded. For this electrolyte, the morphology of the deposits was clearly altered by the presence of ceria (cf. Figure 28). Similar observations have been reported elsewhere [402].

Sulfamate-based electrolyte. Opposite to the Watts electrolyte, the shape of the cyclic voltammogram severely changed upon application of ultrasound. Figure 29a shows current and mass changes measured during cyclic Ni deposition and dissolution in the absence of ceria, under the influence of ultrasound. Whereas the mass trace looked normal for a metal deposition and dissolution system, the current response differed very much from the Watts electrolyte shown above. The currents during the sweep to more negative potentials were smaller than during the backsweep, and stayed negative for most potentials even in a range where Ni dissolution was seen in the EQCM signal. On the cathodic back sweep there was a positive peak superimposed to the current trace, and this peak actually was the Ni dissolution peak (arrow in Figure 29). If one calculates from the mass changes applying Faradays law the corresponding currents of Ni deposition and dissolution without side reactions (i.e. at 100% current efficiency), one obtains a plot corresponding to a normal cyclic voltammogram (Figure 29b). Even more, the curve obtained is very similar to both the corresponding curve and the voltammogram under silent conditions. Therefore ultrasound did not alter Ni deposition itself a lot. However, it strongly accelerated side reactions. These are probably due to the sulfamate ions not present in Watts electrolyte.

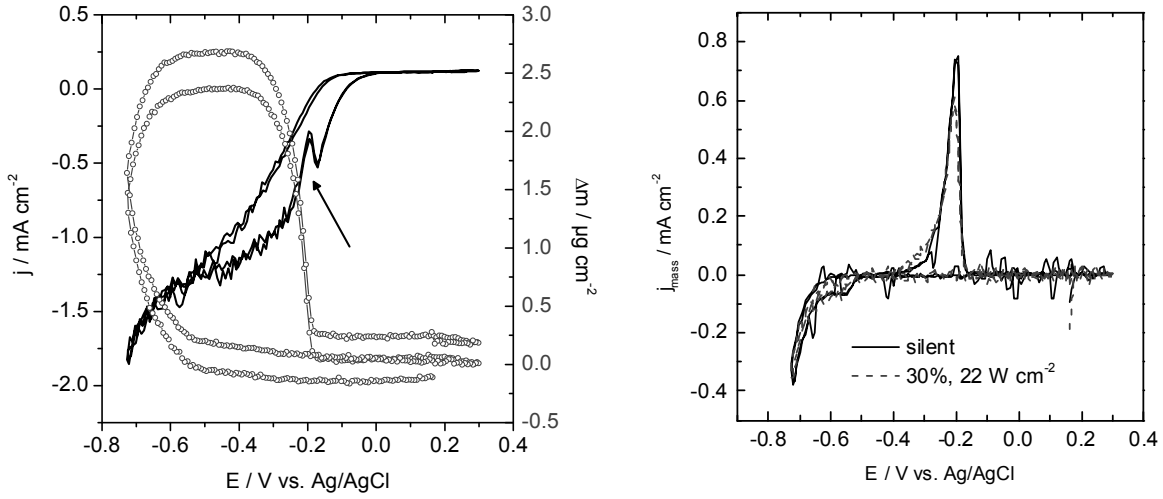

a) **b)**

Figure 29. Cyclic voltammogram recorded at a scan rate of 0.005 V/s in a Ni sulfamate electrolyte in the presence of ultrasound at I_a = 22 W cm^{-2} (left) and comparison of current densities calculated from mass changes during cyclic voltammetry applying Faradays law with data from the analogous experiment in the absence of ultrasound (right) (from [381]).

A number of potentiostatic and galvanostatic depositions of Ni/ceria composites from sulfamate-based electrolytes have been performed. Under silent conditions in the absence of ceria Ni could be deposited at –0.73 V with an ε_{app} of 103%, indicating only a little role of side reactions and of $Ni(OH)_2$ deposition. With 5 g/l ceria and application of ultrasound currents increased and became noisier, but ε_{app} dropped to 30%, and actual deposition slowed down. Higher current densities improved both the current efficiencies (up to 80%) and the amount of ceria incorporated. During the galvanostatic deposition from the sulfamate electrolyte more ceria was incorporated than during the potentiostatic deposition from the Watts electrolyte. However, the current density also was larger. The ceria content obtained still was rather low, less than 2.5 wt%. Literature values range from 5 vol% (50 g/l ceria in solution) [401] up to 20 vol% (in Cu, 20 g/l ceria, strong ultrasound) [380]. In these studies however suspension concentration was much higher. The morphology of the deposits obtained from sulfamate was not strongly altered by the presence of ceria.

The electrochemical behavior of the Watts bath and the sulfamate electrolyte therefore were found to be very different in the presence of ultrasound. From EQCM it was concluded that these differences do not concern so much the deposition of Ni films themselves. Indeed Ni/ceria films deposited from both electrolytes showed a very similar morphology. The Ni deposition was only slightly enhanced during application of ultrasound, because the high Ni concentrations prevented mass transport limitation even under silent conditions. EQCM permitted to directly monitor the deposition of the Ni and composite films even in the presence of ultrasound. However due to current efficiencies far less than 100% and the relatively low amounts of ceria incorporation a direct determination of the ceria content in the growing layers was not possible.

Deposition of Co/CeO_2

Low Co concentration electrolyte. Under silent conditions cobalt deposition on bare gold without CeO_2 was reported to start below –0.7 V (cf. Figure 30). From the absence of a cathodic current peak it was concluded that Co deposition was not under mass transport control. Dissolution started around –0.5 V, and an anodic peak was located around –0.18 V. The general shape of the frequency was as expected for metal deposition / dissolution, however only half of the material deposited was redissolved in the anodic sweep. This was explained by the incorporation of $Co(OH)_2$ in the deposit, in agreement with findings reported in [404], where it was shown that $Co(OH)_2$ incorporation is especially important at low overpotentials. Co is less noble than Ni, and hydrogen evolution takes place in parallel to the metal deposition, causing an increase in pH close to the electrode and thus $Co(OH)_2$ precipitation. The remaining deposit was removed by polarization at 0.65 V for several minutes.

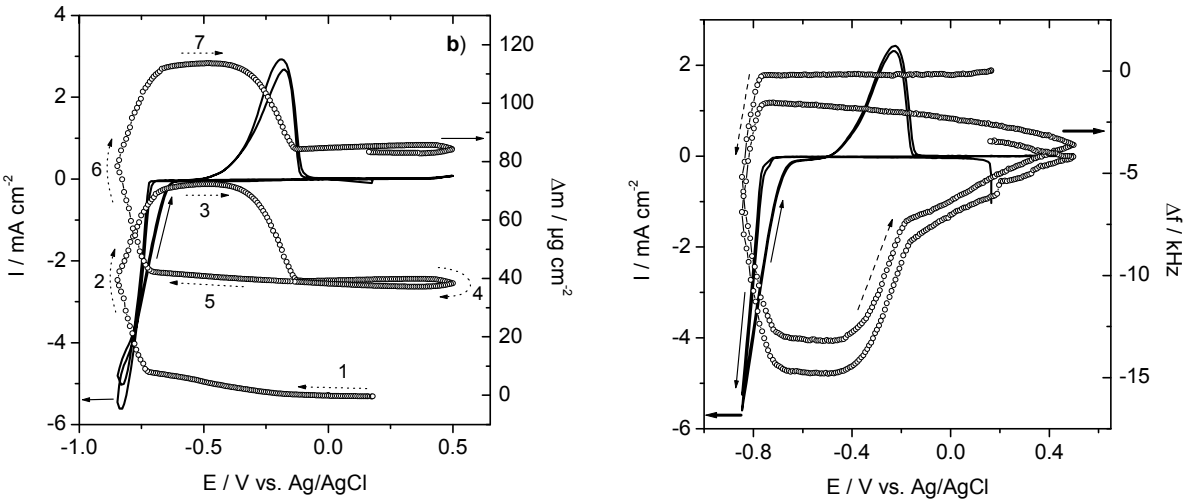

a) **b)**

Figure 30. a) Cyclic voltammogram (line) and frequency change (circles) in 0.1 M $CoSO_4$ + 0.1 M Na_2SO_4 (pH ~ 4) under silent conditions. b) Cyclic voltammogram and frequency change in cobalt electrolyte containing 5 g/l CeO_2 at I_a = 29 W cm^{-2}. Arrows indicate sweep direction. Sweep rate: 5 mV/s (from [368]).

Even though the general shape of the voltammogram did not change much under ultrasonic irradiation of I_a ~ 29 W cm^{-2}, and only a slight increase in currents and mass deposited by a factor of less than two was reported, deposition was completely reversible under sonication. This was explained by the enhanced mass transport reducing the pH increase at the electrode

and therefore the tendency for $Co(OH)_2$ precipitation. The addition of 5 g/l CeO_2 caused a decrease in the currents (cf. Figure 30), and the influence of the I_a on currents and frequency changes was even less than without ceria. Even with ultrasound now the deposition was not completely reversible. This was explained by the presence of ceria particles decreasing the active surface area and inhibiting grain growth, as suggested by Qu et al. to explain changes in morphology of Ni/CeO_2 deposits [402], and by increasing the solution pH.

Potentiostatic Co deposition experiments at – 0.85 V were performed under sonication, until the total frequency change exceeded 250 kHz. The currents were found to increase continuously with time, and a strong frequency decrease was observed (Figure 31). As in cyclic voltammetry currents decreased with increasing ceria concentration. The frequency change took place fastest for 3 g/l CeO_2. In the presence of ceria a strong increase in the damping was reported after a few minutes of deposition, indicating roughening of the electrode (Figure 31). Whereas the damping increase at 3 g/l still was in the range where Equation (7) can be applied, this was not true for 5 g/l ceria. Without ceria, an apparent current efficiency ε_{app} of 93% could be determined from the slope of the mass vs. charge curve. With 3 g/l ceria, ε_{app} was 147%. This large number was explained by the precipitation of $Co(OH)_2$, by a contribution of the deposit roughness, and by the mass of co-deposited ceria. According to EPMA the ceria contents in the deposits were 6.2 wt% for 3 g/l and 7.8 wt% for 5 g/l solution concentration. These numbers are quite large given the low solution concentrations. Cârâc et al. found – using a 1.2 M Co electrolyte and 50 g/l µm-sized CeO_2 particles– values of 22 wt% [401].

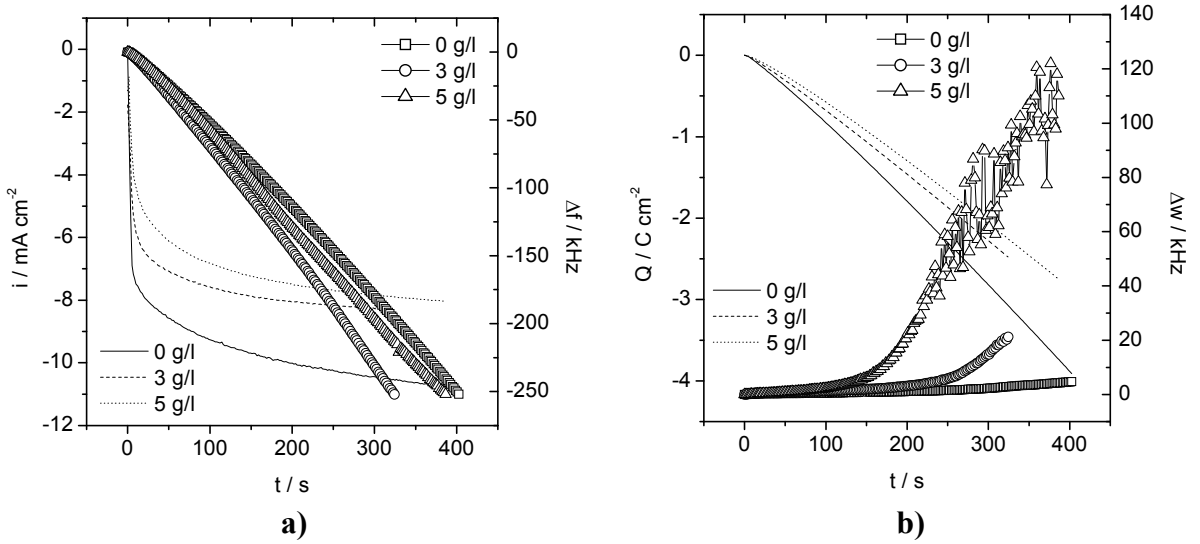

Figure 31. a) Current transients (lines) and frequency changes (symbols) and b) electric charges (lines) and damping changes (symbols) recorded during potentiostatic deposition of Co from 0.1 M $CoSO_4$ + 0.1 M Na_2SO_4 (pH ~ 4) at 40% ultrasonic amplitude after addition of different concentrations of ceria (legend) (from [368]).

SEM indeed demonstrated a strong impact of ceria addition on the morphology of the deposits (Figure 32). The roughness of pure Co deposits already was higher than those found for more concentrated Co electrolytes. In the presence of CeO_2 the morphology of the deposits was distinctively different. It was less uniform especially at the edges of the electrode, and showed a very porous fine structure with fiber-like entities. This fine structure was taken as the explanation for large increase in damping during electrodeposition, and also for the pitch black optical appearance of the layers with 5 g/l CeO_2. Despite the fact that all films were deposited until the same value of Δf_R was achieved the films with ceria were between 2 (3 g/l,

5.8 µm) and 3-4 (5 g/l, 8.9 µm) times thicker than without ceria (2.4 µm), pointing again to the porous nature of the deposits.

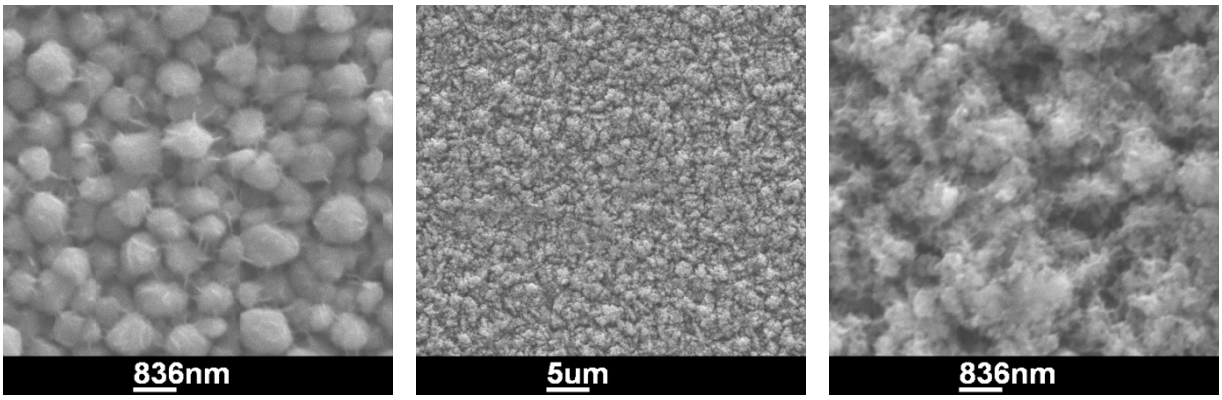

a) **b)** **c)**

Figure 32. Morphology of Co deposited at –0.85 V at 40% ultrasonic amplitude from 0.1 M $CoSO_4$ + 0.1 M Na_2SO_4 (pH ~ 4) after addition of 0 (a) and 3 g/l CeO_2 (b, c), respectively.

From diluted cobalt electrolytes therefore rather rough and in-homogeneous layers were deposited, which caused a strong increase in the damping of the quartz. On the other hand, rather large amounts of ceria were embedded, up to almost 8%. For some applications, such as in fuel cells and catalysis, this type of material might be more suitable than smooth, dense high quality layers.

Watts-type Co electrolyte. In the Watts-type Co electrolyte the morphology of a deposit obtained at -0.85 V at 40% amplitude was very different, more compact, and the increase in damping therefore smaller. The current efficiency in the absence of ceria was comparable (90%) to the more dilute electrolyte. Even under silent conditions, the entire deposit was redissolved during cyclovoltammetric experiments, which can be explained by the buffering capability of the boric acid in the electrolyte. The average current efficiency during cyclic voltammetry was ~90% under silent conditions, and decreased to ~ 82% in the presence of ultrasound. The cause for this decrease in current efficiencies was an enhancement of side reactions that also lead to the appearance of a cathodic current in the potential range where Co was neither dissolved nor deposited. The application of ultrasound increased the deposition rate by approximately 40%. In the presence of 5 g/l CeO_2 some ceramic material was incorporated in the deposit, but clearly less than with the more dilute electrolyte.

2.3.3. Application of EQCM in corrosion research with an emphasis on Al and Al alloys

Baek and Frankel prepared thin films of Al, Al_2Cu and an Al-4%Cu alloy on quartz resonators using the flash evaporation technique [35]. They studied the cathodic currents and pH-induced Al dissolution rate of the materials in 0.1 M NaCl with and without dichromate additions. EQCM allowed determining the true cathodic reaction rates from the net currents and the Al mass loss. They found that on Al and Al-4%Cu the true cathodic reaction rates were three times larger than the measured ones because of strong Al dissolution taking place. Al-dissolution was not so strong for Al_2Cu. ORR rates were much smaller on Al and Al-4%Cu than on Al_2Cu, confirming the limitation by electron transfer reactions through the oxide layer. Chromate decreased current densities and dissolution rates, pointing to a role of a protective chromium(III)oxide layer. Since the authors immersed the quartz in the solution containing already dichromate, they could not see the formation of $Cr(OH)_3$ in the QCM signal. For the corrosion protection of AA2024-T3 by chromate the authors concluded that

both reduction of cathodic reaction rates and therefore less cathodic corrosion as well as inhibition of dissolution of some constituent phases contribute.

Yoon and Buchheit [194] sputter-deposited Al_2CuMg thin films on quartz resonators. They exposed the films to 0.5 M NaCl solution. They saw an initial increase in OCP connected to a high rate of mass loss, followed by a stable period, where neither OCP nor mass changed significantly. The authors interpreted this finding by formation of a protective Cu surface film during initial dealloying. These results were supported by EDS spectra. Later, a slight decrease in OCP was connected with stable corrosion and a high mass loss rate, causing further copper enrichment. The authors also treated some specimen with a commercial chromate conversion bath. During the treatment they reported a small net mass loss, which decreased with time due to the increasing protectiveness of the growing CCC layer. CCC formation lead to a change in surface morphology (shrinking cracks) and a small contrast in Volta potential maps, but did not cause Cu enrichment. After immersion in NaCl, OCP soon assumed similar values as for untreated Al_2CuMg, but the measured mass loss rate was much less than for untreated samples. This showed that even for Al_2CuMg which is considered as a weak spot in technical aluminum alloys after chromate conversion coating the CCC treatment reduces the corrosion rate.

2.3.4. An EQCM study of the corrosion of Al-Cu model alloys [405]

Schneider applied EQCM to study corrosion processes on synthetic Al model alloys of the array type discussed in section 2.1.3. Standard 10 MHz AT cut quartz resonators were used for the preparation of synthetic alloy samples. One of the Au electrodes of the quartz resonators was replaced by a sputter-deposited Al electrode and thereafter photolithographically structured in the piezoelectric active region to allow for the sputter deposition of arrays of Cu or Al-Cu-Mg islands embedded in the aluminum. The composition of the films and the AlCuMg-targets was studied with scanning electron microscopy (SEM) and energy dispersive spectroscopy (EDS). Details about the experimental procedure can be found in [405]. A typical sample containing 20 µm diameter islands of Al-Cu-Mg in Cu is shown in Figure 33.

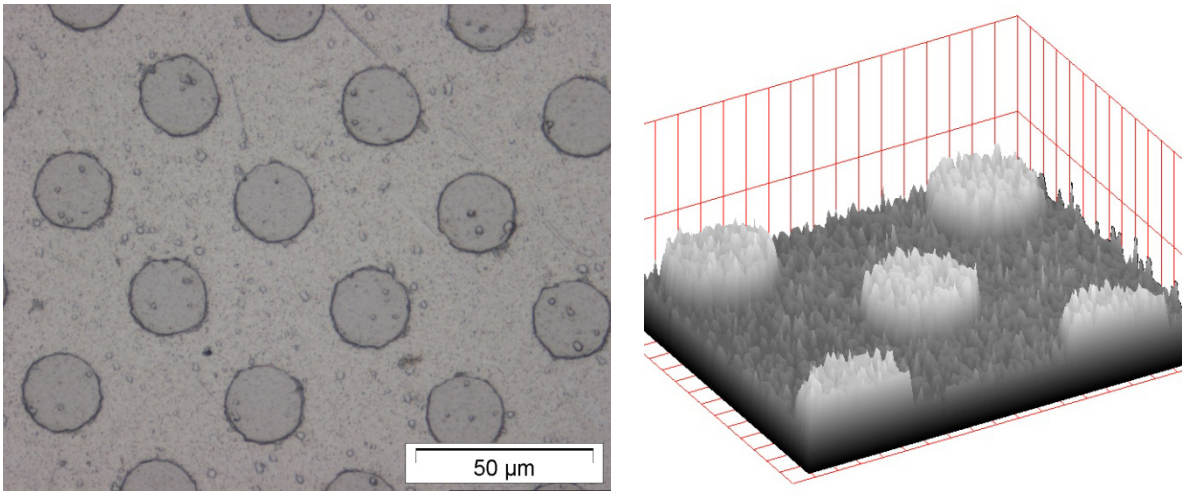

a) **b)**

Figure 33. Array of 8400 Al-Cu-Mg islands embedded in an Al matrix on a quartz resonator. Islands diameter: 20 µm. Spacing: 40 µm. The islands are about 750 nm high.

The corrosion behavior of synthetic Al alloys with large Cu islands was studied in 0.5 M NaCl solutions and 0.5 M NaCl with pH adjusted to 4 or 3.5. Initially, the OCP of a specimen (114 µm island diameter, total Cu area 0.011 cm^2) was around –0.7 V vs. Ag/AgCl, and then

decreased to much lower potentials. OCP was more positive than typically observed for sputter-deposited pure Al samples. There was no clear trend regarding the open circuit potential and the size of the Cu islands (at constant island number), i.e. the relative area covered by Cu. However, the OCP values before and after onset of corrosion were in a range which compares well with observations on AA2024-T3.

The corrosion resistance as determined by EIS first dropped by one order of magnitude, and thereafter increased again slowly with time. For EQCM experiments, typically the free corrosion potential of a specimen was monitored, and the resonance spectrum recorded in parallel. A characteristic result for short immersion times in 0.5 M NaCl is shown in Figure 34a. The potential decrease was accompanied by an increase of the resonance frequency, indicative of mass loss of the sample by Al corrosion. Similar observations were also made for other specimens. The damping changes were insignificant [405]. Therefore the Sauerbrey equation was applicable, and a mass change of approximately $2.4 \cdot 10^{-10}$ g cm^{-2} s^{-1} was calculated, which translated into a corrosion rate of ~ 30 µm/year.

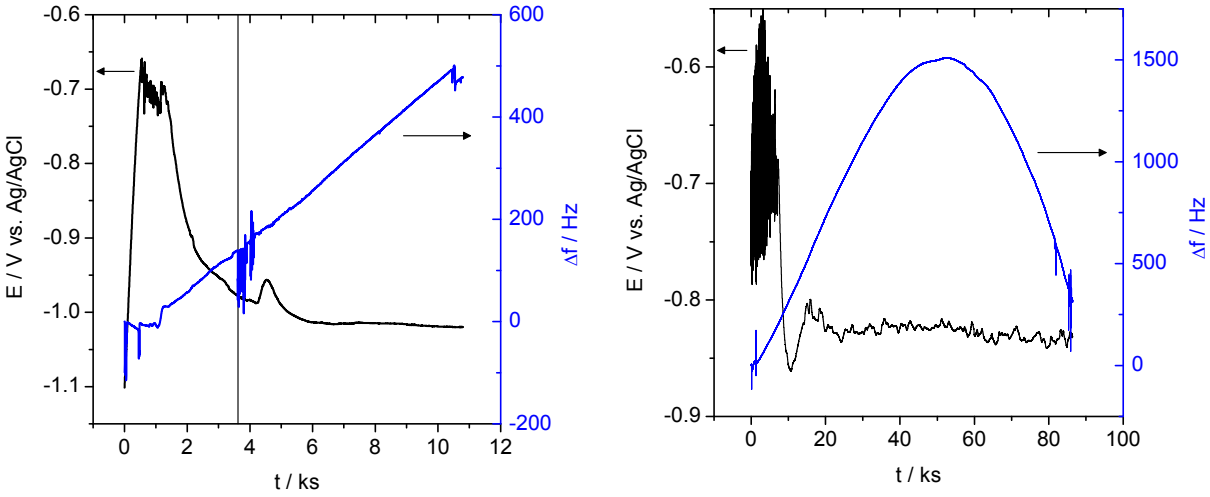

Figure 34. Change in resonance frequency and open circuit potential [405] of a) a quartz resonator coated with a synthetic aluminum alloy (142 µm diameter, 360 µm spacing, 110 islands) during early immersion in 0.5 M NaCl. b) a quartz resonator coated with a synthetic aluminum alloy (185 µm diameter, 400 µm spacing, 110 islands) during one day immersion in 0.5 M NaCl.

At longer immersion times the behavior changed completely. The frequency passed through a maximum and decreased thereafter, while in parallel the damping increased significantly, and the total Δw amounted to about twice the magnitude of Δf (cf. Figure 34b). Occasionally the frequency behavior was very erratic, with large fluctuations in resonance frequency accompanied by transient increases in the damping.

These observations were explained by the deposition of corrosion products especially around the Cu islands [405]. Some examples are given in Figure 35. For samples with large spacing between the islands the corrosion products were mainly on the islands and in their close vicinity (Figure 35a, b). For samples with a small spacing between the Cu islands corrosion products were also present on the entire matrix between the islands (Figure 35c). A band of corrosion products formed outside the entire electrode array, with no corrosion products on the Cu islands in the immediate vicinity (Figure 35d). The latter findings were similar to those reported by Missert et al. [30]. The corrosion products consisted of aluminum hydroxide

sometimes containing some chloride [405]. They were expected to influence the quartz response by their mass, but also by a roughening of the quartz, their gel-like nature and their inhomogeneous distribution across the piezoelectrically active surface. The latter factors can increase the damping and induce another negative frequency shift. From the good correlation between damping increase and frequency decrease it was concluded that the non-gravimetric effects were the major reason for the frequency decrease seen in Figure 34b. This was supported by measurements of the resonance frequency in air before and after the corrosion experiments, that demonstrated that the total mass of the alloy had clearly decreased during corrosion, and not increased due to corrosion product deposition.

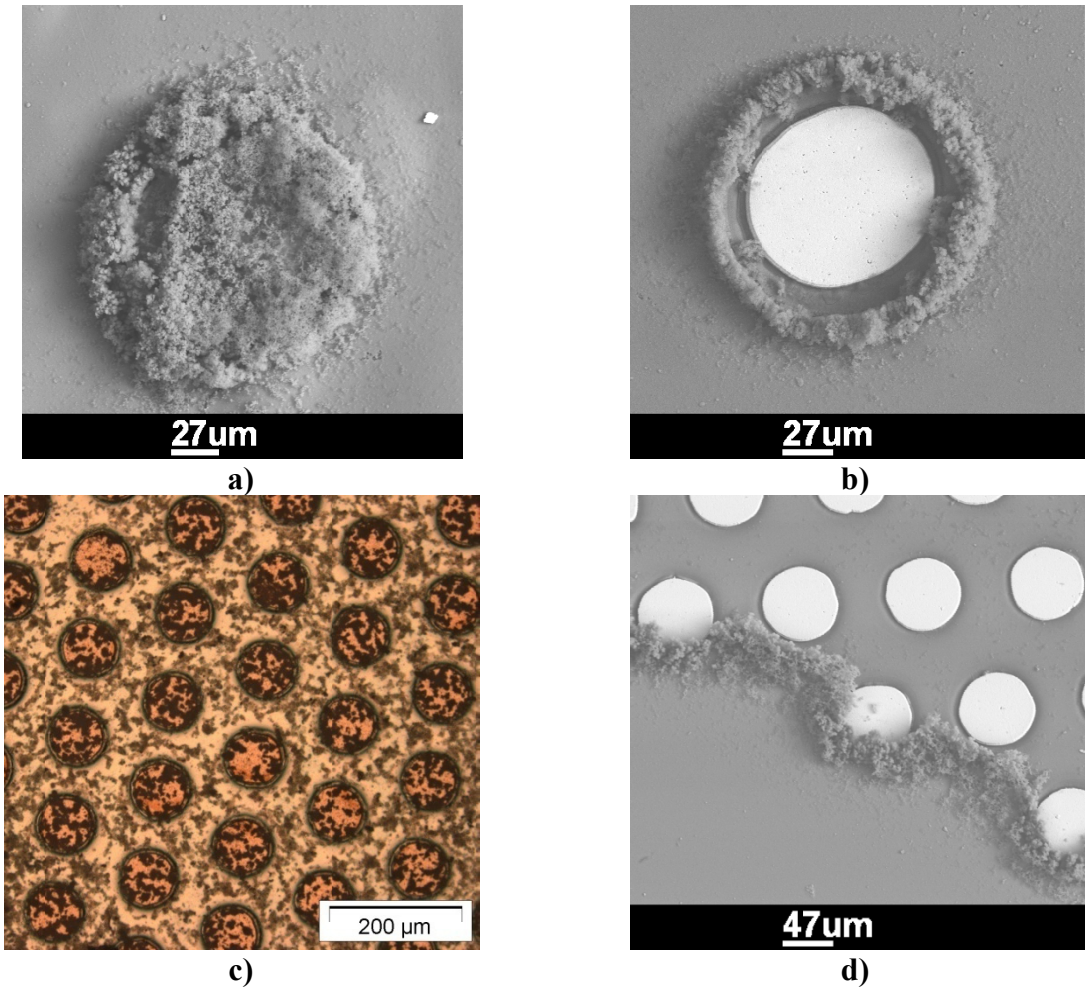

Figure 35: Typical corrosion product morphologies observed on synthetic Al-Cu alloys on quartz resonators [405]: a, b) $\varnothing$ = 140 µm, 400 µm spacing, 0.5 M NaCl, 21 h exposure time c, d) $\varnothing$ = 75 µm, 134 µm spacing, 0.5 M NaCl, 31.5 h exposure time.

From the rather positive open circuit potentials before corrosion onset, from the rapid start of corrosion as indicated by the sudden decrease in OCP and R_{corr} after a noisy period correlated with metastable pitting, and from the deposition of corrosion products especially on and – in ring like patterns – around the Cu islands it was concluded that the large Cu islands deposited on the Al layers in this study served as cathodic sites during open circuit corrosion in 0.5 M NaCl of different pH, similar to findings in the literature [29, 30, 49]. Ring-like patterns were also found on commercial AA2024 around intermetallic phases, and explained by local pH changes [26, 27]. Where the low pH environment of the anodic site at the interface between intermetallic particle and matrix meets the higher pH environment of the bulk electrolyte (or above the cathodic particle) precipitation of $Al(OH)_3$ occurs [26, 30]. A

strong accumulation of corrosion product on the island and in rings exactly at the interface between island and Al-matrix indicated that the material originated from localized corrosion of Al at the interface to the Cu island, similar to trenching observed with commercial AA2024-T3 and other aluminum alloys. For synthetic Al alloys it is known that as long as the Cu islands are apart from each other by a distance larger than the typical thickness of the diffusion boundary layer under the conditions of natural convection (~ 10-100 µm according to [29]), the individual pH fields do not overlap [29, 30]. If the distance between the islands is small enough more uniform pH fields develop. This explains the patterns shown in Figure 35 (c, d).

For the exposure of a synthetic alloy specimen with Al-Cu-Mg islands (cf. Figure 33) to 0.5 M NaCl, pH = 4, it was shown that the potential varied between –0.7 and –0.8 V vs. Ag/AgCl. In general the potential measured shortly after immersion was lower than for samples with Cu islands. This is in agreement with the anodic nature of the original Al-Cu-Mg phase. EQCM data for the specimen shown in Figure 33 were characterized by the quartz resonance frequency passing through a maximum, and then decreasing for 3h, while the damping continuously increased. Afterwards, transient increases in the damping were observed, connected to fluctuations in the frequency signal. After the end of the corrosion experiments some of the islands were completely missing. The remaining islands showed no more Mg. On samples with much larger islands even after one day of corrosion some islands still retained some magnesium. In part dense deposits of corrosion products (mainly Al-oxide) were found on the islands. Some flocs of corrosion products also could be found in the aluminum matrix, and here especially at the outer edge of the specimen. This demonstrates that these islands served as local cathodes. Cu was enriched in the islands, and was also found outside of the islands on the Al-matrix. The absence of Mg proved that these islands had de-alloyed and therefore were Cu rich remnants, which then probably acted as local cathodes. An EDX linescan extending from a point within the matrix to a point on the island showed the presence of Cu up to a distance of 4 µm outside the island. This strongly suggested, that also these synthetic Al alloys show some Cu replating originating from the Al-Cu-Mg phase. In the light of the findings of Jorcin et al. [195] a contribution of crevice corrosion from the boundary region between the Al-Cu-Mg islands and the Al matrix in these synthetic alloys cannot be excluded.

2.3.5. Miscellaneous

EQCM for the study of conducting polymers

Electronically conductive polymers have been intensively studied since 1977 [406, 407]. Examples are polyacetylene, polypyrrole, polythiophene, poly-p-phenylene, polyaniline (PANI) and their derivates, but also many other heterocyclic or aromatic polymers [408]. Many of these polymers can be prepared by electrochemical oxidation from aqueous or non-aqueous electrolyte solutions containing the respective monomer. During electropolymerization itself, charge compensation requires the incorporation of anions, and the polymers are obtained in the doped state. They are characterized by a good electrical conductivity combined with a low weight. The conductivity is based on a conjugated π-electron system, and the formation of charge carriers like polarons or bipolarons by doping. Doping is usually achieved by chemical or electrochemical oxidation of the polymer backbone, in some cases (e.g. PANI) also by exposure to acid. To maintain electroneutrality, doping is accompanied by the incorporation of counter ions into the polymer matrix. The doped polymer therefore has a salt-like character. Dedoping (e.g. by electrochemical reduction) is accompanied by the expulsion of the counter ions from the polymer, or by additional incorporation of cations into the polymer. Cations can only be expelled during

oxidation of a conducting polymer as long as some mobile cations are present in the film, and they only can be incorporated during reduction if space is available [409]. During electrochemical polymerization usually the doped form of the polymer is obtained. The materials possess potential for many applications, like antistatic coatings and composites, electromagnetic shielding, in the production of integrated circuits, the controlled release of substances, in ion exchange membranes, electromechanic actuators, in sensors, as electrochromic materials, in polymer LEDs, batteries, and for corrosion protection [410].

The electrochemical quartz crystal microbalance technique has been applied for a long time in order to study the electrochemical behavior of conducting polymer films. Already 1983 Kaufman et al. reported that the charge compensation during electrochemical oxidation/reduction of polypyrrole (PPy) in $LiClO_4$ electrolyte proceeds via the Li^+ ion and therefore cation exchange [411]. Baker and Reynolds studied the polymerization mechanism of polypyrrole in non-aqueous solvents [412]. Further early studies especially on ion exchange processes followed [357, 413-416]. Over the years, many studies on the subject were published by Hillman, Bruckenstein, and co-authors, considering in depth the processes of ion exchange in connection with salt and solvent transfer [417-419]. In part combination with other techniques like probe beam deflection was applied and also the occurrence of a non-gravimetric response due to film resonance was discussed [417]. In the presence of incorporation / expulsion of solvent and neutral salt in addition to the ion exchange processes it is no longer possible from EQCM to separate anion and cation exchange processes accurately without additional experimental data. Heinze and coworkers performed many studies on synthesis of different forms of polypyrrole and the resulting ion-exchange characteristics [420, 421]. Gabrielli, Perrot and co-workers combined the electrochemical quartz crystal microbalance technique with electrochemical impedance spectroscopy at low frequencies and called the technique ac electrogravimetry [422-425]. In addition to the measurement of the normal alternating current response as a result of an ac small amplitude voltage signal superimposed to the electrode potential, they also measured the resulting periodic mass changes. Bailey et al. as well as Bund et al. performed combined EQCM / Surface Plasmon Resonance studies [426, 427]. Recently, non-gravimetric contributions during redox switching of polypyrrole and other conducting polymers, often neglected in earlier studies, have moved in the focus of interest, and changes in complex shear modulus during polymerization an doping / dedoping have been studied [428-430].

Poly(para)phenylene (PPP) and its derivatives are interesting candidates for the construction of organic light emitting diodes (OLED). PPP can be prepared by polymerization of benzene. Due the high oxidation potential electrochemical polymerization originally was performed in solvents like liquid SO_2, HF/SbF_5 or 18-molar H_2SO_4 [431, 432]. Later deposition was also successful from organic solvents [433] and $AlCl_3$ based ionic liquids that however had the disadvantage of chlorine evolution at the potentials required for benzene oxidation [434-437]. Finally Zein el Abedin et al. succeeded in electropolymerisation of benzene from the ionic liquid 1-hexyl-3-methylimidazolium tris(pentafluoroethyl)trifluorophosphate ([HMIm]FAP) [438]. Ionic liquids (IL) consist only of (organic) cations and anions, basically constitute molten salts with a melting temperature below 100 °C, and often are liquid at room temperature [439]. One of their advantages is the wide electrochemical window permitting the deposition of unnoble metals, semiconductors and also electropolymerisation of polymers from monomers with a very high oxidation potential. In a subsequent study both the electropolymerisation and the ion exchange processes during redox cycling in the monomer free ionic liquid were studied by the electrochemical quartz crystal microbalance technique [440]. This was one of the first applications of the EQCM technique in ionic liquids. As substrates 10 MHz AT cut quartz crystals with Pt electrodes on a Ti adhesion layer on both

sides were used, and all electrochemical measurements were performed in a glove box. The major results of this study are summarized below.

The immersion in ionic liquid caused a strong decrease in the resonance frequency of the quartz by about 24 kHz and an increase in the damping by 49 kHz. These numbers were verified applying Equation (8) by inserting the large values for the viscosity (η = 0.115 Pas, 100 times as big as for water) and density (ρ = 1.56 g cm^{-3}) of the ionic liquid [441], resulting in $\Delta f = \Delta w/2 \sim 28000$ s^{-1}. The applicability of the Sauerbrey approach was verified for both the benzene electropolymerisation and the PPP ion exchange processes.

The shape of the cyclic voltammogram in a solution of 0.2 M benzene in [HMIm]FAP was reported as typical for electropolymerisation of conducting polymers (Figure 36a). Polymerisation started at $E \sim 1.8$ V in the first cycle, as seen by a steep almost linear increase in current accompanied by an irreversible mass increase. Subsequently at lower potentials a shoulder and a cathodic wave accompanied by a mass decrease were observed in the cathodic sweep, and a broad oxidation peak accompanied by a mass increase in the anodic sweep. Both peaks and mass changes were found to increase from cycle to cycle. A separation between reversible (redox switching of the polymer) and irreversible (polymerization) charge and mass changes was possible (Figure 36b). Based on these data and the slopes *dm/dQ* in the linear region the following conclusions were made:

- The amount of polymer newly deposited decreased from cycle to cycle
- In the fully oxidized state, every third to fourth benzene ring carried a positive charge. With increasing thickness of the polymer, reduction reaction no longer involved the entire polymer, leading to lower apparent degrees of doping *x*.
- A certain amount y_{IL} of ionic liquid was absorbed in the growing film and retained even after reduction, and therefore *dm/dQ* measured during electropolymerisation was larger than expected from the molar masses of benzene and the FAP anion. It was possible to calculate y_{IL} from the data shown in Figure 36b and a complete mass-charge balance (disregarding potential loss of oligomer intermediates formed during benzene oxidation). Results are given in
- Table 4.

$$x = \frac{2 \cdot Q_{rev}}{Q_{irr}} = \frac{2 \cdot \left(Q_{\max} - Q_{\min}\right)}{Q_{\min}} \tag{16}$$

$$y_{IL} = \frac{\left(2 + x\right) \cdot F \cdot \left(\frac{dm}{dQ}\right) - M_{C_6H_4} - x \cdot M_{anion}}{M_{IL}} \tag{17}$$

Table 4. Degree of doping *x* and amount of ionic liquid y_{IL} absorbed in PPP-polymer film during electropolymerisation.

cycle	x	y_{IL}
1	0.352	0.26
2	0.318	0.14
3	0.284	0.16
4	0.268	0.16

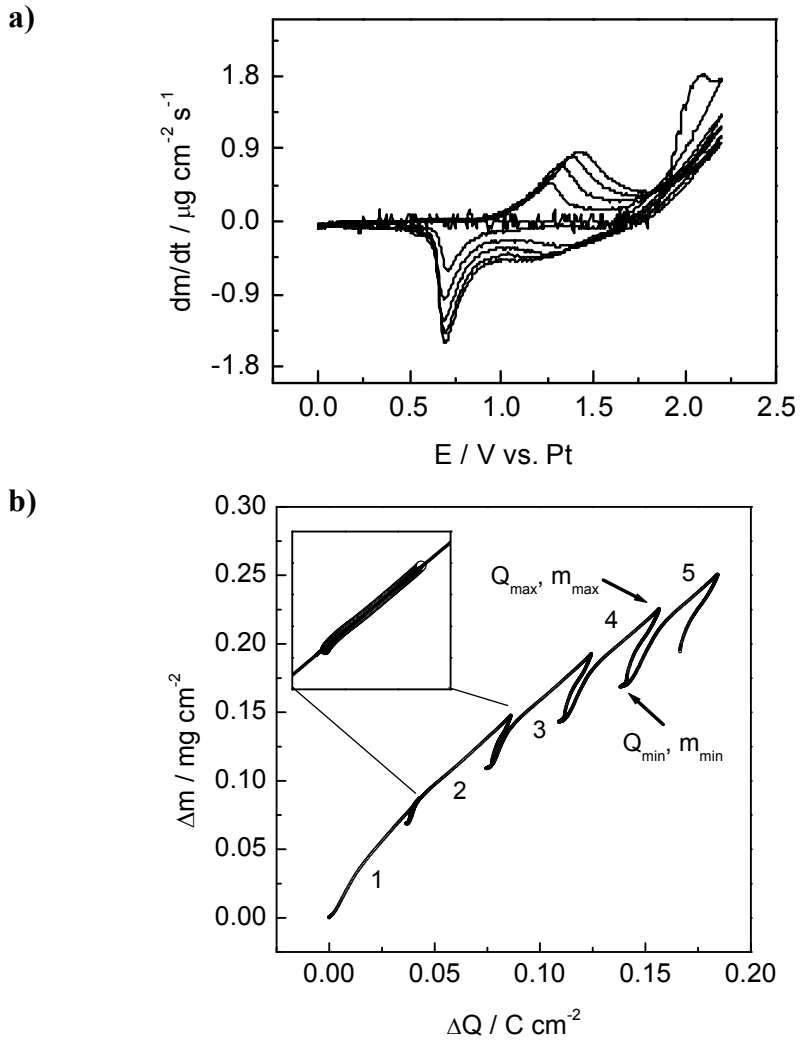

Figure 36. Electropolymerisation of benzene by cyclic voltammetry between 0 and 2.2 V vs. Pt in a solution of 0.2 M benzene in [HMIm]FAP at a scan rate of 10 mV s^{-1} [440]. a) differential mass change b) mass and charge flux for all 5 cycles. The cycle number is indicated in the Figure. In each cycle, charge and mass of the polymer showed a maximum after the end of the polymerization (Q_{max}, m_{max}), and decreased during film reduction to a minimum (Q_{min}, m_{min}). In the electropolymerization region, mass scaled linearly with charge, and the slope $dm\ dQ^{-1}$ was determined by linear regression, as indicated for cycle 2 in the insert. The fit line has been extended for improved visibility.

Analysis of ion-exchange processes during redox cycling of PPP in benzene-free IL was facilitated by the absence of a non-ionic solvent. In an ionic liquid only anions and cations can be involved in the redox reaction of the polymer. A simple formula to split the total mass flux in function of the electrode potential into the (molar) contributions from the cations ($z_c(E)$) and the anions ($z_a(E)$) based on EQCM data alone was given, using procedures similar to those applied for polymers in aqueous solutions:

$$z_a(E) = \frac{\left(\frac{dm}{dQ}\right)_E \bullet F + M_{cation}}{M_{IL}} \qquad (18)$$

$$z_a(E) + z_c(E) = 1$$

However it was considered that the analogue to salt transfer in aqueous solutions could take place, if IL formed within the polymer by cation ingress or included during polymerization is expelled at a later stage of reduction, e.g. by structural changes of the polymer backbone. This additional mass transfer would be unrelated to the current at that time, and the apparent contribution of anions to the redox process would be increased. It was emphasized that normally it is not necessary to distinguish between real and apparent exchange coefficients, because insertion of a cation accompanied by the expulsion of one unit of ionic liquid is formally the same as the expulsion of an anion. This situation has been discussed (for polypyrrole) in detail in the "cube"-model for aqueous electrolytes in the context of salt transfer [409]. The additional contribution from IL expulsion however can cause $z_a(E)$ to become larger than 1, and the corresponding $z_c(E)$ to become negative.

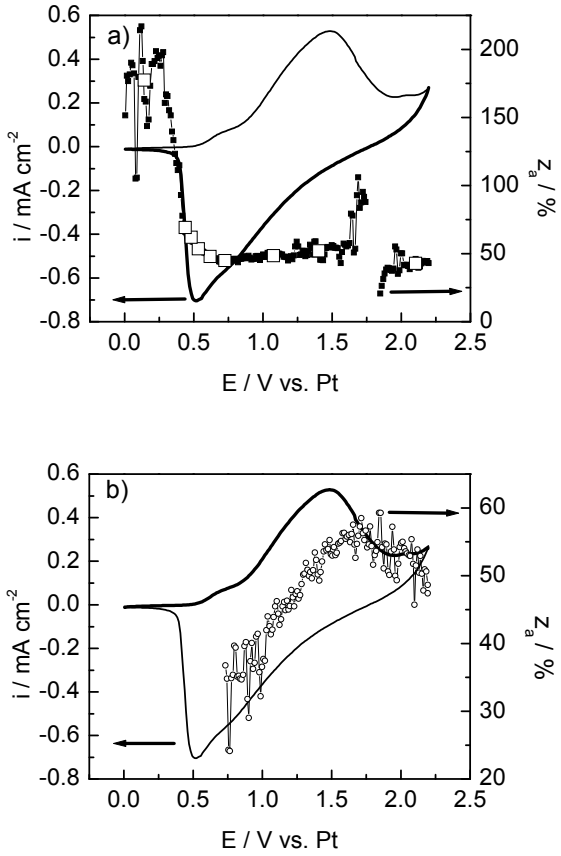

Figure 37. a) Apparent anion exchange coefficients z_a during a cathodic sweep of the polymer film immersed in [HMIm]FAP. b) Apparent anion exchange coefficients during subsequent anodic sweep (open circles). Lines: Corresponding cyclic voltammogram, scan rate: 20 mV/s (from [440]).

The cyclic voltammograms were characterized by rather broad and widely separated peaks. Both peaks were found to shift with increasing scan rate. In the beginning of the reduction reaction cation ingress for charge compensation was significant, whereas at lower potentials anion expulsion was the major process. In addition some (but not all) ionic liquid was expelled, causing an apparent $z_a > 100$ %. This was similar to the reduction of polypyrrole in aqueous solutions and PPP in acetonitrile, where the transfer of neutral species (salt, solvent) into solution had been observed especially for strong reduction [409, 418, 433]. Cation egress was of relevance during reoxidation of the polymer. The average anion exchange coefficients were close to 50% at 20 mV/s, and decreased with increasing scanrates.

Combination of EQCM and local probe techniques

The combination of local probe techniques like AFM and EQCM can provide additional information especially under experimental conditions, where the roughness of the electrochemical interface influences the quartz response. Bund and co-authors studied the influence of the electrode roughness during deposition of the EQCM signal [442]. They used an EQCM based on a phase lock oscillator that measures the resonance frequency and the damping resistance. Roughness was measured in parallel to the EQCM measurements, and no disturbance of the AFM response by the oscillating quartz and vice versa was observed. Cu was deposited galvanostatically at applied currents between -0.226 and -4.5 mA cm^{-2}. AFM measurements showed a decrease in the roughness of the Cu layer at larger current densities. Under these conditions many nuclei are formed across the substrate that can grow and lead to smooth films, whereas at small current densities only very few nuclei form and grow to rather large crystals [443, 444]. Apparent current efficiencies determined from the frequency shifts measured by EQCM were ~ 150% at low current densities, but decreased to 100% at the largest current. In addition the damping resistance strongly increased with time at low current densities, whereas it remained ~ 0 at high current densities. The authors interpreted this behavior by the influence of the surface roughness, which is of the same order of magnitude as the penetration depth of the acoustic wave into the electrolyte, on the quartz response. As mentioned before such interactions cause strong deviations from the Sauerbrey equation. The authors concluded that a direct measurement of surface morphology by AFM could help with the quantitative interpretation of the EQCM response and contribute to a separation between effects caused by external and by internal friction.

3. Mapping and Microscopy in Corrosion Research

3.1. Introduction to microscopy techniques for 3D-monitoring of surfaces

Confocal Laser Scanning Microscopy (CLSM) is an optical microscopy technique. The principle is described in detail in [445]. A laser beam scans the sample in the x-y direction. A small pinhole is located in front of the detector at a position that is optically conjugate to the focal point in the sample plane. The detector measures the intensity of the light reflected from the sample on the focal plane for each x-y-position. If the sample is fluorescent or contains a fluorescent dye, it is also possible to monitor the fluorescence intensity for each x-y-position. Most of the light coming from out-of-focus planes is focused outside the pinhole and, therefore, does not reach the detector. This effect allows sharp imaging of a single sample plane known as a slice. Other parts of the sample, even if they should have a brighter signal (e.g. stronger reflectivity or stronger fluorescence), do not disturb the image. By moving the sample stepwise through the focal plane (upwards and downwards) with a z-scanning stage, from the assembly of the slices recorded at each z-step a truly three-dimensional image can be obtained from a three-dimensional object. This assembly is known as a stack. For instance cross-sections of transparent items like coatings and living cells can be calculated from such stack. In Materials Science it allows reconstruction of the 3D surface topography of almost any material. Quantitative data for surface roughness, surface profiles, pit depths, coating thicknesses etc. can thus be obtained. In addition, a two-dimensional (2D) image with an extended depth-of-focus can be calculated. This process assigns a grey level to each image pixel, which corresponds to the brightest level at this x-y-position in all slices. Therefore, CLSM significantly surpasses the capabilities of conventional optical microscopy to measure and quantify surface metrology [27, 445-447]. With the aid of immersion lenses it is possible to study samples immersed in a liquid medium and thus to perform in-situ studies of corrosion processes. It is also possible to monitor a metal surface underneath a transparent organic coating [74, 448]. Those features permitted Schneider et al. to monitor for the first time three-dimensionally in-situ changes in substrate morphology during underfilm corrosion processes [74, 76].

The maximum resolution in x,y-direction is determined by the laser wavelength and the numerical aperture (NA) of the objective lens, and therefore 300 nm at a typical wavelength of 488 nm and a NA of 1.0 [445], in agreement with the findings from experiments [74]. 180 nm are possible [449]. The resolution in z-direction depends also on the diameter of the pinhole (which determines the number of slices required for a given z-range). Typical values are between 0.4 – 0.6 µm [74, 449].

The presence of a thin polymer coating on a metal and of electrolyte solutions on top of the specimen does not disturb the measurements when appropriate procedures are followed (like using a water immersion lens for direct immersion without cover slip). This was demonstrated by monitoring some IMCs in a coating blister on an AA2024-T3 panel immersed in 0.5 M NaCl (pH = 2.5) with the water immersion lens [74]. After the end of the experiments, the specimen was removed from the cell, the organic coating was stripped and corrosion products were cleaned off. The same IMCs were imaged in air, using a 50x objective optimized for use in air. For a selected IMC, the areas found under both immersed and air conditions were identical within 2%. Also the comparison of IMC monitored both with CLSM and SEM proved accuracy of the method.

This chapter will focus on the application of CLSM in corrosion research, especially with respect to the role of intermetallic compounds in aluminum alloy corrosion. The main emphasis will be on the author's own work, published in a series of papers [32, 33, 74, 76]. In

addition some results from Near-field Scanning Optical Microscopy (NSOM), fluorescence and AFM studies will be reviewed. Mapping techniques or functional microscopy techniques like Scanning Electrochemical Microscopy (SECM), Scanning Kelvin Probe (SKP), Scanning Kelvin Probe Force Microscopy (SKPFM), Scanning Vibrating Electrode Technique (SVET), Raman microscopy and Local Electrochemical Impedance Mapping (LEIM) will be presented briefly towards the end of the chapter.

3.2. Confocal Laser Scanning Microscopy

3.2.1. Applications of CLSM in Materials Science and Corrosion Research

CLSM is a contact-free non-destructive method [27, 445], and can be applied without the need to prepare or alter the sample (no evaporation of conductive layers needed). It was developed for and finds extensive use in biology because it allows the three-dimensional (3D) in-vivo monitoring of transparent biological entities such as cells and the preparation of sections without having to destroy the cells [27, 445]. An early review of the applications in materials science can be found in [450]. An emphasis of that paper lies on the investigation of structural ordering and dynamics in colloidal suspensions. In turbid disordered suspensions of polychlorostyrene styrene sulfonate the existence of voids could be demonstrated and explained by strong attractive forces between the particles leading to a gas-solid transition. In ordered suspensions of fluorescence-labelled silica spheres stacking disorder could be directly observed, which would not have been possible using diffraction methods or conventional light microscopy. Another emphasis is on the observation of phase separation in polymer mixtures [450]. CLSM has further been used to study defects in thermal spray coatings [446], to monitor electropolymerized poly(2-vinylpyridine) films on steel and determine the thickness of the polymer coatings [448], to determine diffusion coefficients from fluorescence recovery after photobleaching [451], to investigate chemical etching of copper [452], and to measure fibre strains in fibre-reinforced titanium matrix composites [453].

Smyrls and co-workers published a number of studies on corrosion of AA2024 and AA6061 in slightly acidic (pH = 4) chloride electrolytes containing fluorescein using CLSM, NSOM or AFM, each in combination with fluorescence microscopy [26, 27, 37, 44, 454]. They demonstrated that fluorescein does not influence the corrosion behaviour of the alloys. At open circuit potential, they observed the formation of fluorescent rings around many inclusions, which were associated with topographic features. With time, the diameter of the rings increased. They concluded the rings were corrosion product consisting of amorphous aluminum oxyhydroxides incorporating the fluorescein anion. The fluorescence signal was confined to the sample surface and was therefore not directly related to a local increase in solution pH. Between matrix and inclusion, a crevice formed [26]. In addition to the fluorescent rings, fluorescence was also found on top of some inclusions. In early work, the rings were attributed to cathodic sites (Al-Cu-Mn-Fe and Al-Cu) causing matrix dissolution and the disk-like fluorescence on inclusions was explained by the corrosion of Mg containing particles the dealloying of which causes the deposition of corrosion product on top of the particle [27, 37]. In later work the rings were said to be exclusively observed on S-phase inclusions as well [26]. The mechanism of the ring formation was attributed to initiation of local attack at the interface between particle and matrix, causing a separation of anodic and cathodic reactions [44]. The cathodic reaction would take place on the particle, but also on other particles nearby causing the site to show a net anodic current. At the interface the pH would decrease due to the corrosion of Al and subsequent hydrolysis of Al ions, causing a high solubility of Al ions. These diffuse into the bulk of the electrolyte, where the pH is more alkaline and the solubility less. Therefore precipitation occurs. The most probable solution species under these conditions is $Al_{13}O_4(OH)_{24}^{7+}$ [454]. With time, especially after

undermining of the particle, the acidic zone increases, causing the ring of corrosion products to dissolve and reprecipitate further away from the particle. The authors also studied AA2024 under an applied cathodic or anodic potential. They found a confinement of the cathodic reaction to the inclusions (by SECM), and despite seeing crevices around the inclusions and some weakly fluorescent rings they concluded that the cathodic reaction was not responsible for the ring formation [26]. However, anodic polarization under deaerated conditions resulted in fluorescent rings. Therefore it was concluded that ring formation is due to an anodic process, and that anodic dissolution, namely pitting, starts preferentially at the interface to S-phase inclusions because there exists a dispersoid-free zone [22, 24, 26, 455]. Later, fluorescence spectroscopy showed that the fluorescence intensity is proportional to the thickness of the corrosion product [454]. In that work Al-ions from the dealloying S-phase itself were considered to contribute to the corrosion product formation.

Keene et al. studied the influence of weathering, especially of UV radiation, on the degradation of aliphatic polyurethane coatings applied to AA2024-T3 [456]. They used different complete coating systems including primer and pigmentation / fillers, and different artificial and natural weathering protocols. Cross sections were prepared by microtomy, and analyzed by SEM/EDS and FTIR. From the ratio of amide and carbonyl peaks they drew conclusions about the extent of photooxidative degradation in these coatings. In a subsequent paper [457], they applied a laser confocal topographic scanner to analyse the topography of pits in coating blisters formed during salt-spray accelerated corrosion protocol. Their measurements however were ex-situ after coating removal. Their IR work indicated that the weathering had not altered the topcoat, but that the primer had failed cohesively due to undercured (D-type) regions.

Moon et al. studied the formation of an anodic oxide film on Al5052 alloy with ex-situ CLSM [458, 459]. Second phase particles can dissolve into the solution during anodization or they can be transferred into the oxide, either in metallic or oxidic form. Moon et al. found that the metal/oxide interface became more irregular during the anodization whereas the morphology of the oxide surface did not alter, and could determine the oxide film thickness from the data. They found different types of imperfections in the oxide films and explained their appearance (dark, bright) in the CLSM images. They concluded that Mg from Al-Mg particles selectively dissolved through the anodic oxide film leaving dark imperfections in the film, whereas the oxidation from Al-Fe-Mg particles caused bright irregular imperfections containing in part metallic iron.

Microbiogically influenced corrosion (MIC) is another field where CLSM is increasingly applied [460-462]. MIC is usually caused by the presence of biofilms on a metal or alloy, which are composed of an exopolysaccharide gel containing microbial cells. Monitoring of the biofilm after staining it with fluorescent dyes by CLSM permits to determine the 3D structure without destruction, even in cases where there are recessed areas under the biofilm, and to distinguish between living and dead cells. In addition corrosion on the metal surface itself can be monitored [461]. Biocorrosion is a very complex process influenced by many different factors, and its understanding therefore requires the combination of many experimental techniques and the careful evaluation of results from electrochemical experiments [460, 462]. Important aspects are changes in the nature of protective films, e.g. due to sulfides produced by the microorganism, production of corrosive species, differential aeration effects, change in transport behavior of electrochemically active species, change of the local redox potential, change in chemical composition of the aqueous environment (e.g. pH), and enzymatic catalysis [460, 461]. A vast amount of research has been dedicated to the corrosion of carbon steel in the presence of sulfate-reducing bacteria [460]. In most cases

biofilms cause (localized) corrosion. However, there are also some reports on corrosion prevention by microorganisms, caused by improved adhesion of protective layers, due to barrier properties of biofilms and to the consumption of cathodic reactants and pH changes [460, 463]. A review covering as well the historical development and the prospects for the future of MIC has been given by Videla and Herrera [460]. They reference some work, in which the simultaneous use of microelectrodes and CLSM allowed the correlation between oxygen concentration and biofilm structure. In other work local potential and biofilm structure were correlated [461] or diffusion coefficients within the biofilms determined [464]. Colonization of sulfate reducing bacteria on Cu-Ni alloys could be observed by CLSM even though no continuous biofilm is formed – Cu ions are toxic for microorganisms [465]. On the substrate Cu_2S formed and organic acids were produced. Cu_2S as a corrosion product lowers the potential for the anodic reaction, and leads to surface films which are not very protective. As a consequence, intergranular corrosion was observed [465].

3.2.2. In-situ studies of corrosion metrology of aluminum alloy 2024-T3 [32, 33]

Schneider, Ilevbare, Scully and Kelly performed a number of CLSM studies of corrosion processes of bare AA2024-T3 in environments of different chloride concentration and pH. These electrolytes in part were chosen in order to mimic the composition of the occluded solutions found in coating blisters on polymer-coated aluminum alloy [85]. Aim of studies on bare alloys was to monitor the corrosion of intermetallic particles and the propagation of corrosion into the matrix, to come to a better understanding of the phenomenon of trenching, to correlate the findings with the electrochemical behavior of synthesized bulk analogues, and to validate the findings with model calculations.

CLSM was carried out using a Zeiss model LSM 510 microscope. Imaging was performed with an argon laser (488 nm wavelength). The studies were conducted on 1.5 mm thick AA 2024-T3 coupons (from Kaiser) that were cut from 90 by 120 cm sheets to squares of about 2.5 by 2.5 cm. One face of the coupons was abraded with SiC paper (from 180 up to 1200 grit), and then polished with 1 μm diamond suspension. A thickness of about 0.1-0.3 mm of the specimen was removed during the grinding and polishing processes.

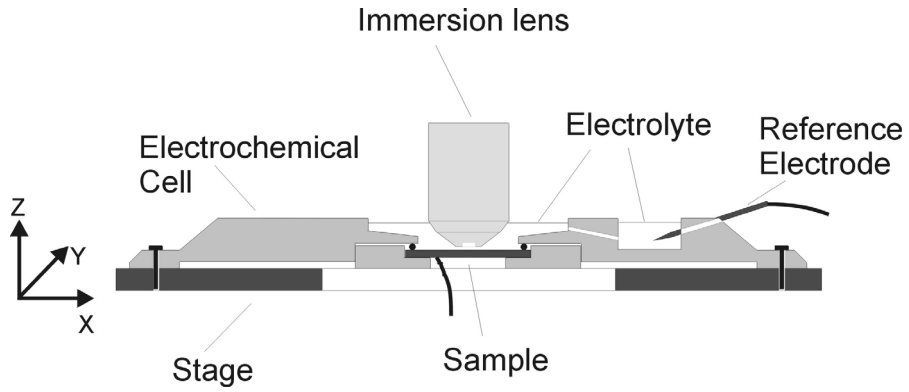

Figure 38. Electrochemical cell for in-situ CLSM of AA2024-T3 specimens (from [74])

In order to monitor the topography changes in-situ, the specimens were placed in a specially constructed flat electrochemical cell mounted on the x-y-z-stage of the CLSM (Figure 38 [74]) designed for use with the 100x water immersion objective lens (Achroplan, numerical aperture 1.0, 1 mm working distance). The electrolytes were not stirred, and there were several mm of electrolyte on the substrate in the flat cell.

Prior to the introduction of any electrolyte, areas of interest for study were selected with the 100x immersion objective lens of the CLSM. In some cases, some of the surface features that were studied were first chosen with the aid of the SEM. Imaging of the areas of interest commenced after the introduction of electrolyte into the flat cell, and any changes in surface morphology were monitored with time.

Four different categories of morphological features associated with micrometer-scale constituent particles were reported [32]: (i) particles which corroded (Al-Cu-Mg, Al-Cu-Fe-Mn), (ii) particles which caused trenching in the adjacent matrix, (iii) particles which did not corrode at all during the time of immersion, and (iv) pitting in the matrix, possibly initiated at IMC particles too small to resolve. In addition the pits initiating at/in the particles were observed to extend into the matrix in some cases.

Particles identified with EDS as Al-Cu-Mg particles were found to start corroding within ten minutes after exposure to a solution of 0.1 M Na_2SO_4 + 0.005 M NaCl. Some Al-Cu-Mg particles were reported to completely dissolve within the first two hours, although no extension of the corrosion into the surrounding matrix was observed [32]. This was consistent with polarization curves of Al-Cu-Mg bulk analogues indicating a corrosion rate of about 20 μm/h at the OCP of AA2024-T3. The bulk Al-Cu-Mg analogue did not exhibit passivity at pH 3, and little if any at pH 6. Therefore, once the alloy was immersed, there was little to no incubation time for the dissolution. In a particle showing distinct regions of Al-Cu-Mg and Al-Cu composition corrosion attack had occurred on the entire Al-Cu-Mg surface after 40 minutes and had expanded into the matrix. The other sections of the constituent particle (the Al-Cu phase) remained intact. These observations were in agreement with expectations from electrochemical measurements with bulk analogues. As corrosion occurred, the enhanced ORR kinetics on the Cu-containing materials compared to high-purity Al exacerbated the situation because the increase in the local pH over the cathode increased the OCP difference between the Al-Cu-Mg and the Cu-bearing particles [32]. Although the irregular shape of the dissolution morphology complicated analysis, a dissolution rate of approximately 2 mA/cm^2 was estimated by the extension rate of the corroded region. The propagation into the matrix was explained by the local chemistry formed during the pitting of the S-phase particle and the local galvanic coupling being sufficiently aggressive to initiate and support dissolution of the matrix. The initiation and growth of regions of attack away from Al-Cu particles demonstrated the ability of the particles to polarize the matrix to above its pitting potential locally.

Several types of localized corrosion attack were observed on the intermetallic particles in both 0.1 M Na_2SO_4 + 0.005 M NaCl and in 0.5 M NaCl. A nearly hexagonally shaped particle exposed to the sulfate-based solution started corroding by forming a pit near its center (cf. Figure 39). From its shape it was concluded that the particle was at least in part of the Al-Cu-Mg type. The corroded area increased and covered the entire particle within a few hours. A line scan across the particle revealed a minimum depth of the corrosion attack of more than 1 μm after 280 min (cf. Figure 39d). An accurate determination was complicated by the accumulation of large amounts of corrosion products within the pit, and also at the outer edge of the particle (Figure 39e). Estimates of the dissolution rates were possible because of the regular shape of the site. Assuming a hemispherical pit, the lateral growth rate of the pit was converted into current densities by application of Faraday's laws. From 17 minutes through 280 min after immersion the average dissolution rate of the pit increased from 350 $\mu A/cm^2$ to 3 mA/cm^2. These rates do not represent the range of stable pitting rates usually observed under potentiostatic control, which are typically on the order of 1 A/cm^2, but are more typical of metastable pits [466, 467]. As the pit reached its interface with the matrix, its growth

slowed and virtually stopped (the radius increased only 700 nm over the last 1 h 40 min of observation, possibly due to undercutting of the surface). The attack on a rectangular-shaped Al-Cu-Fe-Mn IMC started with the formation of many tiny pits close to one edge. In the early stages, the depth changes were too small to be resolved, but later on, pit depths of >4 µm could be verified. The dissolution progressed through the rest of the particle and precipitated corrosion products were observed around and on the particle.

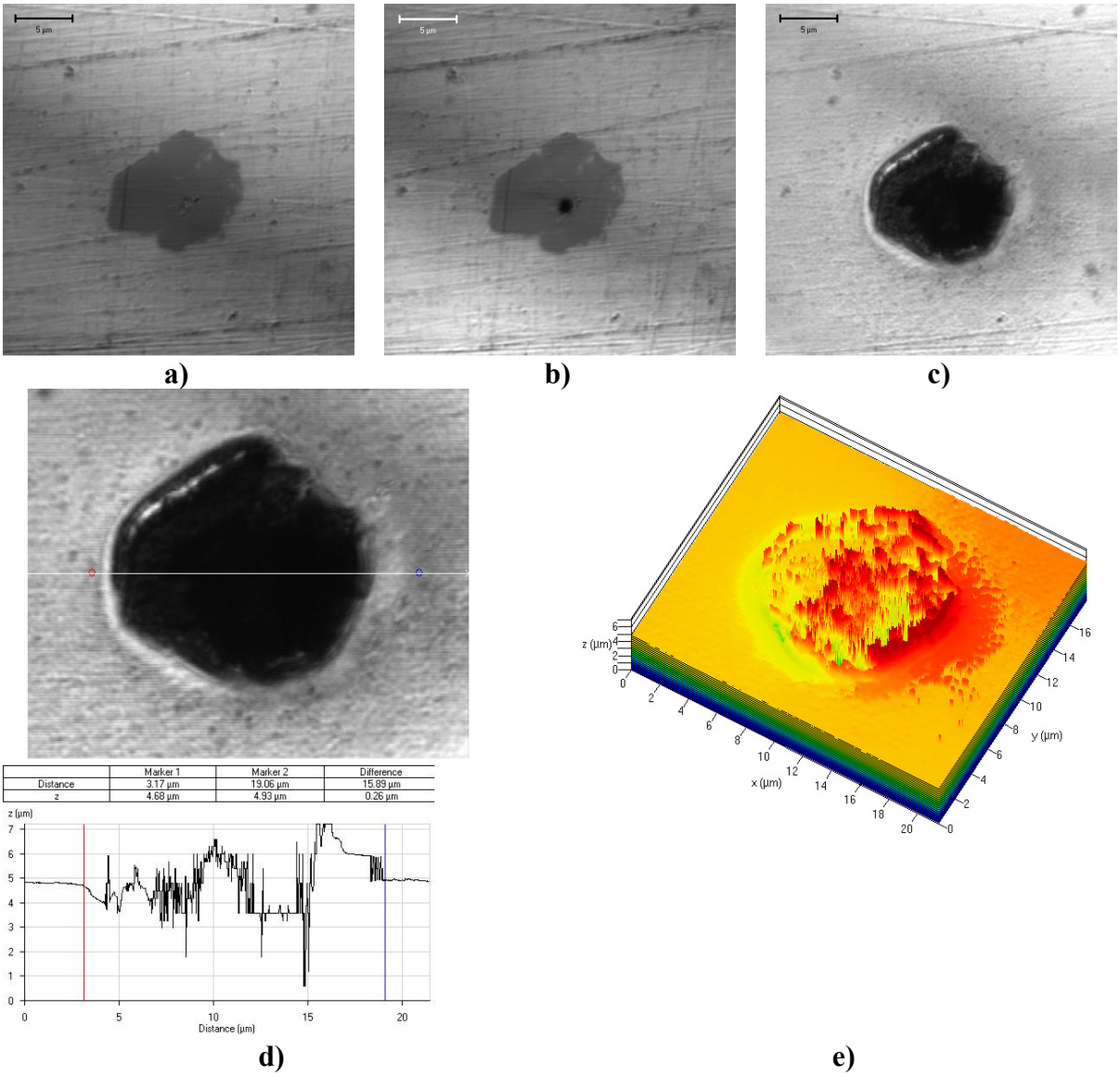

Figure 39. Intermetallic particle corroding on bare AA2024-T3 in 0.1 M Na_2SO_4 + 0.005 M NaCl. Immersion times: (a) 17 min (b) 83 min (c-e) 280 min. (d) height profile across corroded particle (e) 3D topography (color coded) (from [32]).

In 0.5 M NaCl, multiple large pits formed due to the increased aggressiveness (Figure 39). The formation of three larger pits on an Al-Cu-Fe-Mn IMC exposed to 0.5 M NaCl, which began to coalesce, was monitored after 12, 50, and 77 minutes of immersion (Figure 41). Two of these pits initiated within the particle at or close to the interface with the matrix, whereas the other two initiated in the central portion of the particle. The surrounding matrix exhibited round pit formation, as well. The pits all initiated within 10 min of immersion. The pit in the matrix stifled relatively quickly, growing very little after 30 minutes of immersion. The dissolution of the Al-Cu-Fe-Mn particles via pitting would not be expected from its

polarization behavior, as it would be expected to be cathodically polarized by the AA2024-T3 matrix. The two largest pits that form in Figure 41 were estimated to grow initially at a dissolution rate of 2.7 mA/cm^2. Thereafter, the dissolution rate decreased rapidly. All the other pits showed even lower dissolution rates. Assuming that the particle in Figure 41 is indeed of Al-Cu-Fe-Mn type, its pitting can be understood in terms of the potential dependence of the initiation of metastable pits at potentials below the experimentally-determined pitting potential. It is well known that metastable pits form on virtually all alloys well below the potential determined by polarization scans, which is better described as the potential for pit stabilization [226, 467]. Thus, the CLSM images of the Al-Cu-Fe-Mn particle shown in Figure 41 are images of the initiation and growth (including stifling) of metastable pits.

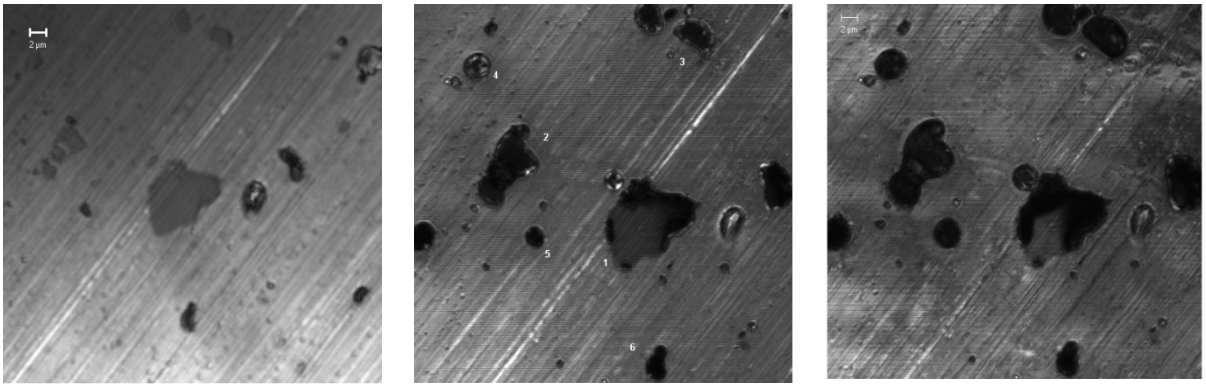

a) **b)** **c)**

Figure 40. Corrosion of a selected area of bare AA2024-T3 in 0.5 M NaCl. a) before immersion b) after 22 min of corrosion c) after 65 min of corrosion.

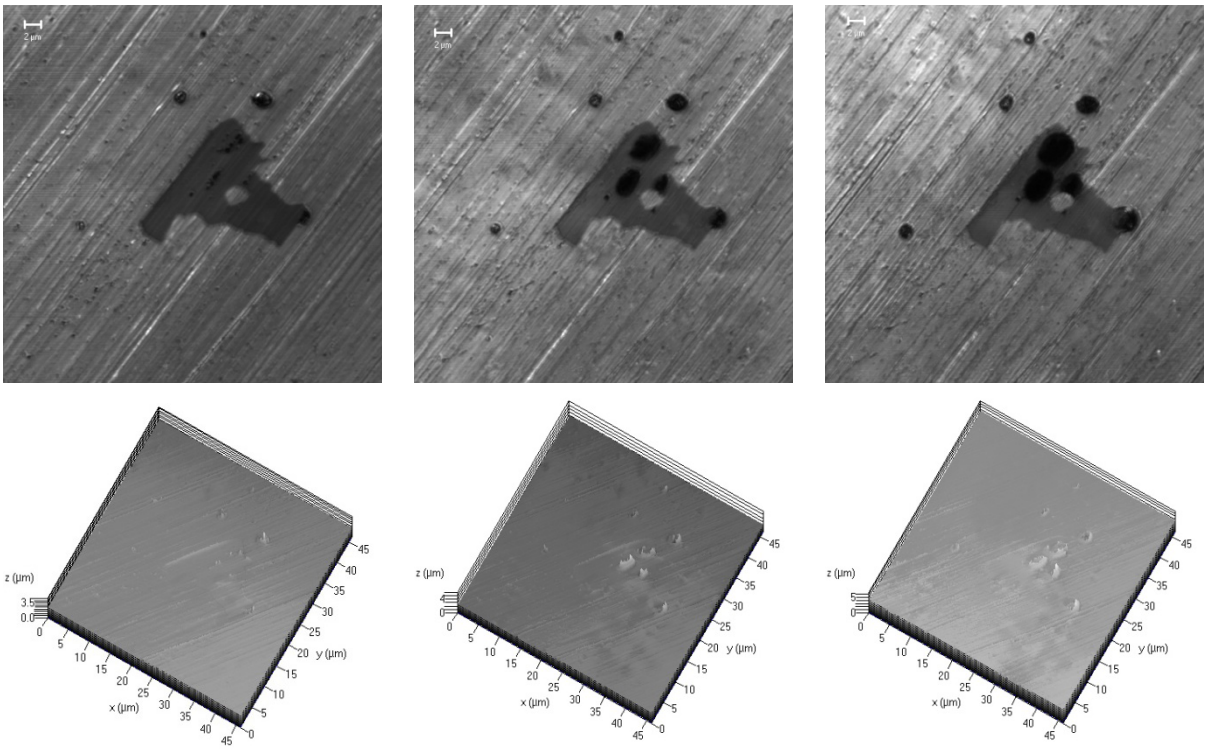

a) **b)** **c)**

Figure 41. Localized attack on IMC particle and the matrix in 0.5 M NaCl [32]. Immersion time: (a) 12.5 (b) 50, (c) 77 min.

In some cases, corrosion initiated at the particle/matrix interface and grew into the particle. Figure 40 (particle in center) shows an example in which corrosion started at several locations along the interface with the matrix. Note that the IMC particle corroded while the matrix in the vicinity of this large IMC particle was only slightly attacked, if at all. In the upper left area, round pit formation was observed near the IMC. This pit initiated at a small particle and grew to a size much larger than the original particle.

Individual IMC particles were attacked much earlier in 0.5 M NaCl solution compared with 0.1 M Na_2SO_4 + 0.005 M NaCl (pH 6). Figure 42 demonstrates this difference by comparing the percentage of IMC lateral area attacked based on the studies of some IMC, e.g. from Figure 39 - Figure 41. The % lateral area attack increases rapidly sooner in 0.5 M NaCl. This result indicates a strong effect of Cl^- concentration on initiation of pitting of these IMC. Nonetheless, once corrosion has started comparable corrosion rates (proportional to the slope of Figure 42) can be achieved even in the 0.005 M Cl^- solution.

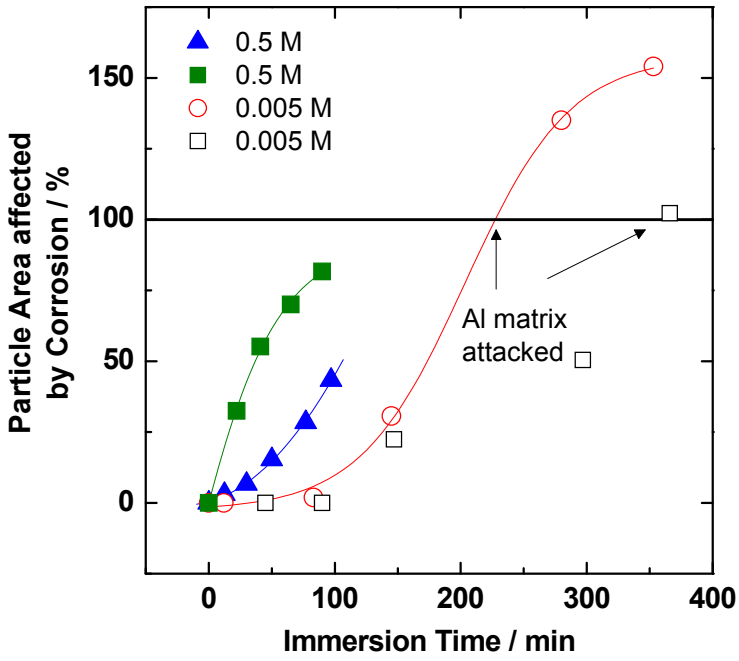

Figure 42. Examples for the progress of intermetallic particle corrosion during immersion in 0.5 M NaCl or 0.1 M Na_2SO_4+ 0.005 M NaCl [32]. Lines: Sigmoidal fits. Legend: Chloride concentration.

Ilevbare et al. explained the inability of most of the observed pits formed in different IMC particles to expand in the surrounding matrix by applying a pit stability criterion based on work of Galvele and Pride. Galvele [466] proposed a stability criterion for stable pitting in one-dimension that was modified for hemispherical pits by Pride et al. [467]. The criterion is in terms of i_{pit}*r_{pit}, where i_{pit} is the current density of the pit and r_{pit} is the radius. Pride et al. found [467] that for stable pits to form on Al in chloride solution, an i_{pit}*r_{pit} of at least $2x10^{-3}$ A/cm must be sustained in order for stable pitting to occur with Al^{3+} transference number taken as 0.45 [468], and D_{eff} (Al^{3+}) = 10^{-6} cm^2/sec. They ascribed this to the need to maintain a concentrated solution of metal chlorides and accompanying low pH within the pit to prevent repassivation. However, it was shown that this number could be reduced to below 10^{-3} or less depending on the precise details [469]. Lower critical values of i_{pit}*r_{pit} imply some combination of (a) lower D_{app}, (b) lower transference number for Al^{3+}, and (c) lower critical concentration for stability (and consequently higher pit pH). Ilevbare et al. showed that an i_{pit}*r_{pit} of between 10^{-7} and 10^{-6} A/cm is capable of dropping the pH from about 8 to 5

considering a completely unbuffered solution. Thus, any intermetallic phase that depassivates at such pH could be rationalized to show stable pitting. Al-Mg-Cu particles will dissolve actively even at pH 6, undergo dealloying and perhaps experience mass transport controlled dissolution, being unable to passivate at any pH. Thus, once there is a breach of the oxide film over such particles, the dissolution proceeds even without the need of a low pit pH. However, an Al-rich matrix would still require a pH below about 3 or an $i_{pit}*r_{pit}$ value of about 10^{-3} A/cm.

From CLSM images the true local anodic current density and pit radius were determined from changes in the corroding perimeter detected by CLSM. For the particle in Figure 41, over the initial period, the average rate of growth was about 2.7 mA/cm^2 for two of the pits in the particle. The $i_{pit}*r_{pit}$ for these pits were approximately 3.0 x 10^{-7} A/cm and 1.8 x 10^{-7} A/cm, respectively, during the fastest portion of the observed growth, and decreased to about 1.5 x 10^{-7} A/cm both. All these values are below the limit for stabilization, explaining why these pits died at an early stage of growth.

In Figure 39, the pit experienced an $i_{pit}*r_{pit}$ that increased from 2.4 x 10^{-8} A/cm up to 5.3 x 10^{-7} A/cm before it decreased slightly to 1.4 x 10^{-7} A/cm as the pit reached the interface with the matrix and virtually stopped. For this and many of the other particles studied the $i_{pit}*r_{pit}$ was less than the criterion for stability for growth of pits in the Al matrix. Thus, all of the pits had to die, albeit after different times of growth. The pit in Figure 39 was able to grow beyond the diameter of the particle, but the $i_{pit}*r_{pit}$ was insufficient to allow propagation into the Al-rich matrix. Thus, the extension of the pit was limited by the size of the susceptible material. Using an average $i_{pit}*r_{pit}$ of 2 x 10^{-7} A/cm led to the conclusion that the pit pH was approximately 6. Thus, it was not surprising that the pit was unable to propagate into the matrix. The additional, slow growth of the pit outside the original diameter was explained by undercutting of the surface due to the presence of additional Al-Cu-Mg material just below the surface. Similar considerations applied to the particle in Figure 40, where the shape did not allow a quantitative analysis.

Ilevbare et al. also discussed the role of the available IMC area to supply the cathodic current for stable pit growth. The calculation showed that for a pit of 1 μm diameter meeting the criteria of $i_{pit}*r_{pit}$ = 2 x 10^{-3} A/cm as an example, with the diffusion limited oxygen reduction current assumed to be 1 mA/cm^2 a radius of 200 μm would be required for the cathodic particle, which is much larger than any cathodic IMC seen on the surface. These calculations explained why most pits observed grew rather slowly and had $i_{pit}*r_{pit}$ values orders of magnitude lower than needed for stable pitting of the matrix. The corrosion products observed in the pits (Figure 39e) might have stabilized the growth of the metastable pits for a short time, leading to much longer lifetimes than usually observed for metastable pits. The facts that extensive pit damage can be observed at open circuit in AA 2024-T3 after long exposure periods was explained by the high Cl- concentration, proximity of the sites to a large number of Cu-rich IMC that can support cathodic reactions and especially Cu replating.

Schneider et al. studied also trench formation in 0.5 M NaCl (pH 6) electrolyte and mixed chloride/sulfate solutions (0.1 M Na_2SO_4 + 0.005 M NaCl) of pH 3 (“acidic solution”), 6, and 10 (“alkaline solution”) [33]. Trench formation occurred around some, but not all, particles in all electrolytes. Examples for mixed chloride/sulfate solutions are given in Figure 43 [33]. The trench around the particle in Figure 43a was at least 2.5 μm wide after 1 day, while the particle itself had not been affected by corrosion at all as clearly evidenced by the presence of the polishing lines. The depth of the trench was about 3 μm. It was reported that some of the particles that showed trenching had rather high Cu-concentrations with little or no Mn or Fe

suggesting that they were Al-Cu IMC. Copper concentrations of greater than 20 at% were found in six of the nine particles that showed trenching. Indeed, several particles for which no trenching occurred after 24 h were identified by EDS as Al-Cu-Mn-Fe. In some cases, the matrix around some Al-Cu particles also remained unattacked although these particles were close to others which trenched. In the alkaline solution (pH 10), where pitting of the Al solid solution matrix was not expected to be prevalent due to the large difference between the open circuit and pitting potentials [32], trenching appeared to be the most common form of corrosion, sometimes involving several IMC. Deposition of corrosion products was observed around all these trenched areas. Interestingly, trenching was observed in acidic solution as well, an example of which is given in Figure 43c. Even after 18 hours of exposure, the width of the trench was only about 0.5 to 1 µm, and the depth (insofar as not obscured by corrosion products) was only 1.3 to 2.3µm. An example for trench formation in 0.5 M NaCl can be seen in Figure 40 on the left side: In an area originally containing 2 large IMC and a small one in-between, separated by a thin strip of matrix material, after 72 minutes of immersion in 0.5 M NaCl a single trench that surrounded all three particles had formed, and the matrix between the IMC particles had corroded. In both alkaline and acidic solutions there were selected particles, which did not corrode and showed no trenching within the duration of the experiment (~1 day).

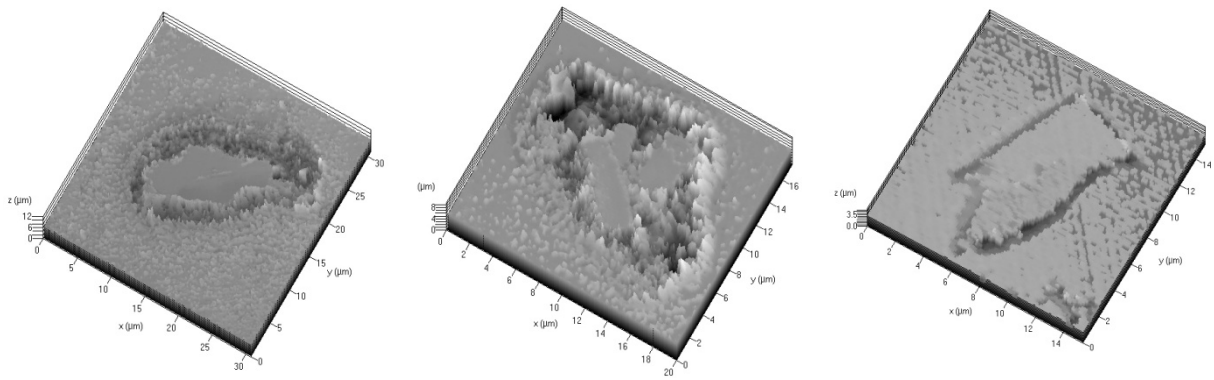

Figure 43. Trench formation in 0.1 M Na_2SO_4 + 0.005 M NaCl solution of (a) pH 6 (immersion time: 1 day) (b) pH 10 (immersion time: 9 h) (c) pH 3 (immersion time: 18 h, 20 min) (from [33]).

Figure 44 demonstrates how matrix corrosion due to trenching evolved with time. The localized corrosion occurring on larger sample areas (130 µm x 130 µm) was monitored over time as well, and related to the total IMC area present at the beginning of the experiment [33]. The corrosion in 0.5 M chloride solution occurred much more rapidly than in the 5 mM NaCl and sulfate at pH 3, 6 or 10. This underscored the importance of Cl^- in trenching and suggested that the detailed corrosion process on AA2024-T3 is not governed solely by cathodic kinetics of ORR on Cu-rich IMC particles as previously speculated [29, 34, 44, 47].

Different areas on the same sample corroded somewhat differently, making it difficult to rank the corrosiveness of the solutions of different pH. Entire clusters of IMC showed variable behavior (ranging from trenching to no attack at all) demonstrating a strong influence on the corrosion rate and morphology by the local combination of anodic and cathodic IMC particles present. Variability in susceptibility to trenching amongst the IMC was explained by differences in the precise IMC composition (linked to electrochemical properties) as well as the precise combinations of anodic and cathodic sites nearby.

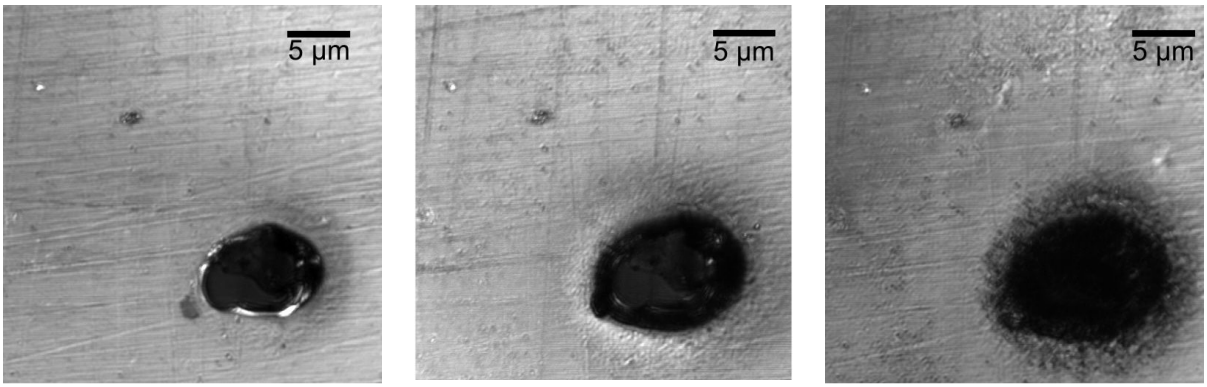

a) **b)** **c)**

Figure 44. Intermetallic particle showing trench formation on bare AA2024-T3 in 0.1 M Na_2SO_4 + 0.005 M NaCl. Immersion times: (a) 45 min (b) 123 min (c) 385 min.

In order to test the hypothesis of cathodic trenching, Schneider et al. performed computational simulations of the pH evolution above IMC particles in the pH 3, 6, and 10 solutions. The goal was to determine the extent to which the pH above the IMC could be driven in the alkaline direction by the galvanic coupling between the passive matrix and the cathodic IMC particle. The simulations assumed a single IMC with a diameter of 10 µm embedded in a passive alloy matrix. The passive current density of the matrix was taken from polarization data of AA2024-T3 as 1.8 µA cm^{-2} in both the neutral and alkaline solutions and 14.4 µA cm^{-2} in the acidic solution [32]. Under the assumption that about 2% of the area of AA2024 consists of IMC cathodic to the matrix [22, 23], such a passive current requires a cathodic current density of 90 µA cm^{-2} at these IMC in alkaline solution in order to balance the anodic and cathodic reaction rates. This value is very close to the estimated diffusion limited current density for oxygen reduction upon which calculations of Alodan and Smyrl were based [37]. Production of hydroxide at the IMC surface (i.e., the net cathode) and of protons at the matrix surface (i.e., the net anode) was considered. Transport in solution was treated as due only to diffusion. It was pointed out that in real electrochemical systems natural convection sets an upper limit for the diffusion boundary layer thickness. Details of the numerical procedure are given in the original publication [33].

Some results are displayed in Figure 45. A clear pH increase was found for solutions of bulk pH 6. In addition, the pH remained high at distances much greater than those over which trenching was seen in CLSM. After 5 sec, a pH of 9.30 was obtained at the interface IMC/matrix, and 10 µm away from the interface the pH still was 9.19, decreasing then almost linearly by 0.06 pH units every 10 µm of radial distance away from the center of the IMC. In alkaline solution the pH at all locations on the surface was higher than the most alkaline spot for a neutral bulk solution and hardly changed. In acidic solution, the pH of the solution near the IMC was raised insignificantly. Chloride was not incorporated in the model. It might be argued that Cl^- would raise the oxide dissolution rate, but it has been shown that it does not affect the kinetics of the ORR.

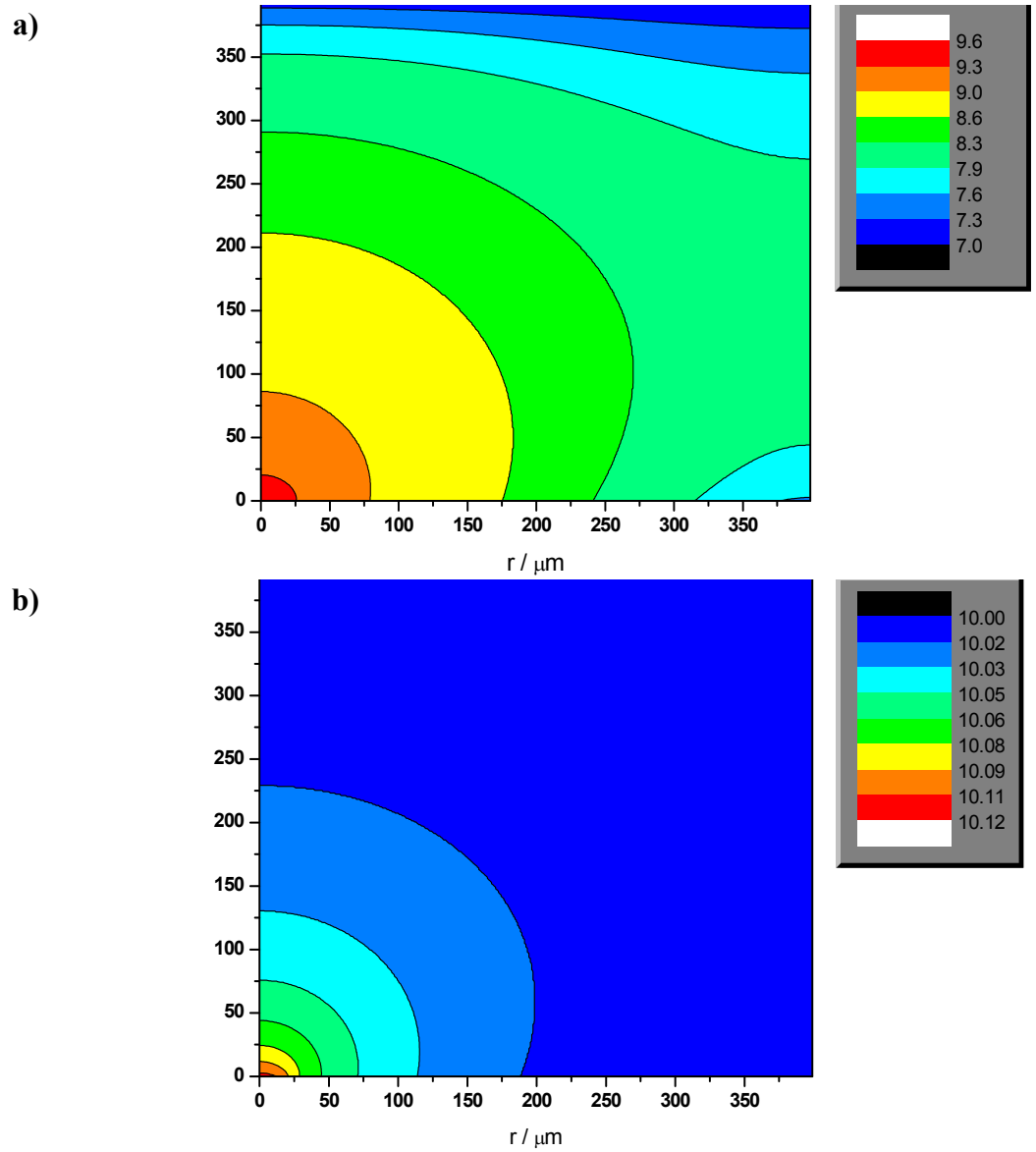

Figure 45. Numerical simulation of the pH near an IMC on passive AA2024 at different bulk pH after five seconds. The IMC is located between r = 0 and r = 10 µm at z = 0. The total r- and z-range considered in the simulation is 0 – 200 µm. The pH values are given for z = 0 (surface). a) bulk pH = 7.0, i_{cath} = 90 µA cm^{-2}, i_{corr} = 1.8 µA cm^{-2}. b) bulk pH = 10.0, i_{cath} = 90 µA cm^{-2}, i_{corr} = 1.8 µA cm^{-2}

Based on these results the different mechanisms of trench formation were compared and discussed in detail in [33]. The conventional explanation for trenching around IMC in literature was the formation of an alkaline region close to the particle/matrix interface [29, 34, 37, 44, 47]. A substantial body of observations and calculations supports this explanation and has been reviewed in Section 1.3. Within the framework of the model, there are two possible mechanisms for the breakdown of the passivity by local OH^- production: (a) the initial pH increase could be due to the low uniform passive dissolution current of the alloy matrix being counterbalanced by the high rates of oxygen reduction reaction localized to the IMC, or (b) it could be caused by still higher local ORR reaction rates on Cu-rich IMC supplying the current to balance the anodic dissolution of Al-Cu-Mg IMC as well as passive matrix dissolution. Either mechanism would account for net cathodes at Cu-rich IMC.

Nonetheless, some of the observations and calculations shown in [33] and summarized above were not compatible to a simple pH-induced corrosion description. Increased chloride content

led to an earlier onset of trench formation, and thus increased the rate of attack, but had only small effects on the ORR kinetics. Trench formation was observed to depend upon the type/composition of the copper-rich particle (i.e., Al-Cu-Mn-Fe vs. Al-Cu) despite very similar ORR kinetics on synthesized Cu-rich particles. If a pH increase near the particle was the sole cause, then only the ORR kinetics of the particles should matter, given equivalent mass transport conditions, and the two types of particles should behave similarly.

On the other hand, it was shown that compositional variations occurred amongst IMC of the same nominal type [32]. They can influence the rates of the ORR reduction, and cause differences between the model alloys used in the electrochemical studies and the behavior of the real particles in the alloy. In this context it is of interest that especially particles rich in Mn were reported to show little tendency to form trenches. This observation was explained by studies from the literature that investigated copper-free IMC containing Al, Fe, and Mn. Increases in Mn content rendered the OCP more negative and thus closer to the OCP of the matrix, and the rate of cathodic reactions such as ORR decreased strongly [470-472]. Compared to model alloys, the actual particles showed lower Mn values, a higher Fe/Mn ratio and more Al. The Cu content was very similar to the model alloy. The composition was not altered during immersion by dealloying, as Al-Cu-Fe-Mn particles were reported not to dealloy [473], and as the compositions before immersion were very similar. Nevertheless, because of the higher aluminum content as compared to the bulk analogue used in [32], a reduced cathodic reaction rate possibly contributes to a smaller tendency to form trenches. A reduced cathodic reaction rate would inhibit both the pH increase and the strength of galvanic coupling.

As an additional challenge to the theory of cathodic trenching the observation of trenching in both alkaline and acidic electrolytes was considered, even though calculations showed no significant local pH increase in either solution. This was exacerbated by the finding that the experimental cathodic currents found on bulk analogues were even lower than those used in the simulations, in agreement with more recent studies [35, 45]. Previous calculations and measurements of pH evolution for trenching [29, 34, 37] have mostly been restricted to neutral pH bulk solutions, in which a pH increase over the particle can occur. However, an inconsistency was found even at neutral pH. The trench widths observed experimentally were much narrower than the alkaline pH zones expected to form in neutral solution above particles, with observed trench widths between 1 and 2 μm, whereas the calculated elevated pH region extended out for greater than 50 μm, although natural convection at longer times than simulated may reduce these regions somewhat. In summary, several inconsistencies regarding the applicability of the cathodic trenching model were given [33].

An alternative model to pure cathodic trenching based on galvanic coupling causing preferential breakdown, or at least enhanced passive dissolution, at the interface particle/matrix was described. The metallurgy at the particle/matrix interface is complex and variable. It has been observed that a 500-nm wide dispersoid-free zone exists around coarse precipitates like large Al-Cu-Mn-Fe IMC, and a Cu-depleted zone in the matrix next to Al-Cu and Al-Cu-Mg particles [24]. A lower Cu content in the matrix will lower the pitting potential [42, 114], which in turn would promote pitting at these specific locations at the galvanic couple potentials associated with IMC. Such reduced pitting potentials would be independent of pH, but strongly dependent on the Cl^- content. Acid pit growth would further be enhanced by the proximity of a good cathodic site (the IMC) and a short ionic current path in solution. Hence, trenching caused by anodic dissolution would depend on the interaction amongst particle composition, the intermetallic compound crystal plane exposed, and microstructural and compositional details in the matrix close to each type of intermetallic. Such a model

explained the difference in susceptibility between different types of IMC observed in [33], relating them to a different degree of Cu depletion or some other compositional variation. Al-Cu-Mn-Fe compounds contain much less Cu than Al-Cu IMC, leading to less copper depletion in the surrounding matrix during their formation. Thus, Al-Cu IMC should be more susceptible to trenching than Al-Cu-Mn-Fe IMC, as observed. In addition, the observation of trenching in acidic electrolytes could be readily explained with an anodically controlled trenching model.

The size of the trenches was also related to the pit stability product $i_{pit}*r_{pit}$ [32] and used to explain why in part the corroded area was only three times as large as the IMC itself, despite an immersion time of 1 day. Similarly at alkaline pH the corroded area was 5-6 times that of the IMC itself, after an immersion time of about 8 h. The increase in corrosion rate as compared to near-neutral bulk solution in fact was related to the high bulk pH weakening the oxide, and especially to the more positive OCP [32]. Both should facilitate the breakdown of the oxide layer. In addition, to explain the temporal evolution of corrosion morphology, it was considered that particle clusters were present on the alloy (Figure 43b), and that the cathodic area available increased with removal of the surrounding matrix. On the other hand, undercutting of an IMC can stop trench growth.

In acidic solution, despite the increased contribution of general corrosion, localized corrosion still was observed. However, there was less trenching than in neutral and especially in alkaline solution, and localized corrosion was often connected with IMC clusters consisting of particles of different composition. The weaker growth of trenches in acidic solution was explained by the lower OCP (cmp. [32]) induced by oxide thinning and the overall observation of more uniform matrix etching [33].

An important finding regarding underpaint corrosion was the preservation of galvanic couple relationships in pH 3, 6, and 10 solutions with NaCl and that the basic modes of attack such as trenching, IMC corrosion and pitting were possible at all pH levels and may be accelerated at alkaline pH levels typical of underpaint corrosion cathode sites. These results meant that all of these forms of corrosion could be operative and observed under paint even if the underpaint corrosion site is acidic or alkaline.

3.2.3. CLSM for the study of underfilm corrosion [76]

The studies on epoxy-coated AA2024-T3 were the first in-situ studies, where three-dimensional changes of the substrate morphology were monitored through an organic coating. The aim of the studies was to ascertain whether or not the same morphology of attack seen on a bare (uncoated) surface [32, 33] containing native oxides occurs in a similar manner underneath an organic coating, to investigate the role of IMC during the early stages of blister formation and growth on epoxy-coated AA2024-T3, to enhance understanding of the effects of pH and chloride content of the external immersion solutions, especially considering that in underfilm corrosion occluded solution chemistries are formed, and to learn more about the blister growth mechanism.

Blister formation can occur as a consequence of underpaint corrosion by anodic undercutting [56, 57, 69, 89], corrosion product wedging [86], cathodic delamination [53, 58, 89], or by chemically induced loss of adhesion [93, 474] as well as osmotic effects [88, 90, 105]. In the mechanisms of underpaint corrosion processes, generally galvanic coupling between heterogeneous sites such as IMC and the matrix is involved. Anodic undermining and / or corrosion product wedging are the accepted processes for Al alloy coating delamination [56, 58]. Delamination and scribe creep on AA2024-T3 are accelerated by IMCs and replated Cu

[475]. The blistering and scribe creep corrosion on high purity Al in near neutral or slightly acidified environments is often slower than on AA2024-T3 substantiating the role of the heterogeneity and the role of replated copper for the cathodic reaction rate [475, 476]. The anode and cathode are likely in close proximity under a blistered coating that apparently has at least enough mechanical integrity to support some pressurization. Therefore, anything that the electrolyte does to damage the coating and allow easier mass transport of cathodic reactants, enable ionic current flow or promote loss of adhesion is a detrimental factor that is additional to the effect of the electrolyte composition on underpaint corrosion. The influence of electrolyte pH on coating deterioration has been discussed in Section 1.3 [85, 121].

For in-situ monitoring of underfilm corrosion, AA2024-T3 specimens (pretreatment cmp. Section 3.2.2) were spin-coated with an epoxy polyamide coating typical for aircraft primers. It was prepared by mixing equal weights of Epon Resin 1001-CX-75 with Epi-Cure 3115 Curing agent X73 (Fatty acid-polyethylenepolyamine based polyamide mixture), and adding 5% Butylcellosolve. The coating thickness was approximately 10 µm. Before immersion, the entire epoxy coated sample was masked off with another coating (XP2000 by Pyramid Plastics), except for a 2 x 2 mm exposure window, and cured for another day. This masking was done in order to restrict the area where a blister could form, and to thus increase the chance of finding it in its initial stage. Electrolytes used were 0.5 M NaCl, 0.5 M NaCl + 0.0032 M HCl (pH 2.5) and 0.1 M Na_2SO_4 (pH 3.5 or pH 3.0, adjusted with H_2SO_4). Stepwise scans of the entire surface (referred to as tile scans, at constant z) were performed periodically to detect the onset of corrosion. Corrosion then was monitored over time. After the end of the experiments, the coating was removed from some samples, the surface treated with 50% nitric acid in order to remove corrosion products [477], and the sample imaged with a 50x air objective (Epiplan-Neofluar) to examine the final surface morphology.

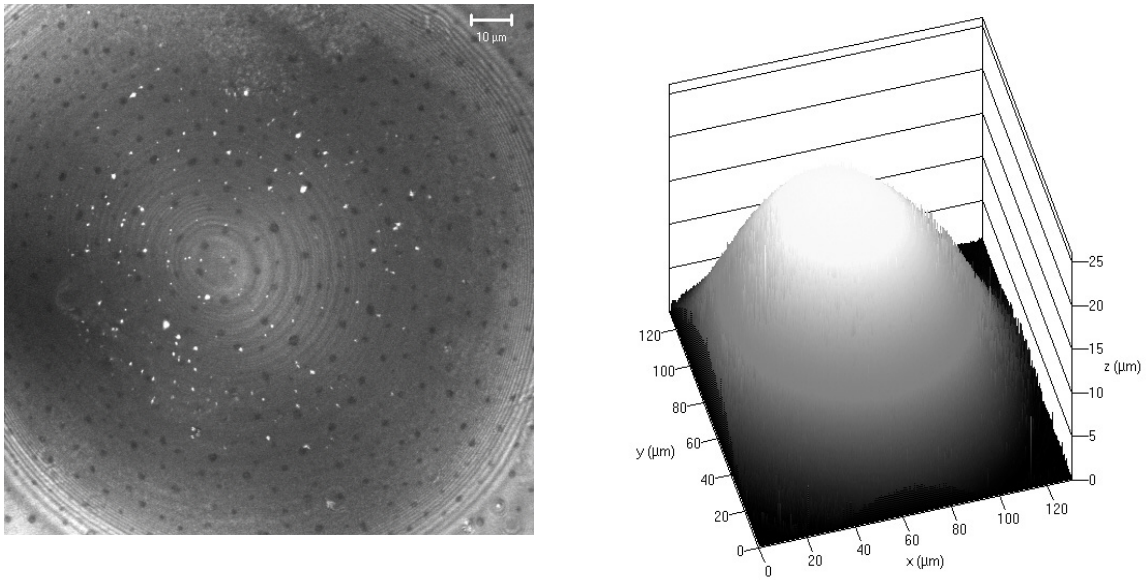

a) **b)**

Figure 46. CLSM image of the coating on top of a coating blister [74]: (a) 2D extended depth-of-focus image (b) 3D representation.

Under the settings used to image the highly reflective alloys surface underneath a transparent organic coating it is usually not possible to image the polymer coating directly. However, by carefully adjusting the z-range of the microscope to exclude monitoring of the alloy surface and brightness and contrast settings of the detector it was possible to image the polymer

coating directly. This is shown in Figure 46 for a coating blister formed on an AA2024-T3 specimen exposed to 0.5 M NaCl for 17 days. The small circular spots in Figure 46a were interpreted as some kind of coating defect. The ring structure was an artifact caused by the finite size of the pinhole and thus the finite thickness of each section of the specimen monitored.

Typical observations preceding the formation of a coating blister during exposure to 0.5 M NaCl are described in detail in [76]. OCP measured were in the range of -0.24 V to -0.27 V vs. SCE between 7 and 14 days of immersion. Figure 47 shows the same part of the surface before and after blister formation. Precorroded surface sites (A, B, and C in Figure 47, corroded during surface preparation before coating) showed no changes. After a blister had formed and grown to a size of 100 µm in diameter, OCP had decreased to -0.8 V vs. SCE, and several intermetallics (marked as 1, 2) were now severely corroded. In addition corrosion pits were found at positions where no IMC had been seen before (marked as 3, 4). Pits 3 and 4 were at least 4 µm deep. Corrosion products inside the pits as well as an IMC remnant (pit 2) prevented a more accurate determination of the pit depth. The pits 1-4 did not change during during the remaining time of immersion (111 hours).

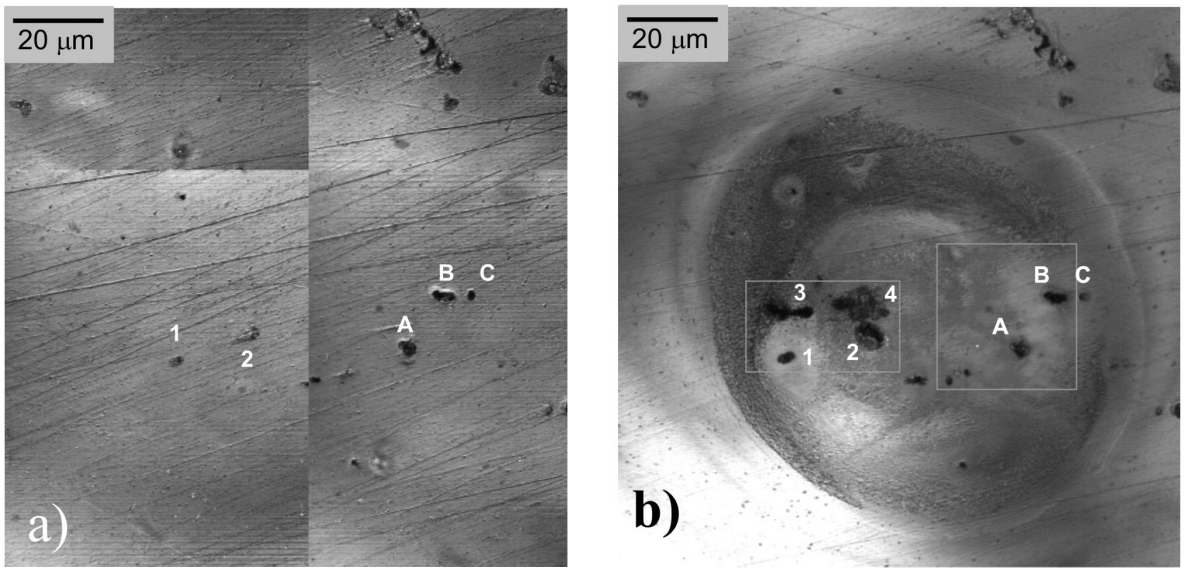

Figure 47. a) Selected area of epoxy-coated AA2024-T3 after 14 days, 3 h immersion in 0.5 M NaCl. The numbers indicate position of intermetallic compounds where pits formed later. A, B, and C indicate pits formed during polishing, before the alloy was coated. b) Extended depth-of-focus image of the blister grown on the same area after 16 days, 7 h of immersion. 1-4: Large pits formed on alloy surface (from [74]).

Corrosion of intermetallic particles also took place during blister growth. This was demonstrated for an intermetallic particle, which originally was located outside the blister and became part of the blister during its growth (cf. Figure 48). The bright diagonal stripes in Figure 48a gave an indication of how far the coating was delaminated from the substrate ("delamination front", moving from left to right), and where therefore the boundary of the blister was. Once the coating over the IMC particle was fully delaminated, corrosion started at the outer edge of the particle all along its circumference and expanded into the matrix. It appeared that in this stage only the matrix had been attacked, but not the particle itself. With time, several corrosion features in the matrix coalesced, and the particle was completely dissolved, while new pits formed at nearby locations. There had been no large IMCs at these sites, but sometimes indications for very small particles (< 1 µm diameter). Finally, most of these sites interconnected, forming one large pit.

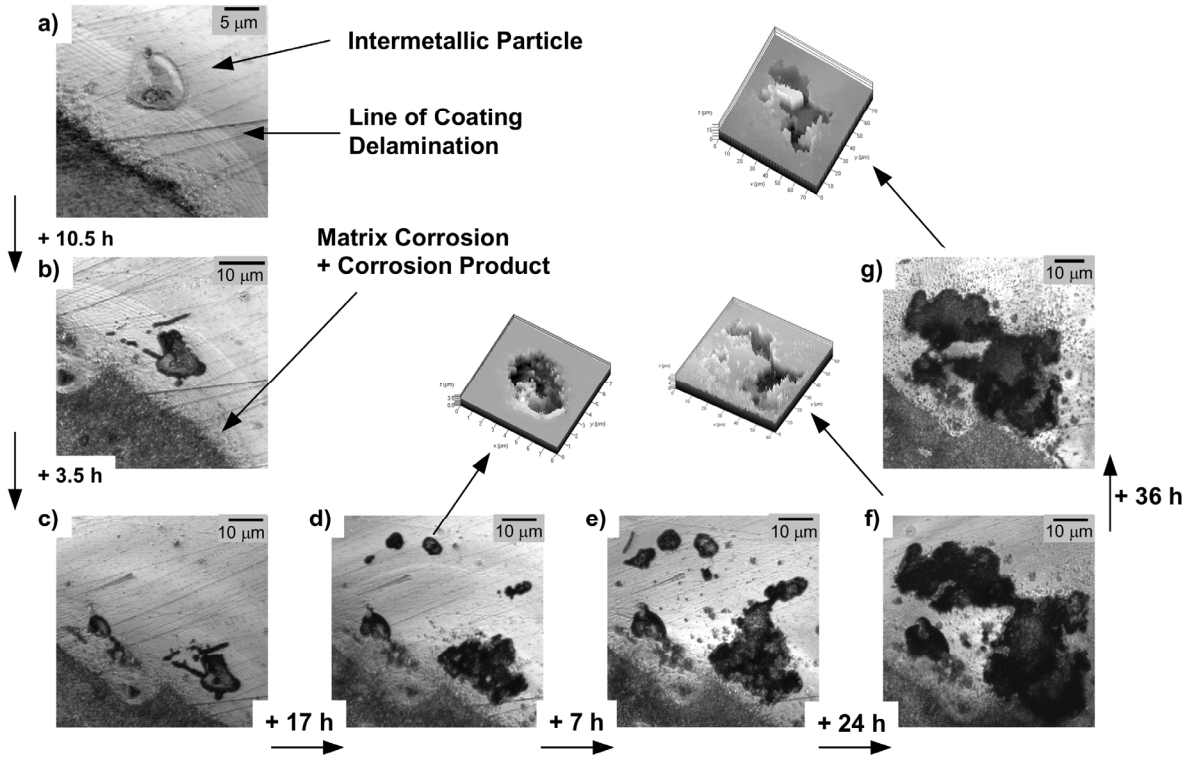

Figure 48. Progressive corrosion starting at an intermetallic particle which becomes exposed to occluded blister solution during blister growth in 0.5 M NaCl [76]. Total period of observation: 98 h.

Besides corrosion of intermetallic particles and pit formation, roughening of the substrate and the deposition of corrosion products (including Cu replating) were also reported. The roughened area was very close to the delamination front, only 10 µm away at some locations. Even very close to the blister edge, where delamination still may have been incomplete, corrosion products were found. The blister radius was reported to increase by more than 1 µm/h in the early stages of blister growth and 0.51 ± 0.04 µm/h in the later stages of blister growth. A maximum delamination rate of 2 µm/h was found. The changes in corroded area followed the ones in delaminated area closely. With increasing blister size, growth rates slowed down.

Blister formation and growth in neutral NaCl involved the corrosion of intermetallic compounds in the early stages and during blister growth, the formation of pits in the alloy matrix, and substrate roughening within the growing blister due to matrix dissolution and corrosion product deposition. The roughened area had a reddish appearance and was very close to the delamination front of the growing blister.

At a low pH of ~ 2.5, already after 1 day 23 hours of immersion a small blister of about 17 µm in length had formed (cf. Figure 49). Within this blister, there was an intermetallic particle which was now pitted, but had not been corroded before blister formation. For further growth, IMC corrosion was not important, even though some pits were found within the blister. Subsequently, the Al matrix started roughening close to the original blister site (Figure 50). In parallel delamination became visible. The delaminated area exceeded the corroded area in size. The original blister seemed to have ceased growing. Later, close by new spots of matrix roughening occurred, causing delamination, leading finally to a rather complex pattern. Monitoring of the coating height over the delaminated area showed that these individual

corroding areas led to several blister lobes, which were not fully interconnected. In the end, one large elongated blister was obtained. No matrix roughening took place at surface positions remote from the blister.

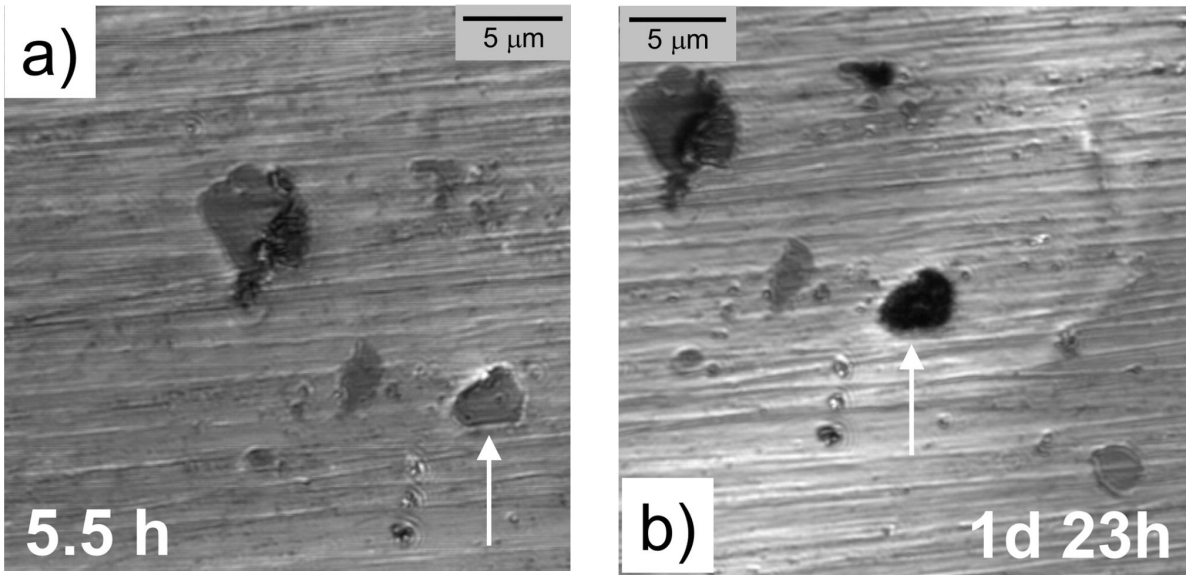

Figure 49. 2D extended depth-of-focus images of epoxy-coated AA2024 exposed to 0.5 M NaCl, pH 2.5 before (a) and at early stage of blister formation (b). Arrow: IMC, which corroded upon blister formation. Numbers in images: Total Immersion Time (from [76]).

Once formed, the roughened areas expanded rapidly with rates were between 3-4 μm/h. Figure 51 shows the area close to the original blister site (arrow) after removal of corrosion products. Besides unattacked surface regions near the center and the roughened regions, curved bands were visible, in which the material loss was much larger than that of the roughened regions, as seen in the 3D topographic representation of the area marked by a square. The depth of the band was little more than 1 μm. The amount of material loss in the corroded areas, except from some pits, was very small, between a few hundred nm and ~ 1 μm in depth normal to the plane of the original surface. Clusters of uncorroded Al-Cu-Fe-Mn IMCs were found also inside the blister, surrounded by corroded area. The CLSM data taken after stripping of the coating and corrosion product removal showed that the IMCs were elevated by 800 nm compared to the surrounding corroded area.

CLSM studies were also performed in order to gather further information about the rapid coating failure seen in acidic sulfate solutions (cmp. Sections 2.2.1 and 2.2.3). OCP was monitored continuously during immersion of an epoxy-coated AA2024-T3 specimen in 0.1 M Na_2SO_4 with pH adjusted to 3.5. The potential soon stabilized at about –0.3 V vs. SCE. At early immersion times the first changes were observed at substrate inhomogeneities like IMC compounds and IMC sites, which showed some corrosion damage due to the polishing procedure. These changes mainly consisted in the formation of rings or irregularly formed boundaries at these sites.

A blister was observed after only 17 h of immersion, and was about 2 μm in height. It had formed at one of the sites showing substrate roughening. Subsequently, within a very short time, blisters started to form over a large area of the sample, much faster than in the acidic chloride solution. The coating failure was accompanied by a continuous drop in OCP, finally stabilizing at -0.6 V. In wide areas, delamination was followed by further substrate roughening. Blister growth rates larger than 5-6 μm/h were found. After coating and corrosion product removal, widespread corrosion damage was seen in CLSM. However, the overall

depth of the corrosion damage was too shallow to be measured with CLSM (<100 nm material loss), was caused after delamination had occurred, and must be considered as regular general corrosion of aluminum alloy in an acidic medium.

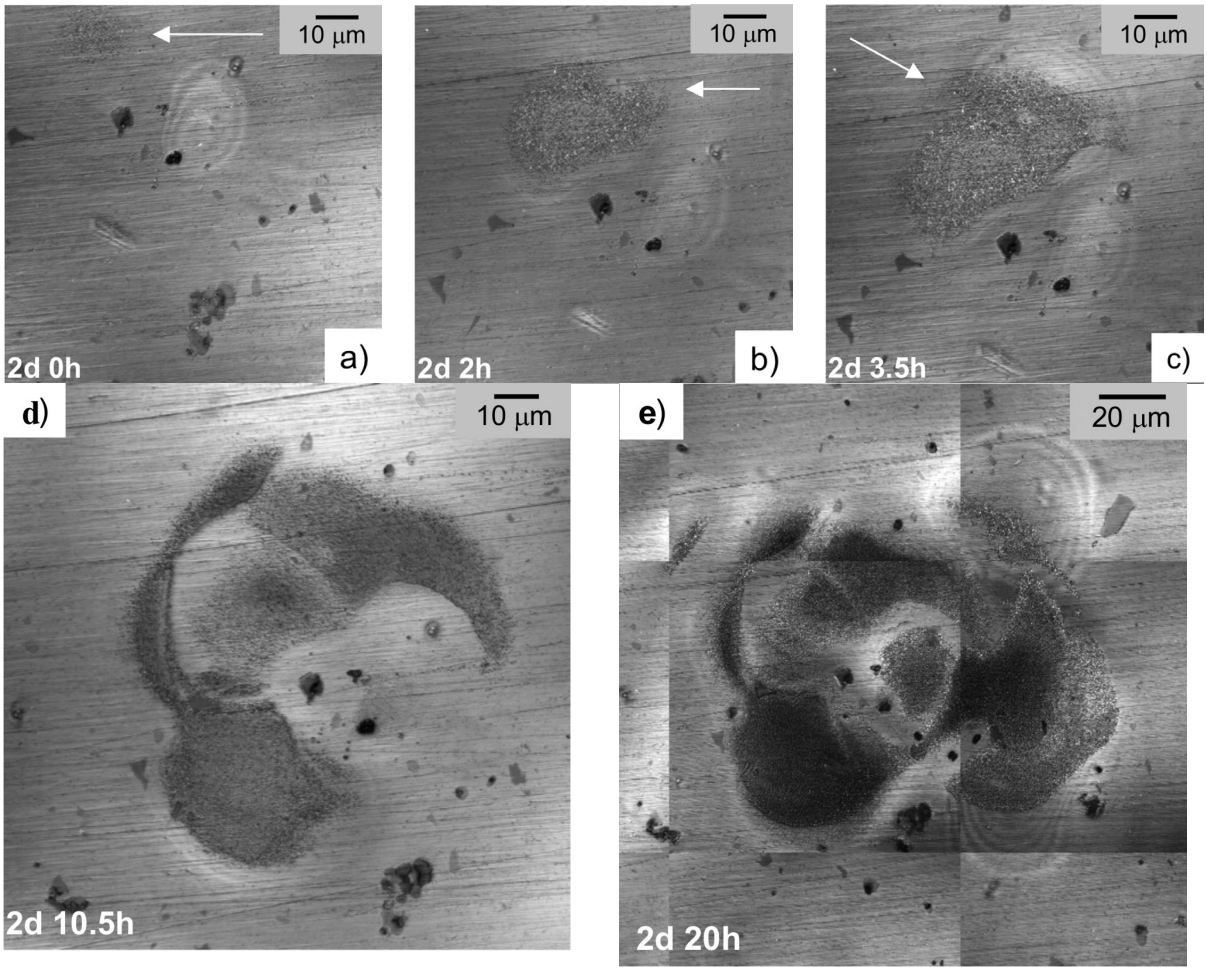

Figure 50. Progress of matrix attack close to original blister on epoxy-coated AA2024-T3 exposed to 0.5 M NaCl, pH 2.5, causing coating delaminations [76]. Numbers in images: Total Immersion Time.

Large-scale coating delamination in acids has been reported in literature, but for much lower pH [474]. It was related to hydrogen evolution destroying the bonds between metal surface and coating. The apparent diffusion coefficient of sulfate at pH 3.5 is smaller than that of chloride at pH 3.0 by a factor of 5, and the ion diffusion coefficients increase with decreasing pH [121]. Therefore one expects more acidic conditions and larger ionic concentrations at the interface for the chloride solution at pH 2.5 than for the sulfate solution at pH 3.5. Corrosivity of the bulk solution alone therefore cannot directly explain the faster coating failure in sulfate solutions. Matrix etching was observed on bare AA2024-T3 in a solution of 0.1 M Na_2SO_4 + 0.005 M NaCl, adjusted to pH 3.0 [33]. It has been reported in the literature that sulfate behaves aggressively towards Cu-bearing IMC in AA2024-T3 [193, 478]. Both effects and a detrimental influence of sulfate species on the adhesion of the coating could contribute to the failure mode in sulfate solutions.

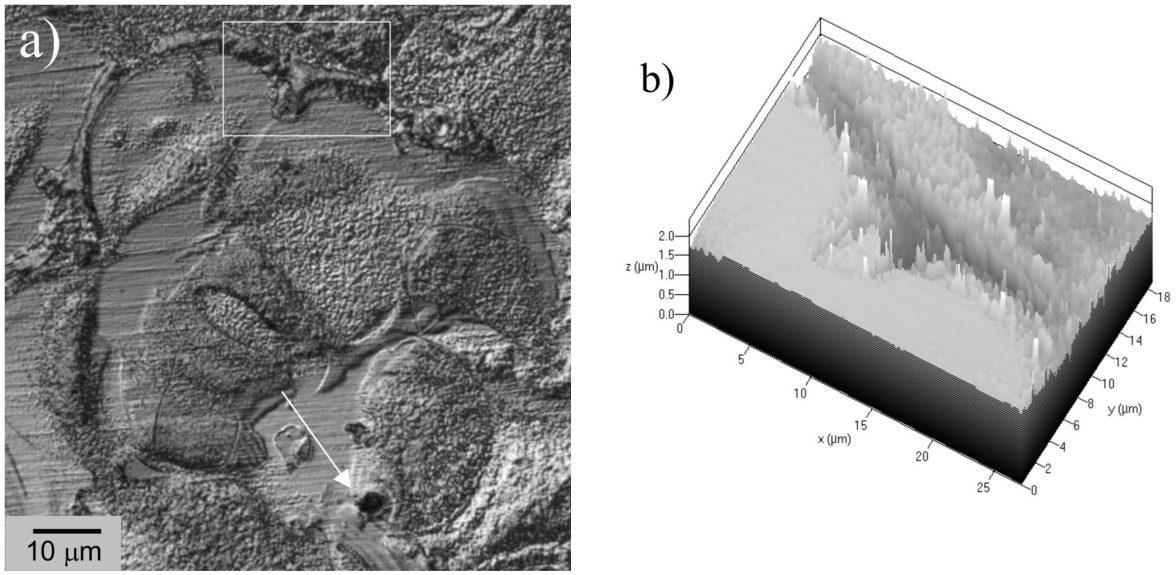

Figure 51. Part of corroded area under blister from Figure 50 after coating and corrosion product removal [76]: a) 2D extended depth-of-focus. Arrow: Pit of initial blister site. b) 3D topographic view of area marked by rectangle in a).

Coating delamination in acidic sulfate solutions was preceded by a couple of steps occurring on a rather fast time scale. The first step seemed to be the localized formation of water pockets at intermetallic compound phases and at precorroded sites that may already be considered as small blisters. The next step was the local substrate roughening possibly stemming from general corrosion of the matrix, similar to the situation in acidic NaCl solutions. Corrosion at these local sites was expected to increase the ionic strength, and further accelerate the local water uptake, in turn fostering delamination by mechanical processes and promote blister growth by both mechanical and electrochemical processes. The formation of blisters at sites with little or no visible corrosion and the rapid spreading of delamination indicated a widespread loss of adhesion. The observation of the localized collection of water and this widespread coating failure were explained by osmotic blistering in combination with superficial corrosion of the alloy matrix and loss of adhesive strength caused by sulfate species.

The blisters on specimens exposed to neutral or acidic 0.5 M NaCl showed several corrosion features similar to those seen in the studies of bare AA2024-T3 [32, 33]: Pit formation at intermetallic particles, pit formation in the matrix, and possibly trenching. In addition there were particles in the blister that were not attacked at all. Some of those could be identified as Al-Cu-Fe-Mn particles, which are not expected to corrode at the potentials typically measured in coating blisters.

It has been established that the first steps of blister formation are water uptake and the creation of conductive pathways to the substrate [53, 54]. Once corrosive ions reach the interface they can initiate corrosion. For AA2024-T3 it was shown that in near-neutral sodium sulfate solution which is not very corrosive, no blister formation took place [85]. Therefore corrosion appears to be required for blister formation. For a heterogeneous alloy like AA2024-T3, the susceptibility to corrosion is very different across the surface. Al-Cu-Mg particles are much more prone to corrosion than the matrix, and there are many of these particles on the alloy surface [22, 23]. Therefore it was reasonable to expect that for exposure to neutral bulk solutions, blister formation is preferentially related to Al-Cu-Mg corrosion. The in-situ CLSM data showing IMC corrosion during the early stages of blister formation in

NaCl supported this assumption. The actual blister initiation was not seen in [76]. Therefore it could not be ruled out that IMC corrosion happened just after blister formation. Another point considered was the location of the cathodic reaction, which is not supported very well by the oxide on the alloy matrix [25, 56, 58, 114, 115]. Therefore the presence of a cathodic IMC particle might also be favorable for blister initiation from the galvanic cell perspective.

Even upon exposure to near-neutral NaCl solutions, the solution occluded in the blister was high in chloride content and low in pH. IMC corrosion continued to be important during blister growth in near-neutral bulk solution (Figure 48). Once the particles newly incorporated into the blister were completely exposed to the aggressive electrolyte, they corroded. The formation of large, stable pits underneath coatings was explained by particle clusters -similar to findings for bare AA2024-T3 [23] - that influenced the further growth of the blister, especially with respect to growth direction and symmetry. On the other hand, evidence was also presented in [76] that a lack of corrodible IMC can contribute to the death of the blister. Therefore, either sufficiently aggressive environmental conditions (local pH and/or local $c(Cl^-)$) and/or easily corrodible IMC were considered necessary for a blister to keep growing.

In NaCl adjusted to pH 2.5, neither IMC corrosion nor the distribution of IMC particles was important to the spreading of coating delamination. These conditions were so aggressive that general corrosion controlled blister growth. In 0.1 M Na_2SO_4 + 0.005 M NaCl, adjusted to pH 3.5, there was no proof that delamination was connected to IMC corrosion at all. However, IMC sites were preferential sites for initial coating delamination and therefore are at least indirectly involved in blister formation.

Besides IMC corrosion, the general attack of the matrix even for near-neutral bulk solutions was emphasized. The general attack was not due only to low pH and high chloride concentration under these immersion conditions, but also to Cu replating. Replated Cu allows cathodic reactions to occur more rapidly [114, 475], and thus fosters widespread corrosion of the underlying alloy. This conclusion was in agreement with observations from blister autopsy showing that the corrosion damage is usually most severe under the regions of Cu replating [85].

In acidic NaCl solutions the mechanism of blister growth was controlled mainly by matrix attack with removal of about 1 μm of alloy within one week of corrosion. The strange patterns of matrix attack shown in Figure 50 were explained by the formation of the original blister weakening the coating in its proximity, and the acidic bulk solution attacking the coating from above. Rapidly spreading matrix attack and coating delamination can take place once low pH solution reaches the alloy/coating interface. The mechanism by which the weakening of the coating happened on a site specific basis was not clear. The formation of these sites did not require the presence of IMC, at least none that were larger than 1 μm in diameter (and therefore easily visible in CLSM). Therefore, enhanced oxygen reduction reaction at cathodic IMC in these areas weakening the coating was ruled out. Weakening was rather explained by stresses in the coating or chemically weakened adhesion. The formation of relatively deep and narrow canyons on the sample was related to a local slowing of delamination, and the development of a situation similar to crevice corrosion.

In NaCl solutions there was strong evidence that anodic undermining and / or corrosion product wedging drove the delamination reaction: The deposition of corrosion products close to the delamination front, the tracking of delaminated area and blistered area, and the close correlation between onset of corrosion reaction and visible delamination. Anodic undermining is well established as a mechanism in the case of filiform corrosion of Al-base materials [56,

58], and results published in [76] provided direct experimental evidence in the case of blistering on AA2024-T3.

The question why rapid adhesion loss was favored in acidic sulfate solutions as opposed to acidic chloride solutions was not fully explained. Some considerations related to differences in Cu replating in chloride and sulfate environment were made. It was considered that chloride increases the exchange current density for Cu deposition strongly, probably due to Cl-bridges changing the mechanism from outer to inner electron transfer or by providing an alternative reaction path involving CuCl [358, 375]. At high overpotentials typical for corrosion potentials of AA2024-T3, mass transport controlled deposition and therefore dendritic or powdery deposits are expected [203, 374, 375, 479]. However, Obispo et al. also stated that in acidic solutions, deposits are less dendritic and loosely structured, but more nodular, and that copper films grown from sulfate solutions on aluminum films look identical [479]. Some preliminary experiments on Cu electrodeposition on AA2024-T3 by Schneider showed more compact deposits in sulfate solutions as long as the overpotential was not too large. At electrode potentials of –0.65 V vs. SCE dendritic deposition was observed for sulfate as well. The intermediate increase in OCP was indicative of an increase in cathodic area [56], which may be caused by coating delamination at cathodic IMC or on replated copper. In fact it was reported elsewhere [121], that the interfacial resistance of a coated AA2024-T3 sample in 0.1 M Na_2SO_4 at pH 3.5 decreased strongly while the potential was still increasing, indicating a loss of adhesion. Further studies are therefore required.

The time required for a blister to form decreased in the order 0.5 M NaCl (pH ~ 6.5)> 0.5 M NaCl (pH ~ 2.5) > 0.1 M Na_2SO_4 (pH $\leq$ 3.5), and growth rates increased in the same order. These data were in agreement with observations from electrochemical impedance spectroscopy (Figure 9). For neutral Cl^- a long series of events must take place to get blistering and blister growth starting with water ingress and local corrosion which eventually causes enough wedging and anodic undercutting. For the purely chloride based-electrolytes, the increase in corrosion rate with decreasing pH was directly related to the decomposition of the polymer by the interaction with the acid, and by the instability of the passive oxide in low pH solution detrimentally affecting the adhesion, and was also connected to a change in corrosion mechanism. In acidic sulfate solution, there seemed to be a rapid ingress of solution at many spots in the coating at the same time, and a massive loss in adhesion.

3.3. Further microscopy techniques

Recently, fluorescent probes have been introduced in biological sciences in order to measure pH and ion concentrations / gradients in living cells by confocal microscopy. Such fluorescent dyes can also be incorporated in organic coatings in order to study the local change in pH underneath the coating during corrosion, to gain information on the uptake of protons (or hydroxide) by the coating, and on the formation of ionically conductive channels. Fluorescent molecules have been applied to study local reactivity at electrodes and pH changes during corrosion of bare aluminum [480-483], as already discussed above. The water interaction with an epoxy coating has been studied using fluorescence without addition of a dye [484]. There are only few studies where fluorescent dyes have been applied to a metal or alloy surface before/after coating application or have been directly incorporated into the coating [485-488]. One study deals with pH changes during underfilm corrosion of aluminum alloys [487], others monitor metal cations released during underfilm corrosion [486, 488], and another one the entry of chloride ions into the coating [485].

Results from the NSOM technique have been included in the discussion above. In NSOM, laser light is transferred to a sample point via an optical fibre [454, 489]. Because the

diameter of the optical fibre can be made much smaller than the optical wavelength, the technique beats the diffraction limit of conventional optical microscopy techniques including CLSM. Instead of scanning the laser beam across the surface, the probe is scanned in x,y-direction. Combination with a shear force feedback with a tuning fork control permits to position the probe as close as 10 nm above the sample, and provides the z-information. Lateral optical resolutions of 60 nm have been reported with this technique, and 5-10 nm appear feasible [489]. The method can also be combined with fluorescence microscopy, SECM and other techniques.

The formation of chromate conversion coatings (CCC), which is still the surface pretreatment technique providing best corrosion protection for aluminum alloys in aerospace applications, and the mechanism of corrosion protection by these coatings has been one example, where a number of different techniques applied in addition to electrochemical studies has been successfully applied to provide mechanistic understanding [43, 114, 115, 117, 118, 490-501]. A CCC coating bath consists mainly of dichromate, $Fe(CN)_6^{3-}$, and fluoride ions at pH 1-2 [115]. The hydrofluoric acid removes oxide layers from the Al alloy and $Fe(CN)_6^{3-}$ serves as a catalyst for the reduction of Cr(VI) by Al. The CCC coating consists of a Cr(III) oxide/hydroxide film with covalently bound chromate(VI) groups attached to. Cr(VI) can desorb, and in case of surface damage and pit formation be relased and repair the damage. Techniques applied for mechanistic studies included surface analytical methods like SIMS, XANES, EXAFS [117, 118], infrared and Raman spectroscopies [491, 492, 501], UV-VIS spectroscopy [496], chemical mapping by EDX, CLSM [117] and also Raman microscopy [492, 493, 501]. The latter technique permitted monitoring of the reaction products in a pit after interaction with Cr(VI) released from the CCC coating. The strength of Raman microscopy is to provide actual information about chemical bonds in-situ, whereas other techniques are operated ex-situ or provide only information about elemental compositions. This allowed to observe the reduction of Cr(VI) in corrosion pit and the formation of mixed oxides [498, 501].

3.4. Local electrochemical properties

Besides the monitoring of three-dimensional topographic and chemical changes, and the measurement and mapping of local electrochemical properties with microcapillary-based techniques, there are some further approaches for local monitoring of electrochemical properties of heterogeneous surfaces. Out of these three will be presented here very briefly, because they are of great importance for corrosion studies on heterogeneous and especially coated Al alloys: the scanning vibrating electrode technique, local electrochemical impedance spectroscopy and the scanning Kelvin probe. These methods permit to map local current distributions and thus reactivities, local impedance and local corrosion potential. Another relevant technique is scanning electrochemical microscopy, where typically a disc type UME is scanned at close distance above the substrate surface. Potential of UME and of the substrate are controlled independently using a bipotentiostat, and the solution contains an electroactive species that can be reduced or oxidized at the UME tip, and provides the actual imaging signal. Over insulating surfaces depletion of electroactive species will take place, whereas over conducting surfaces a feedback mechanism can be established by regenerating the species consumed at the tip. On the other hand the tip can also serve as a collector to detect species generated at the substrate, or be used for surface patterning [502, 503]. Further details can be found in the books by Bard and co-authors [5, 504]. Applications in corrosion science have been reviewed in [505, 506]. The method was also applied to study the electrochemical reactivity at Al alloy surfaces [507-509].

3.4.1. Scanning vibrating electrode technique (SVET)

It has been shown that in corrosion cathodic and anodic reactions are taking place at the same time on one electrode. In the absence of an externally imposed potential the total current averaged over the entire sample is zero. However, the local current varies in magnitude and sign depending on the composition of the specimen studied, the immersion conditions, the atmosphere, and so on. Especially in the case of corrosion of heterogeneous alloys, with any metal combination where galvanic coupling occurs, and in underpaint corrosion there will be distinct local anodic and cathodic sites. This galvanic coupling includes electron flow through the substrate from the anode to the cathode. The circuit is closed by ionic currents flowing through the electrolyte between anodic and cathodic sites, leading to hemispherical equipotential surfaces in the electrolyte [58]. The scanning vibrating electrode technique provides a convenient method to measure these local ionic currents and thereby to identify local anodes and cathodes. It is a modification of the scanning reference electrode technique (SRET): In SRET a 5 electrode setup is used: the specimen (WE), a regular counter and reference electrode, and a local probe consisting of two parallel wires vertically discplaced from each other (i.e. the tip of one wire is at a distance z_1 above the surface and the other one at a distance z_2) [58]. If at the probe position a local ionic current exists, a potential difference caused by the ohmic potential drop in the electrolyte will be measured between the probes. This potential difference can be analyzed in sign and magnitude, using the known electrolyte resistance, to determine direction and magnitude of the local currents. In SVET, the two wire probe is replaced by a single microelectrode tip vibrating in direction normal to the surface, and from the probe potential variation with time (and thus distance from the surface) local currents can be determined. SVET provides a better lateral resolution compared to SRET, probe preparation is more reproducible, and current sensitivity is better [58]. Scanning of the probe in x,y-direction then permits to map the current distribution. In the case of underfilm corrosion local ionic current flow can take place underneath the coating. As long as the current lines are not penetrating the coating and enter the solution, SVET will not give a realistic picture of the local anodic and cathodic processes. The general difficulty to monitor corrosion activity under highly resistive coatings has been emphasized [58]. Typically SVET measurements are calibrated in electrolyte using a point type current source with controlled current [58]. One of the general advantages of the method is also that it is considered as non perturbing. However, McMurray et al. showed that vibration amplitudes > 25 µm can cause jet formation and local thinning of the diffusion layer, thus increasing currents due to diffusion limited oxygen reduction and introducing artifacts in the measurements [510].

A typical example for SVET measurements on coating blisters on Al alloys from a proceedings paper by Williams, Schneider and Kelly [112] is given in Figure 52. Optical microscopy images of two blisters are displayed together with the corresponding color-coded SVET maps. Deposits in the blister are connected to cathodic activity.

A recent very short review on SVET even more focused of LEIS has been given by Rossi et al. [511]. For their equipment they specify the ability to detect local current events down to 5 µA cm^{-2}. The fundamentals of SVET and SRET were also summarized by Grundmeier et al. [58]. Applications like pitting corrosion of Al, coating delamination and detection of defects in welds were summarized in [63]. He et al. applied SVET to study corrosion behaviour of chromate-epoxy-coated steel and AA2024-T3 after scribing [64]. On bare specimen they found one or several regions of anodic activity with currents between 100 and 200 µA cm^{-2}. For AA2024-T3 dynamic behaviour and appearance and disappearance of anodic sites was observed. With plain epoxy coating anodic and cathodic reactions were confined to the defect. For chromated coatings, cathodic reactions were found to take place homogeneously across the coating for steel, and chromate seemed not to induce repassivation in the scribe.

Subsequently the authors performed similar studies on conducting polymer coated steel and AA2024 [65, 512]. Worsley et al. studied cut edge corrosion of organically coated hot dip Zn galvanized steel using SVET [66]. They found that coatings of different thickness on both sides create a differential aeration cell, with the thick coated side being the anode and the thin one the cathode. Some cathodic activity was spread across the panel surface. Connection to an external cathode converted both Zn layers into anodes. Ogle et al. studied the mechanism of self-healing of galvanized steel and found cathodic inhibition by precipitation of Zn-based corrosion products on cathodic sites [513]. Williams and McMurray applied SVET to the study of localized corrosion of 99.9% Mg, where they found that film free cathodic areas evolving hydrogen controlled corrosion rate, and were galvanically coupled with the intact Mg surface [514]. N. Murer et al. performed SVET studies on bimetallic galvanic couples of Al and Al4%Cu in phosphate buffer after activation by a droplet of HF [515]. The aim of their studies was to compare experimental data with numerical finite element simulations as a preliminary work for modelling coupling in real heterogeneous Al alloys. However SVET and microcapillary data turned out to be insufficient to provide unequivocal input parameters for numerical modelling.

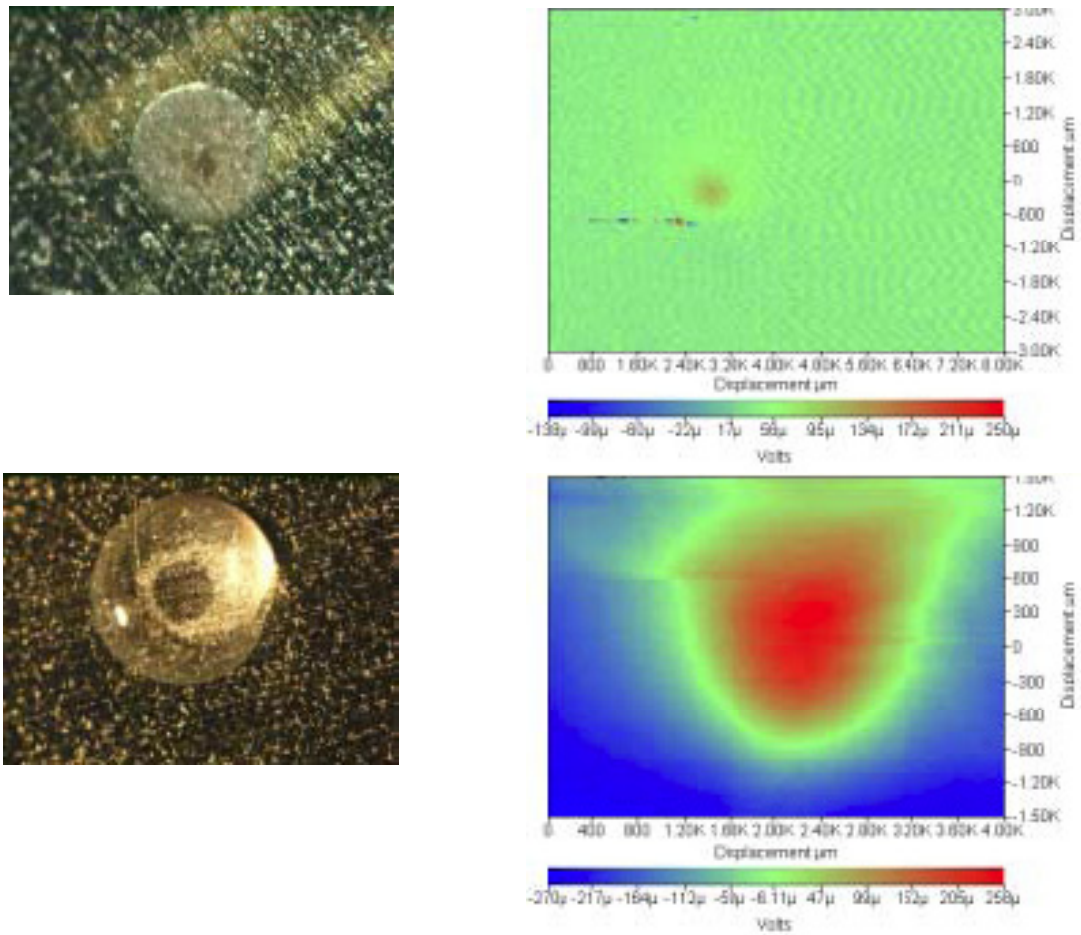

Figure 52. Coating blisters on AA1100-H14 and corresponding SVET maps [112]. Reddish colors indicate cathodic activity, whereas bluish indicates anodic activity.

3.4.2. LEIS and LEIM

Local Electrochemical Impedance Spectroscopy and local electrochemical impedance mapping are based on the techniques already known from SRET and SVET. The method was introduced first by Lillard et al. using the bielectrode (SRET) approach and tested with Al and Al/Mo model electrodes [325]. A sinusoidal alternating voltage is applied globally between the substrate and reference electrode using a global counter electrode, and the alternating

current is measured locally using local current probe. From the ratio of local current / global ac voltage the local impedance can be calculated. Variation of frequency permits measuring local impedance spectra whereas scanning of a larger area at a fixed frequency permits impedance mapping. Bayet at al. adapted the more reproducible SVET for LEIS measurements [322, 516]. The same authors later performed a study on the reliability of such measurements combining experiments and numerical simulation and concluded that reliable local impedance data require both current and potential to be measured on a local scale [323]. Otherwise severe artifacts were possible. Zou and Thierry applied the technique to epoxy-coated carbon steel contaminated with NaCl before coating [306]. Blister formation could be localized by LEIS by the change in coating capacitance registered. Increased activity due to coating rupture was clearly visible. Wittmann et al. used coatings on steel and AA5182 with intentionally induced defects in order to test the capability of LEIS/LEIM for detection of coating defects [324]. They were able to visualize defects as different as spots where machine oil had been absorbed in the coating, pinholes, gas bubbles, and scribes. Mierisch and Taylor applied LEIS and LEIM to organically coated AA2024-T3 specimens in NaCl solutions [68]. They performed LEIM scans at a frequency of 700 Hz, and plotted the admittance as function of position. In the early stage of underfilm corrosion, prior to blister formation, they observed a local depression in the admittance plot at the future blister site, and suggested water nucleation or oxide film thickening as possible origin. Later the blister revealed itself as an admittance peak that however showed fluctuations in size, changes in width, and trenches at the outer rim. Size fluctuations were explained by changes in the electrochemical activity within the blisters. Subsequently numerical simulations and test measurements with gold disc microelectrodes were performed in order to explore the resolution limits of the system used and to identify possible sources of artifacts. It was concluded that the observed depression in admittance was real, whereas the trenches at the rim could be artifacts [119]. Philippe et al. used a local microreference electrode for LEIS measurements on coated galvanized steel with a 250 μm laser ablated hole in the coating [69]. They recorded local spectra above defect and intact coating and compared it to global measurements. Impedance mapping clearly revealed the coating defect and underfilm corrosion spreading from it. From the data the behaviour of defect and intact coating could be separated, similar to the findings by Schneider and Kelly [72]. In further work, LEIS was applied to corrosion of e.g. Mg alloys and to different organic coatings [517, 518].

3.4.3. Scanning Kelvin Probe

The Kelvin probe was introduced to corrosion science by Stratmann for the measurement of corrosion potentials [59, 519-521], and converted into a local probe [103]. The scanning Kelvin probe (SKP) consists of a metallic microprobe serving as a type of reference electrode. The probe is arranged above the surface of interest outside the electrolyte (i.e. separated by air), and electronically connected to the WE substrate by a wire. This assures equality of the electrochemical potential of the electrons both in the WE substrate and in the reference electrode. Therefore the WE will be charged with respect to the Kelvin probe, and a Volta potential difference develops between the surface of the electrolyte covered WE and the probe. A vertical sinusoidal oscillation of the probe causes a variation of the capacitance between the two electrodes, and therefore induces current flow. Introduction of an external voltage source in the external circuit can be used to decrease the current to zero, and then the applied external voltage is equal to the Volta potential difference. It was shown that this Volta potential difference representing the work function of the electrolyte covered WE is under certain conditions proportional to the corrosion potential. Therefore the technique permits to measure local corrosion potentials. The lateral resolution of the original technique is around 100 μm [40]. This method has not only been applied to study atmospheric corrosion, but its real strength arose from its capability in corrosion studies of coated metals: Here the potential

at the buried polymer/metal interface can be measured, and the progress of delamination processes can be studied [58, 60-62, 71, 73, 103, 107, 522]. Detailed studies on the delamination of polymeric coatings on steel and electrogalvanized steel were published in literature, where delamination was started at a defect (coating-free area exposed to electrolyte), and change in Volta-potential with time, position and external atmosphere permitted to draw conclusions about cation migration underneath the coating and the mechanism of coating deterioration at the interface metal/polymer [60-62, 71, 108]. It also was applied to filiform corrosion [107, 523, 524]. An increased lateral resolution (~ 100 nm) can be obtained by using a metal coated AFM tip as Kelvin probe. This variant has been named Scanning Kelvin Probe Force Microscopy (SKPFM) [28, 40] and permitted monitoring of the relative nobility of intermetallic phases in aluminum alloys and studies on the role of the IMC on their localized corrosion behaviour [28, 40, 295, 525-527].

4. Synopsis

In this review methods have been presented capable of elucidating the manifold and complex processes taking place during electrochemical processes in materials science. Two different fields were selected, the corrosion of aluminum alloys and sonoelectrochemical processes with an emphasis on metal deposition. In addition, some studies on conducting polymers were presented in order to further demonstrate the benefits of the electrochemical quartz crystal microbalance technique.

In aluminum alloys a complex microstructure causes a strong heterogeneity in the electrochemical properties. The oxygen reduction reaction takes place preferentially on certain intermetallic compound like Al_2Cu or Al-Cu-Fe-Mn compounds. Other intermetallic compounds are prone to dealloying corrosion, and dissolve at the open circuit potential of the alloy at high rates. The galvanic coupling of the noble phases with the Al matrix introduce corrosion like the so-called trenching, which has been shown to be in fact circumferential pitting. The dealloying of e.g. Al-Cu-Mg leaves porous Cu remnants which themselves may act thereafter as local cathodes – evidence for this was given in the work of Büchler. Both matrix corrosion and Al-Cu-Mg dealloying can contribute to a surface enrichment by copper, in one case by surface clustering, in the other case by Cu replating, and therefore alter the surface composition of the alloy. This has been shown in this work to be especially detrimental in the case of underfilm corrosion, where massive Cu replating accelerate general corrosion of the underlying alloy. Corrosion of the bare alloy will release ions into the neighboring solution and in the trenches and pits formed on the surface. Within pits and crevices, and to a lesser extent above a corroding Al alloy surface, Al ions and complexes will be released into the solution, decreasing pH. Above the cathodic phases, pH will increase. The limited pH range where the protective oxide on Al is stable then can contribute to acceleration of the reactions. Clusters of cathodic particles can carry sufficient cathodic current to stabilize pits growth nearby and to induce stable pitting. Therefore, the anodic and cathodic reactions at a heterogeneous Al alloy surface

- are connected to the microstructure and especially the composition, number density, and distribution of intermetallic compound phases in the alloy surfaces;
- are strongly time dependent due to alteration of surface composition and morphology;
- induce chemical changes in the electrolyte phase influencing corrosion propagation as well.

The information content of standard electrochemical characterization techniques, even if combined with post-dead SEM and surface characterization, is insufficient for quantitative understanding of these processes. Three different approaches for solving this problem were

presented in this review, based on examples of the author's own work and on the work of others:

- The first approach is the use of model compounds: This includes on the one hand model alloys mimicking the composition of individual phases in the true alloy. Then standard electrochemical techniques can be applied to these compounds in order to understand their corrosion behavior including their capability to support cathodic reactions in different environments, their corrosion rate at the open circuit potential, and their pitting potentials. On the other hand photolithographic techniques can be applied for manufacturing of arrays of islands of such model compounds embedded in an Al or Al-Cu matrix. Thereafter, the corrosion evolution at such a model array can be studied with different techniques and in different environments. These arrays lack the microstructural complexity of the true alloys. This facilitates assignment of processes like trench formation or Cu replating to the presence of special phases or to specific electrochemical reactions. In addition the spacing and size and therefore also the areal density of the intermetallic particles can be varied at will, and the influence on galvanic coupling, pH evolution, corrosion intiation and propagation rates be studied.
- The second approach is the use of microelectrochemical methods, especially microcapillaries, or masking techniques, which however are less versatile. These allow to study the electrochemical behavior of selected small regions with a limited number of intermetallic compounds. If the composition of these compounds is known, the relative importance of the compounds for the corrosion processes can be studied, and the dependence of breakdown processes on the areal density of these compounds. In addition the behavior of the true matrix can be properly studied. The advantage of this method is that the real alloy is studied, avoiding artifacts possible in the model alloy approach by deviations in composition of model compounds and real phases, and by the different microstructure in the commercial alloy. One disadvantage is that only large particles can be studied without obtaining a contribution from the alloy matrix as well. Other disadvantages are the partial immersion altering the open circuit potential, the neglect of possible contributions from particles further away, and the alteration of the thickness of the diffusion boundary layer in comparison to full immersion.
- The third approach lies in the combination of classical electrochemical techniques with in-situ microscopic observation of the processes on the alloy. This comprises in situ microscopy studies like the CLSM studies discussed in detail, like NSOM and AFM studies. In addition some local electrochemical mapping techniques have also proved useful: SKPFM allowed characterizing the relative nobility of particles before immersion. SECM, SVET and LEIM may be used to learn about electrochemical reactivity at the IMC phases. However, in these methods it is mandatory that equipment with sufficient lateral resolution is used.

These approaches can be complemented by further in-situ methods like the electrochemical quartz crystal microbalance technique providing information about mass changes, but also indicating surface roughening (difficult with real alloys, even though approaches in literature have been presented where a thin layer of commercial steel was glued onto the quartz), methods to measure the local pH, and in-situ spectroscopy like Raman spectroscopy to learn more about corrosion product formation. Finally ex-situ analysis of corrosion products by surface analytical techniques and of corrosion morphology by metallographic techniques is possible.

The situation further complicates in the case of organic coatings. Here especially local electrochemical techniques like the measurement of local properties with microcapillaries after full immersion for a given time, LEIS and SVET are beneficial, and of course the

scanning Kelvin probe. Further spectroscopy and spectroscopic microscopy can help to monitor chemical changes in the coating and at the interface to the substrate. Especially the addition of fluorescent markers sensitive to pH, chloride concentration and metal ions created during alloy corrosion into the coating can be very useful. Then it is possible to perform CLSM studied in the fluorescent mode in parallel to topographic CLSM, and to learn more about the evolution of ionic channels and in general defects in organic coatings. Studies on coated model alloys also could be helpful to come to a more quantitative understanding of the processes of coating failure.

Besides the general benefit of improved knowledge and the capability to transfer methods to other areas of materials and corrosion science, there are two main ultimate goals of such studies: To find new and better ways to mitigate or stop the corrosion processes, and to have enough information and understanding of the mechanism to perform predictive numerical modeling of corrosion processes in commercial alloys. The latter aspects had been one of the issues of the so-called Yucca Mountain project, where the (unsolved) challenge was to predict the corrosion behavior of nuclear waste containers over a timescale of > 10000 years.

Sonoelectrochemisty introduces new possibilities and challenges in the field of electrochemical materials synthesis. Processes are influenced mainly by two factors: a dramatically increased effective mass transport rate, and cavitation processes at the surface. Difficulties stem from the influence of the experimental setup, especially the cell geometry and the arrangement of ultrasound source and electrode on the acoustic field and therefore the hydrodynamics developing in the cell and at the electrode. This will also influence the extent of cavitation at the electrode surface, the local microstreaming and local mass transport rates at the surface, which in turn may impact nucleation processes. In addition radical formation and local temperature changes might contribute as well to the electrochemical reactions. Another added complication lies in the dependence of cavitation processes on the electrolyte composition, on the presence of inert gas and especially on the concentration of surfactants. This introduces a large variability in the experiments. Results shown from the author's work mainly dealt with characterization of the electrochemical processes taking place in the presence of ultrasound and the application of the technique for production of composite materials. For this, the EQCM technique once more was beneficial. In future work also the acoustic field and the cavitation events have to be characterized. Methods to do that published in the literature have been reviewed in this work as well. Once more, microelectrochemical techniques have been proven useful for the characterization of the sound field of an ultrasonic horn. On the other hand, sonoluminescence, chemiluminescence and high speed photography of cavitation processes can be applied, as well as particle image velocimetry in order to measure actual streaming rates. In the end, computer simulation of the hydrodynamic processes will be required. This is just the prelude to the next big step in sonoelectrochemistry: the upscaling of the process to permit industrial application. As explained in Section 1.4 ultrasound is beneficial for electrochemical deposition. However, ultrasound is not applied on a large scale in electroplating industry, where three-dimensional objects like screws and nuts, or also very large panels have to be coated homogeneously. There are three main reasons for this:

- The introduction of ultrasound modifies deposition processes in a way that the complicated bath chemistry optimized for conventional electroplating does no longer work, re-introducing therefore once more edge effects and deteriorating actual deposit quality.
- It is very difficult to establish a rather uniform sound field on a large scale when heterogeneous processes like electroplating have to be performed. How does one

introduce sound in a drum filled with screw nuts? How does one assure a uniform sound field over a panel area of several square meter.

- Introduction of ultrasound at first sight will increase the energy consumption of the plant. Only if this energy is saved elsewhere thanks to the sono-process, and the overall costs of the production line decrease, ultrasound will become an option for electroplating industry.

Large scale sonoelectrochemistry therefore will require more than a process working in the laboratory. The entire process chain has to be altered and optimized. This will only happen with time and requires further process development. Possibly a good starting point will be a rather new technology: the electroplating of non noble metals and semiconductors from ionic liquids. Ionic liquids show increased viscosity and decreased diffusivity compared to aqueous solvents. The application of ultrasound in these media therefore is considered as highly beneficial [168, 528]. Since it is a new technology, market introduction will require anyway new infrastructure, facilitating the implementation of ultrasonic processing at the same time. Other possibilities are in applications like mass production of nanoparticles, where the ultrasound generator acts as electrode at the same time, and flow reactors can be imagined. However, for these applications the problem of sonotrode erosion has to be solved first.

5. References

1. M. Schlesinger , M. Paunovic (ed.), *Modern Electroplating*, John Wiley & Sons, Inc, New York, Chichester, Weinheim, Brisbane, Singapore, Toronto (2000).

2. K. Nielsch, F. Müller, A.-P. Li , U. Gösele, *Uniform Nickel Deposition into Ordered Alumina Pores by Pulsed Electrodeposition*, Advanced Materials **12** (2000) 582-586.

3. K. Nielsch, R. B. Wehrspohn, J. Barthel, J. Kirschner, U. Gösele, S. F. Fischer , H. Kronmüller, *Hexagonally ordered 100 nm period nickel nanowire arrays*, Applied Physics Letters **79** (2001) 1360-1362.

4. K. Nielsch, F. Müller, G. Liu, R. B. Wehrsporn, U. Gösele, S. F. Fischer , H. Kronmüller, *Magnetic nanowire arrays obtained by electrodeposition in ordered alumina templates*, Proceedings of the electrochemical society, exact source unknown (2000)

5. A. J. Bard , L. R. Faulkner, *Electrochemical Methods: Fundamentals and Applications*, 2nd edition, John Wiley & Sons, New York (2001).

6. J. O. M. Bockris , A. K. N. Reddy, *Modern Electrochemistry Vol. 1. Ionics*, 2nd edition, Plenum Press, New York and London (1998).

7. J. O. M. Bockris, A. K. N. Reddy , M. Gamboa-Aldeco, *Modern Electrochemistry Vol. 2A. Fundamentals of Electrodics*, 2nd edition, Kluwer Academic / Plenum Press, New York, Boston, Dordrecht, London, Moscow (1998).

8. J. O. M. Bockris , A. K. N. Reddy, *Modern Electrochemistry 2B - Electrodics in Chemistry, Engineering, Biology and Environmental Science*, 2nd edition, Kluwer Academic / Plenum Publishers, New York, Boston, Dordrecht, London, Moscow (1998).

9. F. U. Renner, A. Stierle, H. Dosch, D. M. Kolb, T.-L. Lee , J. Zegenhagen, *Initial corrosion observed on the atomic scale*, Nature **439** (2006) 707-710.

10. N. Kanani, *Galvanotechnik: Grundlagen, Verfahren und Praxis einer Schlüsseltechnologie*, 2nd, Hanser, München (2009).

11. G. Schmitt, *Der Korrosionsbegriff bei nichtmetallischen Werkstoffen*, Materials and Corrosion **55** (2004) 367-372.

12. *Korrosion von Metallen und Legierungen*, DIN EN ISO 8044 (2003)

13. G. S. Frankel, *Pitting corrosion of metals: A review of the critical factors*, Journal of the Electrochemical Society **145** (1998) 2186 - 2198.

14. P. Lequeu, P. Lassince, T. Warner , G. M. Raynaud, *Engineering for the future : Weight Saving and Cost Reduction Initiatives*, International Journal of Aircraft Engineering and Aerospace Technology **73** (2001) 147 - 159.

15. P. Lequeu, P. Lassince , T. Warner, *Aluminium Alloy Development for the Airbus A380 — Part 2*, Advanced Materials & Processes **165** (2007) 41-44.

16. http://www.eaa.net/upl/4/default/doc/Moving%20up%20to%20aluminium_de.pdf,

17. ASTM, *Standard specification for aluminum and aluminum-alloy sheet and plate, ASTM B 209-96*, Annual Book of ASTM Standards 95-125.

18. B. Lenczowski, T. Hack, D. Wieser, G. Tempus, G. Fischer, J. Becker, K. Folkers, R. Braun , G. Lutjering, *AlMgSc alloys for transportation technology*, Materials Science Forum **331-3** (2000) 957-963.

19. J. N. Fridlyander, N. I. Kolobnev, L. B. Khokhlatova, K. H. Rendigs, G. Tempus, A. Haszler, C. Keidel, T. Pfannenmuller , A. L. Berezina, *Structure and Properties of Sheets of 1424 Alloy*, Materials Science Forum **331-3** (2000) 1393-1400.

20. I. Haase, K. Nocke, H. Worch, G. Zouhar , G. Tempus, *Untersuchungen zum Ermüdungsverhalten der Aluminiumlegierung AA 6013 T6 in korrosivem Medium*, Praktische Metallographie-Practical Metallography **38** (2001) 119.

21. J. Sinke, *Development of Fibre Metal Laminates: concurrent multi-scale modeling and testing*, Journal of Materials Science **41** (2006) 6777–6788.

22. R. G. Buchheit, R. P. Grant, P. F. Hlava, B. McKenzie , G. L. Zender, *Local Dissolution Phenomena associated with S-Phase (Al_2CuMg) particles in Aluminum Alloy 2024-T3*, Journal of the Electrochemical Society **144** (1997) 2621 - 2628.

23. G. S. Chen, M. Gao , R. P. Wei, *Microconstituent-Induced Pitting Corrosion in Aluminum Alloy 2024-T3*, Corrosion **52** (1996) 8 -15.

24. V. Guillaumin , G. Mankowski, *Localized corrosion of 2024 T351 aluminium alloy in chloride media*, Corrosion Science **41** (1999) 421-438.

25. J. R. Scully, T. O. Knight, R. G. Buchheit , D. E. Peebles, *Electrochemical Characteristics of the Al_2Cu, Al_3Ta and Al_3Zr Intermetallic Phases and their relevancy to the localized corrosion of Al alloys*, Corrosion Science **35** (1993) 185 -195.

26. M. Büchler, J. Kerimo, F. Guillaume , W. H. Smyrl, *Fluorescence and Near-Field Scanning Optical Microscopy for Investigating Initiation of Localized Corrosion of Al 2024*, Journal of the Electrochemical Society **147** (2000) 3691-3699.

27. M. A. Alodan , W. H. Smyrl, *Detection of Localized Corrosion Using Fluorescence Microscopy*, Journal of the Electrochemical Society **144** (1997) L282 - L284.

28. P. Schmutz , G. S. Frankel, *Corrosion Study of AA2024-T3 by Scanning Kelvin Probe Force Microscopy and In Situ Atomic Force Microscopy Scratching*, Journal of the Electrochemical Society **145** (1998) 2295 - 2306.

29. M. B. Vukmirovic, N. Dimitrov , K. Sieradzki, *Dealloying and corrosion of Al Alloy 2024-T3*, Journal of the Electrochemical Society **149** (2002) B428 - B439.

30. N. Missert, J. C. Barbour, R. G. Copeland , J. E. Mikkalson, *The localized corrosion of Al at engineered Cu islands*, The journal of the Minerals, Metals & Materials Society **53** (2001) 34 - 36.

31. N. Birbilis , R. G. Buchheit, *Investigation and Discussion of Characteristics for Intermetallic Phases Common to Aluminum Alloys as a Function of Solution pH*, Journal of the Electrochemical Society **155** (2008) C117-C126.

32. G. O. Ilevbare, O. Schneider, R. G. Kelly , J. R. Scully, *In-situ Confocal Laser Scanning Microscopy of AA 2024-T3 corrosion metrology: 1. Localized corrosion of particles*, Journal of the Electrochemical Society **151** (2004) B453-B464.

33. O. Schneider, G. O. Ilevbare, J. R. Scully , R. G. Kelly, *In-situ Confocal Laser Scanning Microscopy of AA 2024-T3 corrosion metrology: 2. Trench formation around particles*, Journal of the Electrochemical Society **151** (2004) B465 - B472.

34. J. O. Park, C. H. Paik, Y. H. Huang , R. C. Alkire, *Influence of Fe-Rich intermetallic inclusions on pit initiation on aluminium alloys in aerated NaCl.* , Journal of the Electrochemical Society **146** (1999) 517 - 523.

35. Y. Baek , G. S. Frankel, *Electrochemical Quartz Crystal Microbalance Study of Corrosion of Phases in AA2024*, Journal of the Electrochemical Society **150** (2003) B1 - B9.

36. M. J. Pryor , D. S. Keir, *The nature of aluminum as a cathode*, Journal of the Electrochemical Society **102** (1955) 605-607.

37. M. A. Alodan , W. H. Smyrl, *Detection of Localized Corrosion of Aluminum Alloys Using Fluorescence Microscopy*, Journal of the Electrochemical Society **145** (1998) 1571 - 1577.

38. T. Suter , R. C. Alkire, *Microelectrochemical Studies of Pit Initiation at Single Inclusions in Al 2024-T3*, Journal of the Electrochemical Society **148** (2001) B36-B42.

39. N. Dimitrov, J. A. Mann, M. Vukmirovic , K. Sieradzki, *Dealloying of Al_2CuMg in Alkaline Media*, Journal of the Electrochemical Society **147** (2000) 3283-3285.

40. P. Schmutz , G. S. Frankel, *Characterization of AA2024-T3 by Scanning Kelvin Probe Force Microscopy*, Journal of the Electrochemical Society **145** (1998) 2285 - 2295.

41. N. Dimitrov, J. A. Mann , K. Sieradzki, *Copper Redistribution during Corrosion of Aluminum Alloys*, Journal of the Electrochemical Society **146** (1999) 98-102.

42. C. Blanc, B. Lavelle , G. Mankowski, *The role of precipitates enriched with copper on the susceptibility to pitting corrosion of the 2024 aluminium alloy* Corrosion Science **39** (1997) 495 - 510.

43. G. O. Ilevbare, J. R. Scully, J. Yuan , R. G. Kelly, *Inhibition of pitting corrosion on aluminium alloy 2024-T3: Effect of soluble chromate additions vs. chromate conversion coating*, Corrosion **56** (2000) 227-242.

44. M. Büchler, T. Watari , W. H. Smyrl, *Investigation of the initiation of localized corrosion on aluminum alloys by using fluorescence microscopy*, Corrosion Science **42** (2000) 1661-1668.

45. T. J. R. Leclère , R. C. Newman, *Self-regulation of the cathodic reaction kinetics during corrosion of AlCu alloys* Journal of the Electrochemical Society **149** (2002) B52 - B56.

46. K. Nisancioglu, J. H. Nordlien, A. Afseth , G. M. Scamans, *Significance of Thermomechanical Processing in Determining Corrosion Behavior and Surface Quality of Aluminum Alloys*, Materials Science Forum **331-337** (2000) 111 - 126.

47. K. Nisancioglu, K. Y. Davanger , O. Strandmyr, *Cathodic behavior of impure aluminum in aqueous media* Journal of the Electrochemical Society **128** (1981) 1523 -1526.

48. P. Leblanc , G. S. Frankel, *A Study of Corrosion and Pitting Initiation of AA2024-T3 Using Atomic Force Microscopy*, Journal of the Electrochemical Society **149** (2002) B239 - B247.

49. N. Missert, R. G. Copeland, F. D. Wall, C. M. Johnson, J. C. Barbour , P. Kotula, *Aluminum corrosion at systems of engineered copper particles*, in *Corrosion Science*, G. S. Frankel, H. S. Isaacs, J. R. Scully, J. D. Sinclair (eds.), **2002-13**, 307-313, The Electrochemical Society Proceedings Series, Pennington, NJ (2002).

50. N. Missert, R. G. Copeland, F. D. Wall, C. M. Johnson , J. C. Barbour, *Interactions among Pitting Sites in Aluminum at Engineered Copper Particles*, in *Critical Factors in Localized Corrosion IV*, S. Virtanen, P. Schmuki, G. S. Frankel (eds.), **2002-24**, 421-428, The Electrochemical Society Proceedings Series, Pennington, NJ (2002).

51. F. D. Wall, K.-A. Son, N. A. Missert, J. C. Barbour, M. A. Martinez, K. R. Zavidil, J. P. Sullivan, R. G. Copeland, W. R. Cieslak, R. G. Buchheit , H. S. Isaacs, *The influence of nanoengineered Cu defects on Aluminum pitting initiation*, in *Critical Factors in Localized Corrosion III*, R. G. Kelly, G. S. Frankel, P. M. Natishan, R. C. Newman (eds.), **PV 98-17**, 701 - 712, The Electrochemical Society Proceedings Series, Pennington, NJ (1999).

52. M. Kappes, L. Kovarik, M. J. Mills, G. S. Frankel , M. K. Miller, *Usefulness of Ultrahigh Resolution Microstructural Studies for Understanding Localized Corrosion Behavior of Al Alloys*, Journal of the Electrochemical Society **155** (2008) C437-C443.

53. T. Nguyen, J. B. Hubbard , J. M. Pommersheim, *Unified Model for the degradation of organic coatings on steel in a neutral electrolyte*, Journal of Coatings Technology **68** (1996) 45-56.

54. D. Greenfield , D. Scantlebury, *The protective action of organic coatings on steel: A Review*, The journal of corrosion science and engineering **3** (2000) Paper 5.

55. G. M. Hoch, *A review of filiform corrosion*, Localized Corrosion, R. W. Staehle, B. F. Brown, J. Kruger, A. Agrawal, eds.; NACE, Houston, Texas, (1974) 134 -142.

56. H. Leidheiser Jr., *Corrosion of painted metals - a review*, Corrosion **38** (1982) 374-383.

57. H. Leidheiser jr., *Towards a better understanding of corrosion beneath organic coatings*, Corrosion **39** (1983) 189-201.

58. G. Grundmeier, W. Schmidt , M. Stratmann, *Corrosion protection by organic coatings: electrochemical mechanism and novel methods of investigation*, Electrochimica Acta **45** (2000) 2515-2533.

59. M. Stratmann , H. Streckel, *On the atmospheric corrosion of metals which are covered with thin electrolyte layers-I. Verification of the experimental technique*, Corrosion Science **30** (1990) 681-696.

60. A. Leng, H. Streckel, K. Hofmann , M. Stratmann, *The delamination of polymeric coatings from steel Part 3: Effect of the oxygen partial pressure on the delamination reaction and current distribution at the metal/polymer interface*, Corrosion Science **41** (1999) 599-620.

61. A. Leng, H. Streckel , M. Stratmann, *The delamination of polymeric coatings from steel. Part 1: Calibration of the Kelvinprobe and basic delamination mechanism*, Corrosion Science **41** (1999) 547-578.

62. A. Leng, H. Streckel , M. Stratmann, *The delamination of polymeric coatings from steel. Part 2: First stage of delamination, effect of type and concentration of cations on delamination, chemical analysis of the interface*, Corrosion Science **41** (1999) 579-597.

63. T. Schauer , F. Maile, *Untersuchung der Korrosion und Delamination von Beschichtungen mittels SRET und LICT*, Technisches Messen **67** (2000) 537-541.

64. J. He, V. Johnston Gelling, D. E. Tallman , G. P. Bierwagen, *A Scanning Vibrating Electrode Study of Chromated-Epoxy Primer on Steel and Aluminum*, Journal of the Electrochemical Society **147** (2000) 3661-3666.

65. J. He, V. J. Gelling, D. E. Tallman, G. P. Bierwagen , G. G. Wallace, *Conducting Polymers and Corrosion III. A Scanning Vibrating Electrode Study of Poly(3-octyl pyrrole) on Steel and Aluminum*, Journal of the Electrochemical Society **147** (2000) 3667-3672.

66. D. A. Worsley, S. M. Powell , H. N. McMurray, *Influence of remote cathodes on corrosion mechanism at exposed cut edges in organically coated galvanized steels.*, Corrosion **56** (2000) 492-500.

67. A. M. Mierisch, J. Yuan, R. G. Kelly , S. R. Taylor, *Probing Coating Degradation on AA2024-T3 Using Local Electrochemical and Chemical Techniques*, Journal of the Electrochemical Society **146** (1999) 4449-4454.

68. A. M. Mierisch , S. R. Taylor, *Understanding the Degradation of Organic Coatings Using Local Electrochemical Impedance Methods I. Commonly Observed Features*, Journal of the Electrochemical Society **150** (2003) B303-B308.

69. L. V. S. Philippe, G. W. Walter , S. B. Lyon, *Investigating Localized Degradation of Organic Coatings: Comparison of Electrochemical Impedance Spectroscopy with Local Electrochemical Impedance Spectroscopy*, Journal of the Electrochemical Society **150** (2003) B111-B119.

70. W. Fürbeth , M. Stratmann, *The delamination of polymeric coatings from electrogalvanised steel - a mechanistic approach. Part 1: delamination from a defect with intact zinc layer*, Corrosion Science **43** (2001) 207-227.

71. W. Fürbeth , M. Stratmann, *The delamination of polymeric coatings from electrogalvanized steel - a mechanistic approach. Part 2: delamination from a defect down to steel*, Corrosion Science **43** (2001) 229-241.

72. O. Schneider , R. G. Kelly, *Localized Coating Failure of Epoxy-Coated AA2024-T3 in 0.5 M NaCl Solutions: Comparison of Conventional Electrochemical Techniques and Microelectrochemical Methods*, Corrosion Engineering, Science and Technology **38** (2003) 119 - 128.

73. M. Rohwerder, E. Hornung , M. Stratmann, *Microscopic aspects of electrochemical delamination: an SKPFM study*, Electrochimica Acta **48** (2003) 1235-1243.

74. O. Schneider, G. O. Ilevbare, J. R. Scully , R. G. Kelly, *Confocal Laser Scanning Microscopy as a Tool for In Situ Monitoring of Corrosion Underneath Organic Coatings*, Electrochemical and Solid-State Letters **4** (2001) B35-B38.

75. M. Doherty , J. M. Sykes, *A quantitative study of blister growth on lacquered food cans by scanning acoustic microscopy*, Corrosion Science **50** (2008) 2755–2772.

76. O. Schneider, G. O. Ilevbare, J. R. Scully , R. G. Kelly, *In-Situ Confocal Laser Scanning Microscopy of AA 2024-T3 Corrosion Metrology: 3. Underfilm Corrosion of epoxy-coated AA2024-T3*, Journal of the Electrochemical Society **154** (2007) C397-C410.

77. R. G. Kelly, J. Yuan, C. M. Weyant , K. S. Lewis, *Applications of capillary electrophoresis in corrosion science and engineering*, Journal of Chromatography A **834** (1999) 433-444.

78. K. S. Lewis, J. Yuan , R. G. Kelly, *Chemical conditions inside occluded regions on corroding aircraft aluminum alloys*, Journal of Chromatography A **850** (1999) 375-380.

79. J. Vander Kloet, W. Schmidt, A. W. Hassel , M. Stratmann, *The role of chromate in filiform corrosion inhibition*, Electrochimica Acta **48** (2003) 1211-1222.

80. C. H. Chang, J. H. Park, J. S. Kim, M. K. Joo, G. D. Lee, K. Y. Kim, A. Nishikata , T. Tsuru, *Nondestructive evaluation of corrosion beneath organic coatings by synchrotron X-Rays*, Corrosion Science **45** (2003) 2689-2695.

81. H. Leth-Olsen , K. Nisancioglu, *Filiform corrosion of aluminium sheet: I. Corrosion behaviour of painted material*, Corrosion Science **40** (1998) 1179-1194.

82. H. Leth-Olsen, A. Afseth , K. Nisancioglu, *Filiform corrosion of aluminium sheet: II. Electrochemical and corrosion behaviour of bare substrates*, Corrosion Science **40** (1998) 1195-1214.

83. H. Leth-Olsen, J. H. Nordlien , K. Nisancioglu, *Filiform Corrosion Of Aluminium Sheet. III. Microstructure Of Reactive Surfaces*, Corrosion Science **40** (1998) 2051-2063.

84. E. P. M. van Westing, G. M. Ferrari , J. H. W. de Wit, *The determination of coating performance with impedance measurements-II. Water uptake of coatings*, Corrosion Science **36** (1994) 957-977.

85. O. Schneider , R. G. Kelly, *Localized coating failure of epoxy-coated aluminium alloy 2024-T3 in 0.5 M NaCl solutions: Correlation between coating degradation, blister formation and local chemistry within blisters*, Corrosion Science **49** (2007) 594–619.

86. A. T. A. Jenkins , R. D. Armstrong, *The breakdown in the barrier properties of organic coatings due to filiform corrosion.*, Corrosion Science **38** (1996) 1147-1157.

87. K. R. Gowers , J. D. Scantlebury, *Blistering phenomena on lacquered mild steel.*, Corrosion Science **23** (1983) 935-942.

88. C. M. Hansen, *New developments in corrosion and blister formation in coatings*, Progress in Organic Coatings **26** (1995) 113-120.

89. J. H. W. de Wit, H. J. W. Lenderink, J. H. van der Weijde , E. P. M. van Westing, *Mechanisms for delamination of organic coatings*, UK Corrosion and EuroCorr94, Institute of Materials **1** (1994) 1-9.

90. E. P. M. van Westing, G. M. Ferrari , J. H. W. de Wit, *The determination of coating performance with impedance measurements – I. Coating Polymer Properties*, Corrosion Science **34** (1993) 1511-1530.

91. E. P. M. van Westing, G. M. Ferrari , J. H. W. De Wit, *The determination of coating performance with impedance measurements – III. In situ determination of loss of adhesion*, Corrosion Science **36** (1994) 979-994.

92. J. R. Kosek, J. N. DuPont , A. R. Marder, *Effect of Porosity on Resistance of epoxy coatings to cold-wall blistering*, Corrosion **51** (1995) 861-871.

93. P. Mastonardi, C. Carfagna , L. Nicolais, *The effect of the transport properties of epoxy based coatings on metallic substrate corrosion*, Journal of Materials Science **18** (1983) 1977-1982.

94. J. W. Martin, E. Embree , W. Tsao, *Non-osmotic, Defect-Controlled cathodic disbondment of a coating from a steel substrate.*, Journal of Coatings Technology **62** (1990) 25-33.

95. R. D. Armstrong, B. W. Johnson , J. D. Wright, *An investigation into the cathodic delamination of epoxy-polyamine protective coatings*, Electrochimica Acta **36** (1991) 1915-1923.

96. A. S. Castela , A. M. Simoes, *An impedance model for the estimation of water absorption in organic coatings. Part I: A linear dielectric mixture equation*, Corrosion Science **45** (2003) 1631-1646.

97. D. M. Brasher , A. H. Kingsbury, *Electrical Measurements in the study of immersed paint coatings on metal. I. Comparison between capacitance and gravimetric methods of estimating water-uptake.* , Journal of Applied Chemistry **4** (1954) 62-72.

98. R. Hirayama , S. Haruyama, *Electrochemical Impedance for degraded coated steel having pores*, Corrosion **47** (1991) 952-958.

99. D. H. van der Weijde, E. P. M. van Westing , J. H. W. de Wit, *Monitoring the effect of environmental changes on coating properties with EIS*, Materials Science Forum **289-292** (1998) 237-246.

100. P. L. Bonora, F. Deflorian , L. Fedrizzi, *EIS study of organic coating performance*, Materials Science Forum **192-194** (1995) 267-276.

101. P. Gimenz, D. Petit , M. Badia, *Water uptake of polymer coatings: New investigation of the early stages by the electrochemical impedance method*, Materials Science Forum **8** (1986) 315-326.

102. T.-J. Chuang, T. Nguyen , S. Lee, *Micro-Mechanic Model for cathodic blister growth in painted steel*, Journal of Coatings Technology **71** (1998) 75-85.

103. M. Stratmann, M. Wolpers, H. Streckel , R. Feser, *Use of a scanning Kelvinprobe in the investigation of electrochemical reactions at the metal polymer interface*, Berichte der Bunsengesellschaft für Physikalische Chemie **95** (1991) 1365-1375.

104. U. Rekners , M. Kalnins, *Evaluation of the protective properties of organic coatings by using tape and blistering tests.*, Progress in Organic Coatings **38** (2000) 35-42.

105. K. R. Gowers, N. J. Hepburn, G. A. M. Sussex , J. D. Scantlebury, *Electrochemical studies on the conductive pathways during corrosion of lacquer coated mild steel*, Materials Science Forum **8** (1986) 289-302.

106. J. D. Crossen, J. M. Sykes, T. Zhai , G. A. D. Briggs, *Study of the coating/substrate interface by scanning acoustic microscopy: Cathodic disbondment of epoxy-polyamide lacquer from mild steel.*, Faraday Discussions **107** (1997) 417-424.

107. W. Schmidt , M. Stratmann, *Scanning Kelvinprobe Investigations of Filiform Corrosion on Aluminum Alloy 2024-T3*, Corrosion Science **40** (1998) 1441-1443.

108. W. Fürbeth , M. Stratmann, *The delamination of polymeric coatings from electrogalvanized steel - a mechanistic approach. Part 3: delamination kinetics and influence of CO_2*, Corrosion Science **43** (2001) 243-254.

109. E. L. Koehler, *The mechanism of cathodic disbondment of protective organic coatings - aqueous displacement at elevated pH.*, Corrosion **40** (1984) 5-8.

110. M. A. Hernandéz, F. Galliano , D. Landolt, *Mechanism of cathodic delamination control of zinc-aluminum phosphate pigment in waterborne coatings*, Corrosion Science **46** (2004) 2281-2300.

111. M. Doherty , J. M. Sykes, *Micro-cells beneath organic lacquers: a study using scanning Kelvin probe and scanning acoustic microscopy*, Corrosion Science **46** (2004) 1265-1289.

112. J. M. Williams, O. M. Schneider , R. G. Kelly, *Phenomenology of Localized Coating Failure on AA1100-H14*, in *Proceedings of the Tri-Service Corrosion Conference*, R. A. Mantz, P. C. Trulove (eds.), 1171-1195, San Antonio, Texas (2002).

113. D. H. van der Weijde, E. P. M. van Westing , J. H. W. de Wit, *EIS measurements on artificial blisters in organic coatings*, Electrochimica Acta **41** (1996) 1103-1107.

114. G. O. Ilevbare , J. R. Scully, *Mass-transport-limited oxygen reduction reaction on AA2024-T3 and selected intermetallic compounds in chromate-containing solutions*, Corrosion **57** (2001) 134 - 152.

115. G. O. Ilevbare , J. R. Scully, *Oxygen Reduction Reaction Kinetics on Chromate Conversion Coated Al-Cu, Al-Cu-Mg, and Al-Cu-Mn-Fe Intermetallic Compounds*, Journal of the Electrochemical Society **148** (2001) B196-B207.

116. J. A. Grandle , S. R. Taylor, *Electrochemical Impedance spectroscopy of coated aluminum beverage containers: Part 1 - Determination of an optimal parameter for large sample evaluation*, Corrosion **50** (1994) 792-803.

117. M. J. Vasquez, G. P. Halada, C. R. Clayton , J. P. Longtin, *On the nature of the chromate conversion coating formed on intermetallic constituents on AA2024-T3*, Surface and Interface Analysis **33** (2002) 607-616.

118. M. J. Vasquez, G. P. Halada , C. R. Clayton, *The application of synchrotron-based spectroscopic techniques to the study of chromate conversion coatings*, Electrochimica Acta **47** (2002) 3105-3115.

119. A. M. Mierisch, S. R. Taylor , V. Celli, *Understanding the Degradation of Organic Coatings Through Local Electrochemical Impedance Methods II. Modeling and Experimental Results of Normal Field Variations above Disk Electrodes*, Journal of the Electrochemical Society **150** (2003) B309-B315.

120. J. Crank, *The Mathematics of Diffusion*, 2nd edition, Oxford Science Publications, Oxford, UK (1975).

121. O. Schneider , R. G. Kelly, *Localized coating failure of epoxy-coated aluminium alloy 2024-T3 in sulfate-based electrolytes*, in preparation.

122. R. G. Compton, J. C. Eklund , F. Marken, *Sonoelectrochemical Processes: A Review*, Electroanalysis **9** (1997) 509 - 522.

123. D. J. Walton, *Sonoelectrochemistry – The application of ultrasound to electrochemical systems*, Arkivoc (2002) 198 - 218.

124. C. E. Banks , R. G. Compton, *Voltammetric Exploration and Applications of Ultrasonic Cavitation*, ChemPhysChem **4** (2003) 169 - 178.

125. J.-L. Delplancke, J. Dille, J. Reisse, G. J. Long, A. Mohan , F. Grandjean, *Magnetic Nanopowders: Ultrasound-Assisted Electrochemical Preparation and Properties*, Chemistry of Materials **12** (2000) 946 - 955.

126. M. E. Hyde , R. G. Compton, *How ultrasound influences the electrodeposition of metals*, Journal of Electroanalytical Chemistry **531** (2002) 19 - 24.

127. F. Touyeras, J. Y. Hihn, X. Bourgoin, B. Jacques, L. Hallez , V. Branger, *Effects of ultrasonic irradiation on the properties of coatings obtained by electroless plating and electro plating*, Ultrasonics Sonochemistry **12** (2005) 13-19.

128. R. Walker, *Ultrasound improves electrolytic recovery of metals*, Ultrasonics Sonochemistry **4** (1997) 39-43.

129. G. Cravotto , P. Cintas, *Power ultrasound in organic synthesis: moving cavitational chemistry from academia to innovative and large-scale applications*, Chemical Society Reviews **35** (2006) 180-196.

130. W. Lauterborn, T. Kurz, R. Geisler, D. Kröninger , D. Schanz, *The single bubble – a hot microlaboratory*, in *Oscillations, Waves, and Interactions*, T. Kurz, U. Parlitz, U. Kaatze (eds.), 139–170, Universitätsverlag Göttingen, Göttingen (2007).

131. T. G. Leighton, *What is ultrasound?*, Progress in Biophysics and Molecular Biology **93** (2007) 3–83.

132. R. Mettin, *From a single bubble to bubble structures in acoustic cavitation*, in *Oscillations, Waves, and Interactions*, U. P. Thomas Kurz, and Udo Kaatze (eds.), 171-198, Universitätsverlag Göttingen, Göttingen (2007).

133. L. H. Thompson , L. K. Doraiswamy, *Sonochemistry: Science and Engineering*, Industrial & Engineering Chemistry Research **38** (1999) 1215-1249.

134. K. S. Suslick , D. J. Flannigan, *Inside a collapsing bubble: sonoluminescence and the conditions during cavitation*, Annual Review of Physical Chemistry **59** (2008) 659-683.

135. T. J. Mason , J. P. Lorimer, *Applied Sonochemistry. Uses of Power Ultrasound in Chemistry and Processing*, Wiley-VCH, Weinheim (2002).

136. L. A. Crum, *Comments on the evolving field of sonochemistry by a cavitation physicist*, Ultrasonics Sonochemistry **2** (1995) S147-S152.

137. E. A. Neppiras, *Acoustic cavitation*, Physics Reports **61** (1980) 159-251.

138. C. E. Banks , R. G. Compton, *Ultrasonically Enhanced Voltammetric Analysis and Applications: An Overview*, Electroanalysis **15** (2003) 329 - 346.

139. Lord Rayleigh, *On the pressure developed in a liquid during the collapse of a spherical cavity*, Philosophical Magazine Series 6 **34** (1917) 94-98.

140. E. Newton Harvey, D. K. Barnes, W. D. McElroy, A. H. Whiteley, D. C. Pease , K. W. Cooper, *Bubble formation in animals. I. Physical factors*, Journal of Cellular and Comparative Physiology **24** (1944) 1-22.

141. F. J. del Campo, J. Melville, J. L. Hardcastle , R. G. Compton, *Differential Pulse and Chronoamperometric Studies of Insonated Systems: Acoustic Streaming and Cavitational Effects* Journal of Physical Chemistry A **105** (2001) 666-674.

142. M. Ashokkumar , F. Grieser, *The effect of surface active solutes on bubbles in an acoustic field*, Physical Chemistry Chemical Physics **9** (2007) 5631–5643.

143. K. S. Suslick , G. J. Price, *Applications of Ultrasound to Materials Chemistry*, Annual Review of Materials Science **29** (1999) 295–326.

144. H. Xu, N. G. Glumac , K. S. Suslick, *Temperature Inhomogeneity during Multibubble Sonoluminescence*, Angewandte Chemie International Edition **49** (2010) 1079-1082.

145. T. J. Mason, *Ultrasound in synthetic organic chemistry*, Chemical Society Reviews **26** (1997) 443-451.

146. K. Muthukrishnan, K. R. Hebert , T. Makino, *Interfacial Void Model for Corrosion Pit Initiation on Aluminum*, Journal of the Electrochemical Society **151** (2004) B340-B346.

147. P. Riesz, D. Berdahl , C. L. Christman, *Free Radical Generation by Ultrasound in Aqueous and Nonaqueous Solutions*, Environmental Health Perspectives **64** (1985) 233-252.

148. V. Mišík, N. Miyoshi , P. Riesz, *EPR Spin-Trapping Study of the Sonolysis of H_2O/D_2O Mixtures: Probing the Temperatures of Cavitation Regions*, The Journal of Physical Chemistry **99** (1995) 3605-3611.

149. K. S. Suslick, D. A. Hammerton , J. Cline, R. E., *The Sonochemical Hot Spot*, Journal of the American Chemical Society **108** (1986) 5641-5642.

150. M. Ashokkumar , F. Grieser, *A Comparison between Multibubble Sonoluminescence Intensity and the Temperature within Cavitation Bubbles*, Journal of the American Chemical Society **127** (2005) 5326-5327.

151. J. Rae, M. Ashokkumar, O. Eulaerts, C. von Sonntag, J. Reisse , F. Grieser, *Estimation of ultrasound induced cavitation bubble temperatures in aqueous solutions*, Ultrasonics Sonochemistry **12** (2005) 325-329.

152. C. F. Naude , A. T. Ellis, *On the Mechanism of Cavitation Damage by Non-Hemispherical Cavities in Contact with a Solid Boundary*, Journal of Basic Engineering **83** (1961) 648-656.

153. A. Henglein, D. Herburger , M. Gutiérrez, *Sonochemistry: Some Factors That Determine the Ability of a Liquid To Cavitate in an Ultrasonic Field*, Journal of Physical Chemistry **96** (1992) 1126-1130.

154. E. Maisonhaute, B. A. Brookes , R. G. Compton, *Surface Acoustic Cavitation Understood via Nanosecond Electrochemistry. 2. The Motion of Acoustic Bubbles*, Journal of Physical Chemistry B **106** (2002) 3166 - 3172.

155. B. E. Noltingk , E. A. Neppiras, *Cavitation produced by Ultrasonics*, Proceedings of the Physical Society. Section B **63** (1950) 674-685.

156. C. Pétrier, M.-F. Lamy, A. Francony, A. Benahcene, B. David, V. Renaudin , N. Gondrexon, *Sonochemical Degradation of Phenol in Dilute Aqueous Solutions: Comparison of the Reaction Rates at 20 and 487 kHz*, Journal of Physical Chemistry **98** (1994) 10514-10520.

157. P. R. Birkin, C. L. Delaplace , C. R. Bowen, *Electrochemical and Photographic Detection of Cavitation Phenomena within a Variable Frequency Acoustic Field*, Journal of Physical Chemistry B **102** (1998) 10885-10893.

158. E. L. Cooper , L. A. Coury, *Mass Transport in Sonovoltammetry with Evidence of Hydrodynamic Modulation from Ultrasound*, Journal of The Electrochemical Society **145** (1998) 1994-1999.

159. A. Kumar, P. R. Gogate , A. B. Pandit, *Mapping of Acoustic Streaming in Sonochemical Reactors*, Industrial & Engineering Chemistry Research **46** (2007) 4368-4373.

160. G. Madelin, D. Grucker, J.-M. Franconi , E. Thiaudiere, *Magnetic resonance imaging of acoustic streaming: Absorption coefficient and acoustic field shape estimation*, Ultrasonics **44** (2006) 272-278.

161. P. Luchini , F. Charru, *Acoustic streaming past a vibrating wall*, Physics of Fluids **17** (2005) 122106/122101-122106/122107.

162. A. Nowicki, W. Secomski , J. Wójcik, *Acoustic Streaming: Comparison of Low-Amplitude Linear Model with Streaming Velocities Measured by 32-Mhz Doppler*, Ultrasound in Medicine and Biology **23** (1997) 783-791.

163. H. Mitome, T. Kozuka , T. Tuziuti, *Effects of nonlinearity in development of acoustic streaming*, Japanese Journal of Applied Physics, Part 1: Regular Papers, Short Notes & Review Papers **34** (1995) 2584-2589.

164. M. Sato , T. Fujii, *Quantum mechanical representation of acoustic streaming and acoustic radiation pressure*, Physical Review E **64** (2001) 026311/026311-026311/026315.

165. R. Walker , C. T. Walker, *New explanation for the brightness of electrodeposits produced by ultrasound*, Ultrasonics **13** (1975) 79-82.

166. B. G. Pollet, J.-Y. Hihn , T. J. Mason, *Sono-electrodeposition (20 and 850 kHz) of copper in aqueous and deep eutectic solvents*, Electrochimica Acta **53** (2008) 4248–4256.

167. J. Klíma , C. Bernard, *Sonoassisted electrooxidative polymerisation of salicylic acid: role of acoustic streaming and microjetting*, Journal of Electroanalytical Chemistry **462** (1999) 181 - 186.

168. C. Costa, J.-Y. Hihn, M. Rebetez, M.-L. Doche, I. Bisel , P. Moisy, *Transport-limited current and microsonoreactor characterization at 3 low frequencies in the presence of water, acetonitrile and imidazolium-based ionic liquids*, Physical Chemistry Chemical Physics **10** (2008) 2149-2158.

169. J. Reisse, T. Caulier, C. Deckerkheer, O. Fabre, J. Vandercammen, J. L. Delplancke , R. Winand, *Quantitative sonochemistry*, Ultrasonics Sonochemistry **3** (1996) S147-S151.

170. X.-F. Qiu, J.-Z. Xu, J.-M. Zhu, J.-J. Zhu, S. Xu , H.-Y. Chen, *Controllable synthesis of palladium nanoparticles via a simple sonoelectrochemical method*, Journal of Materials Research **18** (2003) 1399 - 1404.

171. B. Yin, H. Ma, S. Wang , S. Chen, *Electrochemical Synthesis of Silver Nanoparticles under Protection of Poly(N-vinylpyrrolidone)*, Journal of Physical Chemistry B **107** (2003) 8898 - 8904.

172. J. González-García, M. D. Esclapez, P. Bonete, Y. V. Hernández, L. G. Garretón , V. Sáez, *Current topics on sonoelectrochemistry*, Ultrasonics **50** (2010) 318–322.

173. M. A. Margulis , I. M. Margulis, *Calorimetric method for measurement of acoustic power absorbed in a volume of a liquid*, Ultrasonics Sonochemistry **10** (2003) 343-345.

174. I. M. Margulis , M. A. Margulis, *Measurement of Acoustic Power in Studying Cavitation Processes*, Acoustical Physics **51** (2005) 695-704.

175. P. R. Birkin, D. G. Offin, P. F. Joseph , T. G. Leighton, *Cavitation, Shock Waves and the Invasive Nature of Sonoelectrochemistry*, Journal of Physical Chemistry B **109** (2005) 16997-17005.

176. C. E. Banks, R. G. Compton, A. C. Fisher , I. E. Henley, *The transport limited currents at insonated electrodes*, Physical Chemistry Chemical Physics **6** (2004) 3147 - 3152.

177. I. E. Henley, A. C. Fisher, R. G. Compton , C. E. Banks, *Computational Electrochemistry: Finite Element Simulation of a Disk Electrode with Ultrasonic Acoustic Streaming*, Journal of Physical Chemistry B **109** (2005) 7843 - 7849.

178. B. G. Pollet, J.-Y. Hihn, M.-L. Doche, J. P. Lorimer, A. Mandroyan , T. J. Mason, *Transport Limited Currents Close to an Ultrasonic Horn Equivalent Flow Velocity Determination*, Journal of The Electrochemical Society **154** (2007) E131-E138.

179. T. Lampke, B. Wielage, D. Dietrich , A. Leopold, *Details of crystalline growth in co-deposited electroplated nickel films with hard (nano)particles*, Applied Surface Science **253** (2006) 2399-2408.

180. M. E. Hyde , R. G. Compton, *Theoretical and experimental aspects of electrodeposition under hydrodynamic conditions*, Journal of Electroanalytical Chemistry **581** (2005) 224 - 230.

181. S. Floate, M. Hyde , R. G. Compton, *Electrochemical and AFM studies of the electrodeposition of cobalt on glassy carbon: an analysis of the effect of ultrasound*, Journal of Electroanalytical Chemistry **523** (2002) 49 - 63.

182. T. Ramgopal, P.Schmutz , G. S. Frankel, *Electrochemical Behavior of thin film analogs of Mg(Zn, Cu, Al)$_2$*, Journal of the Electrochemical Society **148** (2001) B348 - B356.

183. J. Erlebacher, M. J. Aziz, A. Karma, N. Dimitrov , K. Sieradzki, *Evolution of nanoporosity in dealloying*, Nature **410** (2001) 450-453.

184. A. Dursun, D. V. Pugh , S. G. Corcoran, *Probing the Dealloying Critical Potential: Morphological Characterization and Steady-State Current Behavior*, Journal of the Electrochemical Society **152** (2005) B65-B72.

185. A. Dursun, D. V. Pugh , S. G. Corcoran, *A Steady-State Method for Determining the Dealloying Critical Potential*, Electrochemical and Solid-State Letters **6** (2003) B32-B34.

186. K. Sieradzki, N. Dimitrov, D. Movrin, C. McCall, N. Vasiljevic , J. Erlebacher, *The dealloying critical potential*, Journal of the Electrochemical Society **149** (2002) B370 - B377.

187. J. Erlebacher, *An Atomistic Description of Dealloying - Porosity Evolution, the Critical Potential, and Rate-Limiting Behavior*, Journal of the Electrochemical Society **151** (2004) C614-C626.

188. J. Erlebacher , K. Sieradzki, *Pattern formation during dealloying*, Scripta Metallurgica et Materialia **49** (2003) 991-996.

189. A. J. Forty, *Corrosion micromorphology of noble metal alloys and depletion gilding*, Nature **282** (1979) 597-598.

190. R. G. Buchheit, *A compilation of corrosion potentials reported for intermetallic phases in aluminum alloys*, Journal of the Electrochemical Society **142** (1995) 3994 - 3996.

191. R. G. Buchheit, L. P. Montes, M. A. Martinez, J. Michael , P. F. Hlava, *The Electrochemical Characteristics of Bulk-Synthesized Al_2CuMg*, Journal of the Electrochemical Society **146** (1999) 4424-4428.

192. Y. Liu, M. A. Arenas, P. Skeldon, G. E. Thompson, P. Bailey, T. C. Q. Noakes, H. Habazaki , K. Shimizu, *Anodic behaviour of a model second phase: Al–20at.%Mg–20at.%Cu*, Corrosion Science **48** (2006) 1225 - 1248.

193. C. Blanc, A. Freulon, M.-C. Lafont, Y. Kihn , G. Mankowski, *Modelling the corrosion behaviour of Al_2CuMg coarse particles in copper-rich aluminium alloys*, Corrosion Science **48** (2006) 3838 - 3851.

194. Y. Yoon , R. G. Buchheit, *Dissolution Behavior of Al_2CuMg (S Phase) in Chloride and Chromate Conversion Coating Solutions*, Journal of the Electrochemical Society **153** (2006) B151 - B155.

195. J.-B. Jorcin, C. Blanc, N. Pébère, B. Tribollet , V. Vivier, *Galvanic Coupling Between Pure Copper and Pure Aluminum - Experimental Approach and Mathematical Model*, Journal of the Electrochemical Society **155** (2008) C46-C51.

196. C.-M. Liao , R. P. Wei, *Galvanic coupling of model alloys to aluminum — a foundation for understanding particle-induced pitting in aluminum alloys*, Electrochimica Acta **45** (1999) 881-888.

197. W. J. Clark, J. D. Ramsey, R. L. McCreery , G. S. Frankel, *A Galvanic Corrosion Approach to Investigating Chromate Effects on Aluminum Alloy 2024-T3*, Journal of the Electrochemical Society **149** (2002) B179-B185.

198. M. Iannuzzi, J. Kovac , G. S. Frankel, *A study of the mechanisms of corrosion inhibition of AA2024-T3 by vanadates using the split cell technique*, Electrochimica Acta **52** (2007) 4032-4042.

199. Y. Ding, Y.-J. Kim , J. Erlebacher, *Nanoporous gold leaf: "Ancient technology"/advanced material*, Advanced Materials **16** (2004) 1897-1900.

200. M. Stratmann , M. Rohwerder, *A pore view of corrosion*, Nature **410** (2001) 420-423.

201. Y. Ding , J. Erlebacher, *Nanoporous Metals with Controlled Multimodal Pore Size Distribution*, Journal of the American Chemical Society **125** (2003) 7772-7773.

202. A. Dursun, D. V. Pugh , S. G. Corcoran, *Dealloying of Ag-Au Alloys in Halide-Containing Electrolytes: Affect on Critical Potential and Pore Size*, Journal of the Electrochemical Society **150** (2003) B355-B360.

203. R. G. Buchheit, M. A. Martinez , L. P. Montes, *Evidence for Cu Ion Formation by Dissolution and Dealloying the Al_2CuMg Intermetallic Compound in Rotating Ring-Disk Collection Experiments*, Journal of the Electrochemical Society **147** (2000) 119 -124.

204. N. Birbilis , R. G. Buchheit, *Electrochemical Characteristics of Intermetallic Phases in Aluminum Alloys - An Experimental Survey and Discussion*, Journal of the Electrochemical Society **152** (2005) B140-B151.

205. J. Idrac, C. Blanc, Y. Kihn, M. C. Lafont, G. Mankowski, P. Skeldon , G. E. Thompson, *Electrochemical Behavior of Magnetron-Sputtered Al–Cu Alloy Films in Sulfate Solutions*, Journal of the Electrochemical Society **154** (2007) C286 - C293.

206. J. Idrac, G. Mankowski, G. Thompson, P. Skeldon, Y. Kihn , C. Blanc, *Galvanic corrosion of aluminium–copper model alloys*, Electrochimica Acta **52** (2007) 7626–7633.

207. Y. Liu, M. A. Arenas, P. Skeldon, G. E. Thompson, H. Habazaki, K. Shimizu, P. Bailey , T. C. Q. Noakes, *Generation of copper nanoparticles during alkaline etching of an Al–30 at.%Cu alloy*, Corrosion Science **48** (2006) 1874 - 1884.

208. Y. Liu, M. A. Arenas, S. J. Garcia-Vergara, T. Hashimoto, P. Skeldon, G. E. Thompson, H. Habazaki, P. Bailey , T. C. Q. Noakes, *Behaviour of copper during alkaline corrosion of Al–Cu alloys*, Corrosion Science **50** (2008) 1475–1480.

209. N. A. Missert, R. G. Copeland, J. C. Barbour, J. E. Mikkalson , H. S. Isaacs, *In-Situ Fluorescence Microscopy of Al Thin Film Corrosion at Engineered Cu islands*, in *Corrosion and Corrosion Prevention of Low Density Metals and Alloys*, R. G. Buchheit, B. A. Shaw (eds.), **PV 2000-23**, 239-246, The Electrochemical Society Proceedings Series, Pennington, NJ (2001).

210. J. W. Schultze , A. Bressel, *Principles of electrochemical micro- and nano-system technologies*, Electrochimica Acta **47** (2001) 3-21.

211. T. Li, L. Su, W. Hu, H. Dong, Y. Li , L. Mao, *Femtoliter and Attoliter Electrochemical Cells on Chips*, Analytical Chemistry **82** (2010) 1521-1526.

212. F.-M. Boldt, J. Heinze, M. Diez, J. Petersen , M. Börsch, *Real-Time pH Microscopy down to the Molecular Level by Combined Scanning Electrochemical Microscopy/Single-Molecule Fluorescence Spectroscopy*, Analytical Chemistry **76** (2004) 3473-3481.

213. N. Baltes, L. Thouin, C. Amatore , J. Heinze, *Imaging Concentration Profiles of Redox-Active Species with Nanometric Amperometric Probes: Effect of Natural Convection on Transport at Microdisk Electrodes*, Angewandte Chemie International Edition **43** (2004) 1431-1435.

214. D. W. M. Arrigan, *Nanoelectrodes, nanoelectrode arrays and their applications*, The Analyst **129** (2004) 1157-1165.

215. Y. Li, D. Bergman , B. Zhang, *Preparation and Electrochemical Response of 1-3 nm Pt Disk Electrodes*, Analytical Chemistry **81** (2009) 5496–5502.

216. J. Li, J. E. Koehne, A. M. Cassell, H. Chen, H. T. Ng, Q. Ye, W. Fan, J. Han , M. Meyyappan, *Inlaid Multi-Walled Carbon Nanotube Nanoelectrode Arrays for Electroanalysis*, Electroanalysis **17** (2005) 15-27.

217. R. G. Compton, G. G. Wildgoose, N. V. Rees, I. Streeter , R. Baron, *Design, fabrication, characterisation and application of nanoelectrode arrays*, Chemical Physics Letters **459** (2008) 1-17.

218. B. B. Rodriguez, A. J. Smith , A. W. Hassel, *Electrodeposition of gold on tungsten nanowires present in NiAl–W eutectics*, Journal of The Electrochemical Society **618** (2008) 11-16.

219. B. B. Rodriguez , A. W. Hassel, *Passivity of a Nanostructured Directionally Solidified NiAl–Re Alloy as Substrate for Electrodeposition of Gold*, Journal of The Electrochemical Society **155** (2008) K31-K37.

220. A. Errachid, C. A. Mills, M. Pla-Roca, M. J. Lopez, G. Villanueva, J. Bausells, E. Crespo, F. Teixidor , J. Samitier, *Focused ion beam production of nanoelectrode arrays*, Materials Science and Engineering C **28** (2008) 777-780.

221. P. Hugelmann, M. Hugelmann , W. Schindler, *Electrochemical nanoelectrodes for advanced investigations of nanostructures*, Journal of Electroanalytical Chemistry **612** (2008) 131-139.

222. A. Schulte , W. Schuhmann, *Single-Cell Microelectrochemistry*, Angewandte Chemie International Edition **46** (2007) 8760 – 8777.

223. E. J. F. Dickinson , R. G. Compton, *Diffuse Double Layer at Nanoelectrodes*, Journal of Physical Chemistry C **113** (2009) 17585–17589.

224. R. C. Newman , M. A. A. Ajjawi, *A Micro-Electrode Study of the Nitrate Effect on Pitting of Stainless Steels*, Corrosion Science **26** (1986) 1057-1063.

225. A. M. Riley, D. B. Wells , D. E. Williams, *Initiation Events for Pitting Corrosion of Stainless Steel?*, Corrosion Science **32** (1991) 1307-1313.

226. P. C. Pistorius , G. T. Burstein, *Aspects of The Effects of Electrolyte Composition on the Occurrence of Metastable Pitting on Stainless Steel*, Corrosion Science **36** (1994) 525-538.

227. G. T. Burstein , G. O. Ilevbare, *The Effect of Specimen Size on the Measured Pitting Potential of Stainless Steel*, Corrosion Science **38** (1996) 2257-2265.

228. R. Ullmann, T. Will , D. M. Kolb, *Nanoscale decoration of Au(111) electrodes with Cu clusters by an STM*, Chemical Physics Letters **209** (1993) 239-242.

229. R. Ullmann, T. Will , D. M. Kolb, *Nanostructuring of Electrode Surfaces by Tip-Induced Metal Deposition*, Berichte der Bunsengesellschaft für Physikalische Chemie **99** (1995) 1414-1420.

230. G. E. Engelmann, J. C. Ziegler , D. M. Kolb, *Nanofabrication of Small Palladium Clusters on Au(111) Electrodes with a Scanning Tunnelling Microscope*, Journal of The Electrochemical Society **145** (1998) L33-L35.

231. G. E. Engelmann, J. C. Ziegler , D. M. Kolb, *Electrochemical fabrication of large arrays of metal nanoclusters*, Surface Science **401** (1998) L420-L424.

232. Y.-M. Wei, X.-S. Zhou, J.-G. Wang, J. Tang, B.-W. Mao , D. M. Kolb, *The Creation of Nanostructures on an Au(111) Electrode by Tip-Induced Iron Deposition from an Ionic Liquid*, small **4** (2008) 1355-1358.

233. J.-G. Wang, J. Tang, Y.-C. Fu, Y.-M. Wei, Z.-B. Chen , B.-W. Mao, *STM tip-induced nanostructuring of Zn in an ionic liquid on Au(111) electrode surfaces*, Electrochemistry Communications **9** (2007) 633-638.

234. W. Schindler, D. Hofmann , J. Kirschner, *Nanoscale electrodeposition: A new route to magnetic nanostructures?*, Journal of Applied Physics **87** (2000) 7007-7009.

235. W. Schindler, P. Hugelmann, M. Hugelmann , F. X. Kärtner, *Localized electrochemical nucleation and growth of low-dimensional metal structures*, Journal of Electroanalytical Chemistry **522** (2002) 49-57.

236. R. Schuster, V. Kirchner, P. Allongue , G. Ertl, *Electrochemical Micromachining*, Science **289** (2000) 98-101.

237. R. Schuster, *Electrochemical Microstructuring with Short Voltage Pulses*, ChemPhysChem **8** (2007) 34-39.

238. E. M. Moustafa, O. Mann, W. Fürbeth , R. Schuster, *Electrochemical Behaviour of Iron in a Third-Generation Ionic Liquid: Cyclic Voltammetry and Micromachining Investigations*, ChemPhysChem **10** (2009) 3090-3096.

239. X. Ma, A. Bán , R. Schuster, *Electrochemical Machining of Gold Microstructures in LiCl/Dimethyl Sulfoxide*, ChemPhysChem **11** (2010) 616-621.

240. V. Kirchner, L. Cagnon, R. Schuster , G. Ertl, *Electrochemical machining of stainless steel microelements with ultrashort voltage pulses*, Applied Physics Letters **79** (2001) 1721-1723.

241. M. Kock, V. Kirchner , R. Schuster, *Electrochemical micromachining with ultrashort voltage pulses - a versatile method with lithographical precision*, Electrochimica Acta **48** (2003) 3213-3219.

242. A. L. Trimmer, J. L. Hudson, M. Kock , R. Schuster, *Single-step electrochemical machining of complex nanostructures with ultrashort voltage pulses*, Applied Physics Letters **82** (2003) 3327-3329.

243. O. de Abril, A. Gündel, F. Maroun, P. Allongue , R. Schuster, *Single-step electrochemical nanolithography of metal thin films by localized etching with an AFM tip*, Nanotechnology **19** (2008) 325301/325301-325307.

244. V. Kirchner, X. Xia , R. Schuster, *Electrochemical Nanostructuring with Ultrashort Voltage Pulses*, Accounts of chemical research **34** (2001) 371-377.

245. P. Chao, D. Ammann, U. Oesch, W. Simon , F. Lang, *Extra- and intracellular hydrogen ion-selective microelectrode based on neutral carriers with extended pH response range in acid media*, Pflügers Archiv: European Journal of Physiology (Pflugers Archiv) **411** (1988) 216 - 219.

246. R. J. Reid , F. A. Smith, *Measurements of the Cytoplasmic pH of Chara corallina using Double-barrelled pH Micro-electrodes*, Journal of Experimental Botany **39** (1988) 1421-1432.

247. D. J. Walker, S. J. Smith , A. J. Miller, *Simultaneous Measurement of lntracellular pH and K^+ or NO_3^- in Barley Root Cells Using Triple-Barreled, lon-Selective Microelectrodes*, Plant Physiology **108** (1995) 743-751.

248. E. Klusmann , J. W. Schultze, *pH-Microscopy: technical application in phosphating solutions*, Electrochimica Acta **48** (2003) 3325-3332.

249. J. O. Park, C.-H. Paik , R. C. Alkire, *Scanning Microsensors for Measurement of Local pH Distributions at the Microscale*, Journal of the Electrochemical Society **143** (1996) L174-L176.

250. H. Lajain, *Das elektrochemische Verhalten von Schweißverbindungen*, Werkstoffe und Korrosion **23** (1972) 537-545.

251. T. Suter , H. Böhni, *A new microelectrochemical method to study pit initiation on stainless steels*, Electrochimica Acta **42** (1997) 3275-3280.

252. T. Suter, T. Peter , H. Böhni, *Microelectrochemical Investigations of MnS Inclusions*, Materials Science Forum **192-194** (1995) 25-40.

253. H. Böhni, T. Suter , A. Schreyer, *Micro- and Nanotechniques to Study Localized Corrosion*, Electrochimica Acta **40** (1995) 1361-1368.

254. A. W. Hassel , M. M. Lohrengel, *The scanning droplet cell and its application to structured nanometer oxide films on aluminium*, Electrochimica Acta **42** (1997) 3327-3333.

255. A. W. Hassel, K. Fushimi , M. Seo, *An agar-based silver|silver chloride reference electrode for use in micro-electrochemistry*, Electrochemistry Communications **1** (1999) 180-183.

256. J. W. Schultze , M. M. Lohrengel, *Stability, reactivity and breakdown of passive films. Problems of recent and future research*, Electrochimica Acta **45** (2000) 2499-2513.

257. M. M. Lohrengel, A. Moehring , M. Pilaski, *Capillary-based droplet cells: limits and new aspects*, Electrochimica Acta **47** (2001) 137-141.

258. T. Suter , H. Böhni, *Microelectrodes for corrosion studies in microsystems*, Electrochimica Acta **47** (2001) 191-199.

259. A. Vogel , J. W. Schultze, *A new microcell for electrochemical surface analysis and reactions*, Electrochimica Acta **44** (1999) 3751-3759.

260. N. Birbilis, B. N. Padgett , R. G. Buchheit, *Limitations in microelectrochemical capillary cell testing and transformation of electrochemical transients for acquisition of microcell impedance data*, Electrochimica Acta **50** (2005) 3536-3544.

261. R. Oltra, B. Vuillemin, F. Thebault , F. Rechou, *Effect of the surrounding aeration on microcapillary electrochemical cell experiments*, Electrochemistry Communications **10** (2008) 848-850.

262. J.-B. Jorcin, H. Krawiec, N. Pébère , V. Vignal, *Comparison of local electrochemical impedance measurements derived from bi-electrode and microcapillary techniques*, Electrochimica Acta **54** (2009) 5775-5781.

263. L. Eng, E. Wirth, T. Suter , H. Böhni, *Non-contact feedback for scanning capillary microscopy*, Electrochimica Acta **43** (1998) 3029-3033.

264. L. Staemmler, T. Suter , H. Böhni, *Nanolithography by Means of an Electrochemical Scanning Capillary Microscope*, Journal of The Electrochemical Society **151** (2004) G734-G739.

265. F. Assi, T. Suter , H. Böhni, *A New Electrochemical Technique to Study Tribocorrosion at the Micrometric Scale*, Tribotest Journal **6** (1999) 17-28.

266. H. Böhni, T. Suter , F. Assi, *Micro-electrochemical techniques for studies of localized processes on metal surfaces in the nanometer range*, Surface and Coatings Technology **130** (2000) 80-86.

267. J. O. Park , H. Böhni, *Local pH Measurements during Pitting Corrosion at MnS Inclusions on Stainless Steel*, Electrochemical and Solid-State Letters **3** (2000) 416-417.

268. E. G. Webb , R. C. Alkire, *Pit initiation at single sulfide inclusions in stainless steel I. Electrochemical Microcell Measurements*, Journal of the Electrochemical Society **149** (2002) B272 - B279.

269. M. M. Lohrengel, C. Rosenkranz, I. Klüppel, A. Moehring, H. Bettermann, B. Van den Bossche , J. Deconinck, *A new microcell or microreactor for material surface investigations at large current densities*, Electrochimica Acta **49** (2004) 2863-2870.

270. M. Pilaski, T. Hamelmann, A. Moehring , M. M. Lohrengel, *Impedance spectroscopy in micro systems*, Electrochimica Acta **47** (2002) 2127-2134.

271. A. I. Mardare , A. W. Hassel, *Quantitative optical recognition of highly reproducible ultrathin oxide films in microelectrochemical anodization*, Review of scientific instruments **80** (2009) 046106/046101-046103.

272. H. Sugimura, T. Uchida, N. Kitamura , H. Masuhara, *Tip-induced anodization of titanium surfaces by scanning tunneling microscopy: A humidity effect on nanolithography*, Applied Physics Letters **63** (1993) 1288-1290.

273. H. Bloeß, G. Staikov , J. W. Schultze, *AFM induced formation of SiO_2 structures in the electrochemical nanocell*, Electrochimica Acta **47** (2001) 335-344.

274. T. Suter , H. Böhni, *Microelectrodes for studies of localized corrosion processes*, Electrochimica Acta **43** (1998) 2843-2849.

275. J. O. Park, T. Suter , H. Böhni, *Role of Manganese Sulfide Inclusions on Pit Initiation of Super Austenitic Stainless Steels*, Corrosion **59** (2003) 59-67.

276. J. O. Park, S. Matsch , H. Böhni, *Effects of Temperature and Chloride Concentration on Pit Initiation and Early Pit Growth of Stainless Steel*, Journal of the Electrochemical Society **149** (2002) B34-B39.

277. E. C. Webb , R. C. Alkire, *Pit initiation at single sulfide inclusions in stainless steel III. Mathematical Model*, Journal of the Electrochemical Society **149** (2002) B286 - B295.

278. I. Muto, Y. Izumiyama , N. Hara, *Microelectrochemical Measurements of Dissolution of MnS Inclusions and Morphological Observation of Metastable and Stable Pitting on Stainless Steel*, Journal of the Electrochemical Society **154** (2007) C439-C444.

279. I. Muto, D. Ito , N. Hara, *Microelectrochemical Investigation on Pit Initiation at Sulfide and Oxide Inclusions in Type 304 Stainless Steel*, Journal of the Electrochemical Society **156** (2009) C55-C61.

280. R. A. Perren, T. A. Suter, P. J. Uggowitzer, L. Weber, R. Magdowski, H. Böhni , M. O. Speidel, *Corrosion resistance of super duplex stainless steels in chloride ion containing environments: investigations by means of a new microelectrochemical method*

I. Precipitation-free states, Corrosion Science **43** (2001) 707-726.

281. R. A. Perren, T. Suter, C. Solenthaler, G. Gullo, P. J. Uggowitzer, H. Böhni , M. O. Speidel, *Corrosion resistance of super duplex stainless steels in chloride ion containing environments: investigations by means of a new microelectrochemical method*

II. Influence of precipitates, Corrosion Science **43** (2001) 727-745.

282. C.-J. Park, H.-S. Kwon , M. M. Lohrengel, *Micro-electrochemical polarization study on 25% Cr duplex stainless steel*, Materials Science and Engineering A **372** (2004) 180-185.

283. K. A. Lill, A. W. Hassel, G. Frommeyer , M. Stratmann, *Scanning droplet cell investigations on single grains of a FeAlCr light weight ferritic steel*, Electrochimica Acta **51** (2005) 978 - 983.

284. A. Schreiber, J. W. Schultze, M. M. Lohrengel, F. Kármán , E. Kálmán, *Grain dependent electrochemical investigations on pure iron in acetate buffer pH 6.0*, Electrochimica Acta **51** (2006) 2625-2630.

285. A. Schreiber, C. Rosenkranz , M. M. Lohrengel, *Grain-dependent anodic dissolution of iron*, Electrochimica Acta **52** (2007) 7738-7745.

286. S. Hodges, N. J. Laycock, D. P. Krouse, S. Virtanen, P. Schmutz , M. P. Ryan, *A Microelectrochemical Investigation of Alloy C22 in Chloride Solutions below the Critical Pitting Temperature*, Journal of the Electrochemical Society **154** (2007) C114-C119.

287. V. S. Rao , H. S. Kwon, *Corrosion Studies of Fe_3Al–Fe_3AlC Intermetallics in 0.25 N H_2SO_4 using Microelectrochemical Method and SAES Analysis*, Journal of the Electrochemical Society **154** (2007) C255-C260.

288. L. Staemmler, T. Suter , H. Böhni, *Glass Capillaries as a Tool in Nanoelectrochemical Deposition*, Electrochemical and Solid State Letters **5** (2002) C61-C63.

289. J. W. Schultze, M. Pilaski, M. M. Lohrengel , U. König, *Single crystal experiments on grains of polycrystalline materials: Oxide formation on Zr and Ta*, Faraday Discussions **121** (2002) 211-227.

290. A. I. Mardare, A. Savan, A. Ludwig, A. D. Wieck , A. W. Hassel, *A combinatorial passivation study of Ta–Ti alloys*, Corrosion Science **51** (2009) 1519–1527.

291. T. Suter, Y. Müller, P. Schmutz , O. von Trzebiatowski, *Microelectrochemical Studies of Pit Initiation on High Purity and Ultra High Purity Aluminum*, Advanced Engineering Materials **7** (2005) 339-348.

292. F. Eckermann, T. Suter, P. J. Uggowitzer, A. Afseth, M. Stampanoni, F. Marone , P. Schmutz, *In Situ Microtomographically Monitored and Electrochemically Controlled Corrosion Initiation and Propagation in AlMgSi Alloy AA6016*, Journal of the Electrochemical Society **156** (2009) C1-C7.

293. F. Eckermann, T. Suter, P. J. Uggowitzer, A. Afseth , P. Schmutz, *Investigation of the exfoliation-like attack mechanism in relation to Al–Mg–Si alloy microstructure*, Corrosion Science **50** (2008) 2085–2093.

294. F. Eckermann, P. J. Uggowitzer , P. Schmutz, *Influence of Composition and Roughness on Localized Corrosion of Al-Mg-Si alloys Characterized by Microelectrochemistry*, Materials Science Forum **519-521** (2006) 635-640.

295. F. Andreatta, M. M. Lohrengel, H. Terryn , J. H. W. d. Wit, *Electrochemical characterisation of aluminium alloy AA 7075-T6 and solution heat treated AA7075 using a micro-capillary cell*, Electrochimica Acta **48** (2003) 3239 - 3247.

296. J. Wloka , S. Virtanen, *Detection of nanoscale η-$MgZn_2$ phase dissolution from an Al-Zn-Mg-Cu alloy by electrochemicalmicrotransients*, Surface and Interface Analysis **40** (2007) 1219-1225.

297. F. Mansfeld , C. H. Tsai, *Determination of coating deterioration with EIS I. Basic Relationships*, Corrosion **47** (1991) 958-963.

298. F. Mansfeld, M. W. Kendig , C. H. Tsai, *Evaluation of corrosion behavior of coated metals with AC impedance measurements*, Corrosion **38** (1982) 478-485.

299. S. Feliu, J. C. Galvan , M. Morcillo, *The charge transfer reaction in Nyquist diagrams of painted steel* Corrosion Science **30** (1990) 989-998.

300. P.-C. Su , O. F. Devereux, *Alternating and direct current electrochemical studies of a wool wax-based corrosion preventive coating on aluminum alloy 2024.*, Corrosion **54** (1998) 419-427.

301. J. E. G. Gonzalez , J. C. M. Rosca, *Determination of the adhesion properties of an alkyd pigmented coating by electrochemical impedance spectroscopy*, Journal of Adhesion Science and Technology **13** (1999) 379-391.

302. E. P. M. van Westing, G. M. Ferrari , J. H. W. de Wit, *The determination of coating performance with impedance measurements – IV. Protective Mechanisms of Anticorrosion Pigments*, Corrosion Science **36** (1994) 1323-1346.

303. T. Picaud, M. Duprat , F. Dabosi, *Application of electrochemical impedance measurements to the study of the corrosion performance of a coated steel in 3% NaCl solution*, Materials Science Forum **8** (1986) 303-314.

304. C. Corfias, N. Pébère , C. Lacabanne, *Characterization of protective coatings by electrochemical impedance spectroscopy and a thermostimulated current method: influence of the polymer binder*, Corrosion Science **42** (2000) 1337-1350.

305. C.-T. Chen , B. S. Skerry, *Assessing the corrosion resistance of painted steel by ac impedance and electrochemical noise techniques*, Corrosion **47** (1991) 598-611.

306. F. Zou , D. Thierry, *Localized electrochemical impedance spectroscopy for studying the degradation of organic coatings*, Electrochimica Acta **42** (1997) 3293-3301.

307. V. Poulain, J.-P. Petitjean, E. Dumont , B. Dugnoille, *Pretreatments and Filiform corrosion resistance of cataphoretic painted aluminium. Characterization by EIS and spectroscopic ellipsometry*, Electrochimica Acta **41** (1996) 1223-1231.

308. R. C. MacQueen, R. R. Miron , R. D. Granata, *Methods for corrosion inhibitor mechanism studies in epoxy coated aluminum*, Journal of Coatings Technology **65** (1996) 75-82.

309. J. N. Murray, *Long-Term Electrochemical Impedance Spectroscopy and Electrochemical Evaluations of Five Distinct Types of Navy Coatings*, in *Organic Coatings for Corrosion Control*, G. P. Bierwagen (eds.), **689**, 10-22, ACS Symposium Series, Washington, DC (1998).

310. F. Mansfeld , M. W. Kendig, *Electrochemical impedance spectroscopy of protective coatings*, Materials Science Forum **8** (1986) 337-350.

311. R. B. Leggat, *Adhesion of epoxy primer to hydrotalcite conversion coated AA 2024*, Ph.D. thesis, University of Virginia (2002)

312. K. S. Cole , R. H. Cole, *Dispersion and Absorption in Dielectrics I. Alternating Current Characteristics*, Journal of Chemical Physics **9** (1941) 341-351.

313. A. K. Jonscher, *Hopping losses in polarisable dielectric media*, Nature **250** (1974) 191-193.

314. Z. Kerner , T. Pajkossy, *On the origin of capacitance dispersion of rough electrodes*, Electrochimica Acta **46** (2000) 207-211.

315. J. R. MacDonald , M. K. Brachman, *Linear-System Integral Transform Relations*, Reviews of modern physics **28** (1956) 393-422.

316. R. d. Levie, *Fractals and rough electrodes*, Journal of Electroanalytical Chemistry **281** (1990) 1-21.

317. J. B. Bessone, D. R. Salinas, C. E. Mayer, M. Ebert , W. J. Lorenz, *An EIS study of aluminium barrier-type oxide films formed in different media*, Electrochimica Acta **37** (1992) 2283-2290.

318. C. M. J.B. Bessone, K. Jüttner, W.J. Lorenz, *AC-Impedance measurements on aluminium barrier type oxide films*, Electrochimica Acta **28** (1983) 171-175.

319. D. D. MacDonald , M. C. H. McKubre, in *Impedance spectroscopy – emphasizing solid materials and systems*, J. R. Macdonald (eds.), 260–316, John Wiley and Sons, New York (1987).

320. J. B. Bessone, C. Mayer, K. Jüttner , W. J. Lorenz, *AC-Impedance measurements on aluminium barrier type oxide films*, Electrochimica Acta **28** (1983) 171-175.

321. B. B. Katemann, C. G. Inchauspe, P. A. Castro, A. Schulte, E. J. Calvo , W. Schuhmann, *Precursor sites for localised corrosion on lacquered tinplates visualised by means of*

alternating current scanning electrochemical microscopy, Electrochimica Acta **48** (2003) 1115-1121.

322. E. Bayet, F. Huet, M. Keddam, K. Ogle , H. Takenouti, *A novel way of measuring local electrochemical impedance using a single vibrating probe*, Journal of the Electrochemical Society **144** (1997) L87 - L90.

323. E. Bayet, F. Huet, M. Keddam, K. Ogle , H. Takenouti, *Local electrochemical impedance measurement: scanning vibrating electrode technique in ac mode*, Electrochimica Acta **44** (1999) 4117-4127.

324. M. W. Wittmann, R. B. Leggat , S. R. Taylor, *The Detection and Mapping of Defects in Organic Coatings Using Local Electrochemical Impedance Methods*, Journal of the Electrochemical Society **146** (1999) 4071-4075.

325. R. S. Lillard, P. J. Moran , H. S. Isaacs, *A Novel Method for Generating Quantitative Local Electrochemical Impedance Spectroscopy*, Journal of the Electrochemical Society **139** (1992) 1007-1012.

326. R. Feser , M. Stratmann, *An electrochemical study of the corrosion of polymer coated iron*, Steel Research **61** (1990) 482-489.

327. F. Mansfeld, S. L. Jeanjaquet , M. W. Kendig, *An electrochemical impedance spectroscopy study of reactions at the metal/coating interface*, Corrosion Science **26** (1986) 735-742.

328. J. Fleig , J. Maier, *Finite element calculations of impedance effects at point contacts*, Electrochimica Acta **41** (1996) 1003 - 1009.

329. D. A. Buttry , M. D. Ward, *Measurement of Interfacial Processes at Electrode Surfaces with the Electrochemical Quartz Crystal Microbalance*, Chemical Reviews **92** (1992) 1355 - 1379.

330. V. Tsionsky, L. Daikhin, M. Urbakh , E. Gileadi, *Looking at the Metal/Solution Interface with the Electrochemical Quartz Crystal Microbalance: Theory and Experiment*, in *Electroanalytical chemistry: a series of advances*, A. J. Bard, I. Rubinstein (eds.), **22**, 1 - 99, (2004).

331. S. Bruckenstein , M. Shay, *Experimental Aspects of Use of the Quartz Crystal Microbalance in Solution*, Electrochimica Acta **30** (1985) 1295-1300.

332. G. Sauerbrey, *Verwendung von Schwingquarzen zur Wägung dünner Schichten und zur Mikrowägung*, Zeitschrift für Physik **155** (1959) 206-222.

333. R. S. Weis , T. K. Gaylord, *Lithium niobate: summary of physical properties and crystal structure*, Applied Physics A: Solids and Surfaces **37** (1985) 191-203.

334. T. Yamada, N. Niizeki , H. Toyoda, *Piezoelectric and Elastic Properties of Lithium Niobate Single Crystals*, Japanese Journal of Applied Physics **6** (1967) 151-155.

335. I. A. Andreev, *Two Decades Following the Discovery of Thermally Stable Elastic Properties of $La_3Ga_5SiO_{14}$ Crystal and Coining of the Term "Langasite"*, Technical Physics **49** (2004) 1101–1103.

336. H. Fritze , H. L. Tuller, *Langasite for high-temperature bulk acoustic wave applications*, Applied Physics Letters **78** (2001) 976-977.

337. H. Fritze, *High temperature piezoelectric materials: Defect chemistry and electro-mechanical properties*, Journal of Electroceramics **17** (2006) 625–630.

338. H. Fritze, H. Seh, H. L. Tuller , G. Borchardt, *Operation limits of langasite high temperature nanobalances*, Journal of the European Ceramic Society **21** (2001) 1473-1477.

339. H. Fritze, O. Schneider, H. Seh, H. L. Tuller , G. Borchardt, *High temperature bulk acoustic wave properties of langasite*, Physical Chemistry Chemical Physics **3** (2003) 5207–5214.

340. E. Philippot, A. Ibanez, A. Goiffon, M. Cochez, A. Zarka, B. Capelle, J. Schwartzel , J. Détaint, *A quartz-like material: gallium phosphate (GaPO4); crystal growth and characterization*, Journal of Crystal Growth **130** (1993) 195-208.

341. A. L. Kipling , M. Thompson, *Network Analysis Method Applied to Liquid-Phase Acoustic Wave Sensors*, Analytical Chemistry **62** (1990) 1514-1519.

342. A. Glidle, A. R. Hillman , S. Bruckenstein, *Dynamic film rigidity observations during electrochemical deposition of polybithiophene films*, Journal of Electroanalytical Chemistry **318** (1991) 411-420.

343. A. Bund , G. Schwitzgebel, *Investigations on metal depositions and dissolutions with an improved EQCMB based on quartz crystal impedance measurements*, Electrochimica Acta **45** (2000) 3703–3710.

344. S. J. Martin, V. Edwards Granstaff , G. C. Frye, *Characterization of a Quartz Crystal Microbalance with Simultaneous Mass and Liquid Loading*, Analytical Chemistry **63** (1991) 2272-2281.

345. K.-J. Choi, Y. H. Kim, S. M. Chang, A. Egawa , H. Muramatsu, *Characterization of aluminum corrosion with a quartz crystal analyzer*, Analytica Chimica Acta **386** (1999) 229-236.

346. R. Lucklum, C. Behling, R. W. Cernosek , S. J. Martin, *Determination of complex shear modulus with thickness shear mode resonators*, Journal of Physics D: Applied Physics **30** (1997) 346 - 356.

347. H. L. Bandey, M. Gonsalves, A. R. Hillman, A. Glidle , S. Bruckenstein, *Dynamic quartz crystal impedance measurements of polyvinylferrocene film deposition*, Journal of Electroanalytical Chemistry **410** (1996) 219-227.

348. H. L. Bandey, A. R. Hillman, M. J. Brown , S. J. Martin, *Viscoelastic characterization of electroactive polymer films at the electrode/solution interface*, Faraday Discussions **107** (1997) 105-121.

349. L. Daikhin, E. Gileadi, G. Katz, V. Tsionsky, M. Urbakh , D. Zagidulin, *Influence of Roughness on the Admittance of the Quartz Crystal Microbalance Immersed in Liquids*, Analytical Chemistry **74** (2002) 554-561.

350. T. Nomura , M. Lijima, *Electrolytic Determination of Nanomolar Concentrations of Silver in Solution with a Piezoelectric Quartz Crystal*, Analytica Chimica Acta **131** (1981) 97-102.

351. T. Nomura , M. Okuhara, *Frequency Shifts of Piezoelectric Quartz Crystals Immersed in Organic Liquids*, Analytica Chimica Acta **142** (1982) 281-284.

352. K. Kanazawa , J. G. Gordon II, *The oscillation frequency of a quartz resonator in contact with a liquid*, Analytica Chimica Acta **175** (1985) 99 - 105.

353. S. Bruckenstein , S. Swathrrajan, *Potential Dependence of Lead and Silver Underpotential Coverages in Acetonitrile using a Piezoelectric Crystal Oscillator Method*, Electrochimica Acta **30** (1985) 851-855.

354. R. Lucklum, C. Behling , P. Hauptmann, *Gravimetric and non-gravimetric chemical quartz crystal resonators*, Sensors and Actuators B: Chemical **65** (2000) 277–283.

355. D. Johannsmann, K. Mathauer, G. Wegner , W. Knoll, *Viscoelastic properties of thin films probed with a quartz-crystal resonator*, Physical Review B **65** (1992) 7808-7815.

356. A. R. Hillman , A. Glidle, *Electroactive bilayers employing conducting polymers Part 6. Kinetic electrochemical quartz crystal microbalance measurements*, Physical Chemistry Chemical Physics **3** (2001) 3447-3458.

357. C. Dusemund , G. Schwitzgebel, *Investigations on conducting polymer films with a fast electrochemical quartz crystal microbalance*, Berichte der Bunsengesellschaft für Physikalische Chemie **95** (1991) 1543-1546.

358. D. Giménez-Romero, C. Gabrielli, J. J. García-Jareño, H. Perrot , F. Vicente, *Electrochemical Quartz Crystal Microbalance Study of Copper Electrochemical Reaction in Acid Medium Containing Chlorides*, Journal of The Electrochemical Society **153** (2006) J32 - J39.

359. Y. Hoshino, T. Kawasaki , Y. Okahata, *Effect of Ultrasound on DNA Polymerase Reactions: Monitoring on a 27-MHz Quartz Crystal Microbalance*, Biomacromolecules **7** (2006) 682 - 685.

360. C. Arkam, V. Bouet, C. Gabrielli, G. Maurin , H. Perrot, *Quartz Crystal Electrogravimetry with Controlled Hydrodynamics*

Applications to the Study of Nickel Electrodeposition, Journal of The Electrochemical Society **141** (1994) L103-L105.

361. P. Kern , D. Landolt, *Design and Characterization of a Rotating Electrochemical Quartz-Crystal-Microbalance Electrode*, Journal of The Electrochemical Society **147** (2000) 318-325.

362. M. I. Jeffrey, J. Zheng , I. M. Ritchie, *The development of a rotating electrochemical quartz crystal microbalance for the study of leaching and deposition of metals*, Measurement Science and Technology **11** (2000) 560-567.

363. A. Marlot , J. Vedel, *Electrodeposition of Copper-Selenium Compounds onto Gold Using a Rotating Electrochemical Quartz Crystal Microbalance*, Journal of The Electrochemical Society **146** (1999) 177-183.

364. A. Grzegorzewski , K. E. Heusler, *A Kinetic Investigation Of The Manganese Dioxide Electrode With A Rotating Quartz Frequency Balance*, Journal of Electroanalytical Chemistry **228** (1987) 455-470.

365. S. Matić, O. Schneider , C. Argirusis, *An in-situ EQCM study of sonoelectrochemical deposition of metallic materials*, in *Proceedings of the 19th International Congress on Acoustics*, (eds.), paper ULT-12-010, Madrid (2007).

366. O. Schneider, S. Matić , C. Argirusis, *Application of the electrochemical quartz crystal microbalance technique to copper sonoelectrochemistry Part 1. Sulfate-based electrolytes*, Electrochimica Acta **53** (2008) 5485–5495.

367. O. Schneider, S. Martens, J. Zečević , C. Argirusis, *Application of the electrochemical quartz crystal microbalance technique to copper sonoelectrochemistry Part 2. Chloride-based electrolytes*, (2010) in preparation.

368. C. Argirusis, S. Matić , O. Schneider, *An EQCM study of ultrasonically assisted electrodeposition of Co/CeO_2 and Ni/CeO_2 composites for fuel cell applications*, physica status solidi (a) **205** (2008) 2400–2404.

369. O. Schneider, S. Martens , C. Argirusis, *Electrochemical Quartz Crystal Microbalance Technique in Sonoelectrochemistry*, ECS Transactions **25 (28)** (2010) 69-80.

370. S. Martens, O. Schneider , C. Argirusis, *Limits of the application of the electrochemical quartz crystal microbalance in the presence of ultrasound*, Ultrasonics Sonochemistry (2009) in preparation.

371. M. Zhou, N. Myung, X. Chen , K. Rajeshwar, *Electrochemical deposition and stripping of copper, nickel and copper nickel alloy thin films at a polycrystalline gold surface: a combined voltammetry-coulometry-electrochemical quartz crystal microgravimetry study*, Journal of Electroanalytical Chemistry **398** (1995) 5-12.

372. E. Mattsson , J. O. M. Bockris, *Galvanostatic studies of the kinetics of deposition and dissolution in the copper + copper sulphate system*, Transactions of the Faraday Society **55** (1959) 1586 - 1601.

373. A. Jardy, A. L. Lasalle-Molin, M. Keddam , H. Takenouti, *Copper Dissolution in Acidic Sulphate Media studied by QCM and RRDE Under ac Signal*, Electrochimica Acta **37** (1992) 2195-2201.

374. R. Winand, *Electrodeposition of Metals and Alloys-New Results and Perspectives*, Electrochimica Acta **39** (1994) 1091-1105.

375. T. Kekesi , M. Isshiki, *Electrodeposition of copper from pure cupric chloride hydrochloric acid solutions*, Journal of Applied Electrochemistry **27** (1997) 982 - 990.

376. S. N. Ovchinnikova, T. P. Aleksandrova , A. A. Vais, *Copper in Acid Chloride Solutions: Electrochemical Behavior by Quartz Microgravimetry and Voltammetry*, Russian Journal of Electrochemistry **40** (2004) 755-759.

377. C. Nila , I. González, *The role of pH and Cu(II) concentration in the electrodeposition of Cu(II) in NH_4Cl solutions*, Journal of Electroanalytical Chemistry **401** (1996) 171-182.

378. A. Moreau, *Etude du mecanisme d'oxydo-reduction du cuivre dans les solutions chlorurées acides - I. Système Cu-$CuCl_2^-$*, Electrochimica Acta **26** (1981) 497-504.

379. R. Schumacher, A. Müller , W. Stöckel, *An in Situ Study on the Mechanism of the Electrochemical Dissolution of Copper in Oxygenated Sulphuric Acid-An Application of the Quartz Microbalance*, Journal of Electroanalytical Chemistry **219** (1987) 311-317.

380. D. Lee, Y. X. Gan, X. Chen , J. W. Kysar, *Influence of ultrasonic irradiation on the microstructure of Cu/Al_2O_3, CeO_2 nanocomposite thin films during electrocodeposition*, Materials Science and Engineering A - Structural Materials Properties Microstructure and Processing **447** (2007) 209 - 216.

381. O. Schneider, S. Martens , C. Argirusis, *Sonoelectrochemical Deposition of Functional Composite Layers*, in *ECS Transactions*, E. Traversa, C. Bock (eds.), **16 (25)**, 107-118, The Electrochemical Society, Pennington, New Jersey (2009).

382. F.-f. Xia, M.-h. Wu, F. Wang, Z.-y. Jia , A.-l. Wang, *Nanocomposite Ni–TiN coatings prepared by ultrasonic electrodeposition*, Current Applied Physics **9** (2009) 44-47.

383. H. Gül, F. Kılıç, S. Aslan, A. Alp , H. Akbulut, *Characteristics of electro-co-deposited Ni–Al_2O_3 nano-particle reinforced metal matrix composite (MMC) coatings*, Wear **267** (2009) 976–990.

384. V. O. Nwoko , L. L. Shreir, *Electron micrographic examination of electrodeposited dispersion-hardened nickel*, Journal of Applied Electrochemistry **3** (1973) 137-141.

385. A. Hovestad , L. J. J. Janssen, *Electrochemical codeposition of inert particles in a metallic matrix*, Journal of Applied Electrochemistry **25** (1995) 519-527.

386. C. T. J. Low, R. G. A. Wills , F. C. Walsh, *Electrodeposition of composite coatings containing nanoparticles in a metal deposit*, Surface & Coatings Technology **201** (2006) 371 - 383.

387. J. P. Celis , J. R. Roos, *Kinetics of the Deposition of Alumina Particles from Copper Sulfate Plating Baths*, Journal of The Electrochemical Society **124** (1977) 1508-1511.

388. N. Guglielmi, *Kinetics of the Deposition of Inert Particles from Electrolytic Baths*, Journal of The Electrochemical Society **119** (1972) 1009-1012.

389. J. P. Celis, J. R. Roos , C. Buelens, *A Mathematical Model for the Electrolytic Codeposition of Particles with a Metallic Matrix*, Journal of The Electrochemical Society **134** (1987) 1402-1408.

390. J. L. Valdes, *The Joseph W. Richards Summer Fellowship Report - Electrodeposition of Colloidal Particles*, Journal of The Electrochemical Society **134** (1987) 223C-225C.

391. J. Fransaer, J. P. Celis , J. R. Roos, *Analysis of the Electrolytic Codeposition of Non-Brownian Particles with Metals*, Journal of The Electrochemical Society **139** (1992) 413-425.

392. A. Takahashi, Y. Miyoshi , T. Hada, *Effect of SiO_2 Colloid on the Electrodeposition of Zinc-Iron Group Metal Alloy Composites*, Journal of The Electrochemical Society **141** (1994) 954-957.

393. D. L. Wang, J. Li, C. S. Dai , X. G. Hu, *An adsorption strength model for the electrochemical codeposition of α-Al_2O_3 particles and a Fe-P alloy*, Journal of Applied Electrochemistry **29** (1999) 437-444.

394. P. Nowak, R. P. Socha, M. Kaisheva, J. Fransaer, J.-P. Celis , Z. Stoinov, *Electrochemical investigation of the codeposition of SiC and SiO2 particles with nickel*, Journal of Applied Electrochemistry **30** (2000) 429 - 437.

395. V. Terzieva, J. Fransaer , J.-P. Celis, *Codeposition of Hydrophilic and Hydrophobic Silica with Copper from Acid Copper Sulfate Baths*, Journal of The Electrochemical Society **147** (2000) 198-202.

396. P. M. Vereecken, I. Shao , P. C. Searson, *Particle Codeposition in Nanocomposite Films*, Journal of The Electrochemical Society **147** (2000) 2572-2575.

397. C. Dedeloudis , J. Fransaer, *AFM Study of the Behavior of Polystyrene and Glass Particles during the Electrodeposition of Copper*, Langmuir **20** (2004) 11030-11038.

398. J. Lee , J. B. Talbot, *Simulation of Particle Incorporation during Electrodeposition Process - Primary and Secondary Current Distributions*, Journal of The Electrochemical Society **152** (2005) C706-C715.

399. J. Lee , J. B. Talbot, *A Model of Electrocodeposition on a Rotating Cylinder Electrode*, Journal of The Electrochemical Society **154** (2007) D70-D77.

400. M. H. Kim, M. Z. Hong, Y.-S. Kim, E. Park, H. Lee, H.-W. Ha , K. Kim, *Cobalt and cerium coated Ni powder as a new candidate cathode material for MCFC*, Electrochimica Acta **51** (2006) 6145-6151.

401. G. Cârâc, L. Benea, C. Iticescu, T. Lampke, S. Steinhäuser , B. Wielage, *Codeposition of Cerium Oxide with Nickel and Cobalt: Correlation between Microstructure and Microhardness*, Surface Engineering **20** (2004) 353-359.

402. N. S. Qu, D. Zhu , K. C. Chan, *Fabrication of Ni–CeO2 nanocomposite by electrodeposition*, Scripta Materialia **54** (2006) 1421 - 1425.

403. J.-F. Castagnet, *Herstellung und Charakterisierung von nanopartikelverstärkten elektrolytisch abgeschiedenen Nickelschichten*, Ph. D. thesis, Technische Universität Clausthal (2004)

404. J. T. Matsushima, F. Trivinho-Strixino , E. C. Pereira, *Investigation of cobalt deposition using the electrochemical quartz crystal microbalance*, Electrochimica Acta **51** (2006) 1960-1966.

405. O. Schneider, *An EQCM Study of the Corrosion of Synthetic Aluminium Alloys*, ECS Transactions **16 (52)** (2009) 13-24.

406. H. Shirakawa, *Die Entdeckung der Polyacetylenfilme - der Beginn des Zeitalters leitfähiger Polymere (Nobel-Aufsatz)*, Angewandte Chemie **113** (2001) 2642 - 2648.

407. H. Shirakawa, E. Loius, A. G. MacDiarmid, C. K. Chiang , A. J. Heeger, *Synthesis of electrically conducting organic polymers - halogen derivatives of polyacetylene, (CH)x*, Journal of the Chemical Society-Chemical Communications (1977) 578-580.

408. T. A. Skotheim, R. L. Elsenbaumer , J. R. Reynolds, *Handbook of conducting polymers*, 2nd edition, Marcel Dekker, New York (1997).

409. S. Bruckenstein, K. Brzezinska , A. R. Hillman, *EQCM studies of polypyrrole films. 1. Exposure to aqueous sodium tosylate solutions under thermodynamically permselective conditions*, Electrochimica Acta **45** (2000) 3801–3811.

410. J. Jagur-Grodzinski, *Electronically Conductive Polymers*, Polymers for Advanced Technologies **13** (2002) 615-625.

411. J. H. Kaufman, K. K. Kanazawa , G. B. Street, *Gravimetric electrochemical voltage spectroscopy: In situ mass measurements during electrochemical doping of the conducting polymer polypyrrole*, Physical Review Letters **53** (1984) 2461 - 2464.

412. C. K. Baker , J. R. Reynolds, *A quartz microbalance study of the electrosynthesis of polypyrrole*, Journal of Electroanalytical Chemistry **251** (1988) 307-322.

413. V. M. Schmidt , J. Heitbaum, *Ion Exchange Mechanism of Polypyrrole and Poly-N-Methylpyrrole with Toslylate as Doping Anion: An Electrochemical Quartz Crystal Microbalance Study*, Electrochimica Acta **38** (1993) 349-356.

414. K. Naoi, M. Lien , W. H. Smyrl, *Quartz Crystal Microbalance Study: Ionic Motion Across Conducting Polymers*, Journal of The Electrochemical Society **138** (1991) 440-445.

415. M. Lien, W. H. Smyrl , M. Morita, *Cation and anion insertion in separate processes in poly(pyrrole) composite films*, Journal of Electroanalytical Chemistry **309** (1991) 333-340.

416. C. K. Baker, Y.-J. Qiu , J. R. Reynolds, *Electrochemically Induced Charge and Mass Transport In Polypyrrole/Poly(styrenesulfonate) Molecular Composites*, Journal of Physical Chemistry **95** (1991) 4446-4452.

417. C. M. Lagier, I. Efimov , A. R. Hillman, *Film Resonance on Acoustic Wave Devices: The Roles of Frequency and Contacting Fluid*, Analytical Chemistry **77** (2005) 335-343.

418. M. J. Henderson, H. French, A. R. Hillman , E. Vieil, *A Combined EQCM and Probe Beam Deflection Study of Salicylate Ion Transfer at a Polypyrrole Modified Electrode*, Electrochemical and Solid-State Letters **2** (1999) 631-633.

419. S. Bruckenstein, J. Chen, I. Jureviciute , A. R. Hillman, *Ion and solvent transfers accompanying redox switching of polypyrrole films immersed in divalent anion solutions*, Electrochimica Acta **54** (2009) 3516-3525.

420. M. A. Vorotyntsev, E. Vieil , J. Heinze, *Charging process in polypyrrole films: effect of ion association*, Journal of Electroanalytical Chemistry **450** (1998) 121-141.

421. M. Zhou, M. Pagels, B. Geschke , J. Heinze, *Electropolymerization of Pyrrole and Electrochemical Study of Polypyrrole. 5. Controlled Electrochemical Synthesis and Solid-State Transition of Well-Defined Polypyrrole Variants*, Journal of Physical Chemistry B **106** (2002) 10065-10073.

422. C. Debiemme-Chouvy, A. Rubin, H. Perrot, C. Deslouis , H. Cachet, *ac-Electrogravimetry study of ionic and solvent motion in polypyrrole films doped with an heteropolyanion,* $SiMo_{12}O_40^{4-}$, Electrochimica Acta **53** (2008) 3836–3843.

423. C. Gabrielli, J. J. Garcia-Jareño , H. Perrot, *Charge compensation process in polypyrrole studied by ac electrogravimetry*, Electrochimica Acta **46** (2001) 4095–4103.

424. C. Gabrielli, H. Perrot, A. Rubin, M. C. Pham , B. Piro, *Ac-electrogravimetry study of ionic exchanges on a polypyrrole modified electrode in various electrolytes*, Electrochemistry Communications **9** (2007) 2196–2201.

425. D. Giménez-Romero, P. R. Bueno, C. Gabrielli, C. Castaño, H. Perrot, J. J. García-Jareño , F. Vicente, *Mass/charge balance as a tool to estimate dimensional change in polypyrrole-based actuators*, Electrochemistry Communications **8** (2006) 195-199.

426. A. Bund, A. Baba, S. Berg, D. Johannsmann, J. Lübben, Z. Wang , W. Knoll, *Combining Surface Plasmon Resonance and Quartz Crystal Microbalance for the in Situ Investigation of the Electropolymerization and Doping/Dedoping of Poly(pyrrole)*, Journal of Physical Chemistry B **107** (2003) 6743-6747.

427. L. E. Bailey, D. Kambhampati, K. K. Kanazawa, W. Knoll , C. W. Frank, *Using Surface Plasmon Resonance and the Quartz Crystal Microbalance to Monitor in Situ the Interfacial Behavior of Thin Organic Films*, Langmuir **18** (2002) 479-489.

428. S. Koehler, M. Ueda, I. Efimov , A. Bund, *An EQCM study of the deposition and doping/dedoping behavior of polypyrrole from phosphoric acid solutions*, Electrochimica Acta **52** (2007) 3040–3046.

429. W. Plieth, A. Bund, U. Rammelt, S. Neudeck , L. Duc, *The role of ion and solvent transport during the redox process of conducting polymers*, Electrochimica Acta **51** (2006) 2366–2372.

430. S. Koehler, A. Bund , I. Efimov, *Shear moduli of anion and cation exchanging polypyrrole films*, Journal of Electroanalytical Chemistry **589** (2006) 82-86.

431. A. F. Shepard , B. F. Dannels, *Interfacial anodic polymers from benzene in hydrogen fluoride*, Journal of Polymer Science Part A-1 Polymer Chemistry **4** (1966) 511.

432. S. Aeiyach, P. Soubiran, P. C. Lacaze, G. Froyer , Y. Pelous, *A study of the structure and morphology of poly(p-phenylene) films electrosynthesized in liquid SO_2 with different salts at low-temperatures*, Synthetic Metals **68** (1995) 213-219.

433. C. Kvarnström, R. Bilger, A. Ivaska , J. Heinze, *An electrochemical quartz crystal microbalance study on polymerization of oligo-p-phenylenes*, Electrochimica Acta **43** (1998) 355-366.

434. J. P. Lère-Porte, M. Radi, C. Chorro, J. Petrissans, J. L. Sauvajol, D. Gonbeau, G. Pfister-Guillouzo, G. Louarn , S. Lefrant, *Characterization from XPS, FT-IR and raman spectroscopies of films of poly(p-phenylene) prepared by electropolymerization of benzene dissolved in ketyl pyridinium chloride $AlCl_3$ melting salt*, Synthetic Metals **59** (1993) 141-149.

435. V. M. Kobryanskii , S. A. Arnautov, *Chemical synthesis of polyphenylene in an ionic liquid*, Synthetic Metals **55-57** (1993) 924-929.

436. S. A. Arnautov, *Electrochemical synthesis of polyphenylene in a new ionic liquid*, Synthetic Metals **84** (1997) 295-296.

437. L. M. Goldenberg , R. A. Osteryoung, *Benzene polymerization in 1-ethyl-3-methylimidazolium chloride $AlCl_3$ ionic liquid*, Synthetic Metals **64** (1994) 63-68.

438. S. Zein el Abedin, N. Borissenko , F. Endres, *Electropolymerization of benzene in a room temperature ionic liquid*, Electrochemistry Communications **6** (2004) 422-426.

439. F. Endres, *Ionic Liquids: Solvents for the Electrodeposition of Metals and Semiconductors*, ChemPhysChem **3** (2002) 144 - 154.

440. O. Schneider, A. Bund, A. Ispas, N. Borissenko, S. Z. E. Abedin , F. Endres, *An EQCM Study of the Electropolymerization of Benzene in an Ionic Liquid and Ion Exchange Characteristics of the Resulting Polymer Film*, Journal of Physical Chemistry B **109** (2005) 7159-7168.

441. http://www.ionicliquids-merck.de.

442. A. Bund, O. Schneider , V. Dehnke, *Combining AFM and EQCM for the in situ investigation of surface roughness effects during electrochemical metal depositions*, Physical Chemistry Chemical Physics **4** (2002) 3552–3554.

443. W. J. Plieth, *Electrochemical properties of small clusters of metal atoms and their role in Surface Enhanced Raman-Scattering*, Journal of Physical Chemistry **86** (1982) 3166–3170.

444. R. M. Penner, *Brownian dynamics simulations of the growth of metal nanocrystal ensembles on electrode surfaces in solution: 2. The effect of deposition rate on particle size dispersion*, Journal of Physical Chemistry B **105** (2001) 8672-8678.

445. J. B. Pawley (ed.), *Handbook of Biological confocal Microscopy*, 2nd edition, Plenum Press, New York,

London (1995).

446. N. Llorca-Isern, M. Puig , M. Espanol, *Improving the methodology for coating defects detection*, Journal of Thermal Spray Technology **8** (1999) 73 - 78.

447. F. Guillaume, L. F. Darfias-Mesias, M. Büchler , W. H. Smyrl, *Microvisualization of galvanic corrosion of AA2024 with confocal and near-field scanning optical microscopies*, in *Critical factors in Localized Corrosion III*, R. G. Kelly, G. S. Frankel, P. M. Natishan, R. C. Newman (eds.), **PV 98-17**, 155-164, The Electrochemical Society Proceedings Series, Pennington, NJ (1999).

448. X. Ling, M. D. Pritzker, J. J. Byerley , C. M. Burns, *Confocal Scanning Laser Microscopy of Polymer Coatings*, Journal of Applied Polymer Science **67** (1998) 149 - 158.

449. D. Schroth, *Konfokale Laser-Scanning-Mikroskopie*, Materialprüfung **39** (1997) 264 - 266.

450. B. V. R. Tata , B. Raj, *Confocal laser scanning microscopy: Applications in material science and technology*, Bulletin of Materials Science **21** (1998) 263 - 278.

451. S. Seiffert , W. Oppermann, *Systematic evaluation of FRAP experiments performed in a confocal laser scanning microscope*, Journal of Microscopy **220** (2005) 20 - 30.

452. J. P. H. Sukamto, W. H. Smyrl, N. Casillas, M. Al-Odan, P. James, W. Jin , L. Douglas, *Microvisualization of corrosion*, Materials Science and Engineering A **198** (1995) 177 - 196.

453. U. Ramamurty, F.-C. Dary , F. W. Zok, *A method for measuring residual strains in fiber-reinforced titanium matrix composites*, Acta materialia **44** (1996) 3397-3406.

454. W.-J. Lee, F. Guillaume, T. L. Knutson , W. H. Smyrl, *Analysis of Products at Reaction Sites by Fluorescence Microspectroscopy Using the f-NSOM Technique*, Journal of the Electrochemical Society **152** (2005) B111-B115.

455. I. L. Muller , J. R. Galvele, *Pitting potential of high purity binary aluminium alloys—I. Al-Cu alloys. Pitting and intergranular corrosion*, Corrosion Science **17** (1977) 179-193.

456. L. T. Keene, G. P. Halada , C. R. Clayton, *Failure of navy coating systems 1: chemical depth profiling of artificially and naturally weathered high-solids aliphatic poly(ester-urethane) military coating systems*, Progress in Organic Coatings **52** (2005) 173 - 186.

457. L. T. Keene, M. J. Vasquez, C. R. Clayton , G. P. Halada, *Failure of navy coating systems 2: failure pathways of artificially weathered navy coating systems applied to chromate conversion coated AA2024-T3 substrates*, Progress in Organic Coatings **52** (2005) 187 - 195.

458. S.-M. Moon, M. Sakairi , H. Takahashi, *Behavior of Second-Phase Particles in Al5052 Alloy during Anodizing in a Sulfuric Acid Solution*

CSLM Observation, Journal of the Electrochemical Society **151** (2004) B399-B405.

459. S.-M. Moon, M. Sakairi , H. Takahashi, *Application of CSLM to the Surface Morphological Study of Al 5052 Alloy Anodized in Sulfuric Acid Solution*, Journal of the Electrochemical Society **150** (2003) B473-B480.

460. H. A. Videla , L. K. Herrera, *Microbiologically influenced corrosion: looking to the future*, International Microbiology **8** (2005) 169 - 180.

461. A. Bressel, J. W. Schultze, W. Khan, G. M. Wolfaardt, H.-P. Rohns, R. Irmscher , M. J. Schöning, *High resolution gravimetric, optical and electrochemical investigations of microbial biofilm formation in aqueous systems*, Electrochimica Acta **48** (2003) 3363 - 3372.

462. G. Chen, R. J. Palmer , D. C. White, *Instrumental analysis of microbiologically influenced corrosion*, Biodegradation **8** (1997) 189 - 200.

463. A. Jayaraman, J. C. Earthman , T. K. Wood, *Corrosion inhibition by aerobic biofilms on SAE 1018 steel*, Applied Microbiology and Biotechnology **47** (1997) 62 - 68.

464. J. R. Lawrence, G. M. Wolfaardt , D. R. Korber, *Determination of Diffusion Coefficients in Biofilms by Confocal Laser Microscopy*, Applied and environmental Microbiology **60** (1994) 1166 - 1173.

465. G. Huang, K.-Y. Chan , H. H. P. Fang, *Microbiologically induced corrosion of 70Cu-30Ni alloy in anaerobic seawater*, Journal of the Electrochemical Society **151** (2004) B434 - B439.

466. J. R. Galvele, *Transport Processes and the Mechanism of Pitting of Metals*, Journal of the Electrochemical Society **123** (1976) 464-474.

467. S. T. Pride, J. R. Scully , J. L. Hudson, *Metastable Pitting of Aluminum and Criteria for the Transition to Stable Pit Growth*, Journal of the Electrochemical Society **141** (1994) 3028 - 3040.

468. K. P. Wong , R. C. Alkire, *Local Chemistry and Growth of Single Corrosion Pits in Aluminum*, Journal of the Electrochemical Society **137** (1990) 3010-3015.

469. J. R. Scully, S. T. Pride, H. S. Scully , J. Hudson, *Some Correlations Between Metastable Pitting and Pit Stabilization in Metals*, in *Critical Factors in Localized Corrosion II*, P. Natishan, R. G. Kelly, G. S. Frankel, R. C. Newman (eds.), **PV 95-15**, 15, The Electrochemical Society Proceedings Series, Pennington, NJ (1996).

470. K. Nisancioglu, *Electrochemical behavior of aluminum-base intermetallics containing iron*, Journal of the Electrochemical Society **137** (1990) 69 - 77.

471. M. Zamin, *The role of Mn in the corrosion behavior of Al-Mn alloys* Corrosion **37** (1981) 627 - 632.

472. O. Lunder , K. Nisancioglu, *The effect of alkaline-etch pretreatment on the pitting corrosion of wrought aluminum*, Corrosion **44** (1988) 414 - 422.

473. A. Kolics, A. S. Besing , A. Wiechowski, *Interaction of chromate ions with surface intermetallics on aluminum alloy 2024-T3 in NaCl solutions*, Journal of the Electrochemical Society **148** (2001) B322-B331.

474. M. L. White, H. Vedage, R. D. Granata , H. Leidheiser jr., *Failure mechanisms for organic coatings subjected to 0.1M sulfuric acid.*, Industrial & Engineering Chemistry: Product Research and Development **25** (1986) 129-132.

475. D. A. Little, M. A. Jakab , J. R. Scully, *Effect of surface pretreatment on the underpaint corrosion of AA2024-T3 at various temperatures*, Corrosion **62** (2006) 300 - 315.

476. J. M. Williams, *Mechanistic framework of localized coating failure on copper-containing aluminum alloys AA2024-T3 and AA1100-H14*, Master thesis, University of Virginia (2001)

477. K. S. Ferrer , R. G. Kelly, *Comparison of methods for removal of corrosion product from AA2024-T3*, Corrosion **57** (2004) 110-117.

478. C. Blanc , G. Mankowski, *Pit propagation rate on the 2024 and 6056 aluminium alloys*, Corrosion Science **40** (1998) 411-429.

479. H. M. Obispo, L. E. Murr, R. M. Arrowood , E. A. Trillo, *Copper deposition during the corrosion of aluminum alloy 2024 in sodium chloride solutions*, Journal of Materials Science **35** (2000) 3479 - 3495.

480. S. Szunerits , D. R. Walt, *Aluminum Surface Corrosion and the Mechanism of Inhibitors Using pH and Metal Ion Selective Imaging Fiber Bundles*, Analytical Chemistry **74** (2002) 886-894.

481. A. A. Panova, P. Pantano , D. R. Walt, *In Situ Fluorescence Imaging of Localized Corrosion with a pH-Sensitive Imaging Fiber*, Analytical Chemistry **69** (1997) 1635-1641.

482. R. C. Engstrom, S. Ghaffari , H. Qu, *Fluorescence Imaging of Electrode-Solution Interfacial Processes*, Analytical Chemistry **64** (1992) 2525-2529.

483. L. K. White, R. B. Comizzoli, C. A. Deckert , G. L. Schnable, *The detection of corrosion phenomena with pH-sensitive fluorescent dyes on aluminum- and gold-metallized IC devices*, Journal of the Electrochemical Society **128** (1981) 953-956.

484. S. R. Taylor , P. Moongkhamklang, *The delineation of local water interaction with epoxy coatings using fluorescence microscopy*, Progress in Organic Coatings **54** (2005) 205-210.

485. P. Moongkhamklang , S. R. Taylor, *The delineation of ionic pathways in organic coatings using a molecular probe technique*, Progress in Organic Coatings **46** (2003) 259-265.

486. M. P. Sibi , Z. Zong, *Determination of corrosion on aluminum alloy under protective coatings using fluorescent probes*, Progress in Organic Coatings **47** (2003) 8-15.

487. J. Zhang , G. S. Frankel, *Corrosion-sensing behavior of an acrylic-based coating system*, Corrosion **55** (1999) 957 - 967.

488. R. E. Johnson , V. S. Agarwala, *Using fluorescent compounds as early warning detectors for corrosion*, Materials Performance **33(4)** (1994) 25-29.

489. T. L. Knutson, F. Guillaume, W.-J. Lee, M. Alhoshan , W. H. Smyrl, *Reactivity of Surfaces and Imaging with functional NSOM*, Electrochimica Acta **48** (2003) 3229 - 3237.

490. R. G. Buchheit, M. Cunningham, H. Jensen, M. W. Kendig , M. A. Martinez, *A correlation between salt spray and electrochemical impedance spectroscopy test results for conversion-coated aluminum alloys*, Corrosion **54** (1998) 61-72.

491. L. Xia , R. L. McCreery, *Chemistry of a chromate conversion coating on aluminum alloy AA2024-T3 probed by vibrational spectroscopy*, Journal of the Electrochemical Society **145** (1998) 3083 - 3089.

492. J. Zhao, G. Frankel , R. L. McCreery, *Corrosion protection of untreated AA2024-T3 in chloride solution by a chromate conversion coating monitored with Raman spectroscopy*, Journal of the Electrochemical Society **145** (1998) 2258-2264.

493. J. D. Ramsey , R. L. McCreery, *In Situ Raman Microscopy of Chromate Effects on Corrosion Pits in Aluminum Alloy*, Journal of the Electrochemical Society **146** (1999) 4076-4081.

494. L. Xia , R. L. McCreery, *Structure and Function of Ferricyanide in the Formation of Chromate Conversion Coatings on Aluminum Aircraft Alloy*, Journal of the Electrochemical Society **146** (1999) 3696-3701.

495. W. R. McGovern, P. Schmutz, R. G. Buchheit , R. L. McCreery, *Formation of Chromate Conversion Coatings on Al-Cu-Mg Intermetallic Compounds and Alloys*, Journal of the Electrochemical Society **147** (2000) 4494-4501.

496. L. Xia, E. Akiyama, G. Frankel , R. McCreery, *Storage and Release of Soluble Hexavalent Chromium from Chromate Conversion Coatings: Equilibrium Aspects of Cr^{VI} Concentration*, Journal of the Electrochemical Society **147** (2000) 2556-2562.

497. J. D. Ramsey, L. Xia, M. W. Kendig , R. L. McCreery, *Raman spectroscopic analysis of the speciation of dilute chromate solutions*, Corrosion Science **43** (2001) 1557-1572.

498. M. W. Kendig , R. G. Buchheit, *Corrosion inhibition of aluminum and aluminum alloys by soluble chromates, chromate coatings, and chromate-free coatings*, Corrosion **59** (2003) 379-400.

499. F. D. Quarto, M. Santamaria, N. Mallandrino, V. Laget, R. Buchheit , K. Shimizu, *Structural Analysis and Photocurrent Spectroscopy of CCCs on 99.99% Aluminum*, Journal of the Electrochemical Society **150** (2003) B462-B472.

500. W. Zhang , R. G. Buchheit, *Effect of ambient aging on inhibition of oxygen reduction by chromate conversion coatings*, Corrosion **59** (2003) 356-362.

501. J. D. Ramsey , R. L. McCreery, *Raman microscopy of chromate interactions with corroding aluminum alloy 2024-T3*, Corrosion Science **46** (2004) 1729-1739.

502. V. Radtke, C. Heß , J. Heinze, *Generation of platinum microstructures on non-conducting surfaces by means of the scanning electrochemical microscope (SECM)*, Electrochimica Acta **55** (2009) 416-422.

503. J. Ufheil, C. Heß, K. Borgwarth , J. Heinze, *Nanostructuring and nanoanalysis by scanning electrochemical microscopy (SECM)*, Physical Chemistry Chemical Physics **7** (2005) 3185-3190.

504. A. J. Bard , M. V. Mirkin (ed.), *Scanning Electrochemical Microscopy*, Marcel Dekker Inc., New York (2001).

505. L. Niu, Y. Yin, W. Guo, M.Lu, R. Qin , S. Chen, *Application of scanning electrochemical microscope in the study of corrosion of metals*, Journal of Materials Science **44** (2009) 4511–4521.

506. S. E. Pust, W. Maier , G. Wittstock, *Investigation of Localized Catalytic and Electrocatalytic Processes and Corrosion Reactions with Scanning Electrochemical Microscopy (SECM)*, Zeitschrift für Physikalische Chemie **222** (2008) 1463–1517.

507. M. B. Jensen, A. Guerard, D. E. Tallman , G. P. Bierwagen, *Studies of Electron Transfer at Aluminum Alloy Surfaces by Scanning Electrochemical Microscopy*, Journal of the Electrochemical Society **155** (2008) C324-C332.

508. A. Davoodi, J. Pan, C. Leygraf , S. Norgren, *The Role of Intermetallic Particles in Localized Corrosion of an Aluminum Alloy Studied by SKPFM and Integrated AFM/SECM*, Journal of the Electrochemical Society **155** (2008) C211 - C218.

509. J. C. Seegmiller , D. A. Buttry, *A SECM study of heterogenous redox activity at AA2024 surfaces*, Journal of the Electrochemical Society **150** (2003) B413 - B418.

510. H. N. McMurray, D. Williams , D. A. Worsley, *Artifacts Induced by Large-Amplitude Probe Vibrations in Localized Corrosion Measured by SVET*, Journal of the Electrochemical Society **150** (2003) B567-B573.

511. S. Rossi, M. Fedel, F. Deflorian , M. d. C. Vadillo, *Localized electrochemical techniques: Theory and practical examples in corrosion studies*, Comptes Rendus Chimie **11** (2008) 984 - 994.

512. J. He, D. E. Tallman , G. P. Bierwagen, *Conjugated Polymers for Corrosion Control: Scanning Vibrating Electrode Studies of Polypyrrole-Aluminum Alloy Interactions*, Journal of the Electrochemical Society **151** (2004) B644-B651.

513. K. Ogle, S. Morel , D. Jacquet, *Observation of Self-Healing Functions on the Cut Edge of Galvanized Steel Using SVET and pH Microscopy*, Journal of the Electrochemical Society **153** (2006) B1 - B5.

514. G. Williams , H. N. McMurray, *Localized Corrosion of Magnesium in Chloride-Containing Electrolyte Studied by a Scanning Vibrating Electrode Technique*, Journal of the Electrochemical Society **155** (2008) C340-C349.

515. N. Murer, R. Oltra, B. Vuillemin , O. Néel, *Numerical modelling of the galvanic coupling in aluminium alloys: A discussion on the application of local probe techniques*, Corrosion Science **52** (2010) 130–139.

516. E. Bayet, F. Huet, M. Keddam, K. Ogle , H. Takenouti, *Adaptation of the Scanning Vibrating Electrode Technique to ac Mode: Local Electrochemical Impedance Measurement*, Materials Science Forum **289-292** (1998) 54-68.

517. M. C. S. S. Macedo, I. C. P. Margarit-Mattos, F. L. Fragata, J.-B. Jorcin, N. Pébère , O. R. Mattos, *Contribution to a better understanding of different behaviour patterns observed with organic coatings evaluated by electrochemical impedance spectroscopy*, Corrosion Science **51** (2009) 1322–1327.

518. G. Galicia, N. Pébère, B. Tribollet , V. Vivier, *Local and global electrochemical impedances applied to the corrosion behaviour of an AZ91 magnesium alloy*, Corrosion Science **51** (2009) 1789–1794.

519. M. Stratmann , H. Streckel, *On the electrochemical corrosion of metals which are covered by thin electrolyte layers – II. Experimental results*, Corrosion Science **30** (1990) 697 - 714.

520. M. Stratmann, H. Streckel, K. T. Kim , S. Crockett, *On the electrochemical corrosion of metals which are covered by thin electrolyte layers – III The measurement of polarisation curves on metal surfaces which are covered by thin electrolyte layers*, Corrosion Science **30** (1990) 715 - 734.

521. M. Stratmann, *The investigation of the corrosion properties of metals, covered with adsorbed electrolyte layers - A new experimental technique*, Corrosion Science **27** (1987) 869-872.

522. M. Stratmann, *2005 W.R. Whitney Award Lecture: Corrosion Stability of Polymer-Coated Metals—New Concepts Based on Fundamental Understanding*, Corrosion **61** (2005) 1115 - 1126.

523. P. P. Leblanc , G. S. Frankel, *Investigation of Filiform Corrosion of Epoxy-Coated 1045 Carbon Steel by Scanning Kelvin Probe Force Microscopy*, Journal of the Electrochemical Society **151** (2003) B105-B113.

524. H. N. McMurray, G. Williams , S. O'Driscoll, *Chromate Inhibition of Filiform Corrosion on Organic Coated AA2024-T3 Studied Using the Scanning Kelvin Probe*, Journal of the Electrochemical Society **151** (2004) B406-B414.

525. K. A. Yasakau, M. L. Zheludkevich, S. V. Lamaka , M. G. S. Ferreira, *Role of intermetallic phases in localized corrosion of AA5083*, Electrochimica Acta **52** (2007) 7651–7659.

526. L. Lacroix, L. Ressier, C. Blanc , G. Mankowski, *Combination of AFM, SKPFM, and SIMS to Study the Corrosion Behavior of S-phase particles in AA2024-T351*, Journal of the Electrochemical Society **155** (2008) C131-C137.

527. L. Lacroix, L. Ressier, C. Blanc , G. Mankowski, *Statistical Study of the Corrosion Behavior of Al_2CuMg Intermetallics in AA2024-T351 by SKPFM*, Journal of the Electrochemical Society **155** (2008) C8-C15.

528. C. Costa, M.-L. Doche, J.-Y. Hihn, I. Bisel, P. Moisy , J.-M. Lévêque, *Hydrodynamic sono-voltammetry of ferrocene in [Tf2N] based ionic liquid media*, Ultrasonics **50** (2010) 323–328.